High Strain Rate Characterization of Advanced High Strength Steels

by

Alan C. Thompson

A thesis
presented to the University of Waterloo
in fulfillment of the
thesis requirement for the degree of
Master of Applied Science
in
Mechanical Engineering

Waterloo, Ontario, Canada, 2006

I hereby declare that I am the sole author of this thesis. This is a true copy of the thesis, including any required final revisions, as accepted by my examiners.

I understand that my thesis may be made electronically available to the public.

ABSTRACT

The current research has considered the characterization of the high strain rate constitutive response of three steels: a drawing quality steel (DDQ), a high strength low alloy steel (HSLA350), and a dual phase steel (DP600). The stress-strain response of these steels were measured at seven strain rates between 0.003 s^{-1} and 1500 s^{-1} (0.003, 0.1, 30, 100, 500, 1000, and 1500 s^{-1}) and temperatures of 21, 150, and 300 °C. In addition, the steels were tested in both the undeformed sheet condition and the as-formed tube condition, so that tube forming effects could be identified. After the experiments were performed, the parameters of the Johnson-Cook and Zerilli-Armstrong constitutive models were fit to the results

In order to determine the response of the steels at strain rates of 30 and 100 s^{-1}, an intermediate rate tensile experiment was developed as part of this research using an instrumented falling weight impact facility (IFWI). An Instron tensile apparatus was used to perform the experiments at lower strain rates and a tensile split-Hopkinson bar was used to perform the experiments at strain rates above 500 s^{-1}

A positive strain rate sensitivity was observed for each of the steels. It was found that, as the nominal strength of the steel increased, the strain rate sensitivity decreased. For an increase in strain rate from 0.003 to 100 s^{-1}, the corresponding increase in strength at 10% strain was found to be approximately 170, 130, and 110 MPa for DDQ, HSLA350, and DP600, respectively.

The thermal sensitivity was obtained for each steel as well, however no correlation was seen between strength and thermal sensitivity. For a rise in temperature from 21 to 300 °C, the loss in strength at 10% strain was found to be 200, 225, and 195 MPa for DDQ, HSLA350, and DP600, respectively for the 6 o'clock tube specimens.

For all of the alloys, a difference in the stress – strain behaviour was seen between the sheet and tube specimens due to the plastic work that was imparted during forming of the tube. For the DP600, the plastic work only affected the work-hardening response.

It was found that both the HSLA350 and DDQ sheet specimens exhibited an upper/lower yield stress that was amplified as the strain rate increased. Consequently the actual strength at 30 and 100 s^{-1} was obscured and the data at strain rates above 500 s^{-1} to be unusable for constitutive modeling. This effect was not observed in any of the tube specimens or the DP600 sheet specimens

For each of the steels, both the Johnson-Cook and Zerilli-Armstrong models fit the experimental data well; however, the Zerilli-Armstrong fit was slightly more accurate. Numerical models of the IFWI and the TSHB tests were created to assess whether the experimental results could be reproduced using the constitutive fits. Both numerical models confirmed that the constitutive fits were applied correctly.

ACKNOWLEDGEMENTS

Completion of this work would not have been possible without the help, guidance, and hockey related injuries that I received from my supervisor, Dr. Michael J. Worswick. I would also like to thank General Motors of Canada and Dofasco for making this reseach possible, and personally thank Dr. Robert Mayer of General Motors and Isadora Van Riemsdijk and Bruce Farrand of Dofasco for their many insights. Last, I would like to thank Richard Sparks of Imatek, for commissioning the IFWI and teaching me how to use it safely and effectively.

I am grateful to many laboratory technicians, including Rich Gordon, Tom Gawel, Howard Barker, Eckhard Budziarack, and all the guys in the machine shop, without whom this work would not be completed. I would also like to thank Chris Salisbury for his tremendous guidance and for allowing me a brief repose before facing the real world.

I would like to thank my office companions, Mikhail, Oleg, Jose, Alex, Dino, Chris, and Blake for making it enjoyable to come in every day. I would also like to thank Rassin whose intelligence and sense of humour helped me get through my degree and did not letting 'Vibrations' break my spirit. Finally, I would like to thank Dr. Hari Simha for causing all of us to question what we were doing, and how it could be improved.

To my family, I can not say enough. Thank you, mom and dad, for being there for me and for letting me learn how to give my best effort. Thank you, Andrew, Alison, and Simon, for being great siblings and for all of your support. To my wonderful in-laws, Mr. Weber, Karen, Mrs. Ross, Rob, Jason, Jon, Daniel, Dana, Trystan, and Dustin, I can not tell you how much it means for me to be a part of your family.

Last and most importantly, thank you to my beautiful wife Angela. You make life an amazing adventure. Without your love and support, I could not have accomplished any of this work. I feel like I can do anything when I'm with you.

Thank you.

TABLE OF CONTENTS

LIST OF TABLES

LIST OF FIGURES

CHAPTER 1

INTRODUCTION

To meet safety and environmental goals, the automotive industry has increasingly looked for materials that can be used to reduce injury to the vehicle occupants while reducing vehicle weight. One class of materials which shows promise for achieving these goals is advanced high-strength steels. These steels can attain very high strengths while retaining moderate ductility, which makes them ideal for absorbing energy during an automotive crash. Their inherent high strength allows structural components to be thinner, making the vehicle lighter and more fuel efficient.

Included in this class of steels are dual phase and high-strength-low-alloy steels, both developed in the latter half of the 20^{th} century. The microstructure of a dual phase steel consists of martensite grains inside a ferrite matrix. For high-strength-low-alloy steel, the microstructure can consists of any combination of ferrite, martensite, bainite, and retained austenite. These steels differ from more conventional drawing quality steels in that they are strengthened with a combination of manganese, silicon, and copper, as well as other trace elements other than carbon. These additives allow the steel to retain some ductility, even at very high strengths, where as carbon-strengthened steels retain very little ductility at high strengths. For this reason, both of these steels are of great interest to the automotive industry as energy absorbing materials.

Another goal of the automotive industry is to reduce the cost associated with the safety-evaluation of structures. Thus, the industry has increasingly moved towards finite element simulation of crash tests with fewer numbers of actual experiments. To make this possible, the behaviour of the structural materials used within vehicles must be adequately characterized over the complete range of strain rates and temperatures that are experienced in an automotive crash event.

The goal of this research is to obtain high strain rate constitutive data for the as-tubed condition of several steels ranging from low to high strength. The as-tubed condition was characterized so that automotive subframe rails, which are composed of tubes that are bent and hydroformed, can be modeled in numerical crash simulations. The three steels that were investigated are: i) a dual phase steel, DP600; ii) a high-strength-low-alloy steel, HSLA350; and iii) a drawing quality steel, DDQ.

In order to characterize the steels throughout the complete range of strain rates seen in a crash event, uniaxial tensile experiments were conducted on each steel at strain rates ranging from 0.00333 to 1500 s^{-1}. The low strain rate tests (0.00333 – 0.1 s^{-1}) were conducted on a servo-controlled tensile machine. The intermediate strain rate tests (30 – 100 s^{-1}) were carried out using an instrumented falling weight impact machine, while the high rate tests (500 - 1500 s^{-1}) were carried out using a tensile split Hopkinson bar. Experiments were also performed on the as-received steels in the sheet and as-tubed condition in order to assess the change in response due to tube fabrication.

The parameters of two constitutive models, known as the Johnson-Cook and Zerilli-Armstrong models, were fit to the experimental results for each steel. These constitutive models are currently used in impact and vehicle crash simulations and are increasingly available in commercial finite element codes, such as the LS-Dyna finite element code, which was used in the current research.

For the remainder of this chapter, a review of the literature pertinent to this research is presented. This includes a review of the characteristics and properties of dual phase steel and high-strength-low-alloy steels as well as a review of the instrumented falling weight impact tester and split Hopkinson bar apparatus and their use for obtaining constitutive data. A review of the Johnson-Cook and Zerilli-Armstrong constitutive models is also provided.

1.1 HIGH STRENGTH STEEL

In this section, the characteristics and properties of dual phase steels and HSLA steels will be reviewed. The discussion of each steel will begin with a review of the microstructure, followed by a review of the mechanical properties and the high strain rate properties. This encompasses the material information which is necessary for carrying out this research.

1.1.1 Dual Phase Steel

Dual phase steels are essentially low-carbon steels that contain a large amount of manganese (1-2 wt.%) and silicon (0.05-0.2 wt. %) as well as small amounts of microalloying elements, such as vanadium, titanium, molybdenum, and nickel [1-4]. A dual phase steel is created by heating a low-carbon micro-alloyed steel into the intercritical region of the Fe-C phase diagram between the A1 and A3 temperatures, soaking it so that austenite forms, slowly cooling it to the quench temperature, and then rapidly cooling it to transform the austenite into martensite [3-5]. Upon quenching, the austenite is converted mostly to martensite, but will also partially be converted into ferrite if the cooling rate is not sufficiently high [4,6]. Also, depending on the cooling rate, the austenite may be converted at least partially into bainite [5].

The ferrite that forms from austenite is referred to as epitaxial ferrite. The microstructure of a dual phase steel, consisting of ferrite and martensite, is seen in Figure 1.1 and Figure 1.2 [6,9]. Epitaxial ferrite grains, shown in Figure 1.2, are distinguishable from proeutectoid ferrite through use of an alkaline chromate etch [8]. All three constituents have a large effect on the mechanical properties of the steel.

Epitaxial ferrite has a negative effect on the mechanical properties. It dramatically lowers the tensile strength and slightly increases the ductility of the steel [7]. The reason for this is that the epitaxial ferrite forms stress concentrations in the martensite grains,

which compromises its strength [7]. Thus, epitaxial ferrite is undesirable and effort is made to ensure that it does not form.

Upon quenching a dual phase steel, residual stresses are created at the martensite-ferrite interfaces due to the volumetric expansion of the martensite [3,9]. This creates an increased number of dislocations at these interfaces, which can be seen in Figure 1.3. Because the vast majority of the alloying elements are found within the martensite, the density of mobile dislocations within the ferrite matrix is quite high [3].

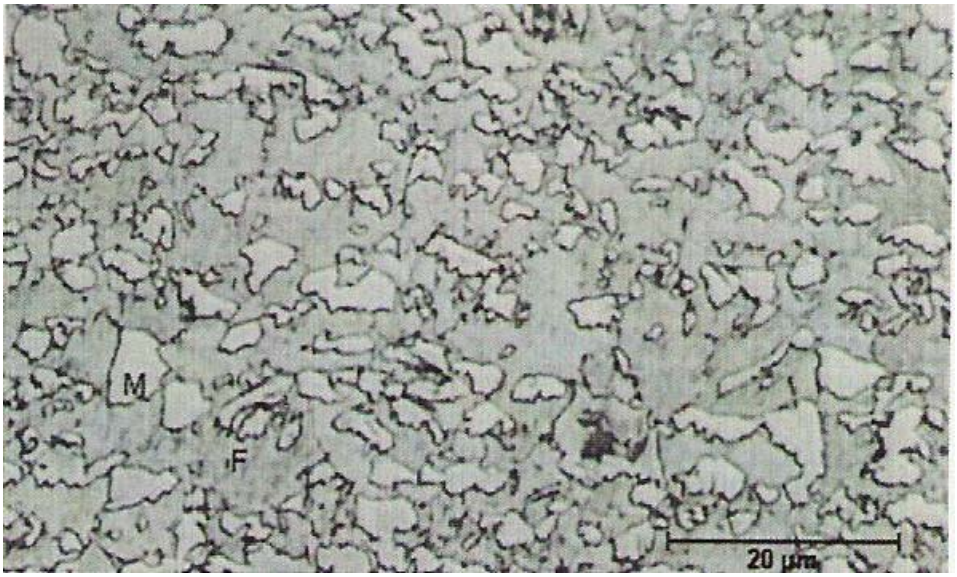

Figure 1.1 - Microstructure of a dual phase steel. The ferrite and martensite grains are dark and light respectively [9].

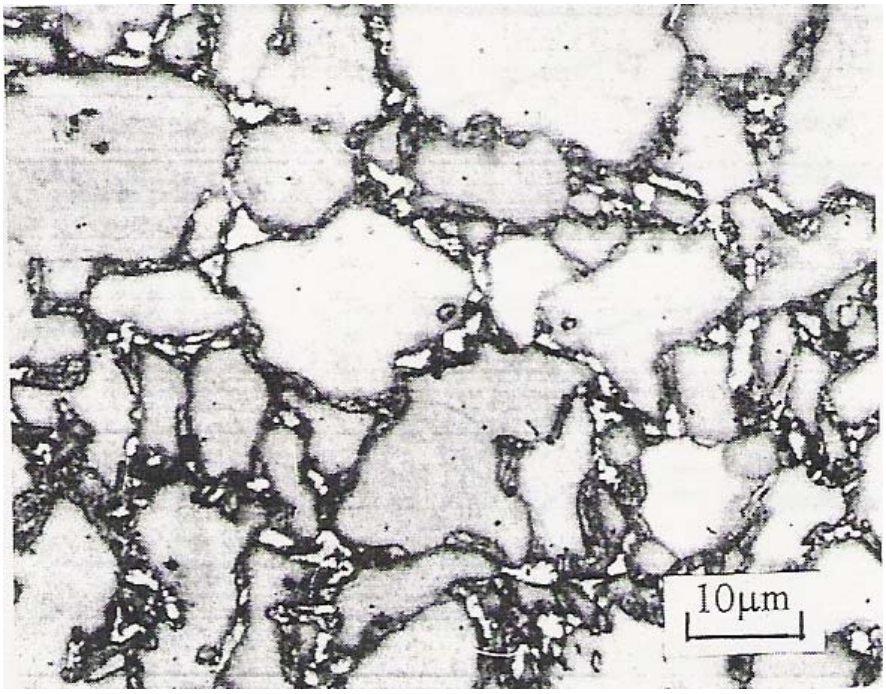

Figure 1.2 - Microstructure of a dual phase steel showing ferrite (gray), martensite (black), and epitaxial ferrite (white) [6].

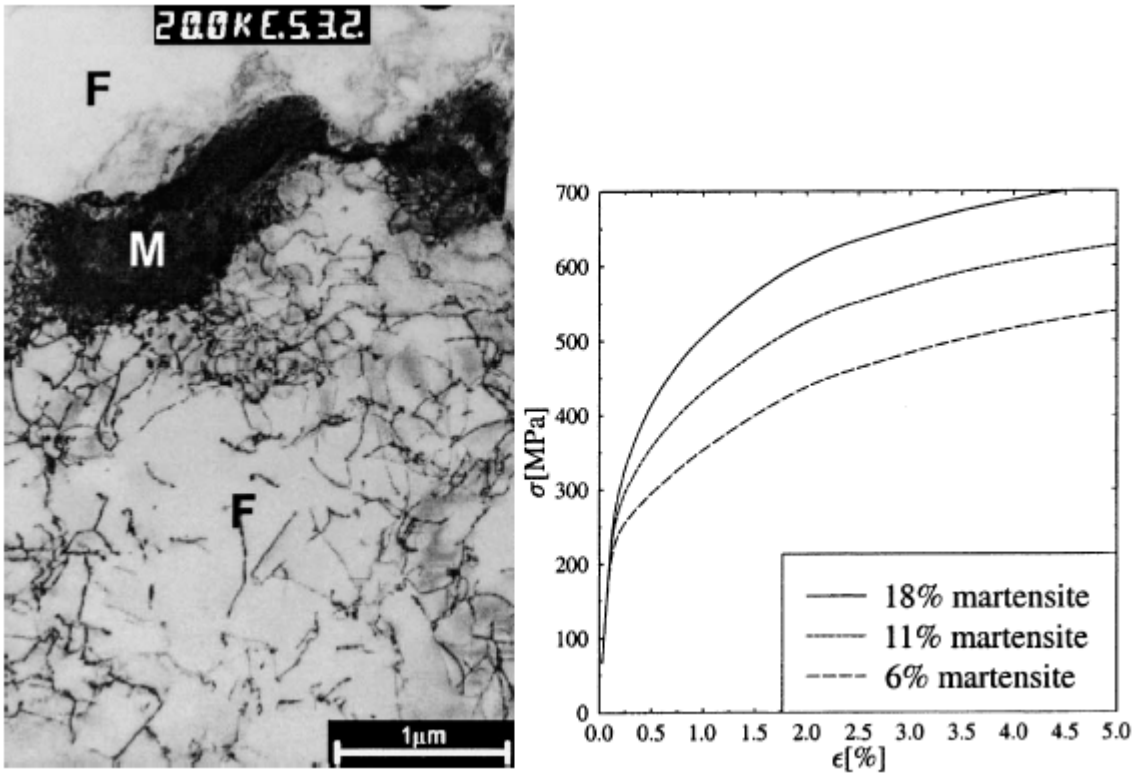

Figure 1.3 - Transmission electron microscope image of the ferrite-martensite interface in a dual phase steel and the corresponding stress-strain curve which shows the effect of the volume percent of martensite [9].

There are three stages to the work hardening of dual phase steel; each has a different hardening rate, as seen in Figure 1.3 [1]. The first stage, in which there is rapid work hardening, residual stresses are eliminated and back stresses are created in the ferrite [10]. This corresponds to stresses below 0.5% strain. In the second stage, the work hardening is caused by the "constrained deformation of the ferrite caused by the presence of rigid martensite" [1,10]. This corresponds to the portion of the curve between 0.5 and 2.0% strain. Beyond this strain, the work hardening is caused by the formation of dislocation cell structures, further deformation of the ferrite, and yielding of the martensite [10]. Dual phase steels containing 10-20% martensite typically have a yield strength of 300-400 MPa, an ultimate strength of 600 MPa, and a ductility of approximately 30% [5].

One important characteristic of dual phase steels is that the 0.2% offset yield strength increases as the martensite content increases, but is not affected by the carbon content [11]. Leidl *et al*. [9] showed that the increase in yield strength is due to the residual stresses which are created in the ferrite due to the volumetric expansion of the martensite. As the amount of martensite increases, so do the residual stresses in the ferrite matrix, which cause the yield stress to rise. As seen in Figure 1.3 there is an increased dislocation density at the ferrite-martensite interface, as well as the stress-strain behaviour that occurs with increasing martensite content. Also, as would be expected, the strength of dual phase steels increase as the amount of martensite increases, as well as when the martensite is more finely dispersed [1,10,12].

Another characteristic of dual phase steels is that they exhibit continuous yielding [3,7,9]. This is unusual for low-carbon steels; most show an elongated yield point followed by strain hardening. The reason for this is that there is a higher dislocation density in dual phase steels than in other low carbon steels. This higher mobile dislocation density in dual phase steels allows for the continuous yielding [3,13,14].

The continuous yielding found in dual phase steels was studied by Sakuma *et al.* [13]. They annealed a dual phase steel at 300 °C for times between 1 and 60 minutes. As the

annealing time increased, the residual stresses around the martensite grains were increasingly relieved. This lowered the mobile dislocation density, causing the steel to exhibit progressively more discontinuous yielding, as seen in Figure 1.4.

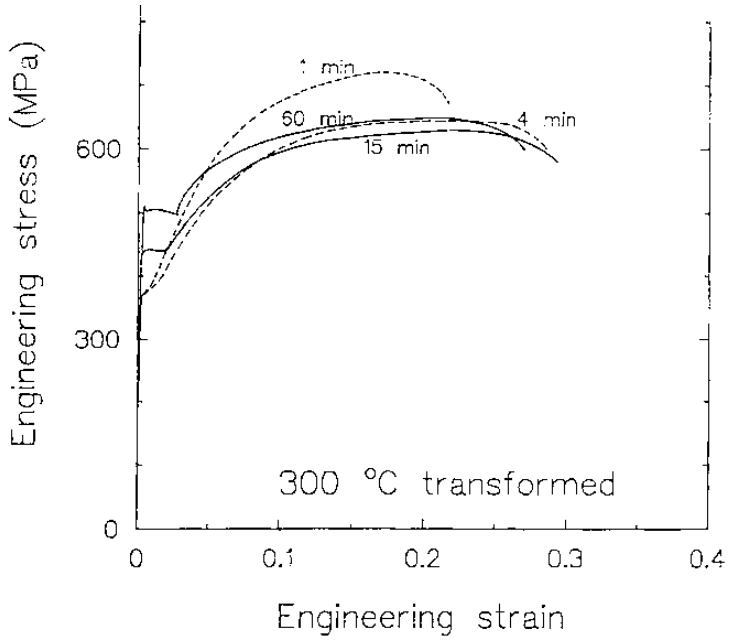

Figure 1.4 - Dual phase steel annealed at 300 °C for 1-60 minutes[13]

The intermediate-rate properties of dual phase steels have been studied up to strain rates of approximately 500 s^{-1}. Beynon *et al*. [15,16] performed tests at strain rates of 0.001, 1, and 100 s^{-1} on DP500 and DP600 using a servohydraulic high rate impact machine. Results from this testing can be seen in Figure 1.5. Both the work-hardening rate and the strength increase with increased strain rate. However, it was also found that the ductility suffered as the strain-rate increased.

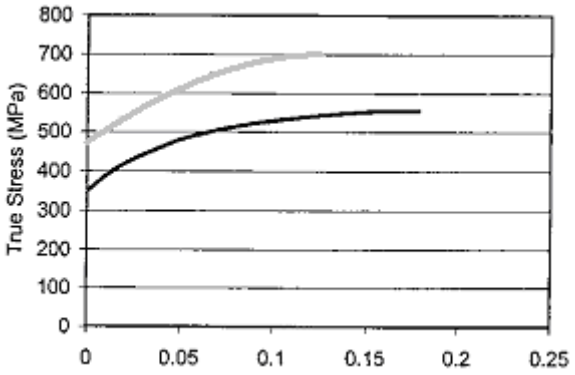

Figure 1.5 - True stress – effective plastic strain results of a dual phase steel. The black line represents the results at 0.001 s^{-1}. The gray line represents the results at 100 s^{-1}[15].

Schael and Bleck [17] also performed tensile tests on DP600 and DP800 at rates ranging from quasi-static to 250 s^{-1} using a servohydraulic tensile apparatus and found positive rate sensitivity as well. Also, at rates beyond 100 s^{-1}, there is a sharp decrease in the ductility as well as a sharp increase in the strain-rate sensitivity, which suggests that dislocation drag mechanisms may be influencing the behaviour of the steel.

Tarigopula *et al*. [18] have performed tensile tests on DP800 using a TSHB at strain rates up to 444 s^{-1}. These results can be seen in Figure 1.6. As with the experiments performed by Beynon *et al*., both the work-hardening and the strength of the steel increased as the strain-rate increased. They did not note any changes in ductility.

Dual phase steels have been developed only recently but, due to their promising mechanical properties, have been studied in great detail. Unlike most low-carbon steels, they do not exhibit discontinuous yielding unless the are annealed. They exhibit high tensile strength and moderate ductility, which is not significantly affected at elevated strain rates. This illustrates the promise for dual phase steel; it can be used to reduce vehicle mass, while providing good energy absorption at high impact velocities.

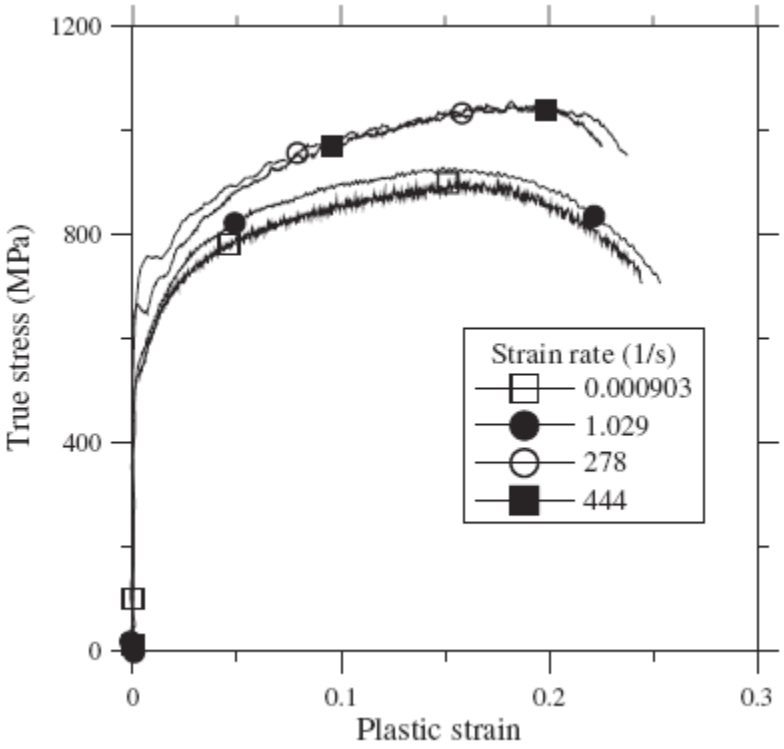

Figure 1.6 - Strain-rate sensitivity of DP800 [17]

1.1.2 High-Strength Low-Alloy Steel

High Strength Low Alloy Steels (HSLA) are another type of steel which show promise for reducing the weight of automobiles. Not only do they show good strength, formability and weldability, but their cost is lower than equivalent heat-treated alloys because they achieve their desired characteristics directly from hot rolling [19]. They have been used for automotive applications as well as warships, off-road trucks, offshore platforms, and equipment for oil-wells [19].

HSLA steels typically have a ferrite-pearlite microstructure. They were developed in the 1960s by adding niobium, vanadium, and titanium to form precipitates in low carbon-high manganese steels [20,21]. These elements, when added to the steel, create Ti-N, Nb-N, and Nb-C precipitates [22], which increase the strength of the steel, but hindered its ductility and weldability [23,24]. They also increased the strength of the steel by retarding the growth of the ferrite grains during cooling [21].

In order to make a more weldable and formable HSLA, the carbon content was reduced [24]. To make up for the loss in strength that was associated with decreasing the carbon content, higher amounts of manganese, silicon, and copper were added [19,22,24]. These steels can be made to great strengths while remaining formable and weldable [19-24].

The microstructure of HSLA generally comprises a fine grained ferrite matrix with pearlite and/or bainite islands, depending on the cooling rate, as seen in Figure 1.7. The microstructure on the right has a higher carbon content than the microstructure on the left. The small grain size (~10 μm) adds to the strength of the steel.

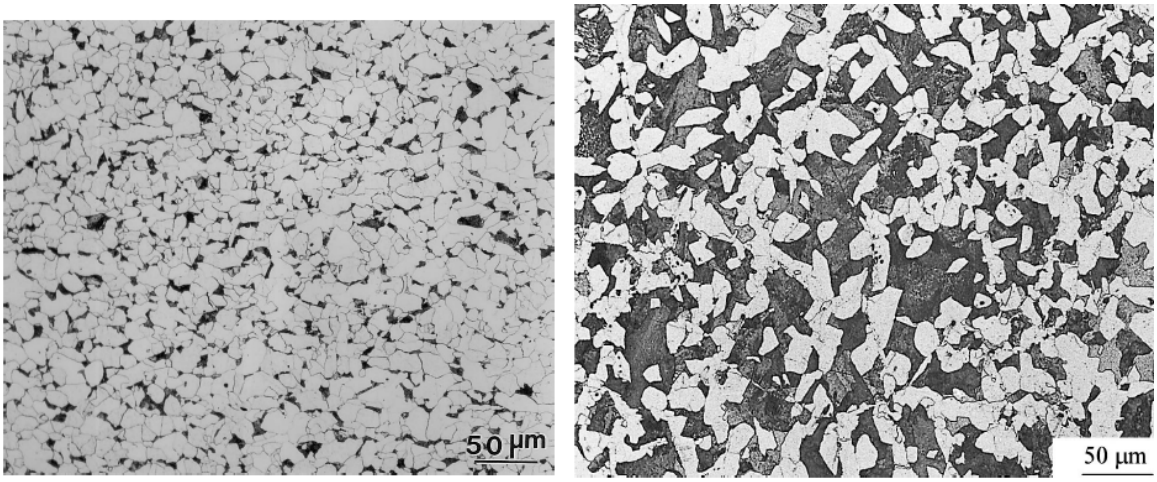

Figure 1.7 – Two examples of HSLA microstructure. The white grains are ferrite, the light gray grains are pearlite, and the dark gray grains are bainite [22,24].

Like many low-carbon steels, the stress-strain relationship of HSLA is characterized by an upper and lower yield point, followed by discontinuous yielding and work-hardening [20] (see Figure 1.8). This is especially true at lower temperatures.

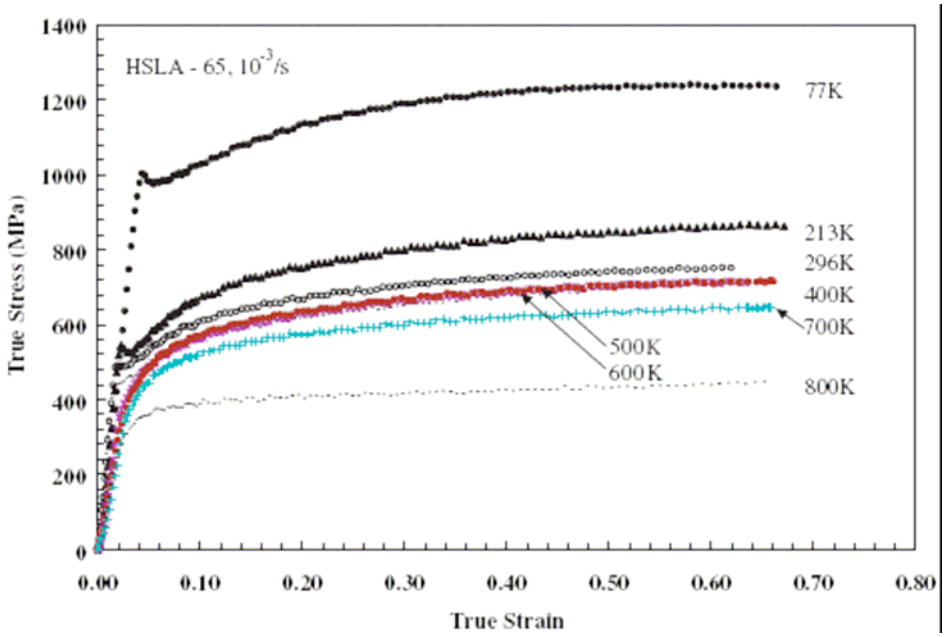

Figure 1.8 - Quasi-static response of HSLA-65 [20]

As with most annealed steels, accelerated cooling after heating substantially increases the strength, due to smaller grain size, as well as stronger constituents (*i.e.* bainite instead of pearlite) [25]. Figure 1.9 shows the ultimate tensile and yield strength of HSLA as the cooling rate increases.

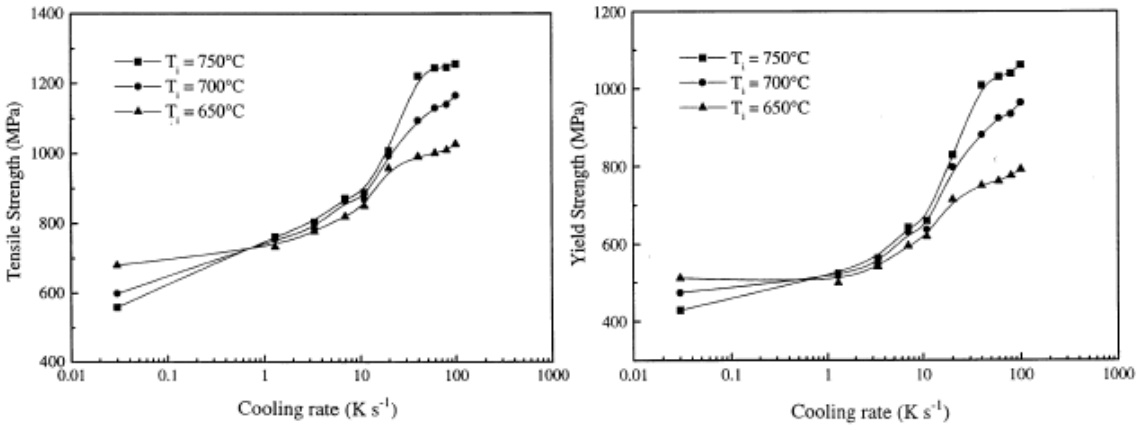

Figure 1.9 - Yield and ultimate tensile strength of HSLA as the cooling rate changes [25]. T_i is the temperature prior to cooling.

Bassim and Panic [26] performed high strain-rate tensile experiments on HSLA and found that the upper/lower yield point effect was present at rates up to 1000 s^{-1}, as seen in

Figure 1.10. They attribute this affect to adiabatic sheer bands which they claim are produced during the drop in yield strength.

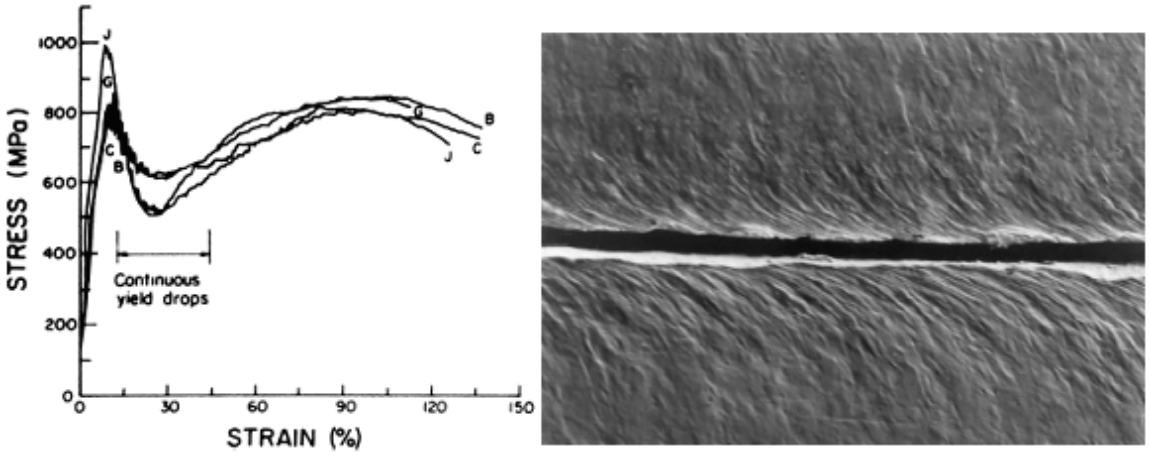

Figure 1.10 - Response of HSLA at various rates and the adiabatic-shear-band [26]

A series of high rate tests has been carried out by Nemat-Nasser and Guo [20]. They performed tests at rates from 10^{-3} s^{-1} to 8500 s^{-1} and temperatures from 77 – 1000 K. All of their tests were performed in compression using a hydraulic compression tester for low rates (10^{-3} and 10^{-1} s^{-1}) and a compressive Hopkinson bar for the high rates (3000 to 8500 s^{-1}). They report a positive rate sensitivity for the strength and a thermal softening effect (Figure 1.11). Also, they see an upper an upper and lower yield point in the response at each strain rate. As the strain rate increases, so does the ratio of upper yield stress-to-lower yield stress, that they claim may be due to dynamic strain aging. The upper yield point disappears at high temperatures, suggesting that the thermal activation energy required to overcome the solute obstacles is severely reduced.

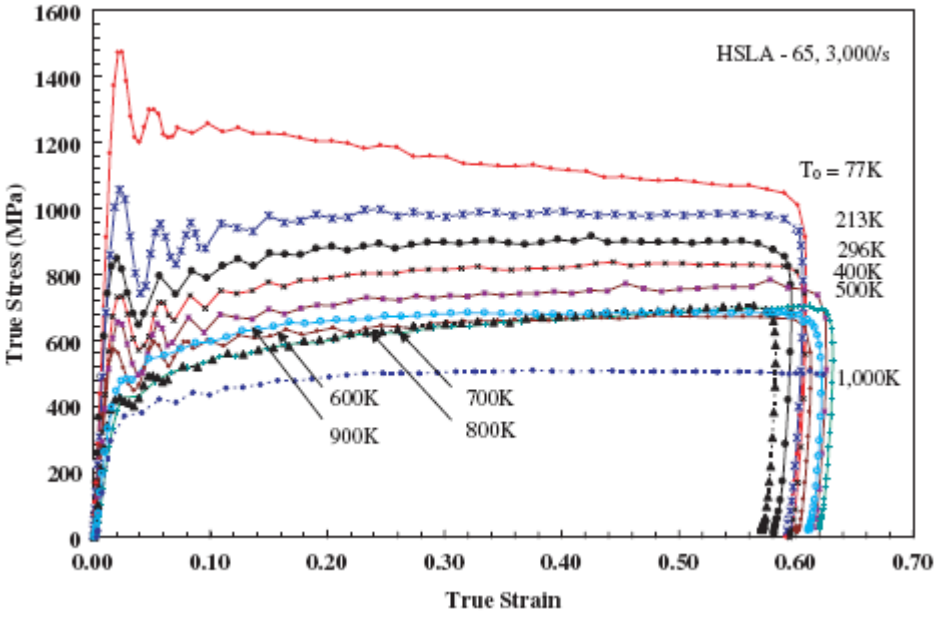

Figure 1.11 - Response of HSLA-65 at 3000 s^{-1} [20]

Another interesting study on high rate behaviour of welded HSLA 100 was conducted by Xue *et al*. [27]. They machined specimens out of the base metal in a welded bar as well as out of the weld and the interface between the weld and the base metal. They performed their tests at strain rates of 10^{-3} and 10^{3} s^{-1}. Similarly to Nemat-Nasser and Guo, they observe a magnified upper and lower yield strength at high rates, as seen in Figure 1.12. However, because the yield behaviour is difficult to explain at high rates, they do not attempt to determine the its cause. Like Nemat-Nasser, they also observe a positive rate-sensitivity for the flow stress.

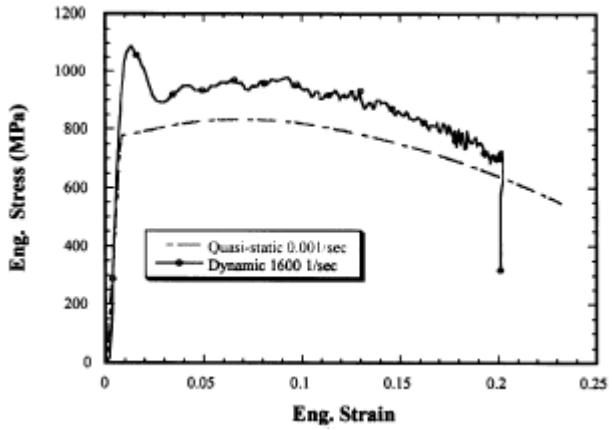

Figure 1.12 - Tensile response of HSLA-100 at 0.001 and 1600 s^{-1} [27]

Compression tests were performed on HSLA with rates from 2-120 s^{-1} by Baragar [28] using a cam plastometer. The cam plastometer was designed so that a constant true strain rate is achieved. The tests were conducted at temperatures of 800, 900, 1000, and 1100 ºC to find the effect of dynamic recrystallization. It was found that HSLA did not have any thermal softening effects between 900 and 1000 ºC.

Like dual phase steel, HSLA retains its ductility at high strengths. However, it behaves more like a traditional low-carbon steel in that it displays an upper and lower yield point. This behaviour makes the modeling of HSLA difficult at small strains and makes it less appealing than dual phase steel for use in automotive applications.

1.2 HIGH STRAIN RATE TESTING METHODS

For this project, two apparati were used for performing tests at strain rates above 10 s^{-1}. An instrumented falling weight impact tester (IWFI) was used to perform experiments at nominal strain rates of 30 and 100 s^{-1} and a tensile split Hopkinson pressure bar (TSHB) was used to perform experiments at nominal strain rates of 500, 1000, and 1500 s^{-1}.

When performing dynamic tensile testing, wave effects can have a large effect on the measured results. These effects must be understood and accounted for in order to obtain data that corresponds to material behaviour.

The following section will outline the history and development of the experimental methods associated with each apparatus as well as the testing limitations. The origins of the wave effects will also be discussed along with measures that have been taken to overcome them.

1.2.1 Falling Weight Impact Testing

For this project, an instrumented falling weight impact tester (IFWI) was used to characterize the steels at rates between 10 and 100 s^{-1}. IFWIs have been used extensively in the characterization of composites and polymers. They can be used to perform experiments in compression, biaxial tension, toughness, and uniaxial tension, as well as in fatigue, through multiple impacts. A schematic diagram of the testing setup can be seen in Figure 1.13.

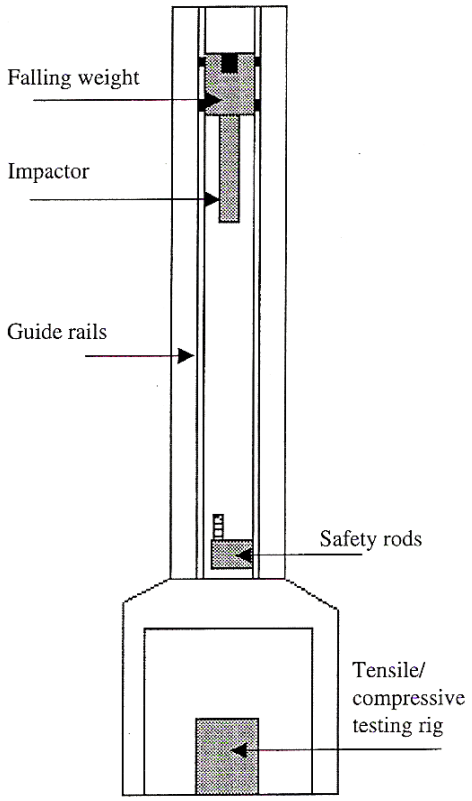

Figure 1.13– IFWI testing setup [29]

In an IFWI experiment, regardless of the type, a striker (impactor) with some added mass is dropped onto either the specimen (compression, toughness, or biaxial tension) or a fixture which is attached to the specimen (uniaxial tension). The guide rails ensure that the striker falls completely vertically. In most configurations, a load cell, either in the

striker or below the specimen, is used to measure force. A number of methods are used to measure specimen deformation.

Compression testing has been performed on many different sizes and geometries of tubes and cylinders, for composites, polymers and metals [29-36]. In these tests, the force is measured by a load cell, which is located either in the striker or below the specimen [32-34]. The setup for a compression test, as seen in Figure 1.13, generally consists of a flat pedestal upon which the specimen sits (compressive testing rig). The face of the striker is also flat.

IFWI dynamic compression testing can be used for a number of different applications. Abramowicz and Jones [30,31] used an IFWI to determine the impact velocity at which the mode of buckling in tubes change from global bending to dynamic buckling, as well as to determine the difference in energy absorption between square and circular tubes.

Dynamic compression testing can also be used to obtain material constitutive data. Lee and Swallowe [32,33] used perhaps the most advanced method for obtaining constitutive data in compression. They sandwich their specimen between glass anvils so that a high-speed camera can be used to measure the radial strain in their specimens, as seen in Figure 1.14. They use this system to obtain the stress-strain relationship for PMMA cylinders to the point where the PMMA begins to crack. One benefit of this system is that the point at which the data becomes invalid, *i.e.* at the onset of cracking, is easily determined. This setup has also been used by Walley *et al.* [34].

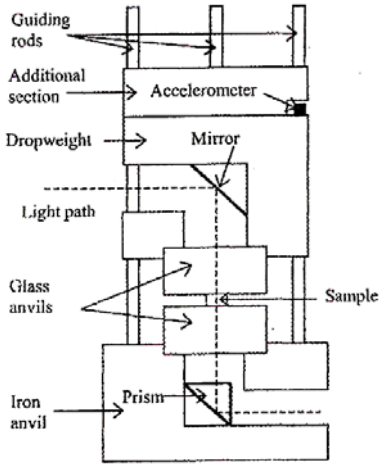

Figure 1.14 - Setup for compression test using glass anvils [32]

One method of measuring strain during compression tests for sheet metal is to attach strain gauges to the specimen. Fernie and Warrior [29] have taken this approach. They use a compression rig that only allowed the striker to fall to a prescribed level such that the sheet only deformed in a uniaxial manner rather than buckling. This prevented buckling and damage to the gauges.

Another common approach to determine displacement during dynamic testing is to integrate the force signal twice with respect to time and divide the integrand by the mass. This was the method used by Hsiao and Daniel [35] and Salvi *et al.* [36] to determine strain in the compression of rectangular composite specimens. For this method to be completely accurate, the deformation of the striker must be subtracted from the final result.

Charpy-type dynamic toughness testing has also been performed using IFWIs. Fasce *et al.* [37] used an IFWI to determine the toughness of a number of polymers, while Ishak and Berry [38] performed the same tests for composites. They both used a load cell, positioned above the striker, to measure the force of the impact, which they then converted to energy, by integrating the force signal with respect to the striker displacement. This was done to determine how much energy each material could absorb during impact. The IFWI toughness test has the potential to be more useful than the

normal Charpy test because tests can be run at the same initial energy, but with different masses and speeds, allowing for additional material characterization [38].

IFWI dart testing has been gaining popularity for acquiring the high-rate properties of polymers because it has the advantage of biaxiality and allows, in some cases, for the testing to be performed on "finished" products (*i.e*. sheet and plate) [39]. Figure 1.15 shows the typical setup for dart testing. These tests are performed on an IFWI by using a hemispherical dart at the tip of the striker, creating a biaxial stress state in the material upon impact [39].

This technique has been used to obtain the biaxial properties of many polymers [40-42], foams [43], and composites [39]. In these tests, the force is generally measured by a load cell located within the striker. The strain can be determined from the force signal (integrating with respect to time), assuming that there is no anisotropy in the specimen. Strain can also be measured by mounting strain gauges on the specimen [39,40]. Friction between the dart and plate can affect the measured strain greatly.

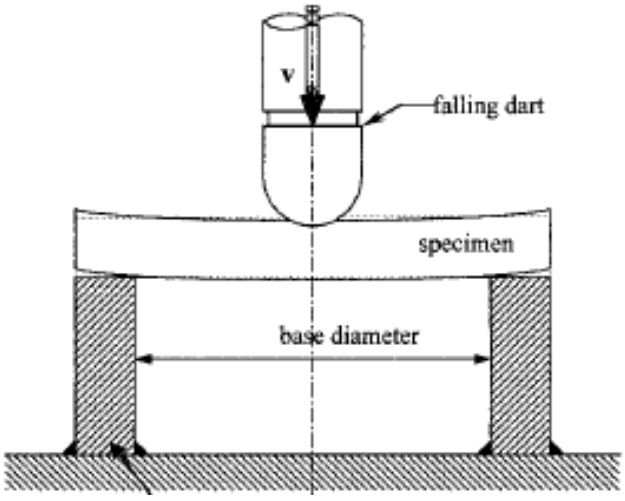

Figure 1.15 – Schematic diagram of a dart test [39]

A plaque test is one in which an IFWI is used to strike a thin disc or square of a material. It is similar to the biaxial tension test except that, in a plaque test, the tip of the striker can have many different shapes (Figure 1.16). Plaque tests are generally used to obtain energy absorption and damage information.

Molina and Haddad [44] performed plaque testing on polyvinyl chloride sheet. They struck it repeatedly at a consistent energy level to find the reduction in strength and energy absorption due to repeated impacts. In addition, they used acoustic-ultrasonic measurements to determine the damage to the material after each impact.

Song *et al*. [45] performed the same test to determine how many impacts were necessary to crack and penetrate concrete. This allowed them to determine which fiber additives were most beneficial for energy absorption and crack control.

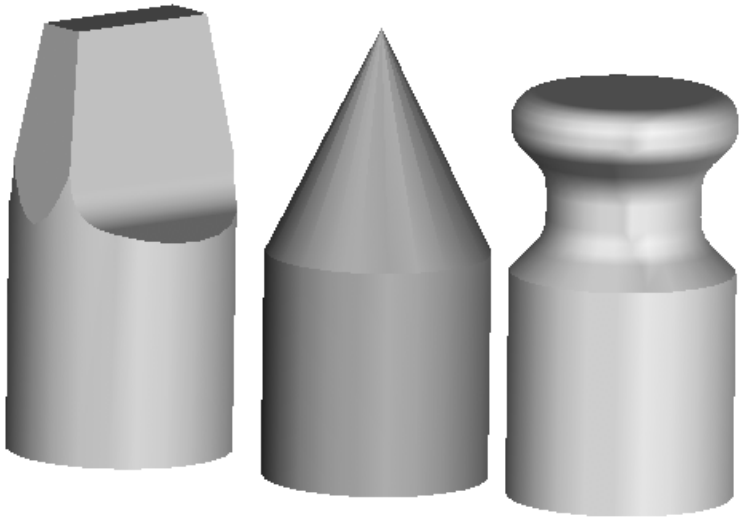

Figure 1.16 - A few of the different striker heads that are used in a plaque test

Relatively little work has been done using IFWIs for uniaxial tensile experiments. This is largely due to the fact that high-speed servohydraulic machines can be used to perform tests at strain rates that are similar to those that can be obtained in an IFWI. Still, there is an important advantage to using an IFWI. Servohydraulics are generally unable to accelerate the specimen quickly enough to achieve a constant strain rate throughout the majority of the test [46].

Shin, Lee and Kim [47] have used a tensile IFWI to gather constitutive data for cylindrical steel specimens. The setup for this experiment can be seen in Figure 1.17. Force was measured in the load cell, located above the specimen. Strain was measured by optically measuring the displacement of the lower grip. The optical displacement measurement system they used would give more accurate results, however, if the displacement of the upper grip was measured in addition to that of the lower grip. This would ensure that only the specimen elongation is measured.

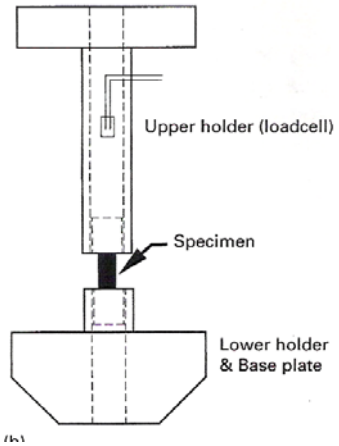

Figure 1.17 - Setup for tensile impact as done by Shin *et al*. [47]

Tensile IFWI tests on have been conducted on steel bolts by Mouritz [48]. He measured load in a method similar to that of Shin *et al*. [47] and he measured displacement by attaching an extensometer to the bolt. The results were then used to aid in assessing the damage done to the bolts when subjected to different impact energies.

Fernie and Warrior have also performed tensile impact testing [29]. Their apparatus, illustrated in Figure 1.18, is similar to that used in the other tensile tests. The specimen is held at the top by a fixed carriage, and the bottom is attached to the moving carriage. They measured strain by mounting strain gauges on the sides of the specimen.

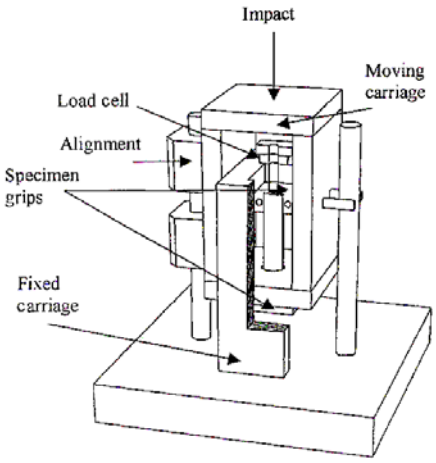

Figure 1.18 - Setup for tensile impact as done by Fernie and Warrior [29]

Wave effects in impact tests have been studied in great detail for compression and toughness tests [49-52]. In general, this has been done by modeling the IFWI as a multiple-degree-of-freedom spring-mass-damper system. The lumped model for compression testing used by Found *et al*. [51] can be seen in Figure 1.19. They model the load cell as a spring-damper system (C1 – K1) between the drop mass (M1) and the striker tip (M2). The end of the striker tip (C2 - K2) and the specimen (C3 – K3) are both modeled as a spring-damper systems, and the testing fixture is modeled as a spring-mass-damper system (M4 – C4 – K4). By performing a modal analysis on their model, they were able associate oscillations in their measured data with the natural frequency of each part of their model. This approach was taken by Cain *et al.* [49] for compression testing. Williams and Adams [50] and Lifshitz [52] performed this type of analysis for toughness testing.

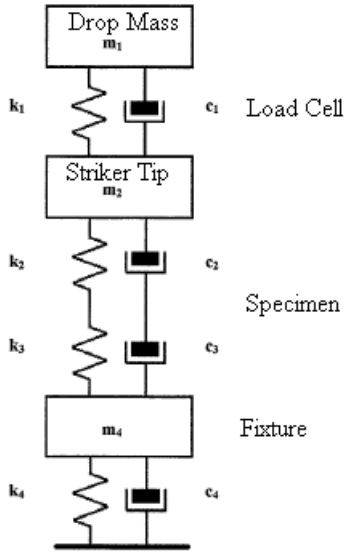

Figure 1.19 - Model of impact testing [51]

In each case, the authors were interested in the origins of two sets of waves: relatively low frequency waves (1 – 5 kHz) and high frequency waves (10 – 50 kHz). An example of the high frequency waves can be seen in the data of Walley *et al*. [34] on the left side of Figure 1.20.a. An example of the low frequency waves can be seen in the force measurement of Shin *et al*. [47] in Figure 1.20.b.

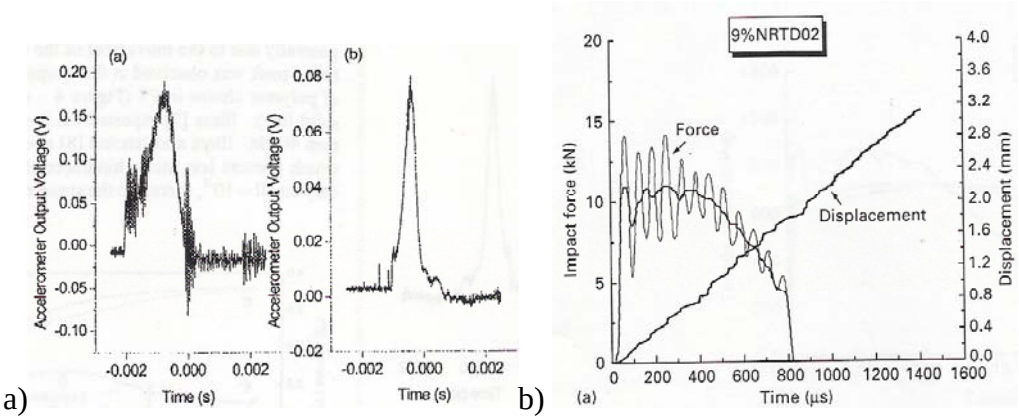

Figure 1.20 - waves in impact data at a) high frequency [34] and b) low frequency [47]

The high frequency waves correspond to the natural frequency of the striker, and are present in experiments where the load cell is located within the striker [49-51]. There is no filter that can be used to eliminate these waves because, if the mechanical properties

of the striker and the specimen are closely related, applying a filter will remove a portion of the specimen response from the load cell signal [50]. These wave effects can be eliminated by the use of a momentum trap above the striker as was done by Walley *et al*. [34] (right side of Figure 1.20.a), or by mounting the load cell below the specimen [29,32-34,51]. In uniaxial tension, the load cell is not positioned on the striker and, therefore, these waves are not present.

The low frequency waves are associated with the contact between the striker and the specimen (compression or toughness) or between the striker and the lower grips (uniaxial tension) [50,51]. They can be reproduced by considering the load cell to be a spring-mass system with a dynamically applied load (Figure 1.21). The displacement of the system, *x(t)*, is related to the input force, *f(t)*, by Equation 1.1, where *m* and *k* are the mass and stiffness of the load cell, and ω_n is its natural frequency [53].

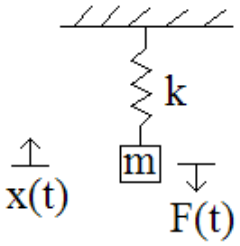

Figure 1.21 - Spring-mass model of load cell

$$x(t) = \frac{1}{\omega_n m} \int f(t) \sin(\omega_n t) \qquad (1.1)$$

If, for example, the shape of the input force is a step with a magnitude F_0, the resulting load cell force will oscillate about F_0 with an amplitude of F_0, as seen in Equation 1.2.

$$f(t) = F_0 (1 - \cos(\omega_n t) \qquad (1.2)$$

$$\text{where: } f(t) = k \cdot x(t) \qquad (1.3)$$

Therefore, the amplitude of the waves in the load cell is dependent on the manner in which it is excited. In essence, the amplitude of these waves increases as the stiffness of the impact increases [49,50].

While no real material can generate a true step input (this would require a rigid material), it is not uncommon for these waves to be on the same order of magnitude as the specimen response. This can make the data extremely challenging to analyze. These waves can be seen in Figure 1.20.b as well as in the work of Roos and Majzoobi [47,54,55]. The work of Shin *et al*. [47] is particularly effective in showing how these waves can distort the analysis of the data (Figure 1.20.b). They use a running average to determine the force in the specimen. This results in a force-time response that is not consistent with what would be expected in terms of material behaviour, particularly below 200 μs.

The amplitude of these waves can be reduced in two ways. The first method is to mount strain gauges above the specimen to measure the load [50,54]. Roos and Mayer [54] were able to reduce the size of the oscillations by replacing their load cell with a sheet of high strength steel which has strain gauges mounted on it. The reason for the reduction in size of the oscillations is likely that the strain gauge averages the strain over a much larger distance than a piezoelectric crystal. This method, while somewhat effective, decreases the sensitivity of the load measurement.

The second method is to introduce a material between the striker and lower grips that act as a damper, as is seen in the work of Hsiao and Molina [35]. This approach can significantly reduce the amplitude of the waves, but also reduces the rate at which the specimen can accelerate to the speed of the striker. For this method, the initial portion of the experiment does not occur at the desired strain rate.

Impact testing can be used to characterize materials in numerous ways through, compression, toughness, biaxial tension, and uniaxial tension. For the current research, IFWI uniaxial tensile experiment was used to characterize the steels of interest at strain rates ranging from 10 – 100 s^{-1}.

The dynamic nature of the IFWI experiments, while being useful for emulating real events, poses a challenge when conducting and analyzing results. For this reason, wave effects in IFWI testing must be minimized.

1.2.2 Split Hopkinson Pressure Bar

The Hopkinson bar was first described in 1914, when Bertrand Hopkinson used a long steel bar with a projectile at one end to measure the detonation energy of explosives [56]. In 1949, Kolsky used the same concepts as Hopkinson to create an apparatus that could be used to measure material behaviour at high rates of strain [57]. This will hereafter be referred to as the split Hopkinson pressure bar (SHB).

A schematic diagram of a compressive SHB can be seen in Figure 1.22. It consists of a striker bar, an incident bar, and a transmitted bar. The test specimen is placed between the incident and transmitted bar.

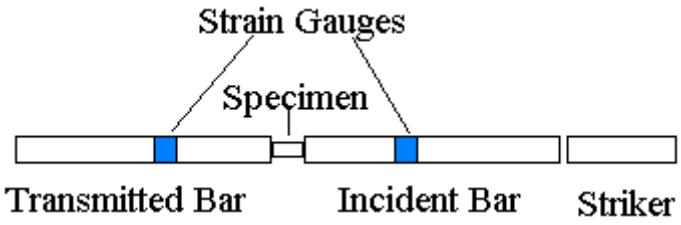

Figure 1.22 - Schematic diagram of a compressive SHB

To perform a test, the striker impacts the incident bar, causing a pressure wave to be created which is twice the length of the striker [58]. As the wave reaches the incident bar-specimen interface, part of it is reflected back along the incident bar and the rest is transmitted into the specimen and then into the transmitted bar. These waves are measured by strain gauges located on the bars. A sample of the waves produced in a SHB can be seen in Figure 1.23.

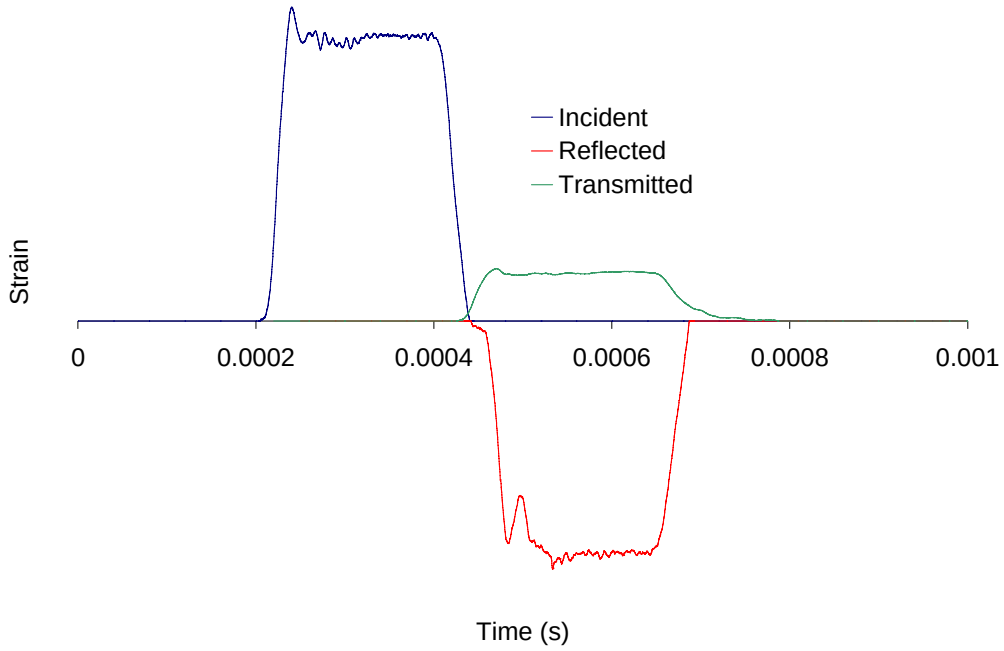

Figure 1.23 - Strain waves created in a TSHB experiment, where positive strains are tensile.

The stress, strain rate, and strain can be computed from the reflected and transmitted waves using the Equations 1.4-1.6, derived by Kolsky, assuming one-dimensional wave propagation [57]. In Equation 1.4, σ is the stress in the specimen, A_b is the cross-sectional area of the bars, A_s is the cross-sectional area of the specimen, and ε_t is the strain in the transmitted bar. In Equation 1.5, $\dot{\varepsilon}$ is the specimen strain rate, C_0 is the elastic wave speed in the bars, L is the specimen gauge length, and ε_r is the reflected strain. In Equation 1.6, ε is the specimen strain. It is determined by integrating Equation 1.5 with respect to time.

$$\sigma = E\frac{A_b}{A_s}\varepsilon_t \tag{1.4}$$

$$\dot{\varepsilon} = -2\frac{C_0}{L}\varepsilon_R \tag{1.5}$$

$$\varepsilon = -2\frac{C_0}{L}\int \varepsilon_R dt \tag{1.6}$$

The following assumptions were used to derive Equations 1.4 - 1.6: the wave only travels longitudinally along the bars; the specimen must be in dynamic equilibrium at all times (*i.e*. the force must be the same on both sides of the specimen); the incident and transmitter bar have the same cross-sectional area; the incident and transmitted bar are both elastically-deforming structures.

There are many reviews of SHB testing and the techniques necessary for proper data analysis [48,58-61]. For this study, only work which specifically covers tension and sheet-metal testing will be reviewed. All of the theory which is used to extract data from a compressive SHB can be used for a tensile SHB [46].

The assumption of one-dimensional wave propagation has been studied intensely. Upon impact between the striker and incident bar, the created pressure wave consists of a longitudinal wave as well as many other waves which disperse as they travel along the incident bar [62]. Pochhammer [63] and Chree [64] independently derived the equations which describe the wave propagation in an infinitely long cylindrical bar. Davies [65] applied these results to the SHB in order to address the problem of dispersing waves. It was found that by the time the wave has gone approximately 10 diameters along the length of the bar the non-longitudinal waves have dissipated to the point where a one-dimensional wave assumption is valid [62,65]. Thus, it is important to use bars which are at least 20 diameters long.

As can be seen in the incident, reflected, and transmitted waves shown in Figure 1.23, there are small oscillations, which are inherent in the waves [62]. The reason for this is that the pressure wave, rather than being sinusoidal, is trapezoidal [65]. A trapezoidal wave is composed of many sinusoidal waves of different frequencies and amplitudes. Since the velocity of the wave decreases as its frequency increases, the higher frequency waves lag behind the lower frequency waves [62], which appears as oscillations in the measured waves [62], as seen in Figure 1.24.

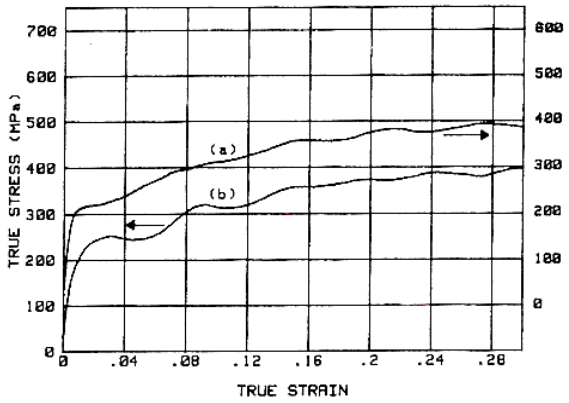

Figure 1.24 - The true stress measured in a SHB when a) wave dispersion is corrected for and b) when it is not [62].

In order to correct the data, the reflected and transmitted waves must be converted to the frequency domain. Then, the phase of each frequency must be corrected to account for the distance between the strain gauge and the end of the bar. The waves can then be converted back to the time domain [62].

For the current research, the SHB was constructed out of AA6061-T6. Wave propagation in this material was studied by Salisbury [66], who found that the phase velocities generally remain constant for frequencies below 30 kHz. Based on these results, dispersion correction is not considered when analyzing the results of the current research.

There are also many practical considerations to SHB testing, the main one involving the time for the specimen to reach a state of dynamic equilibrium, as assumed in Equations 1.4-1.6. The time that is needed for the waves to propagate through the specimen to create a uniform stress state is referred to as the ring-up time. For a solid which deforms plastically, Davies and Hunter [65] have derived the value for the ring-up time. In essence, they show that the pressure wave must reflect inside the specimen π times before a uniform stress state is reached. This makes the elastic properties of the material difficult to obtain.

However, Chen *et al*. [67] were able to obtain the dynamic elastic properties for steel by placing a copper disk between the striker and incident bar. By distorting the incident

pulse, they were able to have the specimen achieve a uniform stress state at a much lower level of strain. Also, they were able to measure the elastic properties of the steel at rate of approximately 26 s^{-1}, and measured their stress at plastic strains at approximately 1300 s^{-1}. The pulses and stress results are shown in Figure 1.25.

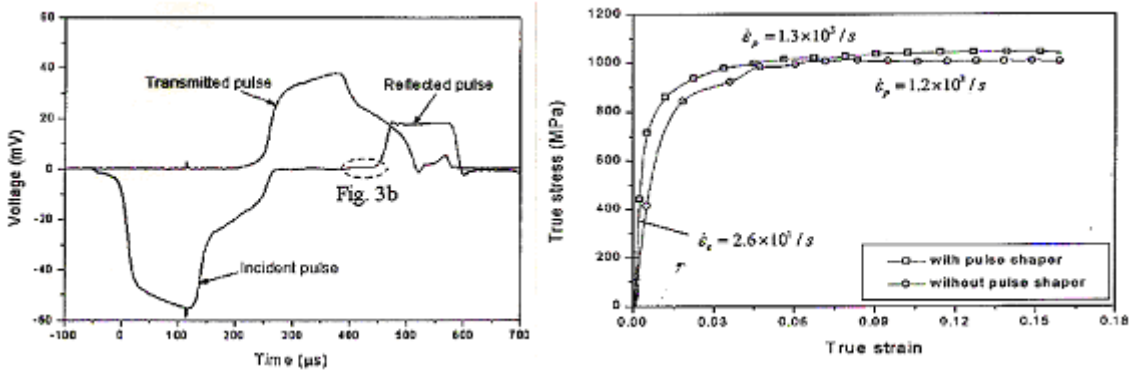

Figure 1.25 - The use of pulse shaping to extract elastic data from a SHB. The circled area is the portion of the reflected pulse at 26 s^{-1}[67]

When performing TSHB experiments, many different methods of gripping the specimen have been attempted. The first tensile experiments were done using a compressive SHB with a specimen that was shaped like a top-hat (Figure 1.26) [66]. This has not been used very frequently, because it is difficult to limit the amount of material flow from the clamped region into the gauge region and, therefore, strain is difficult to measure.

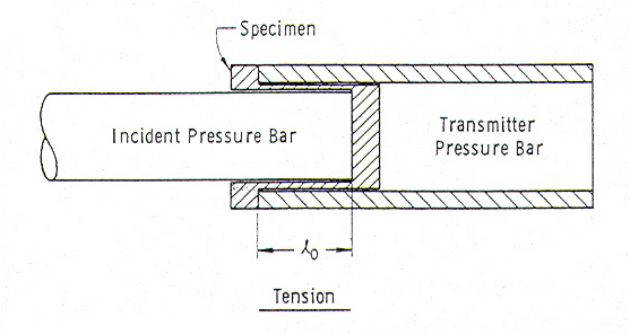

Figure 1.26 - Top-hat tensile specimen [66]

A method developed by Nicolas [47,68], also involving a compressive SHB, is to place a hardened bushing or shoulder over the specimen, between the incident and transmitted

bar (Figure 1.27). In this arrangement, the sample and bushing are first loaded in compression, which does not yield the specimen because the bushing allows the wave to pass through without plastic deformation of the specimen. The wave then reaches the end of the transmitted bar and is reflected back as a tensile wave, which returns and then loads the specimen in tension. This method has not been used frequently because the distortion of the wave as it passes through the bushing is too significant to allow for easy data analysis.

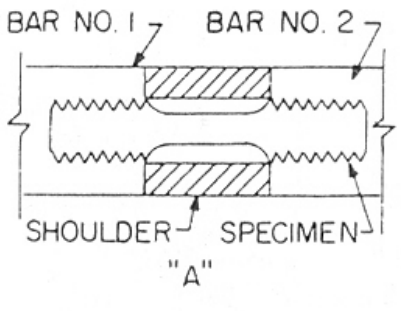

Figure 1.27 - Tensile experiment setup from Nicolas [47]

Most commonly, tensile experiments are performed by generating a tensile wave in the incident bar, and the specimen geometry is some variation of the ASTM standard shape [69-73] (Figure 1.28). Specimens are either threaded into the bars, bonded, or clamped into the end of the bars.

Figure 1.28 - Tensile SHB specimen [42]

Staab and Gilat [70] studied the effect of specimen geometry and found that Equations 1.4-1.6 can be used to analyze SHB data if the gauge length-to-diameter ratio of the specimen is greater than 1.6. If it is smaller, deformation outside the gauge length influences the strain measurements. Rodriguez *et al*. [71] used this result as a baseline to establish that the necessary gauge length-to-diameter ratio is a function of the material

behaviour. Materials which exhibit smaller strain-hardening require greater aspect ratios than those that exhibit more strain-hardening.

This was confirmed by Li and Ramesh [69], as long as the specimen has not necked. If necking occurs early in the experiment, they found that the radial strain in the neck region was a far better indicator of the strain which should be used for constitutive modeling.

Alternative methods for sheet specimen testing have been attempted by Zhao and Gary [74]. They laminated the sheets together in a compression SHB, shown in Figure 1.29. This did not provide accurate data because the epoxy was not strong enough to prevent the sheets from delaminating during the experiment.

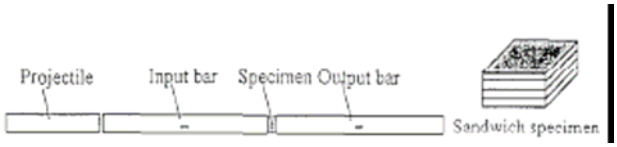

Figure 1.29 - Laminated sheet metal specimen [47]

1.2.3 Summary

The tensile SHB is a very useful tool for determining the response of materials at strain rates ranging from 100 – 3000 s^{-1}. For this reason, it has been widely used and the physics behind it are well understood. Like the IFWI, there are wave effects in the SHB which must be accounted for when analyzing experimental results.

Through the use of an IFWI and a tensile SHB, the steels in this study can be characterized throughout the complete range of strain rates that are predicted in an automotive crash. This gives confidence that the results of the crash simulations will be accurate and useful for future vehicle design.

1.3 CONSTITUTIVE MODELS

For this project, two constitutive models will be used to fit the experimental data so that it can be used in numerical simulations: the Johnson-Cook model and the Zerilli-Armstrong model. While other models exist, these two models are the easiest to use and are incorporated into the LS-Dyna finite element software, which is used for the crash simulations

1.3.1 Johnson-Cook

In 1983, Johnson and Cook [75,76] created a constitutive model for metals which captures the strain-rate and temperature dependency of the material. This was done so that they could accurately simulate cylinder-impact tests for Armco iron, 4340 steel, and OFHC copper. This model can be seen in Equation 1.7.

$$\sigma = (a + b\varepsilon^{n})(1 + c\ln(\dot{\varepsilon}))(1 - T^{*m}) \qquad (1.7)$$

In Equation 1.7, σ is the true stress, ε is the effective plastic strain, $\dot{\varepsilon}$ is the strain rate, and T^{*} is a form of homologous temperature, as given in Equation 1.8. *a*, *b*, *n*, are constants which describe the work-hardening behaviour, *c* describes the strain-rate sensitivity, and *m* describes the thermal softening.

$$T^{*} = \frac{T - T_{room}}{T_{melt} - T_{room}} \qquad (1.8)$$

The terms within the first set of parentheses in Equation 1.7 imposes a power-law relationship on the true stress versus effective plastic strain. The second term in parentheses introduces a logarithmic dependence on strain-rate. The final term gives the stress an exponential decay as temperature increases. An example of a set of experiments on 4340 tempered martensite, which have been fit with the Johnson-Cook model, is seen in Figure 1.30 [79].

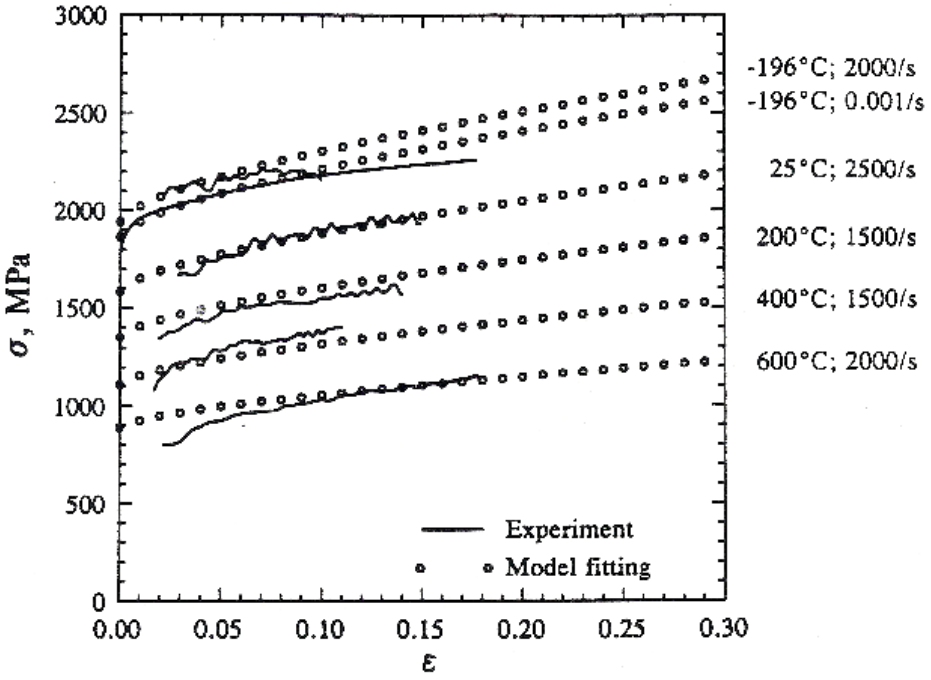

Figure 1.30 - Johnson-Cook constitutive fit for 4340 tempered martensite. The parameters used to fit the data are a=2100 MPa, b=1750 MPa, n=0.65, c=0.0028, m=0.75, and Tmelt=1783 K [79]

The main consideration when using this model is that it is strictly phenomenological. It assigns a power-law hardening behaviour to the material and scales that behaviour up or down, depending on the strain-rate and temperature. It does not account for materials where the effect of strain-rate and temperature on the flow stress is dependent on strain (*i.e.* Al-5083, OFHC copper) [77,78]. The Johnson-Cook fit for Al-5083 is seen in Figure 1.31. It can be seen that the amount of strain-hardening increases as the strain rate increases. This means that the material cannot be fit with the same power-law at all rates. Because of this, the Johnson-Cook fit should only be used within the limits of the experimental data [77].

Another consideration is that most ductile metals experience a large increase in strain-rate sensitivity at rates above 10^4 s^{-1}. The Johnson-Cook model has been modified by Rule and Jones [19] and Kang *et al*. [80] so that this issue can be addressed. However, at the rates seen in vehicle crashes ($>10^3$ s^{-1}), this issue is not a concern.

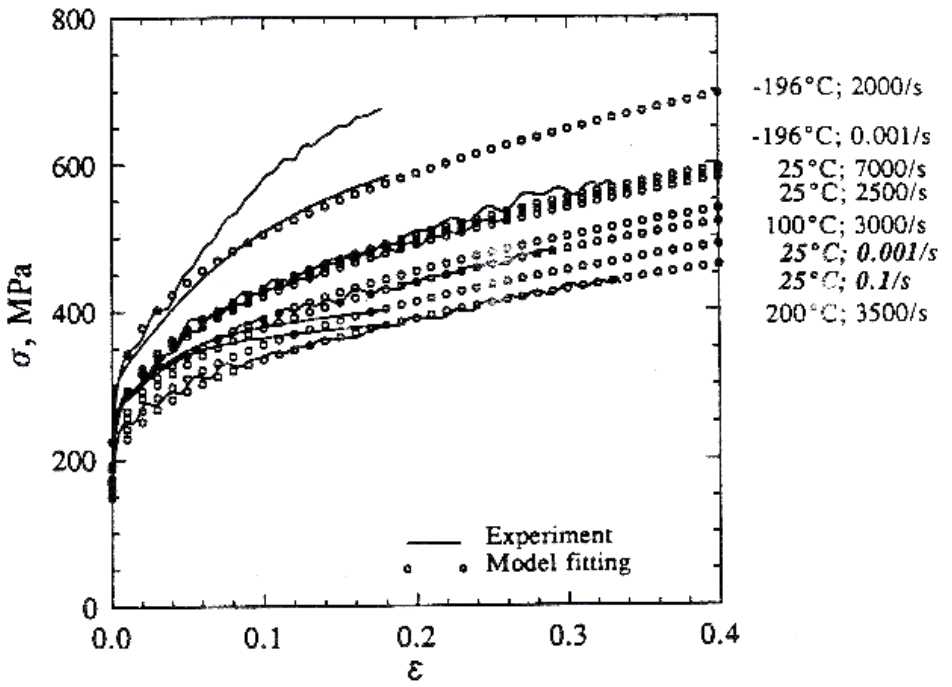

Figure 1.31 - Johnson-Cook constitutive fit for Al-5083. The parameters used to fit the data are a=210 MPa, b=620 MPa, n=0.375, c=0.0125, m=1.525, and Tmelt=933 K [79]

1.3.2 Zerilli-Armstrong

In 1986, Zerilli and Armstrong created a constitutive equation that is based on dislocation mechanics in an attempt to better describe material behaviour, as well as to be able to extrapolate beyond the strain-rates and temperatures seen in their experiments [78,81]. Their constitutive model, Equation 1.9, consists of a thermal and an athermal part, and introduces a grain-size dependence.

$$\sigma = \sigma_{thermal} + \sigma_{athermal} + kl^{-1/2} \qquad (1.9)$$

$$\text{where} \quad \sigma_{thermal} = B\exp(\beta T)$$

The thermal stress is the stress necessary to overcome thermally activated dislocation barriers. Thus, it increases as the strain-rate increases and decreases as the temperature increases. For FCC metals, the thermal activation energy is dependent on dislocation interactions [82]. Since the dislocation density increases as the strain increases, the thermal portion of the stress is dependent on the strain as well as the strain-rate and temperature (Equation 1.10). This can also be seen in Figure 1.32, which shows the

Zerilli-Armstrong fit for Al-5083. The strain-hardening rate matches the experimental data much more closely than that seen in Figure 1.31. For BCC materials, the thermal activation energy is based on the movement of single dislocations, meaning that the thermal portion of the stress is not dependent on the amount of strain (Equation 1.11) [78].

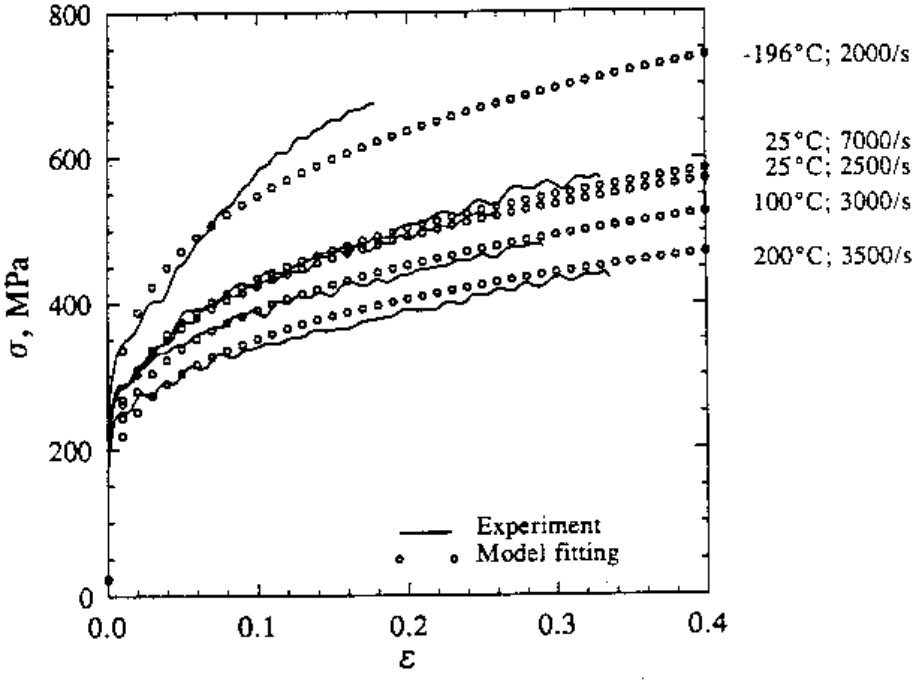

Figure 1.32 - Zerilli-Armstrong constitutive fit for Al-5083. The parameters used to fit the data are σ_0=23 MPa, c_2=970 MPa, c_3=0.00185, c_4=0.00008, n=0.225 [77]

$$\sigma_{thermal-FCC} = c_2 \varepsilon^{1/2} \exp(-c_3 T + c_4 T \ln \dot{\varepsilon}) \qquad (1.10)$$

$$\sigma_{thermal-BCC} = c_1 \exp(-c_3 T + c_4 T \ln \dot{\varepsilon}) \qquad (1.11)$$

The athermal portion of the stress is assumed to be a power-law fit, similar to that of Johnson-Cook (The first two terms in Equation 1.12). The final constitutive equation for BCC metals is shown in Equation 1.12, where σ_0 accounts for the grain size and initial yield strength [78].

$$\sigma = \sigma_0 + c_5 \varepsilon^n + c_1 \exp(-c_3 T + c_4 T \ln \dot{\varepsilon}) \qquad (1.12)$$

Of note is that the Zerilli-Armstrong equations can not be used for strain rates at which the maximum dislocation velocity is exceeded. The dislocation velocity (v) is related to

the shear strain rate ($\dot{\gamma}$), by Equation 1.13, where *m* is the orientation factor, *N* is the dislocation density, and *b* is the Burgers vector [83].

$$\dot{\gamma} = mbNv \tag{1.13}$$

The maximum velocity of the dislocation is near the elastic shear wave speed [78]. When the strain rate is high enough such that the maximum dislocation velocity would be exceeded, the relationship becomes Equation 1.14, where $\dot{N}$ is the rate of increase of the dislocation density and Δx is the average dislocation displacement [84]. In this case, dislocations increase in density through nucleation rather than just multiplication [84].

$$\dot{\gamma} = mb\dot{N}\Delta x \tag{1.14}$$

Zerilli and Armstrong explicitly state that their model is based on Equation 1.13. Thus, the limit of extrapolation is the strain-rate at which the maximum dislocation velocity is reached. However, this is only the case at strain-rates that are higher than those seen in crash models. Thus, for the current study, the Zerilli-Armstrong constitutive equation should be sufficient for capturing the material behaviour at all necessary strain-rates and temperatures.

1.3.3 Plastic Deformation of BCC structures and Discontinuous Yielding

Plastic deformation in a steel is controlled by the movement of its dislocations past obstacles in the lattice. These obstacles are overcome by an increase in applied stress or with the aid of thermal fluctuations [85].

As stated previously, the mechanism which controls the thermally activated motion of dislocations in BCC materials is the interaction between the dislocation and the lattice [78]. This is the Peierls-Nabarro stress, which is the stress necessary for a dislocation to move by one atomic space, shown in Equation 1.15, where *G* is the shear modulus, *b* is the Burgers vector, *c* is the lattice spacing, and *a* is the lattice parameter.

$$\tau_{PN} = \frac{Gb}{2c}\exp(-\pi a/c)\sin(2\pi x/c) \tag{1.15}$$

The thermally activated dislocation motion controls plastic deformation until a rate at which the movement and multiplication of existing dislocations can no longer

accommodate the plastic deformation [84]. In most BCC metals, this occurs at approximately 10^4 s^{-1}, with a density of 10^6 - 10^8 dislocations per square centimetre [14].

A large increase in strength can be seen in metals at strain rates around 10^4 s^{-1}. This is caused by the dislocations reaching their maximum velocity and requiring the nucleation of new dislocations, in a situation described by Equation 1.14. This can be seen in Figure 1.33, where section I contains the quasi-static strain rate dependence, section II encompasses the strain rates at which thermally activated dislocation motion controls the strain rate sensitivity, and section III encompasses the strain rates at which dislocations are being nucleated.

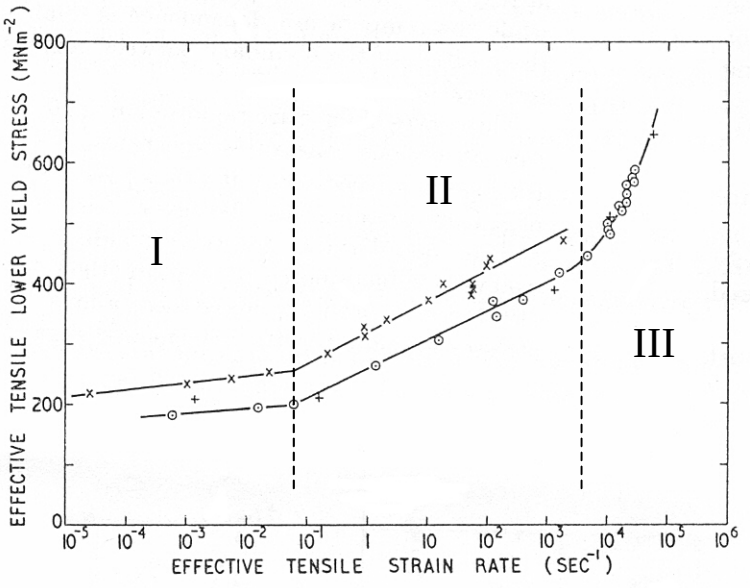

Figure 1.33 - Effective tensile stress as a function of strain rate for En3B Steel [86]

Most low-carbon steels exhibit discontinuous yielding at low rates of strain. However, it has been found repeatedly that HSLA shows discontinuous yielding even at high strain-rates [20,26,27]. Under high strain rate conditions, the ratio of upper-to-lower yield point is amplified tremendously. Two possible explanations exist for this behaviour: adiabatic shear banding [26] and Luders banding [14].

Bassim and Panic [26] have proposed that adiabatic shear banding is the cause for the stress drop at yield under high rate deformation in the HSLA. Their stress versus strain

results are shown in Figure 1.10. Shear banding is due to dislocation pile-ups at grain boundaries which are pinned strongly by solutes [87,88]. The large stress needed for these dislocations to break free is related to the upper yield point, and the corresponding smaller stress needed for the dislocations to continue moving unabated corresponds to the lower yield stress. Materials which have a high microstructural stress intensity factor and a low thermal conductivity are more prone to shear banding. This is one explanation as to why BCC metals are more prone to shear banding than FCC materials.

While shear-banding is undoubtedly present in Figure 1.10, it is difficult to imagine that this is the cause for the drop in yield strength. The reason for this is that the material work-hardens after the yield drop. In shear banding, the large increase in temperature causes thermal softening, which – in turn – causes the material in the shear band to be weaker than the rest of the material. Thus, once shear banding occurs, deformation becomes very localized and work-hardening does not take place. The shear bands were most likely created just before failure at large strains.

The theory that the upper yield stress is due to dislocations being pinned by solute atoms, which tend to form dislocation atmospheres around them was proposed by Cottrell and Bilby [89]. They postulate that the stress needed to unlock the dislocations from the solute atoms is relatively high and that, once free, they can move freely at a lower stress. This mechanism is supported by observations of strain aging where the solute atoms migrate to the dislocations and re-pin them, causing the upper and lower yield points to again become visible [90].

The problems with the second theory are outlined by Hahn [14]. He created a constitutive model for materials which exhibit an upper and lower yield point. His work is based on the work by Gilman and Johnson, in which they created etch pits in a LiF crystal and watched them move during plastic deformation [91]. They found the dislocations responsible for slip are heterogeneously nucleated at stress concentrations, and multiply rapidly. He theorized that the unlocked dislocations would take less energy

to move than the locked dislocations, and thus would be the governing mechanism for Luders banding.

Hahn created a constitutive model for steel based on the multiplication of mobile dislocations (Equation 1.16). *q*, *f*, and *n* are material parameters, *b* is the burgers vector, τ_0 is the resolved shear stress corresponding to unit velocity, and ρ_m is the mobile dislocation density. The mobile dislocation density is modeled as a function of the plastic strain by Equation 1.17. ρ_0 is the initial dislocation density and *C* and *a* are material constants. The theoretical results of this model, shown in Figure 1.34, show how the upper yield point is accentuated as the initial density of mobile dislocations decreases.

$$\sigma = q\varepsilon_p + 2\tau_0\left(\frac{\dot{\varepsilon}}{0.5bf(\rho_m)}\right)^{1/n} \tag{1.16}$$

$$\rho_m = \rho_0 + C\varepsilon_p{}^a \tag{1.17}$$

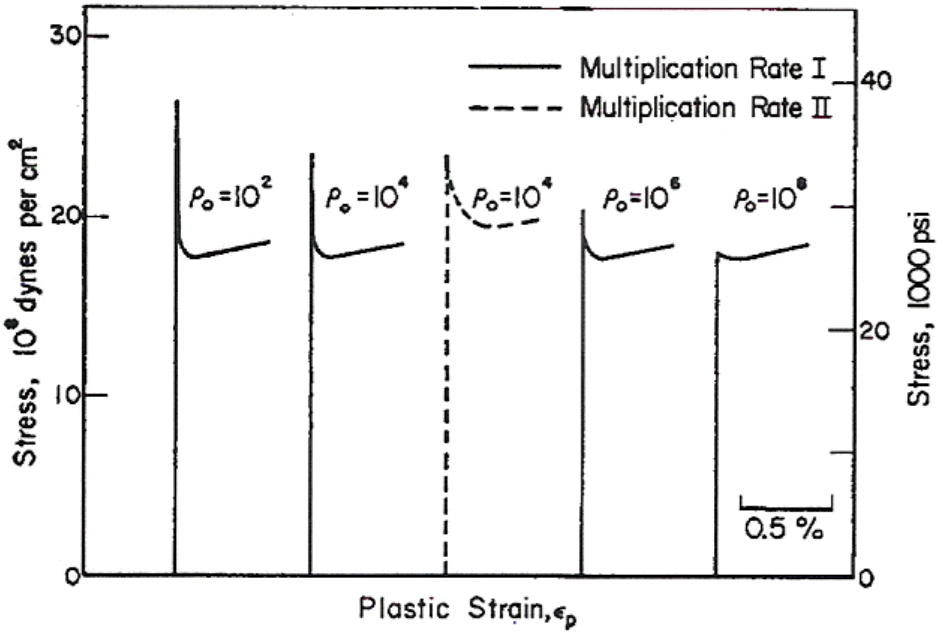

Figure 1.34 - Equation 2.16 plotted for different initial dislocation densities [14]

This theory is supported by the work of Sakuma *et al*. [13] (Figure 1.4), which shows that, as residual stresses in a dual phase steel are increasingly relieved, the mobile

dislocation density decreases and the steel exhibits an increasingly large discontinuous yielding effect.

Material which has a lower mobile dislocation density is more prone to instabilities which cause one part of the gauge length to deform plastically before the rest of the material [90]. The Luders band is created when, at one or both ends of the gauge length, an instability causes the material to deform plastically. This leads to a multiplication of the mobile dislocation density, which hardens the deformed material.

Hahn theorized that the created dislocations would be injected, just ahead of the band, into the undeformed material, causing it to become less stable and to deform plastically [14]. However, Neuhauser and Hampel determined that dislocation multiplication in front of the band is due to moving stress fields, rather than dislocation injection [90]. The geometry of a Luders band can be seen on the left side of Figure 1.35. The band is at a 45° angle to the direction of motion [92]. At the interface between the band and the undeformed material, there is a discontinuity caused by the shearing which has occurred in the deformed band [92]. This discontinuity creates a bending-stress concentration which causes the band to propagate along the gauge length of the specimen [92].

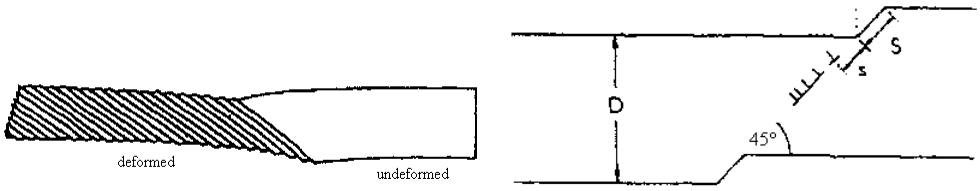

Figure 1.35 - Propagation of a Luders band [92]

It has been noted that the initial yield stress increases as strain rate increases, followed by deformation at a near-constant stress. A possible explanation for this is that, since the initial plastic deformation is localized, the actual strain rate for the deformed material is large enough that dislocations are being nucleated rather than multiplying. If this is the case, providing a constitutive model for HSLA will be quite challenging.

1.3.4 Summary

The Johnson-Cook constitutive model was developed empirically to describe the strain rate and temperature sensitivity of metals. The Zerilli-Armstrong constitutive model was developed based on the thermally activated dislocation motion of metals as a function of strain rate and temperature. Because the Zerilli-Armstrong model is less phenomenologically based than the Johnson-Cook model, it is generally able to model the behaviour of metals more precisely. The Zerilli-Armstrong model is also able to account for changes in the work-hardening rate of FCC metals as the strain rate increases.

Discontinuous yielding, or Luders banding, can be caused by a lack of mobile dislocations, which is seen in low-carbon steels. This effect is amplified at high strain rates. Because when a material displays Luders banding is not deforming uniformly, this portion of the stress-strain data can not be used for constitutive modeling.

1.4 CURRENT RESEARCH

Prior to the current research, testing of dual phase steel has not been performed at strain rates exceeding 600 s^{-1}. This range of available data is inadequate for use in experiments or crash events where tubes are crushed in the axial direction, and experience localized strain-rates on the order of 1000 s^{-1} [93]. Therefore, one focus of the present research will be to characterize dual phase steel at high strain rates.

Conversely, HSLA steels have been characterized at low and high rates, but not at intermediate rates (10 – 100 s^{-1}). Data at these intermediate rates are necessary because these are the rates which are seen locally in S-rail crush events [93]. Thus, focus of this work will be to characterize an HSLA350 alloy at intermediate strain rates.

There is also a lack of data for these alloys in the as-tubed condition. This is an important requirement in view of the extensive use of hydroformed tubular structures in automobiles.

To address these requirements in the current research, three steels (DDQ, HSLA350, and DP600) were characterized in the as-tube condition throughout the complete range of strain rates experienced in s-rail and axial crush tubes during crash events. The motivation for testing three steels whose strengths vary greatly is to evaluate the crashworthiness of the dual phase steel against a low-strength baseline steel (DDQ) and a medium strength baseline steel (HSLA350).

To obtain the strain rate data, uniaxial tensile experiments were conducted on each steel at the following strain rates: 0.00333, 0.1, 30, 100, 500, 1000, and 1500 s^{-1}. The low strain rate tests (0.00333 – 0.1 s^{-1}) were conducted on a quasi-static servo-controlled tensile machine. The intermediate strain rate tests (30 – 100 s^{-1}) were carried out using an instrumented falling weight impact (IFWI) machine, while the high rate tests (500 - 1500 s^{-1}) were carried out using a tensile split Hopkinson bar (TSHB). Also, to characterize the thermal sensitivity of these steels, high rate experiments (500 and 1500 s^{-1}) were performed at initial temperatures of 150 and 300 °C. Specimens cut from the as-received sheet were also tested for comparison with the as-tubed results.

After the data was collected at each of the eleven conditions, the results were fit with both the Johnson-Cook and the Zerilli-Armstrong constitutive models. These models were chosen because they were developed to describe the high strain rate constitutive behaviour of metals [75,76,78,81] and because they are readily available for use in the commercially available finite element codes. As part of this research, these models were then used in finite element simulations of the IFWI and TSHB experiments to verify that the material behaviour was adequately captured by the constitutive fits.

By characterizing and modeling the materials, their behaviour in automotive crash events can be predicted using finite element simulation, rather than through crash tests. This

will enable automotive manufacturers to save money and will provide more flexibility in terms of the different crash conditions considered to evaluate the behaviour of light weight automotive structures.

The balance of this thesis is organized as follows. In Chapter 2, the experimental equipment and methods used to capture the data are described. In Chapter 3, the method used to perform the constitutive analysis of the experimental results is provided in detail for the DP600 sheet specimens. In Chapter 4, the experimental results and trends are presented for all of the alloys considered. These results consist of the strain rate sensitivity, thermal softening, effects of tube fabrication, and elongation to failure. In Chapter 5, the fits of the parameters for the Johnson-Cook and Zerilli-Armstrong constitutive models to the experimental results are described and the accuracy of the fits are discussed. In Chapter 6, numerical models of the IFWI and TSHB experiments are presented as well as the utility of the constitutive fits in numerically reproducing the experimental results. Chapter 7 provides a discussion of the results from this research. Finally, in Chapter 8, conclusions that can be drawn from this body of work are presented as well as suggestions for future work.

CHAPTER 2

EXPERIMENTAL METHODS

2.1 EXPERIMENTS

Three steels were characterized as part of the current research: a dual phase steel (DP600), a high-strength-low-alloy steel (HSLA350), and a drawing quality steel (DDQ). The composition of these steels is given in Table 2.1. The steels were characterized in both the as-received sheet and as-tubed conditions in order to determine the tube forming effects on the mechanical strength.

Table 2.1. Chemical composition of DDQ, HSLA350, and DP600

STEEL	NOMINAL COMPOSITION (*wt. %*)															
	C	Mn	P	S	Si	Cu	Ni	Cr	Sn	Al	N	Mo	V	Nb	Ti	Ca
DDQ	0.039	0.22	0.005	0.01	0.013	0.03	0.01	0.03	0.002	0.048	0.002	0.002	0.002	0	0.009	0
HSLA350	0.054	0.65	0.035	0.005	0.069	0.015	0.07	0.06	0.007	0.033	0.008	0.024	0.005	0.02	0.015	0.002
DP600	0.106	1.53	0.012	0.001	0.201	0.03	0.03	0.19	0.003	0.031	0.006	0.22	0.006	0.002	0.018	0.003

To form tube from sheet, the original sheet coil is cut into five slits, and then each slit is then roll formed into a tube. For consistency, the sheet and tube specimens were taken from the same slit. For DP600, the outer slit was used. For HSLA350 and DDQ, the centre slit was used. Each steel has a nominal thickness of 1.8mm.

To characterize each steel, uniaxial tensile experiments were performed on the sheet and tube over the complete range of strain rates and temperatures that are seen in automobile forming and crash events. This corresponds to strain rates from 0.00333 to 1500 s^{-1} and temperatures up to 300 °C. The elevated temperature tests were carried out at 150 and 300 °C at strain rates of 500 and 1500 s^{-1}. Testing was performed on specimens from three positions on the perimeter of the tube, corresponding to the 3, 6, and 9 o'clock positions, seen in Figure 2.1 (the weld seam is located at 12 o'clock). The sheet specimens were tested along the rolling direction, which corresponds to the tensile axis of the tube specimens. A complete test matrix can be seen in Table 2.2 (room temperature)

and Table 2.3 (high temperature). Three tests were carried out at each condition to assess repeatability. In total, 198 room temperature experiments and 72 high temperature experiments were performed.

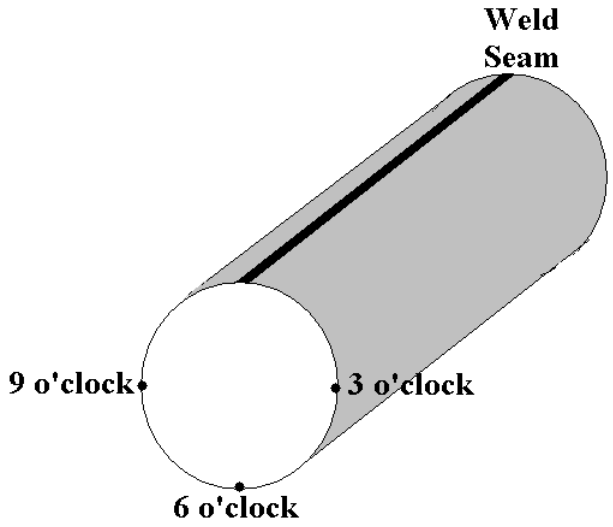

Figure 2.1. Specimen positions for the steel tubes

Table 2.2. Matrix of experiments conducted at room temperature

STEEL		NOMINAL STRAIN RATE (s^{-1})						
		0.00333	0.1	30	100	500	1000	1500
DDQ	*SHEET*	X	X	X	X	X	X	X
	TUBE-3 o'clock	X	X	X	X	X	X	X
	TUBE-6 o'clock	X	X	X	X	X	X	X
	TUBE-9 o'clock	X						
DP600	*SHEET*	X	X	X	X	X	X	X
	TUBE-3 o'clock	X	X	X	X	X	X	X
	TUBE-6 o'clock	X	X	X	X	X	X	X
	TUBE-9 o'clock	X						
HSLA	*SHEET*	X	X	X	X	X	X	X
	TUBE-3 o'clock	X	X	X	X	X	X	X
	TUBE-6 o'clock	X	X	X	X	X	X	X
	TUBE-9 o'clock	X						

Table 2.3. Matrix of experiments conducted at elevated temperatures

STEEL		NOMINAL STRAIN RATE (s^{-1})			
		500 150 °C	500 300 °C	1500 150 °C	1500 300 °C
DDQ	*SHEET*	X	X	X	X
	TUBE-6 o'clock	X	X	X	X
DP600	*SHEET*	X	X	X	X
	TUBE-6 o'clock	X	X	X	X
HSLA	*SHEET*	X	X	X	X
	TUBE-6 o'clock	X	X	X	X

During the tubing process, the sheet is roll formed and the two edges are induction-welded together. By forming the tube in this way, the amount of plastic work imparted into the steel is not uniformly distributed around the perimeter of the tube. Due to the nature of the tube forming process, the material at the 6 o'clock position experiences the most deformation, while the material adjacent to the weld seam experiences the least. Thus, to properly characterize the tube, experiments were performed on multiple locations around the perimeter of the tube. Experiments were performed on the 3 and 6 o'clock positions of the tube at elevated rates. Since the plastic work was assumed to be symmetric about the weld seam-6 o'clock plane, the response at 3 and 9 o'clock was assumed to be identical. This was confirmed in the experiments at 0.00333 s^{-1}. The weld seam and adjacent material were not characterized.

At elevated temperatures, only specimens from the 6 o'clock position of the tube and the rolling direction of the sheet were tested. The reason for considering only one position is that the temperature sensitivity of a BCC material is not related to the amount of plastic work that has gone into the material [81]. Thus, it is expected that the sheet and tube will display the same thermal softening response, regardless of position within the tube.

The strain rates for this research were chosen to emphasize the higher rates seen in an automobile crash. This can be seen in Figure 2.2, which shows the strain rates chosen for this study on a logarithmic scale. The logarithmic nature of strain rate sensitivity has been well established experimentally [77-80].

Figure 2.2. Nominal strain rates considered in the experimental test matrix

To carry out these experiments, a servo-controlled tensile tester was used for the low-rate tests (0.00333 and 0.1 s^{-1}), an instrumented falling weight impact tester (IFWI) was used to carry out the intermediate-rate tests (30 and 100 s^{-1}), and a tensile Hopkinson bar

(TSHB) was used to carry out the high-rate tests (500 – 1500 s^{-1}). The elevated temperature tests were also performed on the TSHB.

2.2 SPECIMEN GEOMETRY

Smerd *et al*. [95] performed high-rate tests on aluminum alloy AA 5754 using the same TSHB that was used for this research. They determined that a proper specimen geometry for these tests is one that has a gauge length of 12.5 mm and a width of 1.75 mm, (Figure 2.3). This geometry was chosen to optimize two opposing factors: i) maintaining stress equilibrium in their TSHB specimens, which favours a small specimen gauge length; and, ii) at quasi-static rates, maintaining a close relationship to the data generated by the geometry given in ASTM standard E8 [96], which requires a longer gauge length. It is necessary to optimize these two opposing factors so that any specimen geometry effects can be identified and to ensure that a consistent geometry can be used at each strain rate.

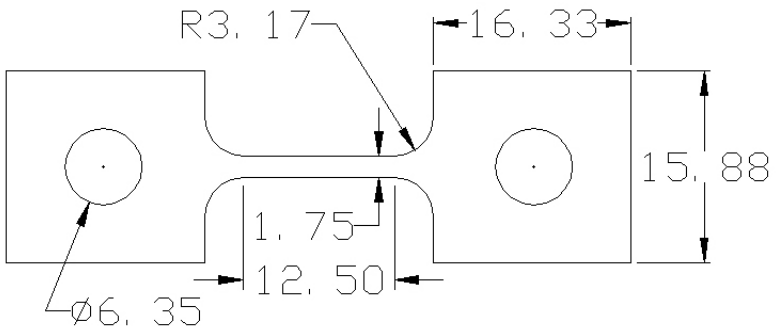

Figure 2.3. Tensile specimen geometry. All dimensions are in mm.

2.3 LOW-RATE EXPERIMENTS

An INSTRON Universal-Materials-Testing-Machine (Model 3365) was used for the low-rate experiments. The specimen and grips are shown in Figure 2.4. Tests were performed at 2.5 and 75 mm/min, corresponding to 0.003 s^{-1} and 0.1 s^{-1}, respectively, and data was collected at a sampling rate of 20 Hz. Force was measured using a load cell

with a capacity of 5 kN. Strain was measured using an INSTRON G51-14 extensometer, which was calibrated before each set of experiments. Tensile grips were fabricated to ensure that neither the specimen nor the extensometer slipped during the tests.

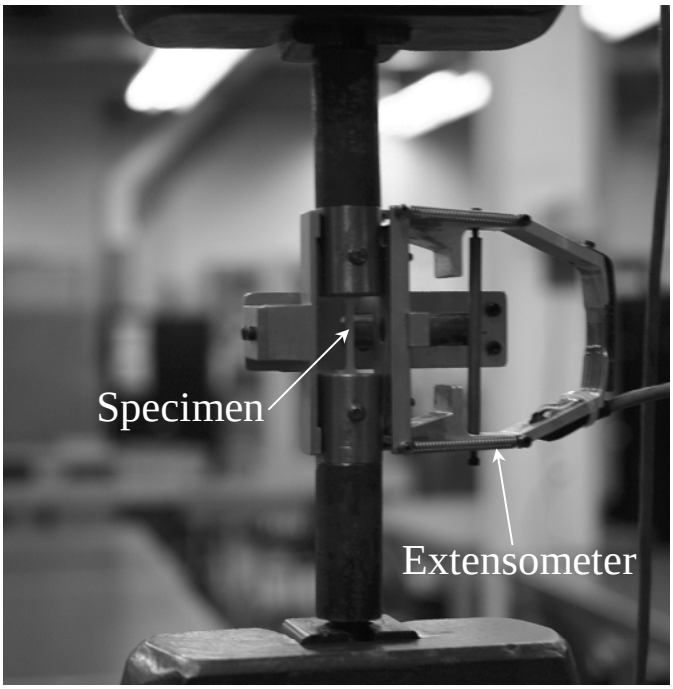

Figure 2.4. Tensile specimen situated for low-rate testing

2.4 INTERMEDIATE-RATE EXPERIMENTS

2.4.1 Experimental Methods

Intermediate-rate experiments were performed on an IMATEK IFWI machine. The setup for this experiment is shown in Figure 2.5. The specimen is held between the upper and lower grips. The upper grip is attached to the load cell, which is fixed in place, and the lower grip hangs freely from the specimen. At the beginning of the experiment, the striker falls and hits the lower grip. The downward force of the striker loads the specimen in tension.

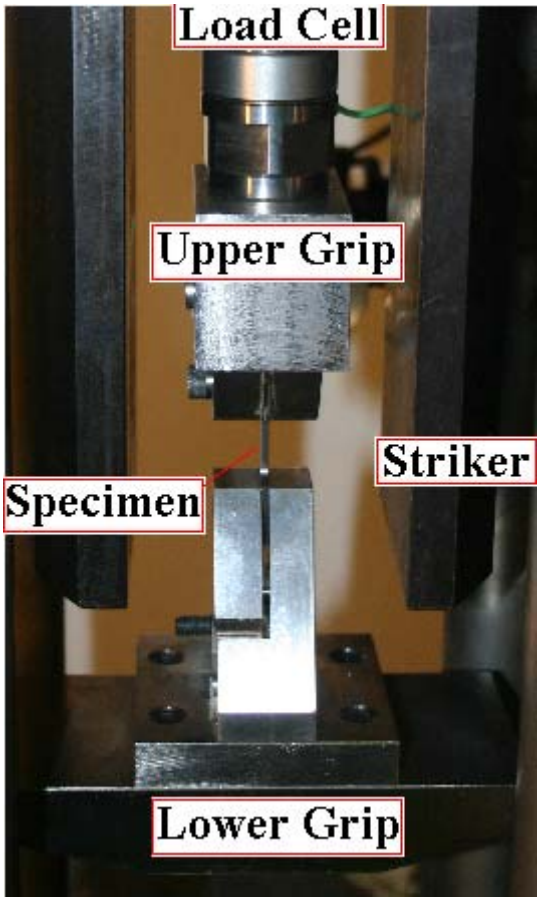

Figure 2.5. Schematic diagram of the IFWI experimental setup

The lower grip must be as light as possible for two reasons: i) the weight of the lower grip can preload the specimen; and, ii) the lighter the grip is, the faster it will accelerate (to reach a constant strain rate) when it is hit by the striker. However, the lower grip must also be strong enough to withstand repeated impacts without deforming plastically or fracturing. For these reasons, the lower grip is constructed out of titanium alloy Ti-6Al-4V. The grip has a mass of 1.58 kg, which translates into a preload of approximately 4.90 MPa on the specimen. The upper grip is constructed out of type-S tool steel so that it can withstand repeated impacts. The striker is made out of aluminum alloy AA 6061-T6.

Force was measured using a KISTLER 9500A4 ±30 kN piezoelectric load cell, stationed above the upper grip. The force signal was measured at a sampling rate of 0.6 MHz,

which provided more than adequate temporal resolution of the experiments, which have a duration of 4 – 15 ms.

Elongation of the specimen was measured by an enhanced laser velocity system (ELVS), developed at the University of British Columbia, shown in Figure 2.6. The arrangement of the ELVS with respect to the specimen can be seen schematically in Figure 2.7. During operation, the laser projects a sheet of laser light which disperses as it moves forward. This sheet is then collimated by the plano-cylindrical lens. The laser width adapter ensures that the sheet has a width of 25.4 mm. The symmetric convex lens refocuses the sheet to a point, and the intensity of this point is measured by the high-speed PIN photodetector. The intensity is converted to a voltage, which is read by the data acquisition system.

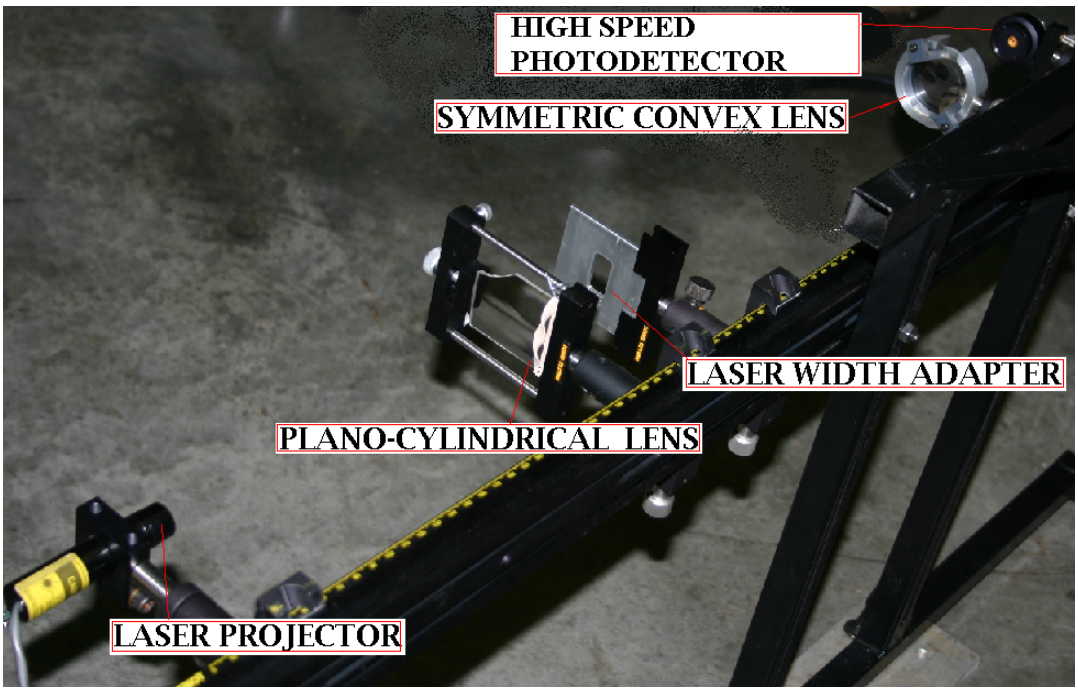

Figure 2.6. Enhanced Laser Velocity System

For these experiments, the ELVS is situated such that the sheet of light is partially obstructed by the upper and lower grips (Figure 2.7). Upon impact from the striker, the lower grip moves downward. This increases the distance between the upper and lower

grip by an amount corresponding to the specimen elongation, allowing more of the laser sheet to pass through. In this way, the elongation of the specimen can be measured directly from the ELVS light-intensity measurement. This measurement was also recorded at a sampling rate of 0.6 MHz.

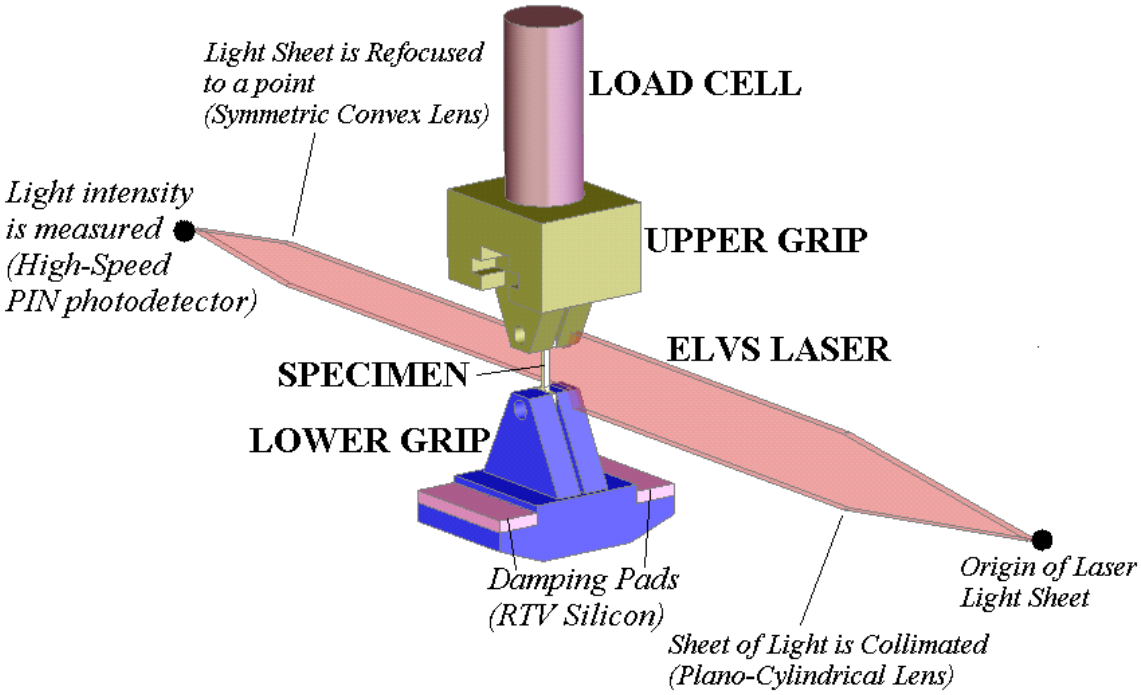

Figure 2.7. Arrangement of the ELVS laser sheet with respect to the specimen and lower grip

The ELVS output follows a linear relationship of 0.0712 V/mm very closely, as seen in the calibration curve in Figure 2.8. Calibration of the ELVS was performed at the beginning of each set of experiments. The high-speed PIN photodetector has a digital resolution of 0.3 mV, which corresponds to a displacement of approximately 0.005 mm for the current research.

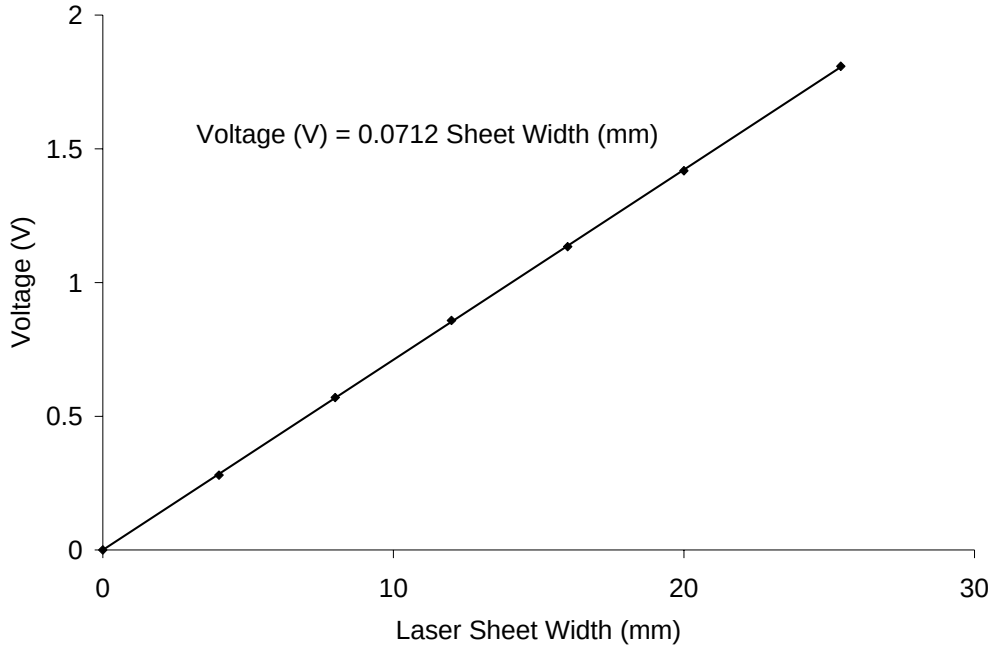

Figure 2.8. Calibration curve of the ELVS

2.4.2 Experimental Procedure and Validation

As discussed in Section 1.2.1.6, inertial effects and ringing can severely distort dynamic load cell measurements. Low frequency oscillations (between 1 and 5 kHz) can be on the same order of magnitude as the actual specimen response. In order to eliminate these oscillations, a force-shaping method was employed which used pads made of RTV silicon to dampen the impact such that the natural frequency of the load cell (2.807 kHz) was not excited. The arrangement of the pads on the lower grip can be seen in Figure 2.7.

The ringing that is present when pads are not used can be seen in Figure 2.9, which shows two force vs. time measurements of HSLA350 tube specimens that were tested at 100 s^{-1}. The red curve represents the force-time response when the striker strikes the lower grips directly. The blue curve represents the response when the impact is damped by placing 19 mm thick RTV silicon pads between the striker and the lower grip. With the use of the damping pads, the oscillations are completely eliminated and the force

measurement reflects the behaviour of the material. Without the pads, the material response is greatly obscured. The natural frequency of the load cell – 2.807 kHz – can be seen clearly in this signal.

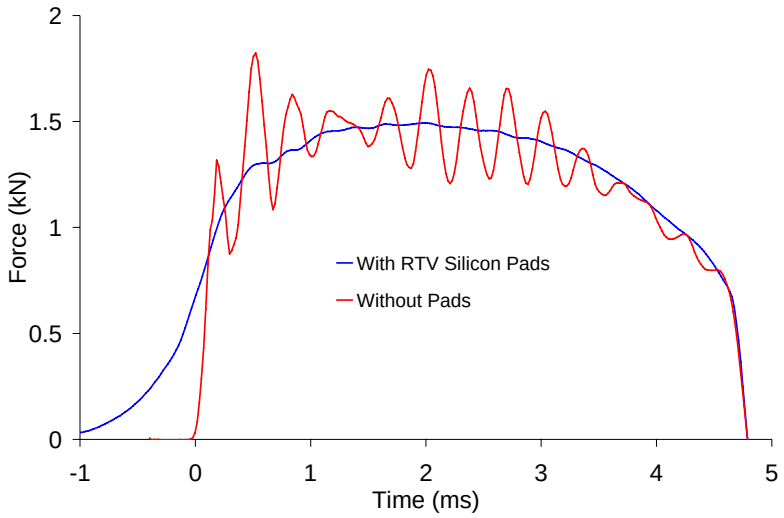

Figure 2.9. Force vs. time response of HSLA350 for damped and undamped impacts

The unfortunate side effect of using damping pads is that the time required for the specimen to reach a constant strain rate (velocity of the lower grip) is increased. This is illustrated in Figure 2.10, which shows the measured displacement of the lower grip for the two specimens shown in Figure 2.9. In the case of the undamped impact, the lower grip accelerates to a constant velocity almost instantly, while the damped impact does not reach a constant velocity until approximately 1.9 ms, which corresponds to almost 11% strain. In order to properly model the material behaviour, the amount of strain which occurs prior to a constant strain-rate being reached must be identified. Therefore, the thickness of the pads was minimized such that the time needed to reach a constant strain rate was reduced while ensuring that the ringing was eliminated from the force measurement.

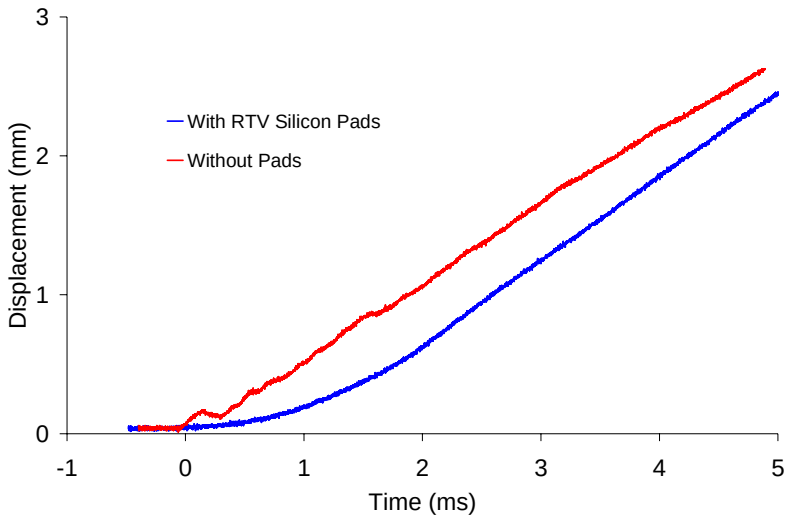

Figure 2.10. Displacement vs. time of HSLA350 for damped and undamped impacts

In order to determine the minimum thickness of the damping pads, experiments were performed where the pad thickness was systematically increased until the ringing was eliminated. These results were then confirmed through the use of a theoretical model of the load cell, shown in Section 1.2.1.

Figure 2.11 shows the force-time response of the HSLA350 specimens tested at 100 s^{-1} with four different damping conditions (pad thicknesses). The curves of the damped conditions are shifted such that the peaks of the oscillations occur at the same time. It can be seen that, as the thickness of the damping pad increases, the oscillations decrease. From this work, it was determined that 13.5 mm thick pads should be used to eliminate the oscillations in the data. Beyond the upper yield point, the amplitude of the oscillations is approximately 0.044 kN, which is about 3% of the material strength. This level of oscillation will be discussed further in Chapter 4, but it is due to the discontinuity of the upper yield point rather than the striker impact. The reason that these pads were chosen over the 19 mm pads is that the specimen reached 100 s^{-1} at approximately 4% strain for the 13.5 mm pads as opposed to 11% strain for the 13.5 mm pads.

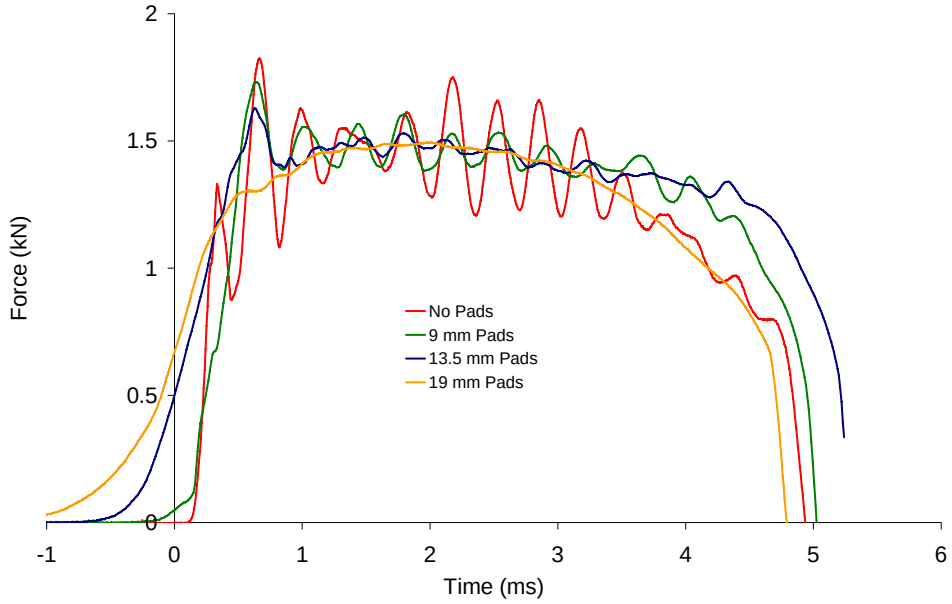

Figure 2.11. Oscillations in the load cell measurements for increasingly damped impacts.

To verify the selection of pad thickness based on the experimental observations of ringing, a simple spring-mass system was used to model the load cell (Figure 1.2.9). The displacement response ($x(t)$) of the load cell to an arbitrary impact is given in Equation 1.1, where ω_n is the natural frequency of the load cell, m is the mass of the load cell, and f_s is the excitation force. To eliminate the sinusoidal nature of the measured force, an input force which has the initial shape ($\omega_n t < \pi/2$), given in Equation 2.1, should be employed. By shaping the force input to the load cell in this manner, the input force matches the measured force.

$$x(t) = \frac{1}{\omega_n m}\int f_s(t)\sin(\omega_n t) \tag{1.1}$$

$$f_s(t) = \exp\{-\cos(\omega_n t)\} \tag{2.1}$$

In order to give the force this shape, the lower grip must be accelerated in a defined manner. Figure 2.12 shows a free-body diagram of the lower grip, where F_A is the force applied by the striker and F_s is the reaction force of the specimen. From this diagram, the

equation of motion for the lower grip can be obtained (Equation 2.2). Assuming that the applied force has the same transient shape as the specimen force (*i.e.* F_A is proportional to Equation 2.1), the equation for the acceleration of the lower grip is given in Equation 2.3. C is a constant which depends on the magnitude of the impact force and the damping pad response and m is the mass of the lower grip. The displacement of the lower grip can then be found by numerically integrating Equation 2.3.

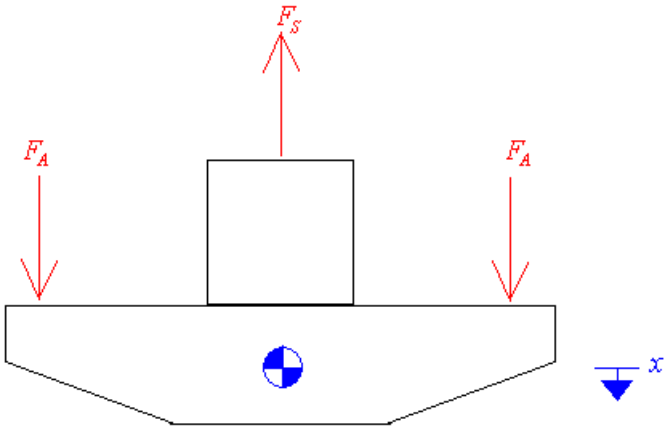

Figure 2.12. Free body diagram of the lower grip

$$m\ddot{x} = F_A - F_s \tag{2.2}$$

$$\ddot{x} = \frac{C}{m}\exp(-\cos(\omega_n t)) \tag{2.3}$$

In order for the velocity of the lower grip to reach the desired strain rate, it was found that C = 0.270 kN and 0.101 kN for strain rates of 80 and 30 s^{-1} respectively. These displacement profiles were achieved experimentally with pads that were 13.5 and 4.85 mm thick respectively. A comparison of the theoretical and experimentally determined displacement of the lower grip is shown in Figure 2.13. There is good agreement between the theoretical and experimental curves. Therefore, the experimentally determined pad thicknesses were used for each material. Discussion of the shape of the input force (matching the shape of the force to Equation 2.1) is considered further in Chapter 6, where numerical modeling of the IFWI experiment is discussed.

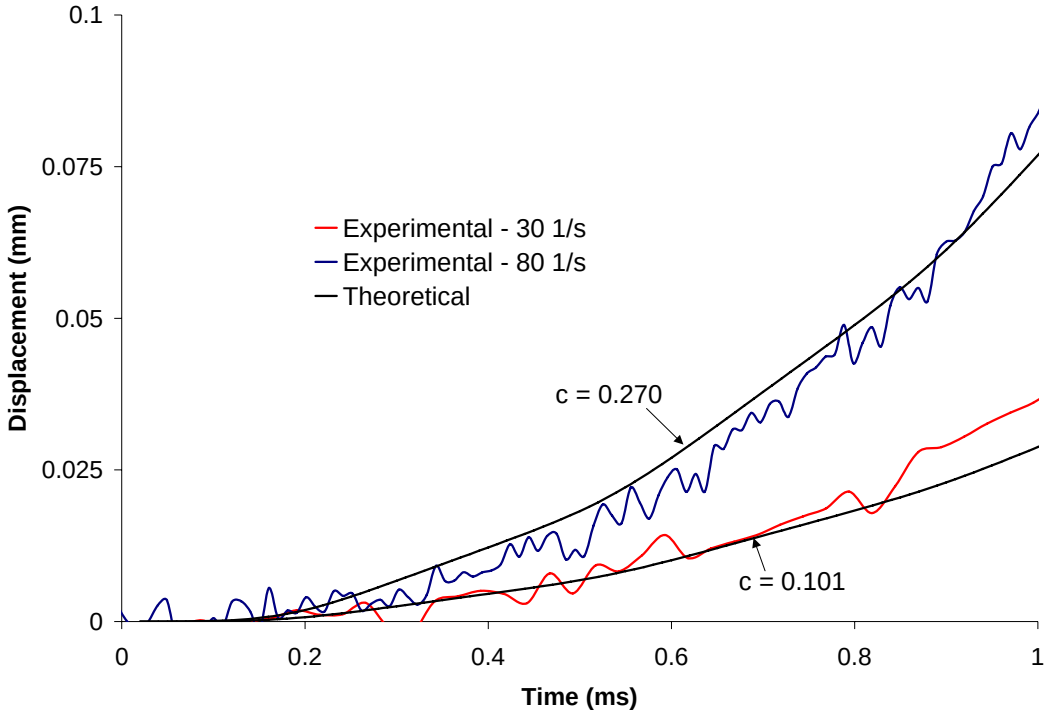

Figure 2.13. Displacement of the lower grip as determined theoretically and experimentally

2.5 HIGH-RATE EXPERIMENTS

The high-rate experiments were conducted on a TSHB. A schematic diagram of the apparatus can be seen in Figure 2.14. A complete description of the apparatus can be found in the thesis by Smerd [97]. The incident bar, transmitted bar, striker, and end cap are made of aluminum alloy 6061-T6 and data was recorded at a sampling rate of 5 MHz.

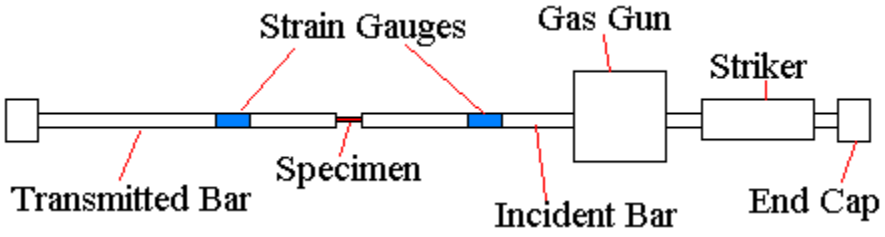

Figure 2.14. Schematic diagram of the TSHB

In a typical TSHB experiment, the striker is fired along the incident bar by the gas gun until it reaches the end cap. Upon impact with the end cap, a longitudinal tensile wave is created in the incident bar which is twice the length of the striker. The wave then travels along the incident bar until it reaches the specimen. The specimen is then loaded in tension, as part of the wave is transmitted through the specimen into the transmitted bar and part is reflected back into the incident bar. The incident, reflected, and transmitted waves are recorded by strain gauges and used to evaluate the stress-strain response of the specimen using Equations 1.4 – 1.6, where σ is the stress in the specimen, A_b is the cross-sectional area of the bars, A_s is the cross-sectional area of the specimen, and ε_t is the strain in the transmitted bar, $\dot{\varepsilon}$ is the specimen strain rate, C_0 is the elastic wave speed in the bars, L is the specimen gauge length, and ε_r is the reflected strain, and ε is the specimen strain. These equations are discussed in further detail in Section 1.2.2.

$$\sigma = E\frac{A_b}{A_s}\varepsilon_t \tag{1.4}$$

$$\dot{\varepsilon} = -2\frac{C_0}{L}\varepsilon_R \tag{1.5}$$

$$\varepsilon = -2\frac{C_0}{L}\int \varepsilon_R dt \tag{1.6}$$

The striker used in these experiments was 508 mm long, which resulted in a test duration of approximately 0.2 ms. Due to the finite duration of the experiment, specimens could not be tested to failure. A specimen tested at 500 s^{-1} was only strained to approximately 0.10 strain. At 1000 and 1500 s^{-1}, strains of approximately 0.2 and 0.3, respectively, were reached. Unfortunately, this is a limitation of this testing method.

The specimen is held in the grip region via slots which were wire-EDM machined into the ends of the incident and transmitted bar, as shown in Figure 2.15. The specimen is then clamped into place by a steel screw, which is threaded into the bars. This provides a tight friction fit which prevents the specimen from slipping during the experiment. It was

also found by Smerd [97] that this method of gripping provided a low degree of distortion of the waves.

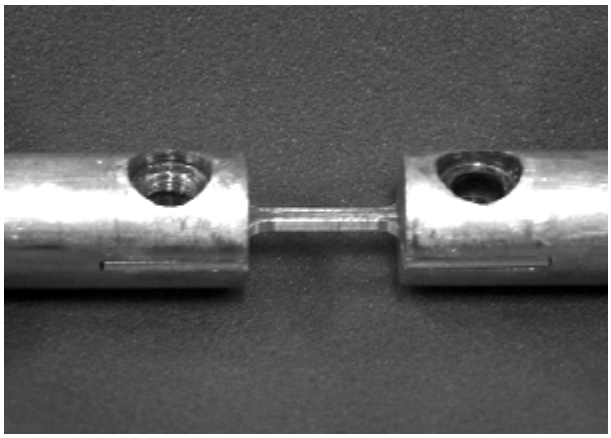

Figure 2.15. TSHB specimen held between the incident and transmitted bar [97]

1000 Ω foil strain gauges were used to measure the incident, reflected, and transmitted waves (an example of the waves is shown in Figure 2.16). Two strain gauges were located on each bar; one on the top and one on the bottom, so that any bending that was present in the waves would be cancelled. The strain gauges were calibrated prior to testing, and were found to output 647.4 mV per unit of strain.

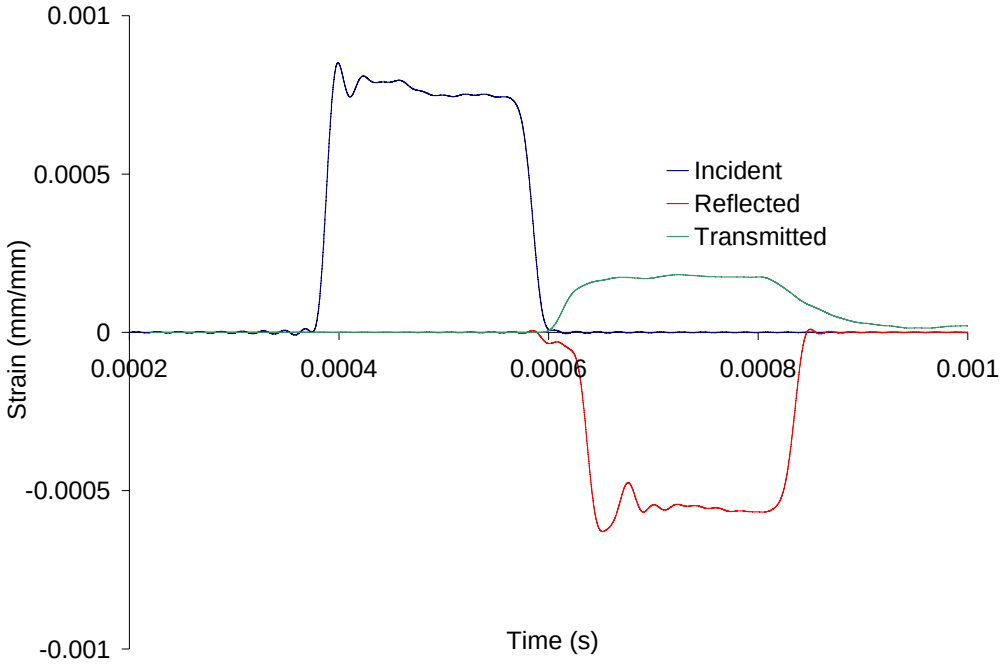

Figure 2.16. Incident, reflected, and transmitted waves of a TSHB experiment on DP600 tube (6 o'clock) at 500 s^{-1}.

2.6 ELEVATED TEMPERATURE EXPERIMENTS

For each steel, elevated temperature tests were conducted at temperatures of 150 and 300 °C on the TSHB. A radiative furnace, shown in Figure 2.17, was used to heat the specimens. The heat source comprises four 1000 W quartz lamps. The rest of the inside of the furnace is made of highly-polished aluminum, which reflects heat and light towards the specimen. A mixture of antifreeze and water was pumped from a freezer through the furnace to cool the lamps between tests. The specimen was situated directly in the middle of the furnace to promote a uniform temperature rise within the specimen.

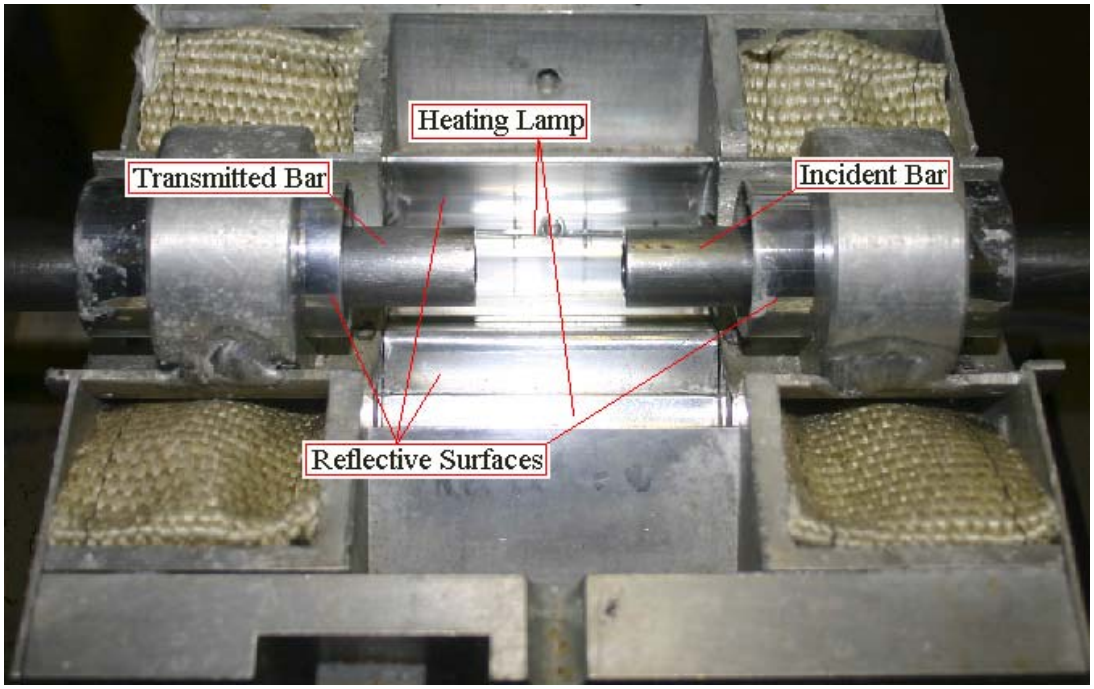

Figure 2.17. Arrangement of the furnace on the TSHB (specimen not shown)

To calibrate the time needed for the furnace to heat the specimens to the required temperature, a 1.5 mm diameter hole was drilled into the gauge length of a calibrated specimen and a type-K thermocouple was inserted. The thermocouple measured the temperature of the specimen as it was heated. In order to reach 150 °C, it was found that two of the furnace lamps needed to be in operation for 13 seconds. For the specimen to reach 300 °C, all four of the furnace lamps needed to be in operation for 11 seconds. These heating times were assumed to be fast enough that only limited annealing effects were occurring.

For each test, the striker was fired after the lamps had been activated for the appropriate amount of time (11 or 13 seconds). A thermocouple was attached to the transmitted bar, just outside the furnace, to ensure that the initial temperature of the bar was the same for each experiment. Bags filled with refrigerated anti-freeze were used to cool the bars between tests.

CHAPTER 3

ANALYSIS OF EXPERIMENTAL RESULTS

In order to model the constitutive response of a material, a key requirement is to determine its true stress (or flow stress) as a function of plastic strain, plastic strain rate, and temperature. In this chapter, the procedure for obtaining constitutive properties describing this relationship from the experimental results is discussed. To illustrate the procedure for analyzing the experimental results, the raw data from the experiments performed on DP600 sheet specimens is presented in detail. The raw data for the rest of the materials and specimens is presented in Appendix A, as well as a complete set of specimen data, including initial dimensions, nominal strain rate, measured strain rate, temperature and elongation to failure.

3.1 LOW-RATE RESULTS

3.1.1 Specimen Geometry Effects

For low-rate testing, the effect of using a non-standard specimen size (a geometry not corresponding to ASTM standard E8) was evaluated in addition to determining the constitutive properties. The engineering stress – strain curve at 0.0033 s^{-1} for both the standard (ASTM) and small (12.5 mm) geometries can be seen in Figure 3.1. There is very little difference in behaviour prior to the specimen reaching its ultimate tensile strength (UTS). Beyond the UTS, the smaller specimen exhibits a much larger strain-to-failure. This apparent increase in elongation is due to the strains associated with local necking. The length of the necked region is relatively constant, regardless of the initial gauge length of the specimen. When this constant length is converted to strain, it gives the appearance that greater post-uniform deformation occurs as the specimen gauge length decreases. This effect can be seen in Figure 3.1, where the standard sized

specimens are seen to fail between 0.24 and 0.25 strain, while the smaller specimens fail between 0.30 and 0.33 strain. This change in elongation between specimen geometries is not a concern for constitutive modeling because the behaviour beyond the UTS is not considered in constitutive fitting. It is only relevant when discussing the elongation to failure.

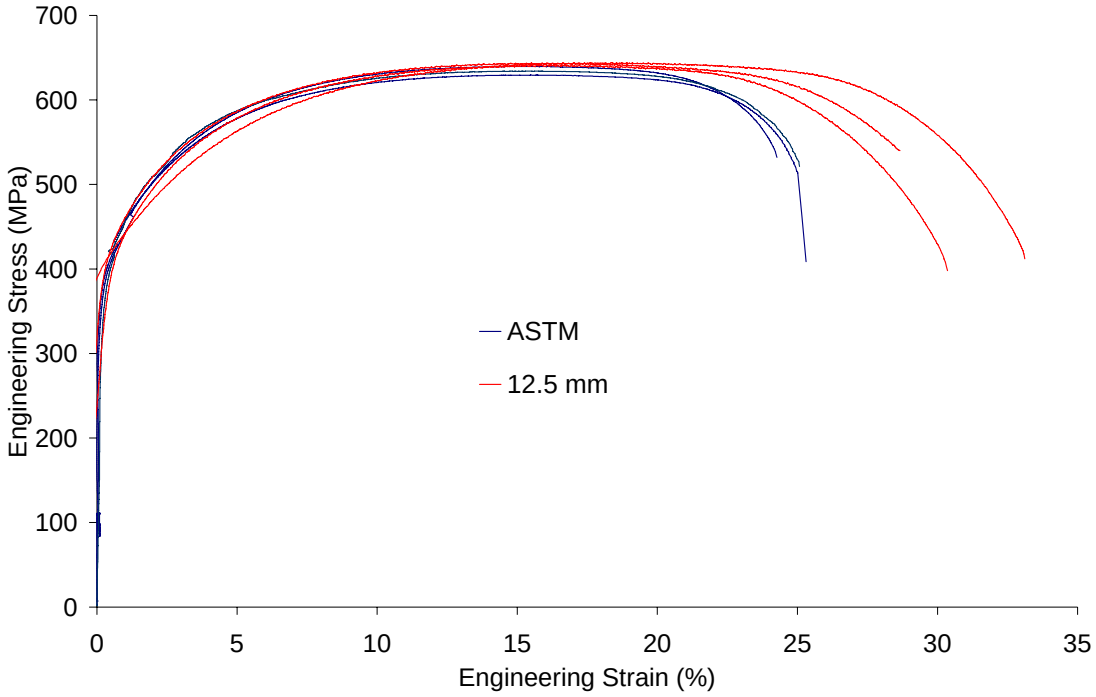

Figure 3.1. Engineering stress vs. engineering strain of DP600 sheet at 0.0033s^{-1}

3.1.2 True Stress – Effective Plastic Strain Calculations

True stress was calculated using Equation 3.1, where σ_t is the true stress, σ_{eng} is the engineering stress, and ε_{eng} is the engineering strain.

$$\sigma_t = \sigma_{eng}(1+\varepsilon_{eng}) \tag{3.1}$$

The effective plastic strain (Equation 3.2) was calculated by converting the engineering strain into true strain and subtracting the elastic portion of the response.

$$\varepsilon_{eps} = \ln(1+\varepsilon_{eng}) - \frac{\sigma_t}{E} \qquad (3.2)$$

Effective plastic strain is used as a state variable when calculating work-hardening in the Johnson-Cook and Zerilli-Armstrong constitutive models.

The true stress versus effective plastic strain response is shown in Figure 3.2 for both sizes of specimen. As with the engineering stress – strain, the difference in behaviour is negligible until the UTS is reached.

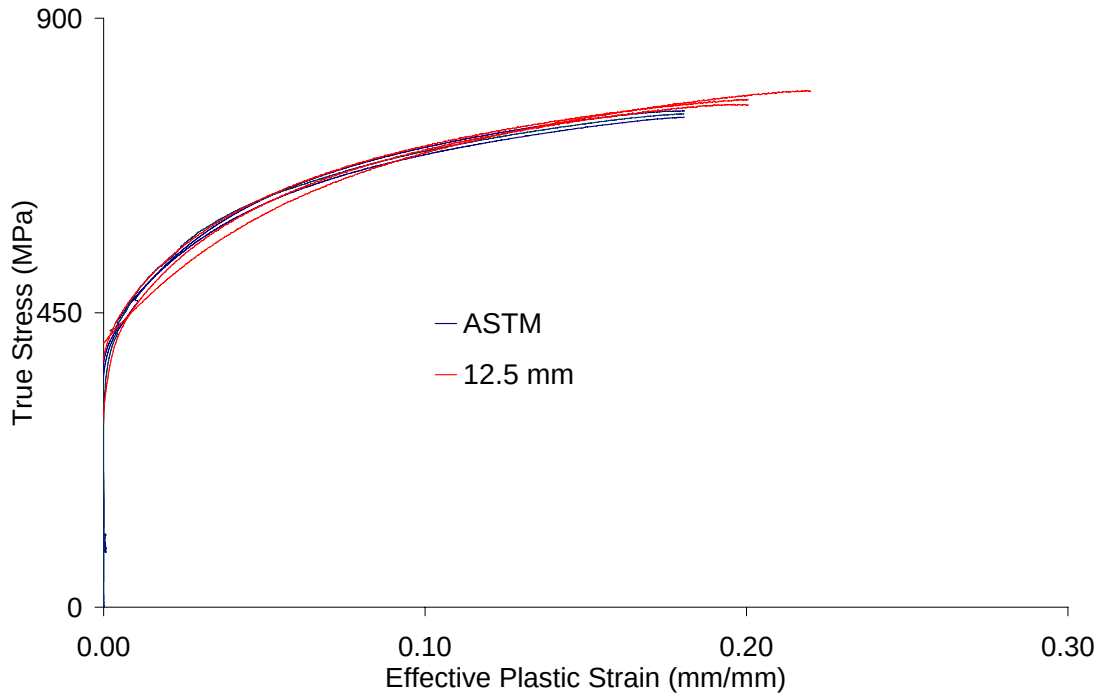

Figure 3.2. True stress vs. effective plastic strain of DP600 sheet at 0.0033s^{-1}

Due to the slow nature of the low-rate experiments, the testing equipment was able to maintain a constant strain rate throughout the majority of the test. This can be seen in Figure 3.3, which shows the strain rate versus strain for the two low-rate conditions (nominal strain rates of 0.0033 and 0.1 s^{-1}). Therefore, all of the data from the onset of yielding until the UTS is reached was used for constitutive fitting.

Due to the slow nature of the experiments, it was assumed that the temperature in the specimen remained constant (isothermal assumption). This assumption implies that all of the heat that was generated within the specimen during the experiment was dissipated either through conduction to the grip regions or through convection to air.

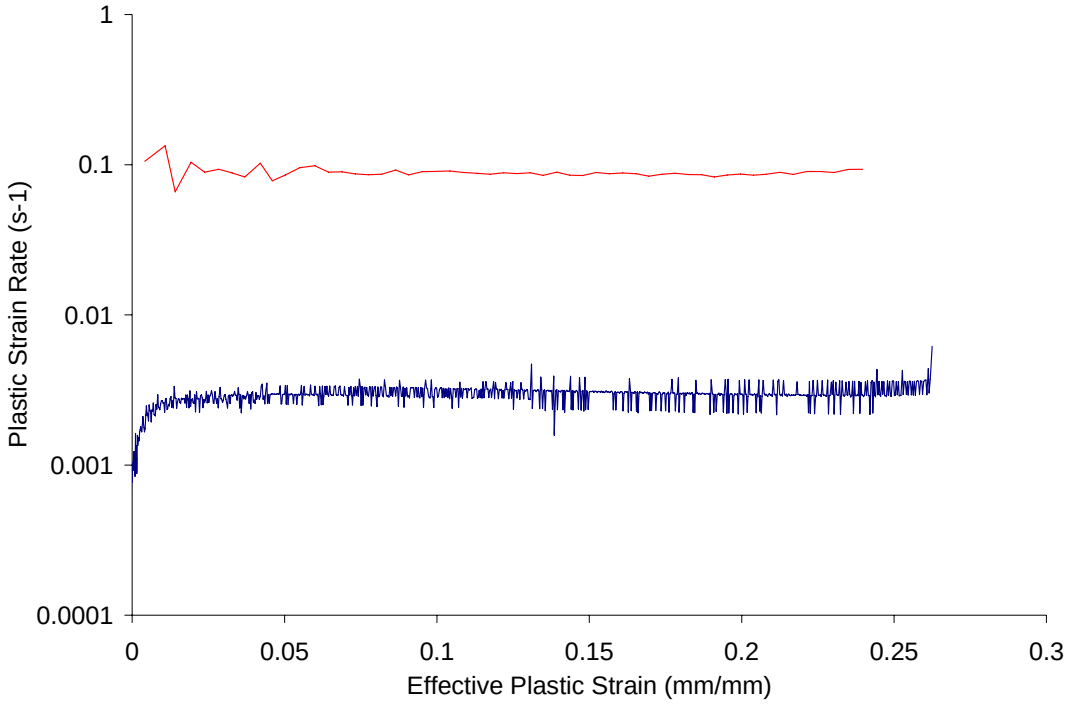

Figure 3.3. Strain rate versus strain for the two low rate experiments

3.2 INTERMEDIATE-RATE EXPERIMENTS

The true stress and effective plastic strain were determined for the intermediate strain rate results using Equations 3.1 and 3.2 in the same way as for low strain rate results. However, unlike the low strain rate results, the apparent elastic modulus in the intermediate strain rate experiments is not 207 GPa. This can be seen in the engineering stress-strain results at nominal strain rates of 30 and 100 s^{-1} (Figure 3.4). The average elastic modulus is 53.77 GPa. This difference in modulus between strain rates is a testing artifact and does not reflect material properties. Confirmation that the change in modulus

is a testing artifact is shown in Chapter 6, where the IFWI experiment is modeled numerically.

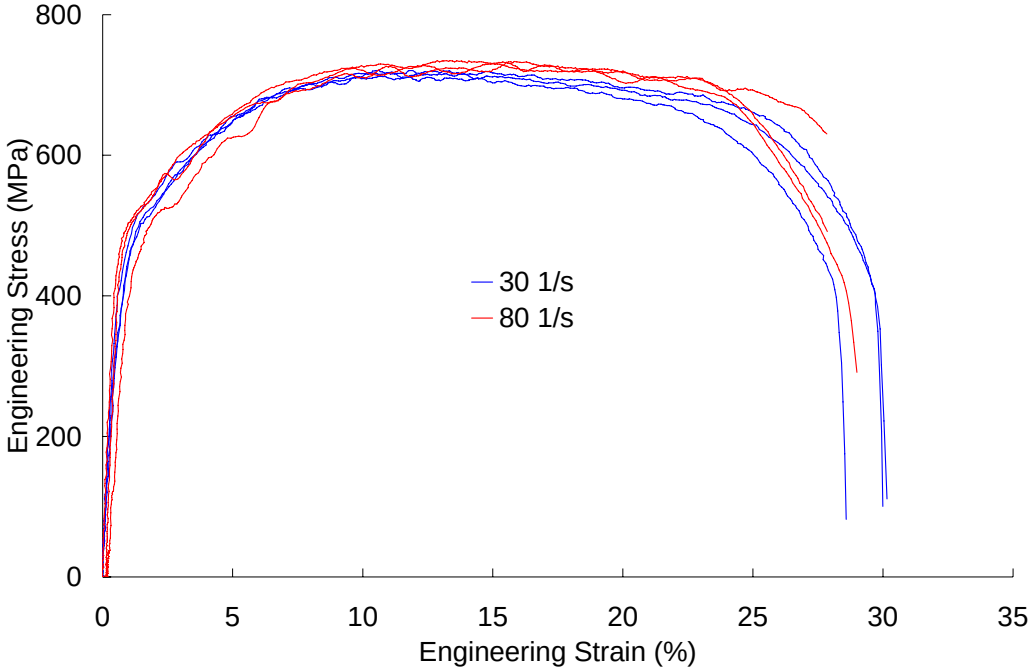

Figure 3.4. Engineering stress vs. engineering strain of DP600 sheet at 30 and 80 s^{-1}

Because the apparent lower modulus is not indicitive of a material property, the elastic modulus used to calculate the plastic strain (Equation 3.2) remained unchanged at 207 GPa. To account for the additional strain that is measured prior to yielding, a slight offset was applied to the engineering strain such that the effective plastic strain was equal to zero at the yield point. The procedure for calculating the offset, shown in Figure 3.5, was to first find the strain at the 0.2%-offset yield stress using the apparent modulus, and then subtract the corresponding strain that would have occurred if the elastic modulus had been 207 GPa. By offseting the result in this manner, the apparent modulus (a testing artifact) does not negatively impact the experimental results during analysis. Application of this offset can be seen in Figure 3.6, which shows the true stress versus effective plastic strain at 30 s^{-1}. For the DP600 sheet specimens, the offset was between 0.6% and 1.4% strain. The offset for each experiment is given with the specimen data in Appendix A.

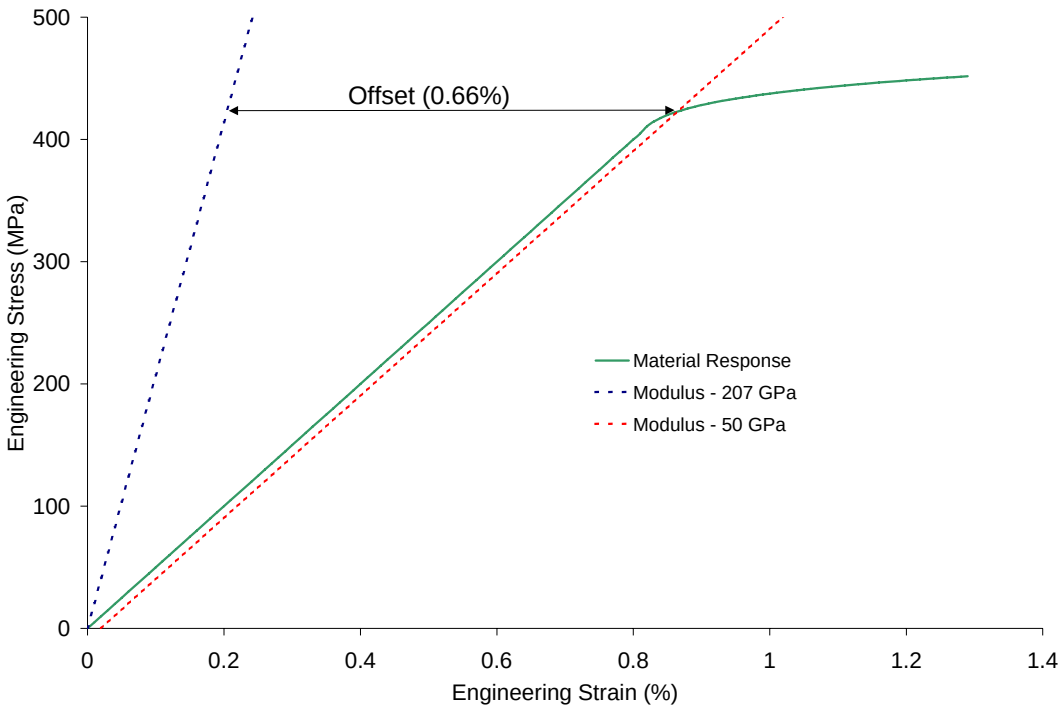

Figure 3.5. Determination of the offset for a general stress-strain curve

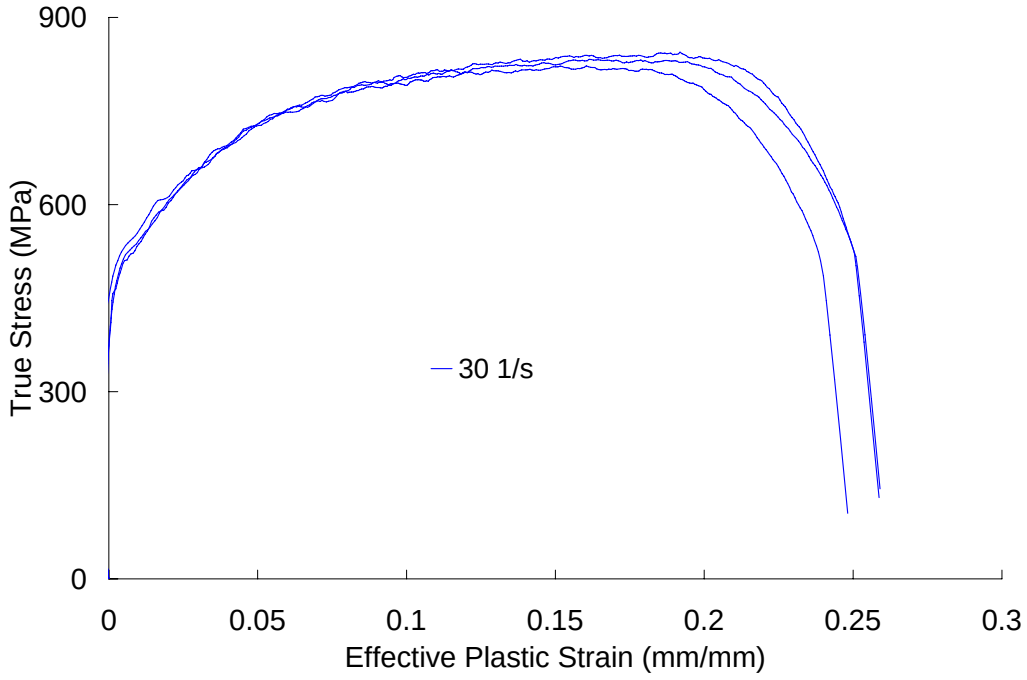

Figure 3.6. True stress vs. effective plastic strain of DP600 sheet at $30s^{-1}$.

3.2.1 Strain Rate Time History for IFWI Experiments

Due to the constraints of the testing method outlined in Section 2.4, the IFWI specimens do not reach the desired strain rate immediately. Since the results can only be used in constitutive fitting when the desired strain rate has been reached, the strain rate behaviour must be identified for each experiment. Figure 3.7 and Figure 3.8 show the strain rate versus strain for the tests at nominal strain rates of 30 and 100 s^{-1} respectively. For the DP600 sheet specimens, the nominal strain rate of 100 s^{-1} was never actually reached and, instead, the tests were carried out at 80 s^{-1}. The tests at 30 s^{-1} do not reach 30 s^{-1} until approximately 0.012 strain. For the 80 s^{-1} tests, a constant strain rate is not reached until 0.037 strain.

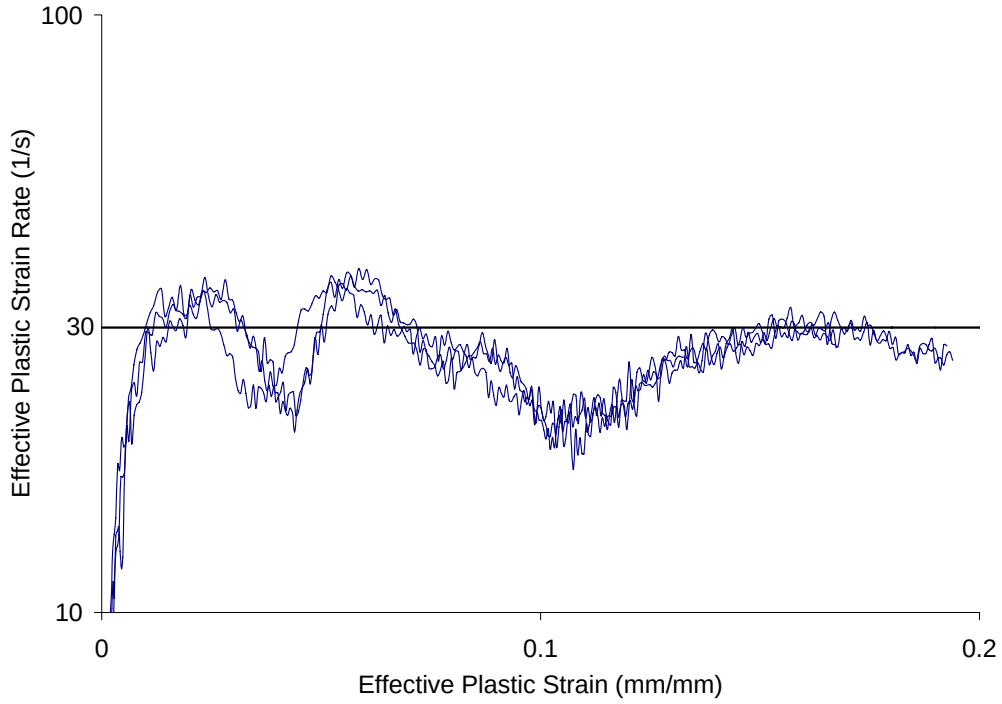

Figure 3.7. Strain rate vs. strain at a nominal rate of 30 s^{-1}.

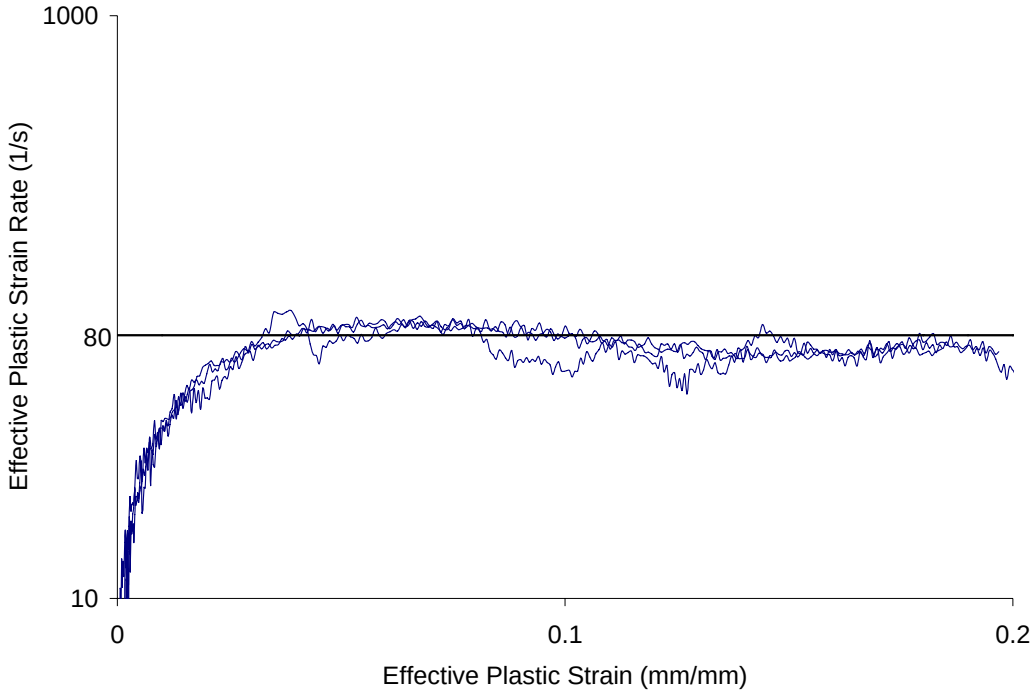

Figure 3.8. Strain rate vs. strain at a nominal rate of 80 s^{-1}.

3.2.2 Temperature Rise in IFWI Experiments

The heat generated in the specimens in the IFWI experiments is only partially dissipated. The temperature rise (ΔT) due to heat generation from plastic work is given in Equation 3.3, where ρ is the density and C is the specific heat capacity of the steel, and β is the fraction of work converted into heat.

$$\Delta T = \beta \frac{\int \sigma_T d\varepsilon_P}{\rho C} \qquad (3.3)$$

During each experiment, MacDougall [96] found that approximately 90% of the plastic work which is done to the specimen is converted to heat, while the rest is converted to other types of energy (*e.g.* sound, microstructural changes, etc…).

For quasi-static experiments, the specimen is considered to be isothermal ($\beta = 0$), which implies the assumption that all of the heat which is generated is lost to either the surrounding apparatus through conduction or to the surrounding air through convection.

For the TSHB experiments, it is assumed that the experiments are essentially adiabatic ($\beta = 0.9$), since there is very little time for the heat to leave the specimen [96].

For the IFWI experiments, the amount of heat generated which is lost from the specimen was estimated using a finite difference solution for Equation 3.4, where k is the thermal conductivity constant (0.0802 W/mmK), and L is the gauge length of the specimen (12.5 mm).

$$\rho c \Delta T = \beta \int_{\varepsilon_0}^{\varepsilon_1} \sigma_T d\varepsilon_{eps} - \frac{k}{L}\frac{\partial T}{\partial x} \tag{3.4}$$

For this calculation, the specimen gauge length was discretized into 11 points (Figure 3.9) and an explicit calculation for the transient temperature distribution was found for each node and time step (0.1 ms) using Equations 3.5.

$$T_i^{\,j} = T_i^{\,j-1} + \frac{1}{\rho c}\{\beta \int_{\varepsilon^{j-1}}^{\varepsilon^j} \sigma_T d\varepsilon_{eps} - \frac{k}{L}\frac{T_{i+1}^{\,j} - T_{i-1}^{\,j}}{2\Delta x}\} \tag{3.5}$$

A power law hardening curve was used to describe the stress as a function of strain (Equation 3.6), where A and B are material constants (Equation 3.7).

$$\int_{\varepsilon_i^{j-1}}^{\varepsilon_i^j} \sigma_T d\varepsilon_{eps} = \int_{\varepsilon_i^{j-1}}^{\varepsilon_i^j} (A + B\varepsilon_{eps}{}^n) d\varepsilon_{eps} = A(\varepsilon_i^j - \varepsilon_i^{j-1}) + \frac{B}{n+1}(\varepsilon_i^{j^{n+1}} - \varepsilon_i^{j-1^{n+1}}) \tag{3.6}$$

$$\sigma_T = A + B\varepsilon_{eps}{}^n \tag{3.7}$$

The strain was then related to time by Equation 3.8, from which the transient behaviour of the plastic work can be determined, based on the strain rate (Equation 3.9).

$$\varepsilon_{eps}(\dot{\varepsilon}, t) = \dot{\varepsilon} t \tag{3.8}$$

$$\int_{\varepsilon_i^{j-1}}^{\varepsilon_i^j} \sigma_T d\varepsilon_{eps} = A\dot{\varepsilon}(t^{\,j} - t^{\,j-1}) + \frac{B}{n+1}\dot{\varepsilon}^{n+1}(t^{\,j^{n+1}} - t^{\,j-1^{n+1}}) \tag{3.9}$$

The boundary nodes are assumed to be constant at 21 °C, since they are attached to the grips, which constitute a large heat sink. Also, because of the small time scale (< 15 ms), convection was found to be insignificant. The predicted temperature distribution as a function of time is shown in Figure 3.10 for a DP600 specimen tested at 30 s^{-1}. For this

specimen, the material constants *A*, *B*, and *n* were given a value of 300 MPa, 900 MPa, and 0.3, respectively.

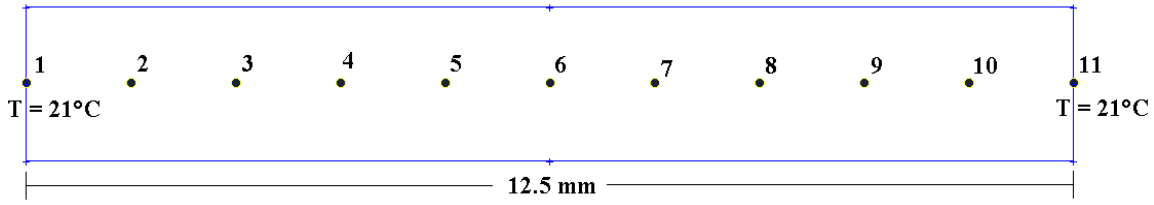

Figure 3.9. Discretization of specimen gauge length

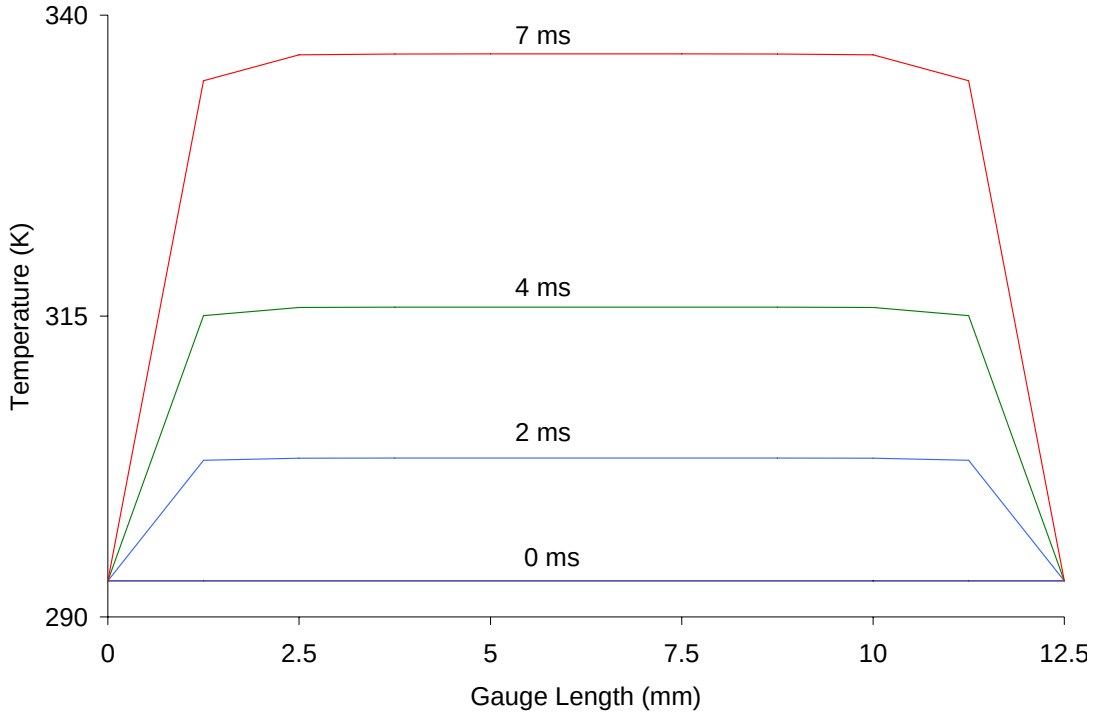

Figure 3.10. Gauge length temperature as a function of distance and time at 30 s^{-1}

For the DP600 specimen, the percentage of created energy that is retained as heat in the specimen is shown as a function of time in Figure 3.11. Throughout the duration of the test, the amount of plastic work that contributes to a rise in the specimen temperature varies from approximately 73.5% to 72%. For the calculations done using the material parameters for the DDQ and HSLA350 specimens, the amount of heat generated from platic work that is not dissipated varies between 74% and 72%, depending on the material and strain rate. Therefore, for constitutive fitting purposes, the retained energy converted

into heat in the specimen can be simply modeled by treating $\beta = 0.73$ for all of the IFWI experiments. This approximation gives a temperature rise of approximately 32°C over the course of the DP600 tests.

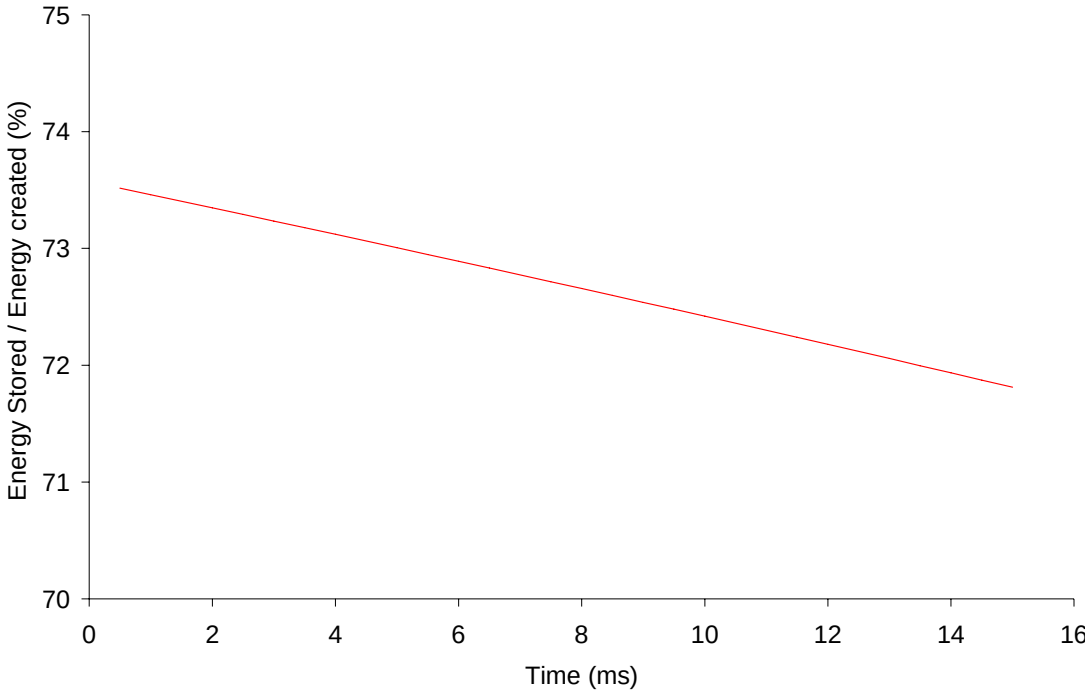

Figure 3.11. Total heat energy stored in the specimen divided by the plastic work as a function of time

3.3 HIGH-RATE EXPERIMENTS

The true stress and effective plastic strain were determined for high strain rate results using Equations 3.1 and 3.2 in the same way as for low and intermediate strain rate results. Also, like the intermediate rate tests, the apparent modulus is not equal to that of the quasi-static experiments. This can be seen in the engineering stress-strain curves of the high rate experiments (Figure 3.12). The average apparent moduli are 73.7, 58.3, and 34.2 GPa for the 369, 846, and 1212 s^{-1} (nominal strain rates of 500, 1000, and 1500 s^{-1}) experiments respectively. This is accounted for by offsets of, on average, 0.005, 0.010 and 0.017 strain, respectively. The offsets were calculated using the same procedure that

was used for the IFWI experiments. The resulting manipulation can be seen in the true stress – effective plastic strain curves (Figure 3.13).

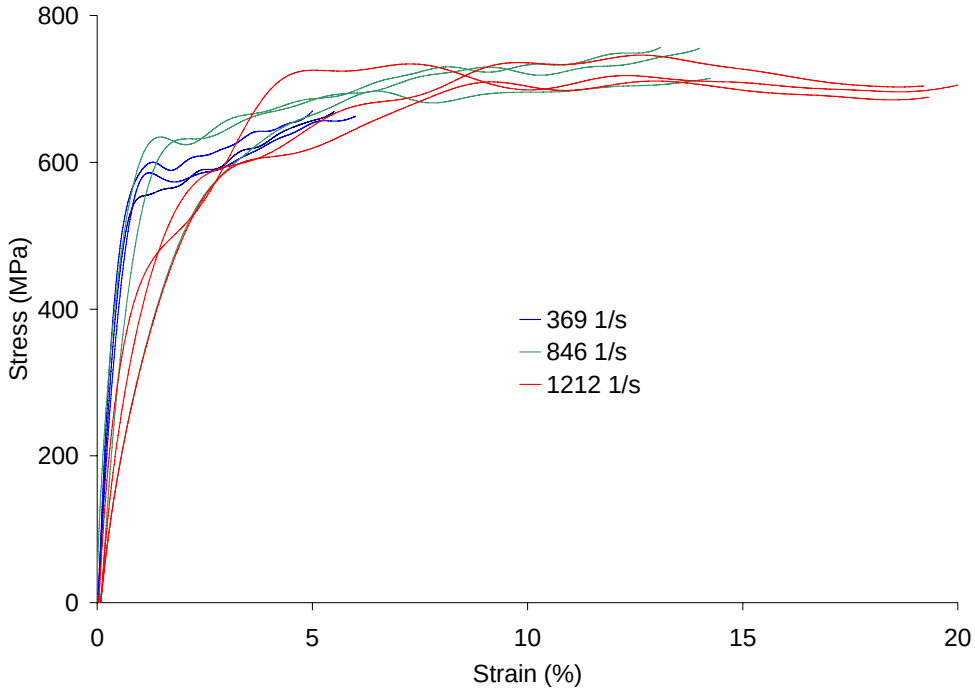

Figure 3.12. Engineering stress vs. engineering strain of DP600 sheet at 369, 846 and 1212 s^{-1}

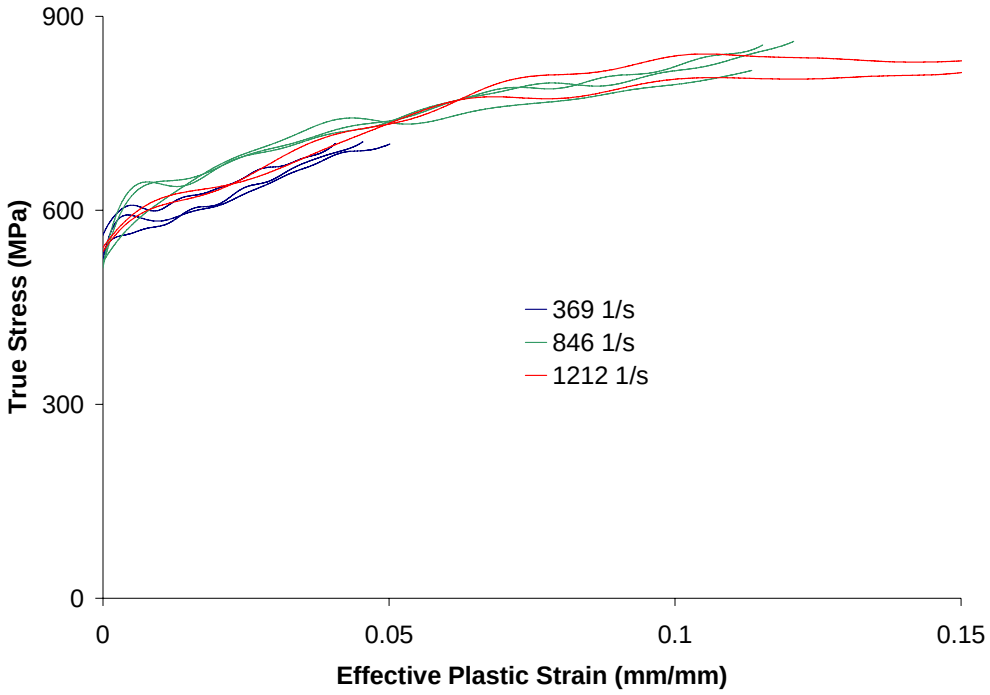

Figure 3.13. True stress vs. effective plastic strain of DP600 sheet at 369, 846 and 1212 s^{-1}

As mentioned previously, the amount of strain that can be achieved on the first pulse of a TSHB experiment is related to the strain rate, which is why, for example, the experiments at 369 s^{-1} in the TSHB experiment cannot achieve strains above 7%. For this reason, determining the strain-to-failure in the TSHB experiments is quite challenging and is beyond the scope of this work.

The strain rate of the specimens is relatively constant over the duration of the experiment. This is shown in the strain rate versus strain curves (Figure 3.14). A constant strain rate is reached after yielding for all cases, due to the applied offset. Thus, all of the data was used for constitutive modeling.

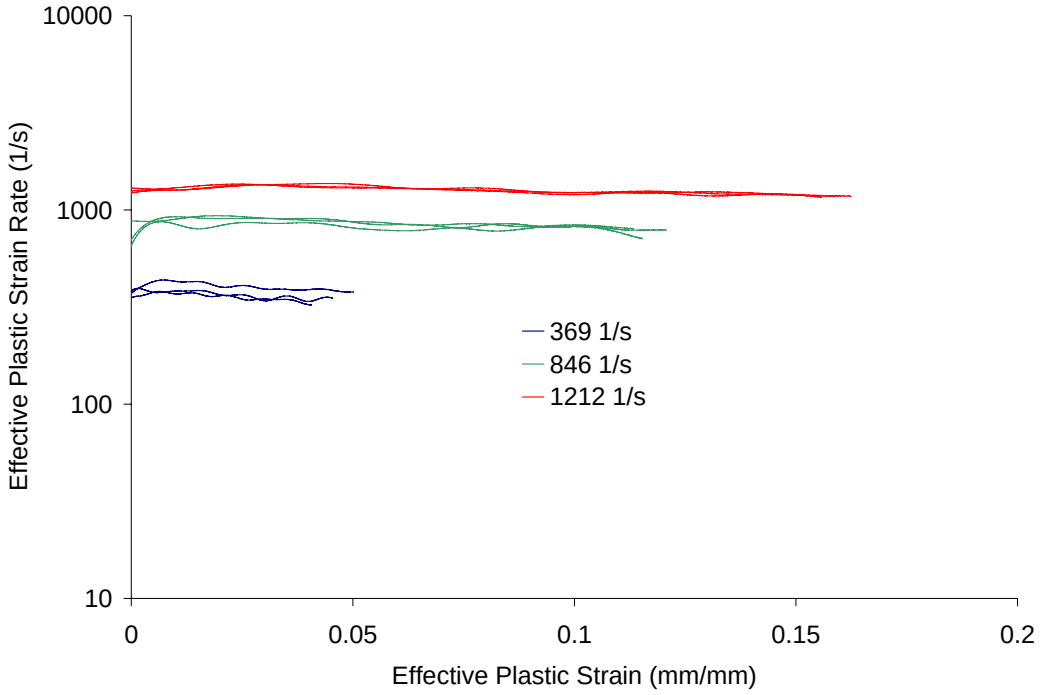

Figure 3.14. Strain rate vs. strain at a 369, 846, and 1212 s^{-1}.

The TSHB specimens were assumed to be adiabatic due to the short duration of the experiment. Thus, Equation 3.3 was used to calculate the temperature rise in the specimens, where 90% of the plastic work was converted to heat energy ($\beta = 0.9$). At 1212 s^{-1}, the temperature rise was calculated to be approximately 30°C at 19.2% strain, which is not the failure strain.

CHAPTER 4

EXPERIMENTAL RESULTS

In this chapter, the experimental results for each steel are discussed, beginning with DP600 and followed by HSLA350 and DDQ. For each steel, the strain rate sensitivity, thermal softening, forming effects, strain to failure, and reduction in cross-sectional area are discussed. For DDQ and HSLA350, yield stress elongation effects are also discussed.

4.1 DATA MANIPULATION FOR TREND VISUALIZATION

In order to facilitate visualization of the work-hardening, strain rate sensitivity, thermal softening, and tube preforming effects, the 'averaged results' from each set of experiments are used. To obtain the averaged true stress for a given strain, values of true stress for each test were selected at increments of 0.25% effective plastic strain (eg. 0.25%, 0.5%, 0.75%, etc…). If data was not collected at these exact strains, a value was found from linear interpolation of the surrounding data points. Then, for each set of experiments performed at the same nominal strain rate and temperature, the true stress values for each strain level were averaged. This procedure was also applied to obtain curves of average effective plastic strain rate and temperature versus strain. In addition to being useful for trend visualization, the averaged curves are beneficial for constitutive modeling for two reasons: i) so that each experiment contributes to the constitutive fit; and, ii) so that each set of experiments contain the same concentration of data points (four points per 1% effective plastic strain) and therefore are weighted equally.

The strain to failure was determined from the engineering strain at which the specimen could no longer support any load. The reduction in cross-sectional area was determined by measurement of the width and thickness of the specimen at the point of fracture. These results were then compared with the trends seen in the initial necking strain using

Considere's criterion [98]. Considere's criterion states that the onset of diffuse necking will occur when the true stress (σ_T) is equal to the work hardening rate, which is the derivative of the true stress with respect to plastic strain (ε^P).

$$\sigma_T = \frac{d\sigma_T}{d\varepsilon^P} \tag{4.1}$$

4.2 DP600 RESULTS

4.2.1 Strain Rate and Thermal Sensitivity

The strain rate and thermal sensitivity of the DP600 sheet specimens as well as the 3 and 6 o'clock positions of the tube can be seen in the true stress versus effective plastic strain results for all strain rates and temperatures (Figure 4.1 - Figure 4.5) (Note that the sheet specimens were tested along tested along the rolling direction). As discussed earlier, elevated temperature experiments were not conducted at the 3 o'clock position of the tube because the thermal sensitivity was assumed to be the same at all tube positions.

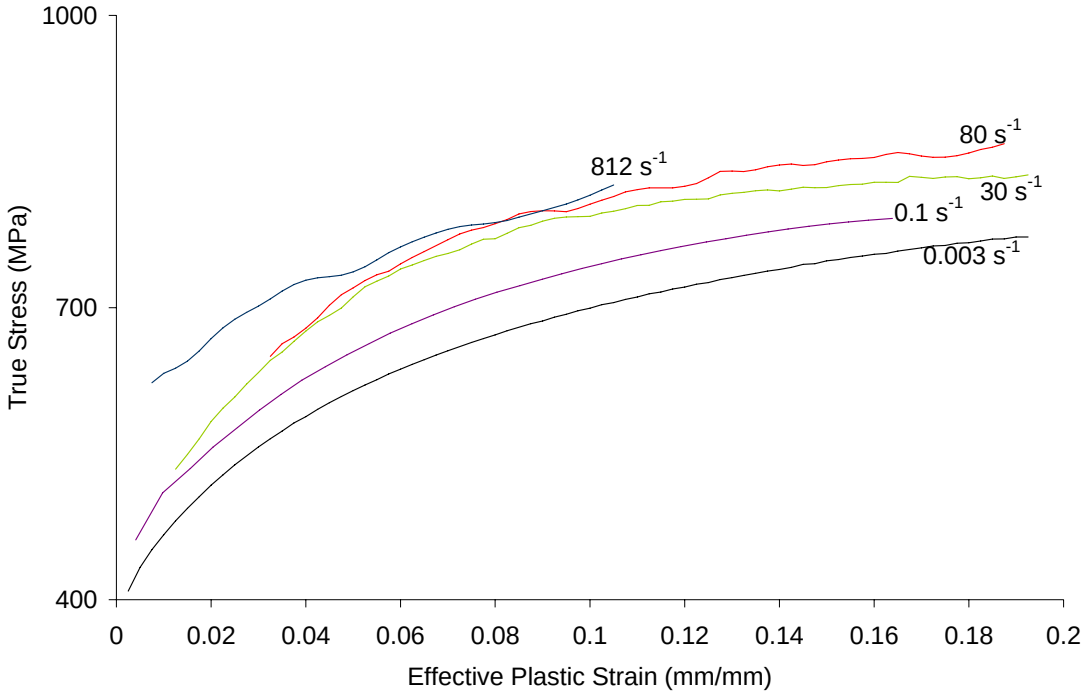

Figure 4.1. True stress vs. effective plastic strain for DP600 sheet specimens at room temperature and strain rates from 0.003 to 812 s^{-1}

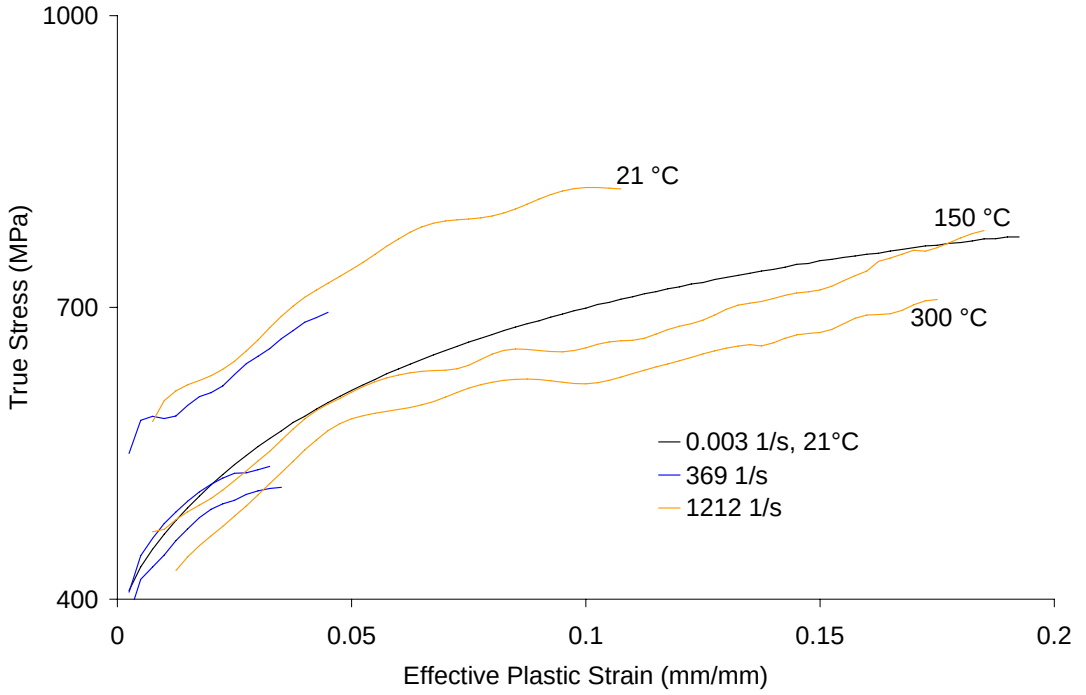

Figure 4.2. True stress vs. effective plastic strain for DP600 sheet specimens at strain rates of 369 and 1212 s^{-1} and temperatures from 21 to 300 °C

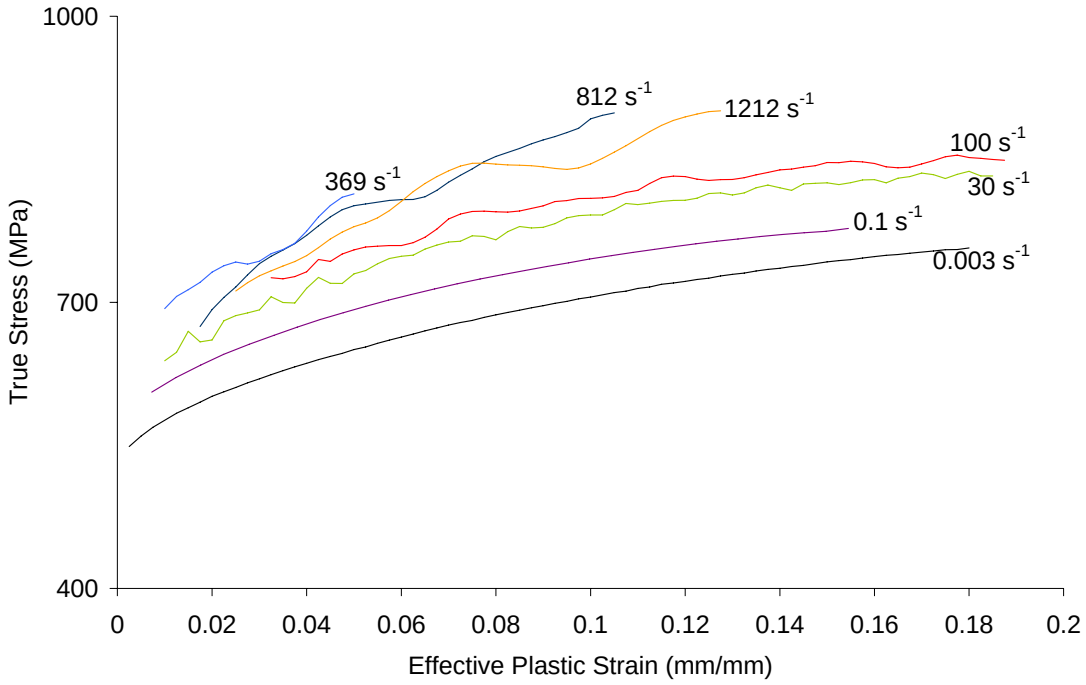

Figure 4.3. True stress vs. effective plastic strain for DP600 tube specimens (3 o'clock) at room temperature and strain rates from 0.003 to 1212 s^{-1}

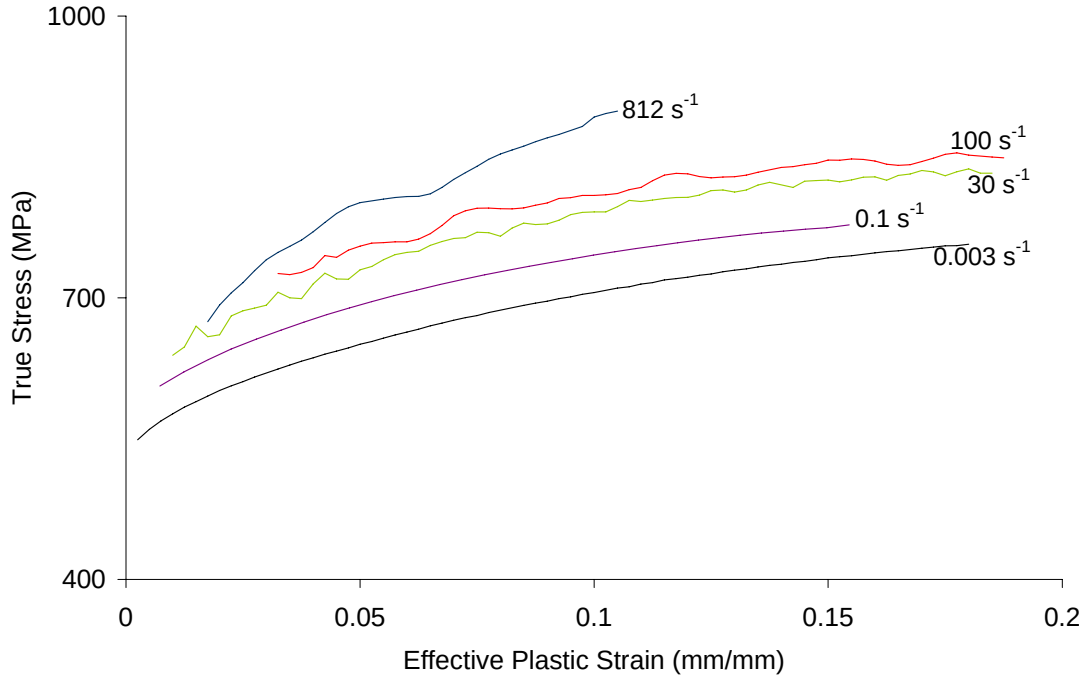

Figure 4.4. True stress vs. effective plastic strain for DP600 tube specimens (6 o'clock) at room temperature and strain rates from 0.003 to 812 s^{-1}

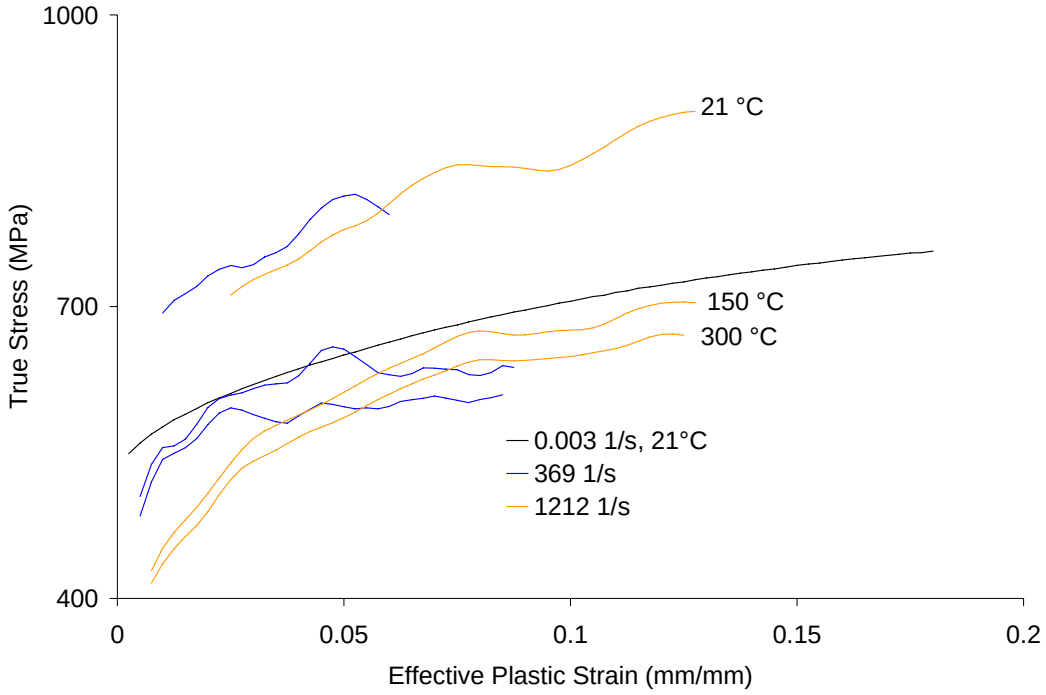

Figure 4.5. True stress vs. effective plastic strain for DP600 tube specimens (6 o'clock) at strain rates of 369 and 1212 s^{-1} and temperatures from 21 to 300 °C

For both the sheet and tube, the strength increases as strain rate increases, and decreases as the initial temperature increases. It is worth noting that the strength increase associated with a rise in strain rate from 0.003 to 1212 s^{-1} is roughly the same as the decrease in strength associated with an increase in initial temperature from 21 to 150 °C (Figure 4.2 and Figure 4.5).

The strain rate sensitivity of both the sheet and tube can also be seen in Figure 4.6, which shows the true stress at 10% strain as a function of strain rate for each room temperature experiment. At 10% strain, the difference between the strength of the sheet and tube is negligible at the low and intermediate strain rates. The strain rate sensitivity of the sheet and tube are seen to be nearly identical up to strain rates of 100 s^{-1}.

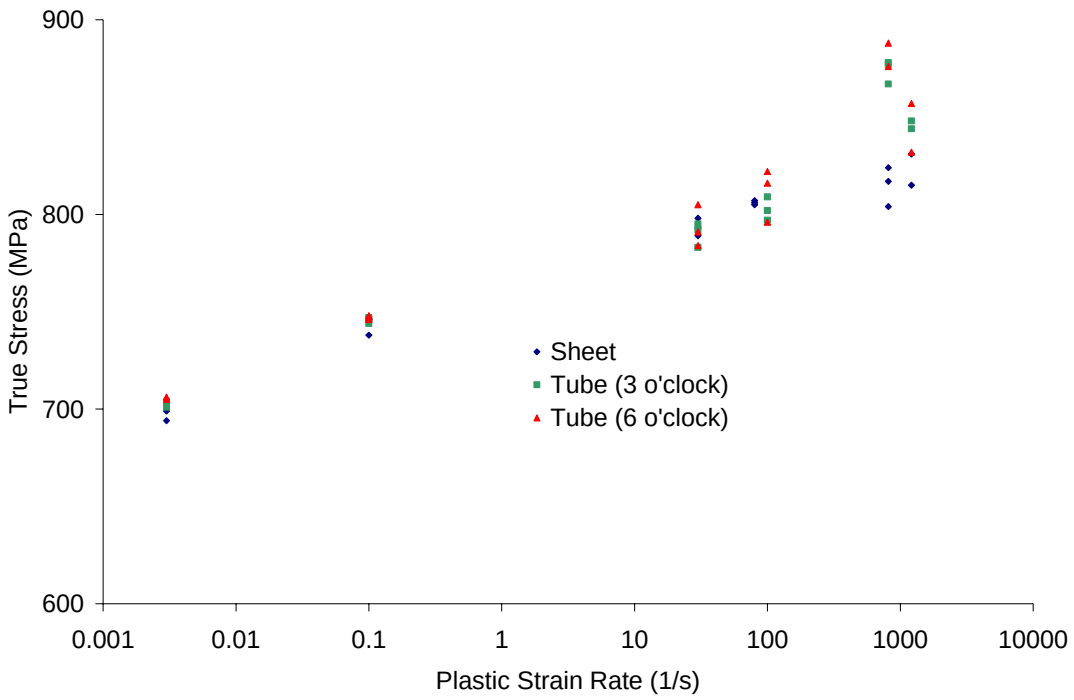

Figure 4.6. True stress vs. strain rate at 10% strain for DP600 tests performed at an initial temperature of 21 °C

At high rates, the tube displays more strength than the sheet, although the exact amount is difficult to quantify because of oscillations in the data. The effect of the oscillations on the high-rate results can be seen clearly in Figure 4.3, which shows the results for the tube specimens at the 3 o'clock positions at all strain rates. These oscillations also account for the apparent decrease in strength associated with the increase in strain rate from 812 s^{-1} to 1212 s^{-1} at 10% strain in the tube specimens (Figure 4.6).

The thermal sensitivity for both the sheet and tube can also be seen in Figure 4.7, which shows the true stress as a function of the homologous initial testing temperature ($T^* = \frac{Temperature - T_{ref}}{T_{melt} - T_{ref}}$, T_{ref} = 20°C and T_{melt} = 1640°C) at 10% strain for the experiments at 1212 s^{-1}. The quasi-static room temperature results are also plotted to emphasize the decrease in strength that accompanies the rise in temperature.

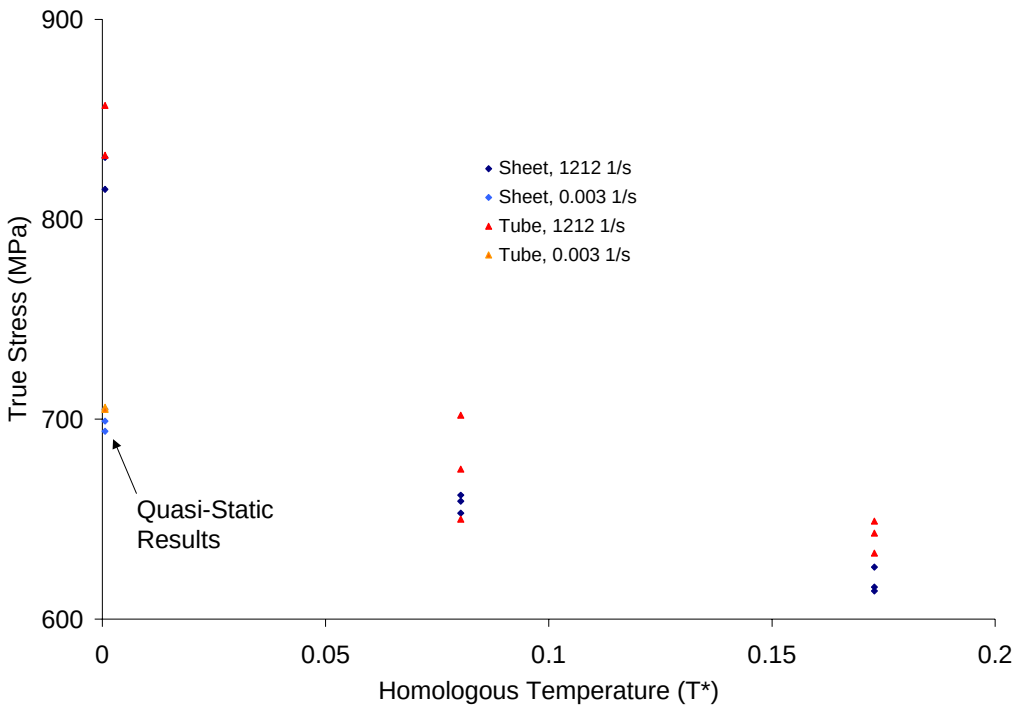

Figure 4.7. True stress vs. homologous temperature at 10% strain for DP600 specimens tested at 1212 s^{-1}

4.2.2 Tube Forming Effects

During the rolling process used to fabricate the tube, a significant amount of work-hardening is imparted into the original sheet, which affects its stress-strain response. This effect can be seen in Figure 4.8, which shows the response of the sheet and tube (3, 6, and 9 o'clock positions) at 0.003 s^{-1}. The strength of the sheet lies below that of the tube until approximately 10% strain. It can also be seen that there is very little difference in the stress-strain response between any of the positions on the tube, which suggests that the work-hardening imparted during tube forming is relatively uniform.

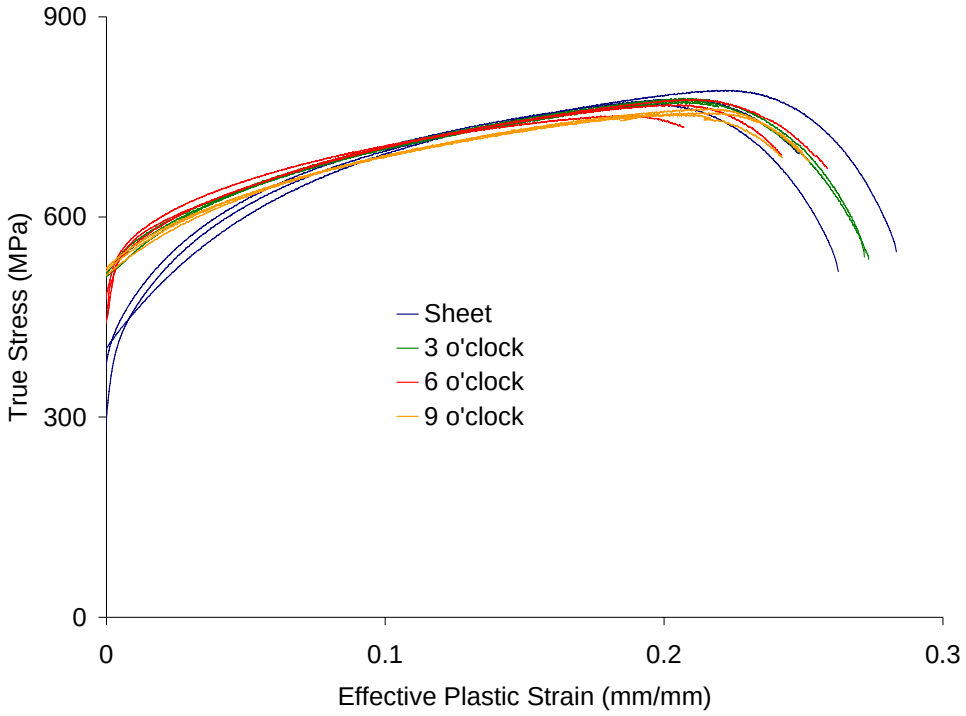

Figure 4.8. Comparison of DP600 sheet and tube behaviour at 0.003 s^{-1}

As the strain rate increases, the relationship between the sheet and tube strength remains largely unchanged until the high strain rate tests. This can be seen in Figure 4.9, which compares the behaviour of the sheet (Figure 4.1) and tube at the 6 o'clock (Figure 4.4) position as the strain rate increases. The sheet strength lies below the tube strength until approximately 11.5%, 10.6%, 7.8%, and 8.5% plastic strain for strain rates of 0.003, 0.1, 30, and 80 s^{-1}, respectively. At the highest strain rate (812 s^{-1}), the strength of the tube diverges from the strength of the sheet as the plastic strain increases. The reason for this change in behaviour is unknown.

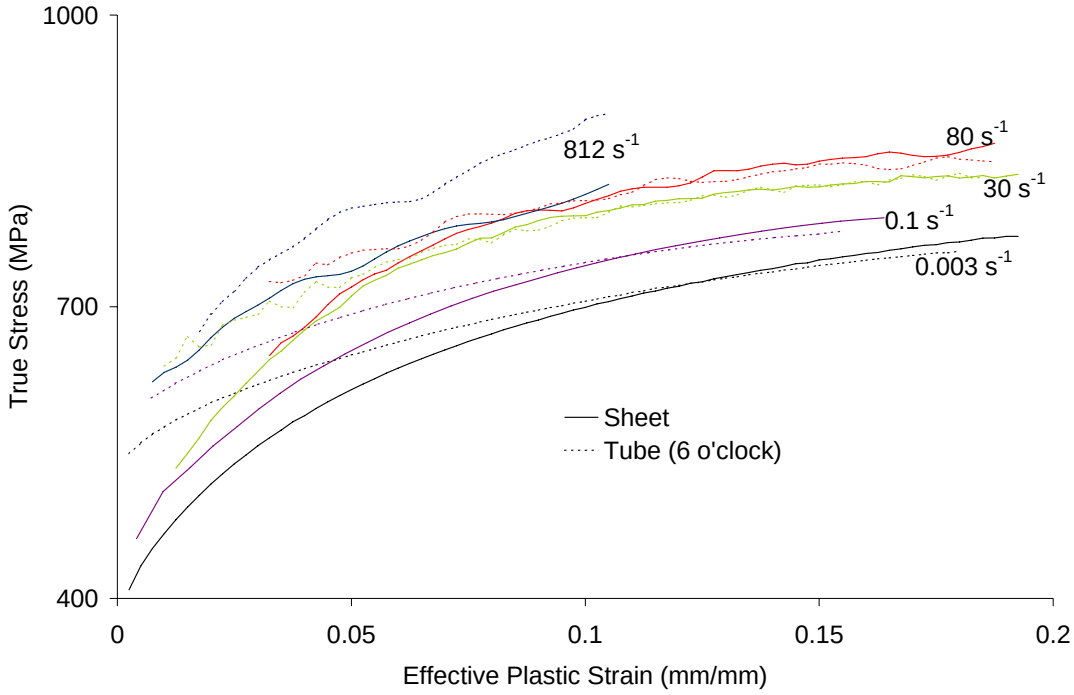

Figure 4.9. Comparison of DP600 sheet and tube (6 o'clock) behaviour at strain rates from 0.003 to 812 s^{-1}

4.2.3 Failure Strain and Reduction in Cross-Sectional Area

The average strain to failure for the sheet and tube specimens is predicted in Table 4.1 for strain rates up to 100 s^{-1}. As mentioned earlier, the specimens do not fail during the measured portion (first loading pulse) of the TSHB experiments, so the failure strain can not be determined. The overall trend is that the ductility drops from 0.003 to 0.1 s^{-1}, and then rises as the strain rate increases. This trend can be seen in Figure 4.10, which shows 6 o'clock tube specimens tested at each strain rate, and Figure 4.11, which shows the failure strain and reduction in cross-sectional area as a function of strain rate for the 6 o'clock tube specimens. The reduction in cross-sectional area follows the same trend with respect to strain rate as the failure strain. The failure strain and reduction in cross-sectional area for the sheet and 3 o'clock tube specimens can be found in Appendix B.

Table 4.1. Percent strain at failure for DP600 sheet and tube

	NOMINAL STRAIN RATE (1/s)			
	0.003	**0.1**	**30**	**100**
Sheet	30.71	28.86	29.58	30.19
Tube (3 o'clock)	30.42	26.58	30.36	32.95
Tube (6 o'clock)	29.85	26.03	28.22	32.71

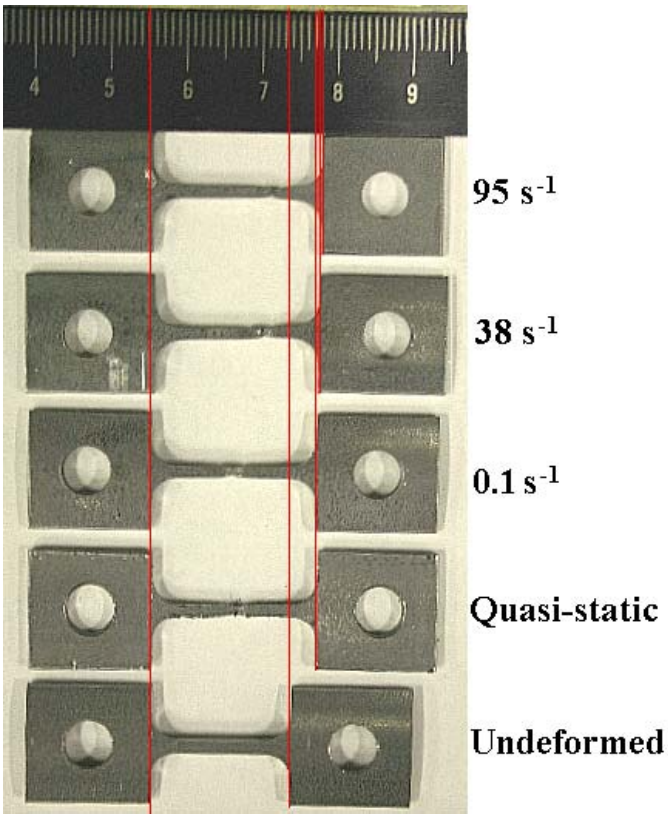

Figure 4.10. Elongation to failure of tested DP600 tube (6 o'clock) specimens

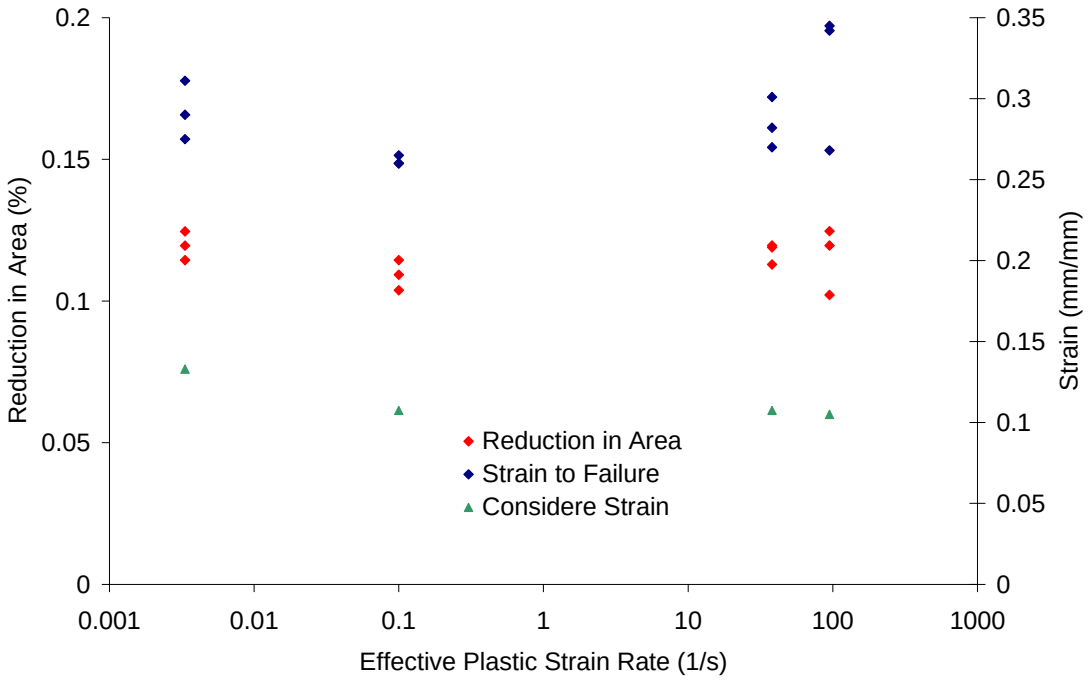

Figure 4.11. Strain to failure and reduction in area of the DP600 tube (6 o'clock) specimens

The relationship between strain at the onset of diffuse necking and strain rate can be seen in Figure 4.12, which shows the true stress and the work-hardening rate as a function of plastic strain for the 6 o'clock tube specimens. The work-hardening rate was calculated by approximating the true stress versus effective plastic strain relationship with a fourth order polynomial and then differentiating. Using Considere's criterion, the onset of necking occurs at 13.3% plastic strain at strain rates of 0.003 and at 812 s^{-1}. At the intermediate strain rates, diffuse necking is predicted to initiate at between 10.5% and 10.9% plastic strain. This is similar to the trend seen in the failure strain, where the specimens tested at 0.003 s^{-1} show more elongation, on average, than the specimens tested at 0.1, 30, and 100 s^{-1}.

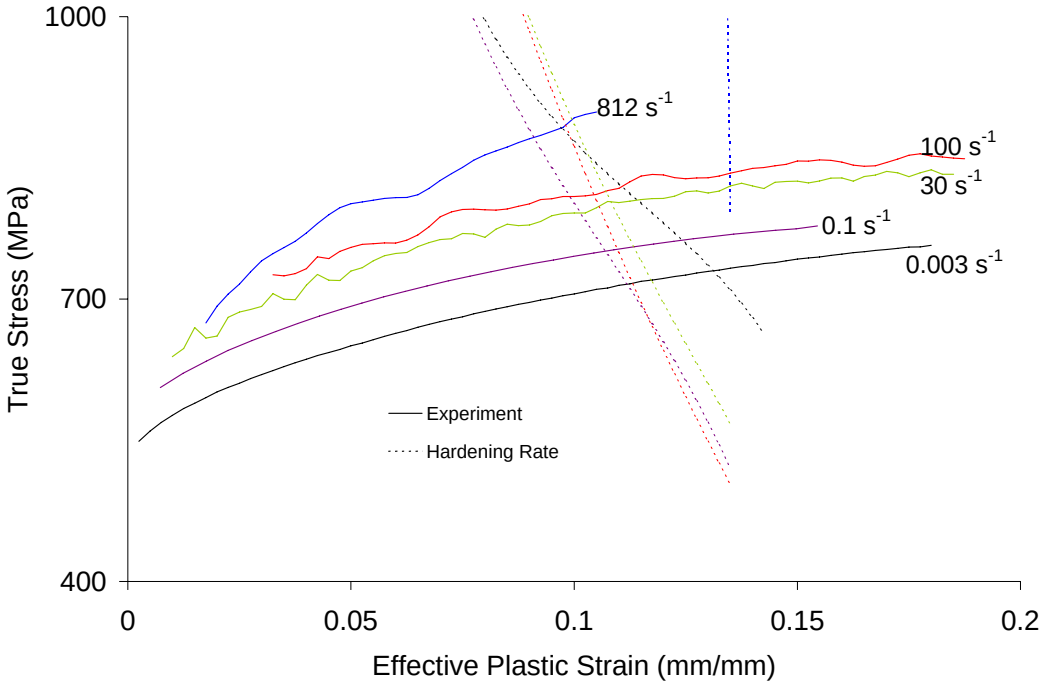

Figure 4.12. True stress and work-hardening rate vs. plastic strain for DP600 tube (6 o'clock) at strain rates from 0.003 to 812 s^{-1}

For the sheet specimens, the true stress and work-hardening rate are shown in Figure 4.13. The onset of diffuse necking is predicted at 15%, 13.5%, 10.5%, 11.8%, and 9.5% strain at strain rates of 0.003, 0.1, 30, 80, and 812 s^{-1}, respectively. The result at 812 s^{-1} is suspect for both the sheet and tube results because necking has not occurred during the measured portion of the test in either case. Diffuse necking appears to occur in the calculated work-hardening rate of the sheet result, due to the true stress versus plastic strain relationship having been fit with a second order polynomial to ensure that the work-hardening rate did not increase continuously with plastic strain. The overall trend in strain-to-necking for the sheet specimens is the same as the trend exhibited by the tube specimens; however, there is slightly more strain to necking in the sheet specimens than the tube specimens.

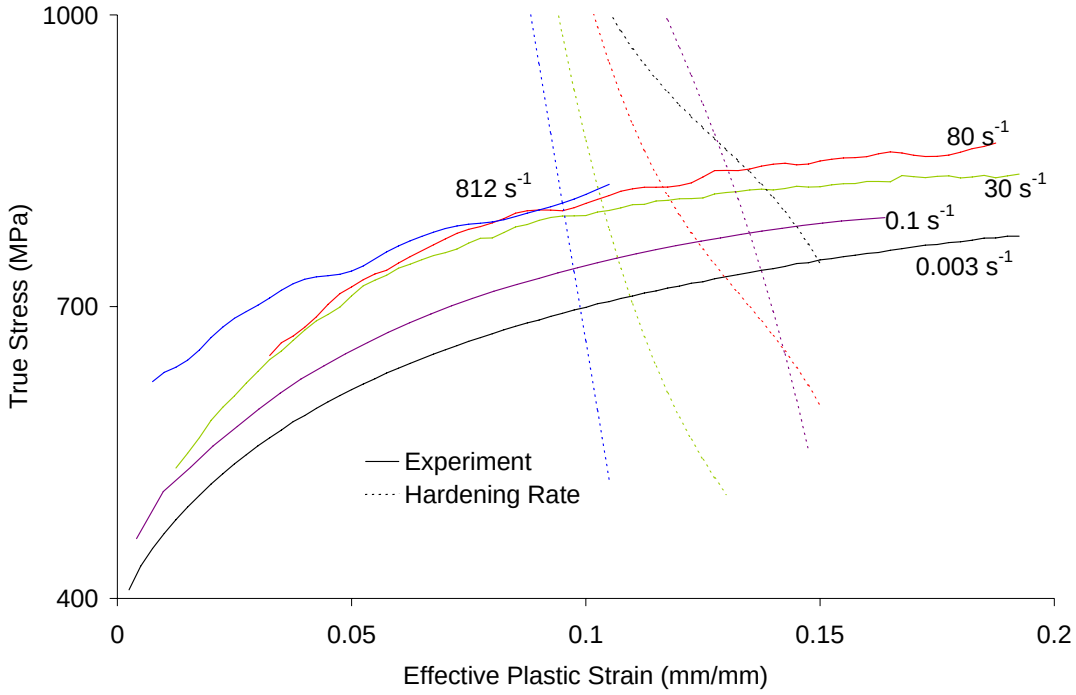

Figure 4.13. True stress and work-hardening rate vs. plastic strain for DP600 sheet at strain rates from 0.003 to 812 s^{-1}

4.3 HSLA350 RESULTS

4.3.1 Strain Rate and Thermal Sensitivity

The strain rate and thermal sensitivity of HSLA350 for the specimens from the rolling direction of the sheet as well as the 3 o'clock and 6 o'clock positions of the tube can be seen in the true stress versus effective plastic strain results for all strain rates and temperatures (Figure 4.14 - Figure 4.17). As with the DP600, a positive strain-rate sensitivity was measured. Also, as seen in Figure 4.17, the increase in strength that is seen when increasing the strain rate from 0.003 to 1265 s^{-1} is approximately equal to the decrease in strength that results from a rise in temperature from 21 to 150 °C.

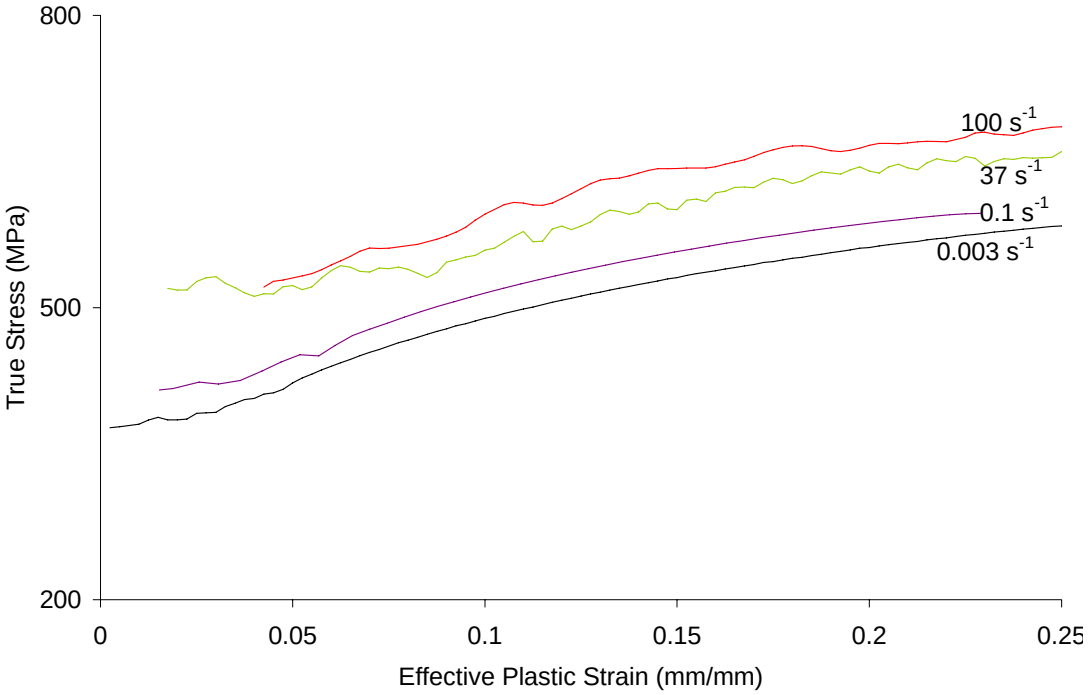

Figure 4.14. True stress vs. effective plastic strain for HSLA350 sheet specimens at room temperature and strain rates from 0.003 to 100 s^{-1}

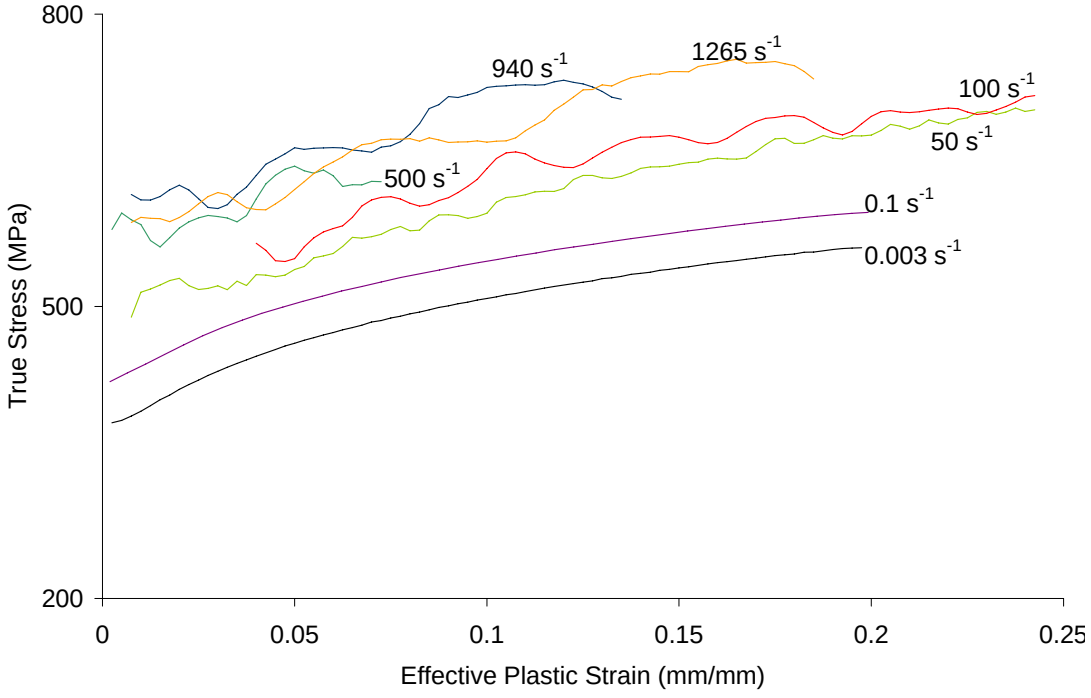

Figure 4.15. True stress vs. effective plastic strain for HSLA350 tube specimens (3 o'clock) at room temperature and strain rates from 0.003 to 1265 s^{-1}

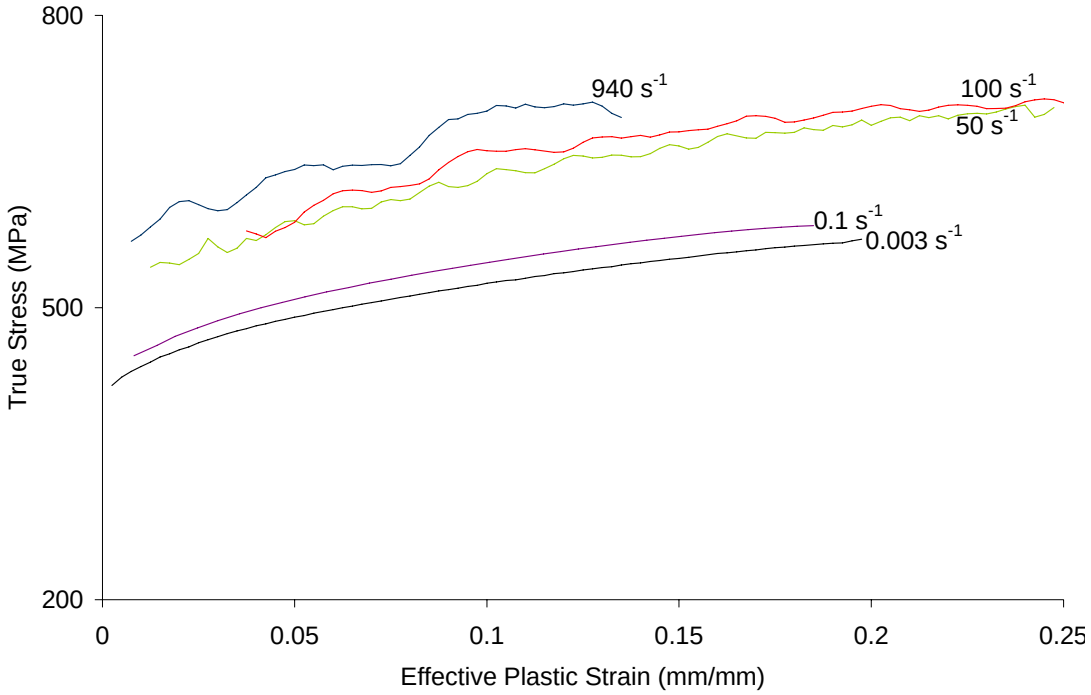

Figure 4.16. True stress vs. effective plastic strain for HSLA350 tube specimens (6 o'clock) at room temperature and strain rates from 0.003 to 940 s^{-1}

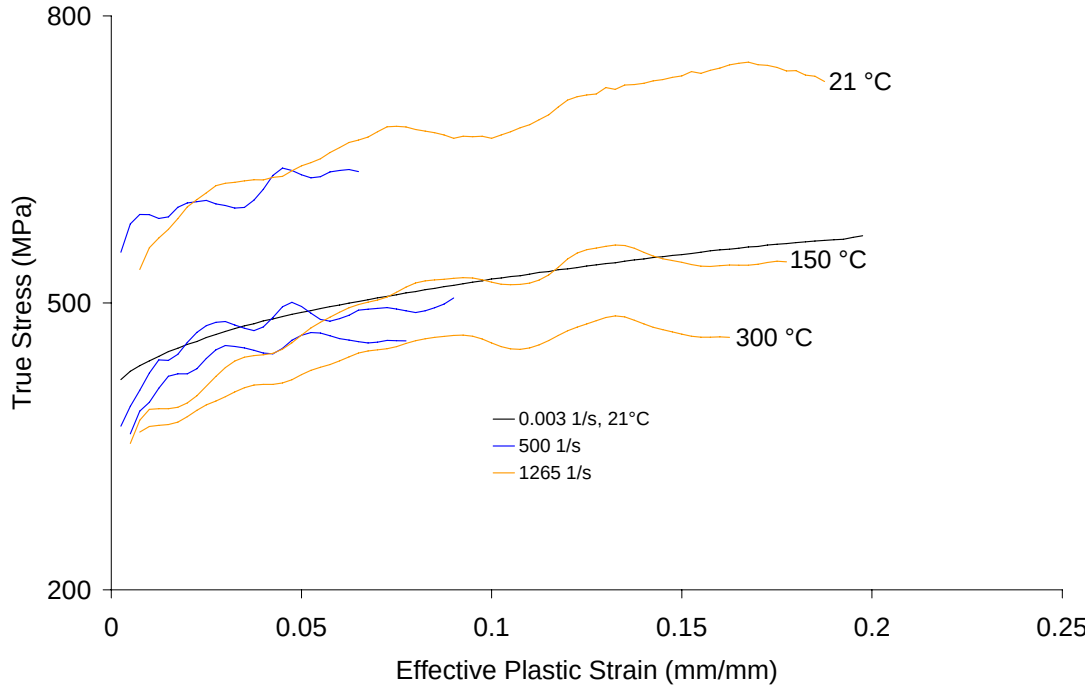

Figure 4.17. True stress vs. effective plastic strain for HSLA350 tube specimens (6 o'clock) at strain rates of 500 and 1265 s^{-1} and temperatures from 21 to 300 °C

The strain rate sensitivity of the HSLA350 sheet and tube can also be seen in Figure 4.18, which shows the true stress at 10% strain as a function of strain rate for each room temperature experiment. At 10% strain, the difference in strength between the sheet specimens and the two orientations of tube specimens is significant. Furthermore, there is also a difference in strength between the tube specimens at the 3 and 6 o'clock positions. The difference is difficult to accurately quantify due to oscillations in the data.

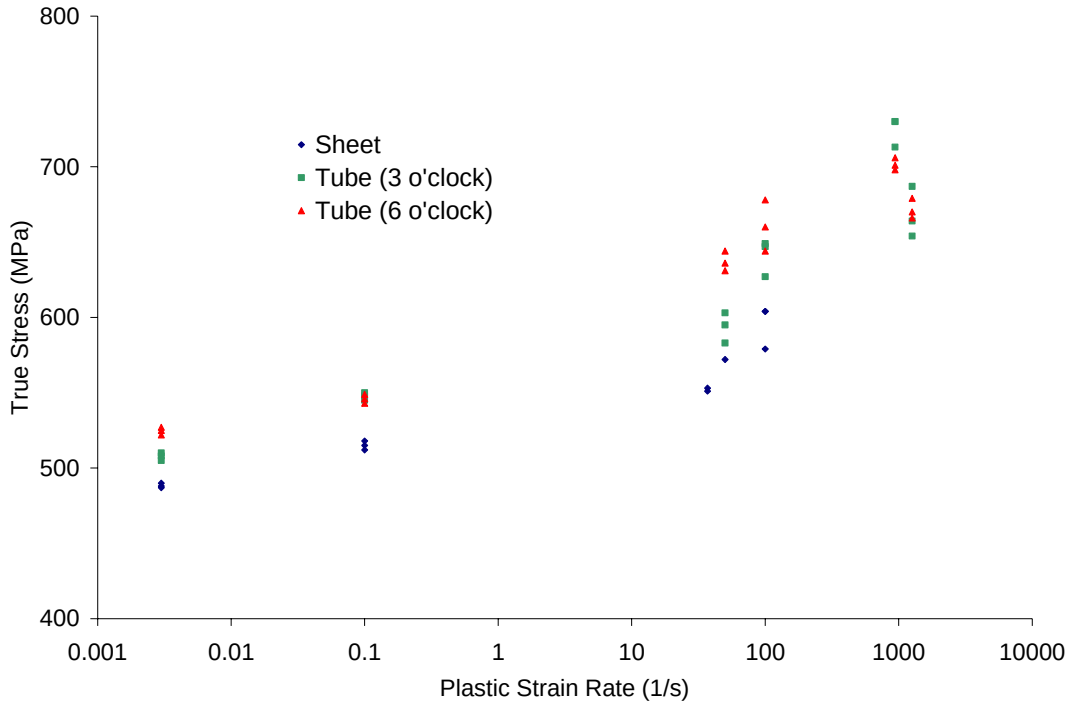

Figure 4.18. True stress vs. strain rate at 10% strain for HSLA350

The thermal sensitivity for the HSLA350 6 o'clock tube specimens can be seen in Figure 4.19, which shows the true stress as a function of the initial homologous testing temperature at 10% plastic strain for the experiments at 1260 s^{-1}. The quasi-static results are also shown to emphasize the decrease in strength that accompanies the rise in temperature.

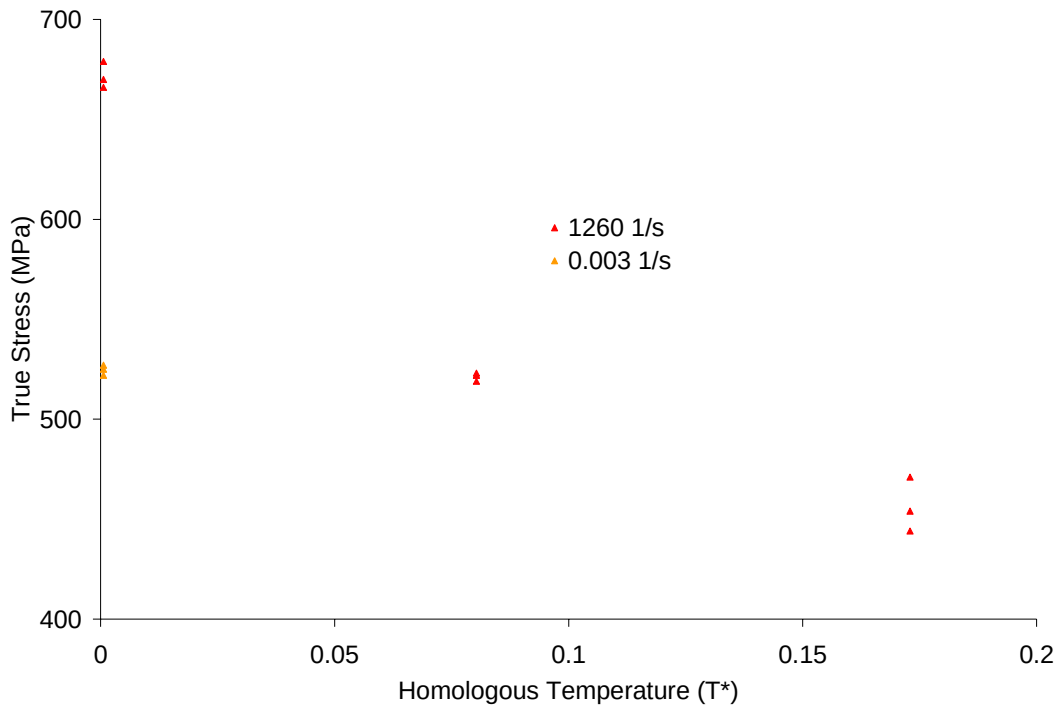

Figure 4.19. True stress vs. homologous temperature at 10% strain for HSLA350 tube (6 o'clock) specimens tested at 1260 s^{-1}

4.3.2 Yield Point Elongation Effects and Luder's Banding

The engineering stress-strain results for the HSLA350 sheet specimens tested at 0.003 s^{-1} are shown in Figure 4.20. Of particular interest is the presence of discontinuous yielding, or Luder's banding, that occurs prior to approximately 5% strain. Discontinuous yielding is not seen in the tube specimens, due to the plastic work imparted by the tube fabrication process. The discontinuous yielding that is seen in the sheet specimens makes analysis of the intermediate-rate and especially the high-rate results quite challenging.

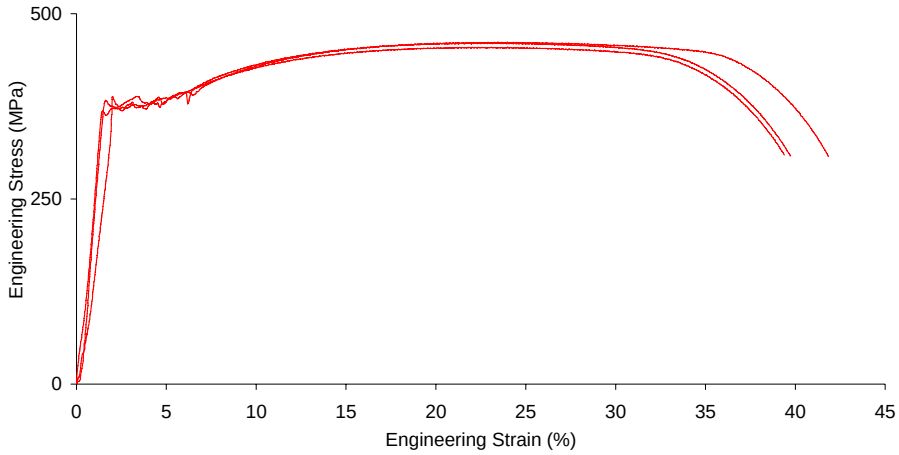

Figure 4.20. Engineering stress vs. strain for HSLA350 sheet specimens tested at a quasi-static strain rate

For the sheet specimens, the true stress and plastic strain can only be found for the strain rates below 100 s^{-1} (Figure 4.14). The reason for this limitation is that, at higher strain rates, the upper yield stress and Luder's banding dominate the response of the specimen. This behaviour is seen in Figure 4.21, which shows the engineering stress versus time at nominal strain rates of 500, 1000, and 1500 s^{-1}, and Figure 4.22, which shows the engineering stress versus time at high strain rates and elevated temperatures. Because uniform deformation along the gauge length of the specimen does not occur until after the Luder's band has encompassed the gauge length, this portion of the data can not be used for constitutive modeling.

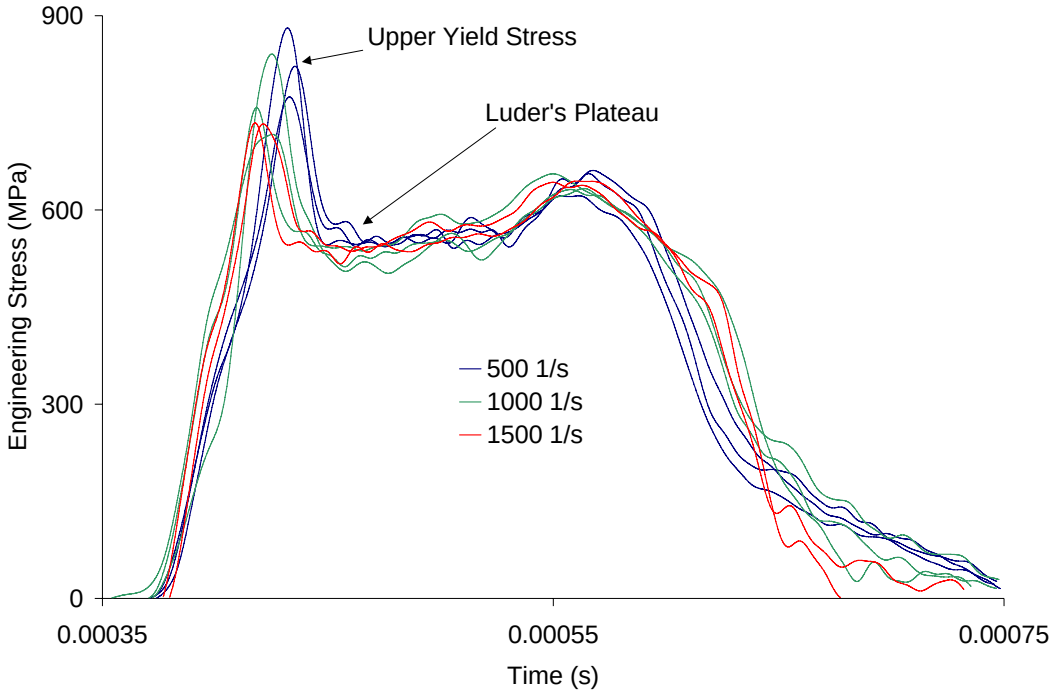

Figure 4.21. Engineering stress vs. time for HSLA350 sheet specimens at room temperature and nominal strain rates of 500, 1000, and 1500 s^{-1}

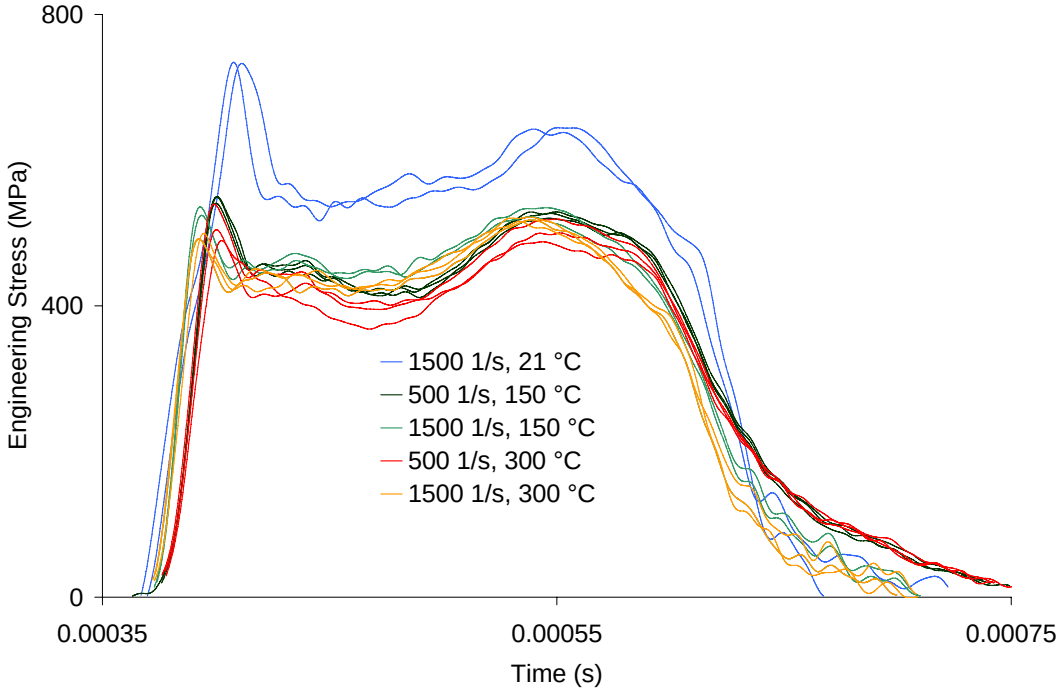

Figure 4.22. Engineering stress vs. time for HSLA350 sheet specimens at temperatures between 21 and 300 °C and strain rates of 500 and 1500 s^{-1}

At room temperature (Figure 4.21), the time between the beginning of the rise in stress and the lower yield point decreases as the strain rate increases, with an average duration of 71, 66, and 56 μs for the 500, 1000, and 1500 s^{-1} experiments, respectively. However, it takes an additional period of approximately 76 μs for the Luder's band to propagate across the gauge length of the specimen, regardless of the nominal strain rate. Since the duration of the TSHB experiment is approximately 200 μs, an average of 70.1% of the experiment is devoted to the yield point and Luder's banding. Thus, the TSHB experiments are of very little use for constitutive modeling for this alloy. Finally, because a constant length of time is necessary for the Luder's band to propogate along the specimen, regardless of strain rate, the results suggest that the maximum velocity of the Luder's band has been reached.

At elevated temperatures (Figure 4.22), the time that is required for the Luder's band to propagate is identical to that at room temperature conditions; however, the time between the initial rise in stress and the point at which the Luder's stress is reached decreases. For the 1500 s^{-1} experiments, the lower yield stress is not reached until an average of 56 μs at 21 °C while at 150 and 300 °C, the Luder's stress is reached at approximately 36 μs.

Another feature of the high strain rate results is that the upper yield stress drops as the strain rate increases (Figure 4.21). This behaviour may be a testing artifact because the measured yield stress for the TSHB experiment occurs before the specimen has reached a state of dynamic equilibrium. Nonetheless, the average upper yield stress is 820, 766, and 729 MPa for the 500, 1000, and 1500 s^{-1} experiments, respectively. The Luder's stress, however, remains relatively constant at approximately 545 MPa. The upper and lower yield stress as a function of strain rate are shown in Figure 4.23, where the nominal strain rate is used for the TSHB experiments and the actual strain rate is used for the IFWI experiments.

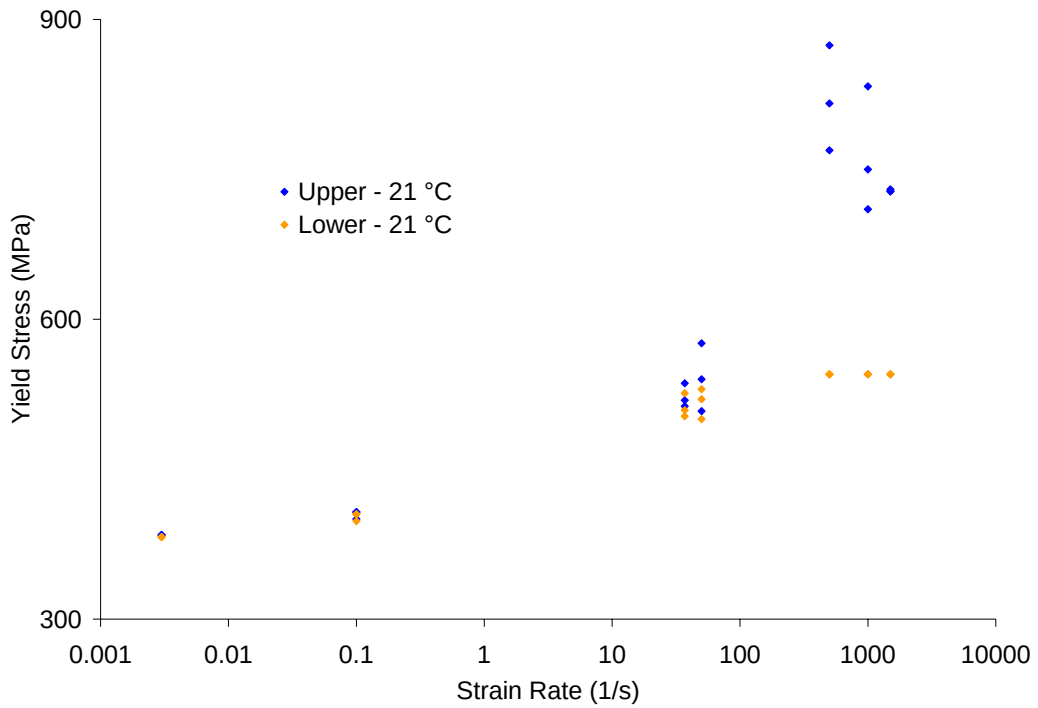

Figure 4.23. Upper and lower yield stress vs. strain rate for HSLA350 sheet specimens

As the initial experiment temperature increases, the upper yield stress drops dramatically (Figure 4.22). At 21 °C, the upper yield stress is approximately 728.5 MPa for the experiments at 1500 s^{-1}. As the temperature rises, the upper yield stress drops to 528 and 484.3 MPa at 150 and 300 °C, respectively. The Luders stress also drops from 545 MPa at 21 °C to approximately 440 and 415 MPa at 150 and 300 °C, respectively. These trends are seen in the results at 500 s^{-1} as well.

In addition to the challenge that the upper/lower yield stress response imposes on analysis of the results at high strain rates, the sudden drop in stress creates oscillations in the intermediate strain rate force measurments, which obscure the actual force values. This behaviour is illustrated in Figure 4.24, which shows the HSLA350 and DP600 stress versus time response for sheet specimens tested at a nominal strain rate of 100 s^{-1}. The amplitude of the oscillations in the DP600 measurements, in which there is no upper/lower yield stress transition, is less than 3 MPa. For the HSLA350, the average oscillation amplitude is approximately 11 MPa. The larger oscillations in the HSLA350 measurements are the result of the discontinuity, or sudden drop, in the strength of the

specimen, which causes a discontinuous input to the load cell. This discontinuity causes the load cell measurement to oscillate about the actual value and thus, the upper/lower yield stress in the HSLA350 sheet results causes the load measurements to be obscured.

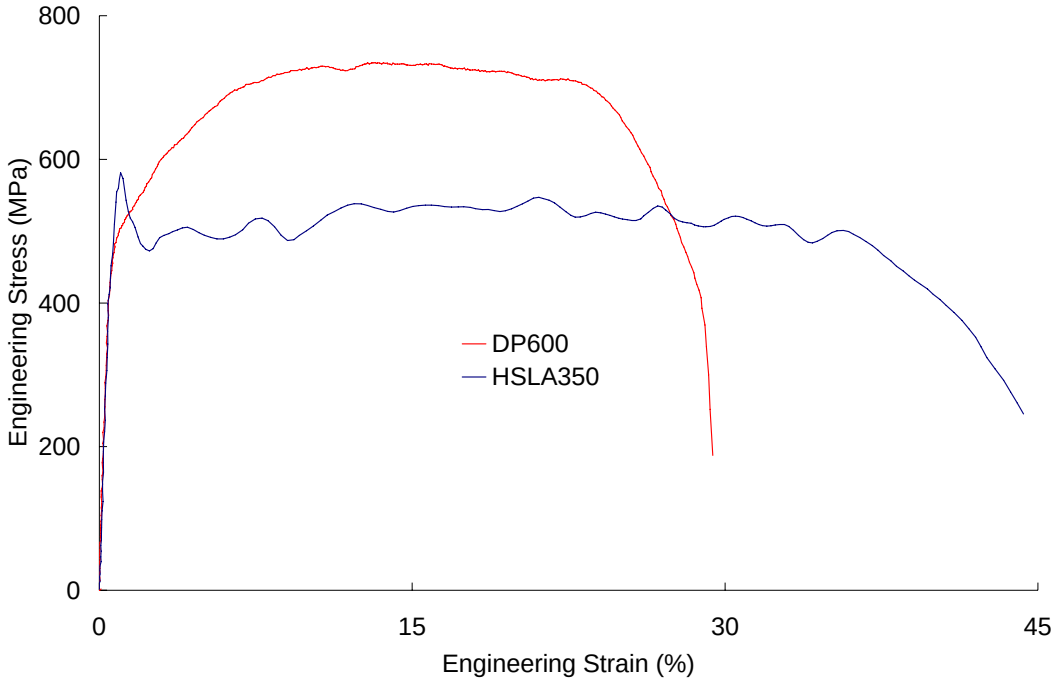

Figure 4.24. Comparison of oscillations in the engineering stress vs. strain results for DP600 and HSLA350 sheet specimens

4.3.3 Tube Forming Effects

During the tube forming process, a significant amount of work-hardening is imparted to the original sheet, which affects the stress-strain response. This effect can be seen in Figure 4.25, which shows the response of the sheet and tube specimens (3, 6, and 9 o'clock positions) at 0.003 s^{-1}. The strength of the sheet specimens lies below all of the tube specimens until approximately 20% strain, just prior to necking of the tube specimens. Also of note is that, while there is not a significant difference in strength between the 3 and 9 o'clock positions of the tube, there is a considerable difference in

strength between the 3 and 6 o'clock positions of the tube, which suggests that the work-hardening that is imparted to the tube during forming is symmetric but not uniform.

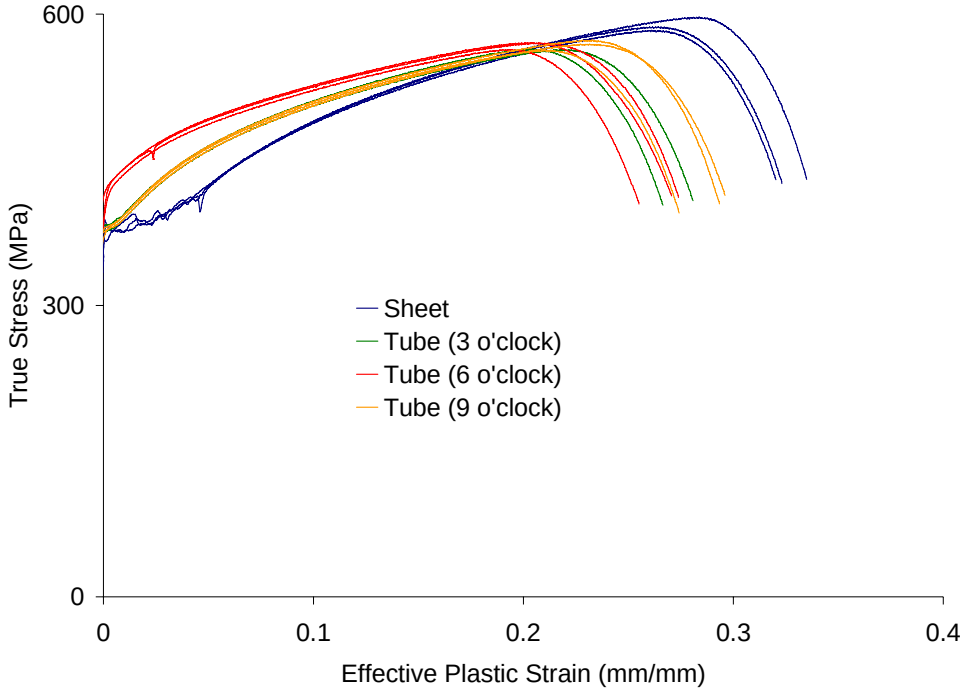

Figure 4.25. Comparison of HSLA350 sheet and tube behaviour at 0.003 s^{-1}

As the strain rate increases, the difference in strength between the sheet and tube specimens increases. This trend is illustrated in Figure 4.26, which compares the behaviour of the sheet and 6 o'clock tube specimens at strain rates up to 100 s^{-1}. At 20% strain, the difference between the strength of the sheet and the 6 o'clock tube specimens is approximately 10 MPa at 0.003 and 0.1 s^{-1}. At 37 and 100 s^{-1}, the difference is approximately 50 MPa.

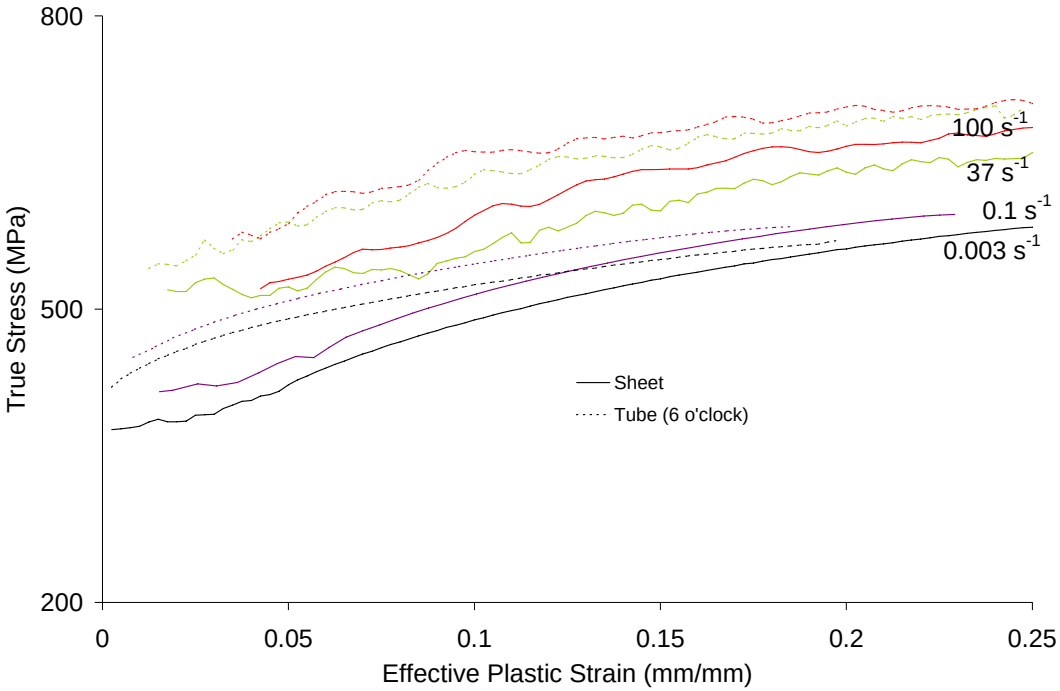

Figure 4.26. Comparison of HSLA350 sheet and tube (6 o'clock) behaviour at strain rates from 0.003 to 100 s^{-1}

The variation of the plastic work that is imparted into the tube during forming remains relatively unchanged. This can be seen in Figure 4.27, which compares the behaviour of the specimens from the 3 and 6 o'clock positions of the tube at increasing strain rates. At all rates, the difference in strength decreases as the amount of strain increases.

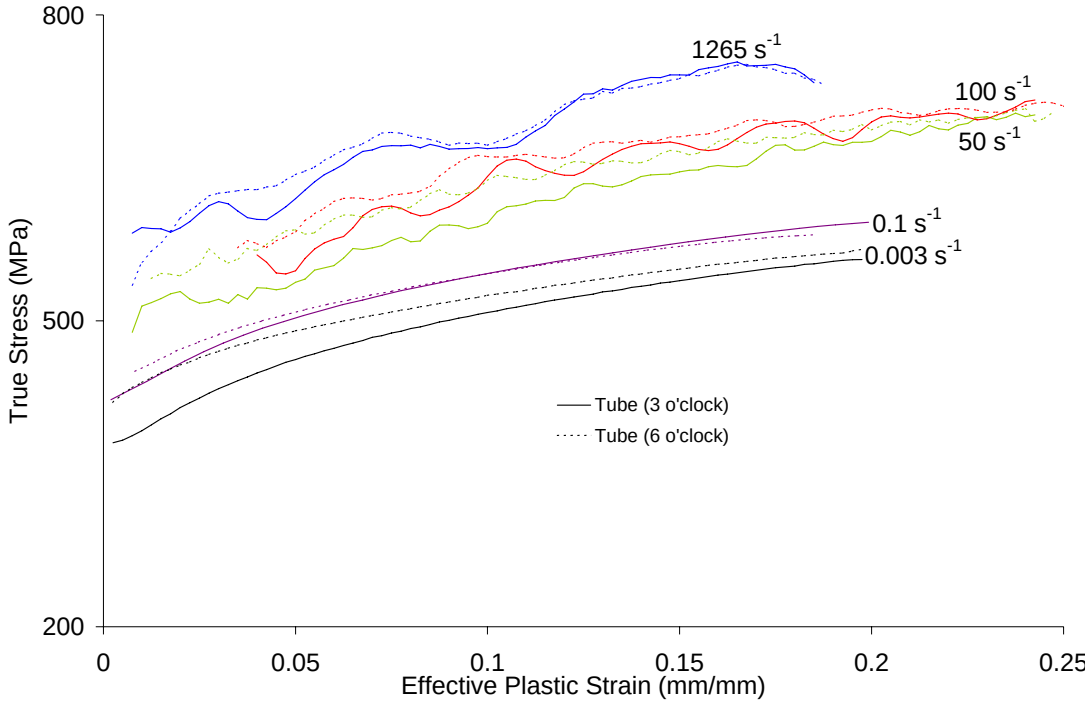

Figure 4.27. Comparison of HSLA350 3 o'clock and 6 o'clock tube specimens at strain rates from 0.003 to 1265 s^{-1}

4.3.4 Failure Strain and Reduction in Cross-Sectional Area

The average strain to failure for the sheet and tube specimens are shown in Table 4.2 for strain rates up to 100 s^{-1}. Overall, the trend shows that ductility is relatively constant from 0.003 to 0.1 s^{-1}, and that it rises as the strain rate increases beyond 0.1 s^{-1}. This trend can also be seen in Figure 4.28, which shows 6 o'clock specimens tested at each strain rate and Figure 4.29, which shows the failure strain and reduction in cross-sectional area as a function of strain rate for the 6 o'clock tube specimens. The reduction in cross-sectional area follows the same trend with respect to strain rate as the failure strain. The failure strain and reduction in cross-sectional area for the sheet and 3 o'clock tube specimens can be found in Appendix B.

Table 4.2. Percent strain at failure for HSLA350 sheet and tube

	NOMINAL STRAIN RATE (1/s)			
	0.003	0.1	30	100
Sheet	38.76	35.56	40.32	44.61
Tube (3 o'clock)	30.66	31.93	45.87	45.21
Tube (6 o'clock)	30.78	31.06	34.81	45.18

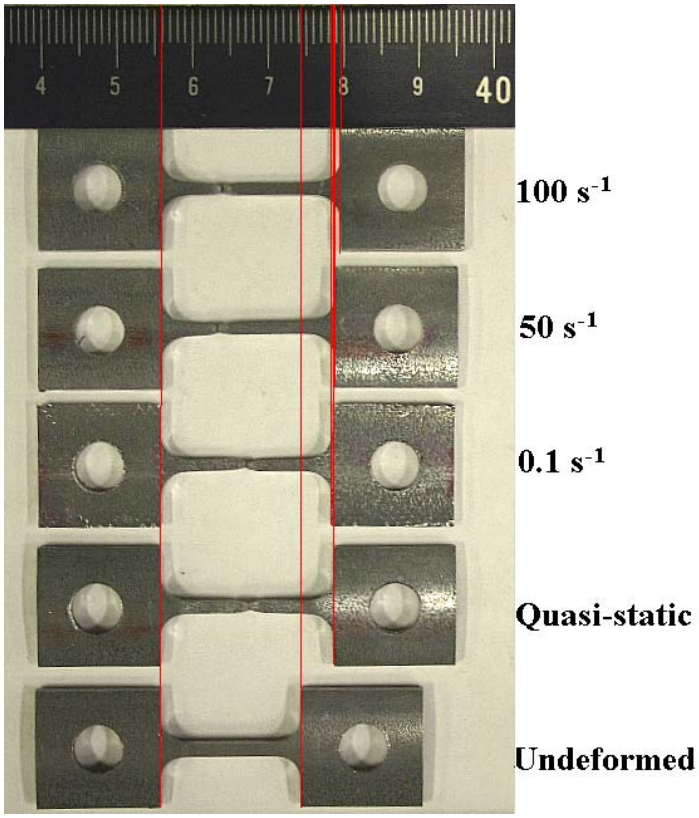

Figure 4.28. Elongation to failure of tested HSLA350 tube (6 o'clock) specimens

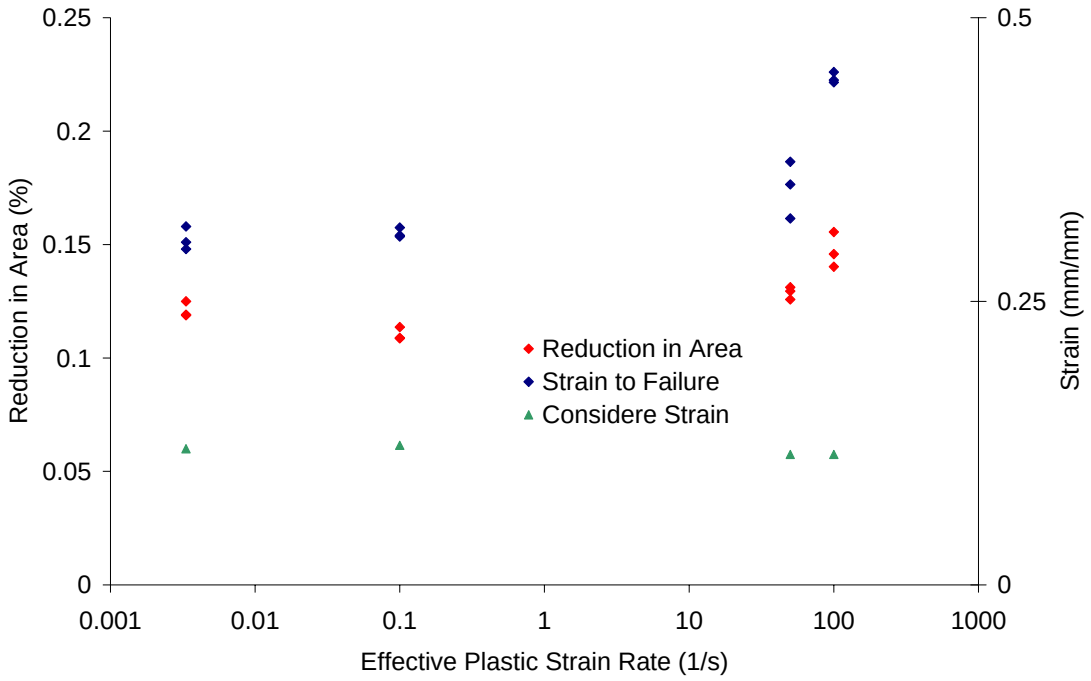

Figure 4.29. Strain to failure and reduction in area of the HSLA350 tube (6 o'clock) specimens

The relationship between strain at the onset of diffuse necking and strain rate can be seen in Figure 4.30, which shows the true stress and the work-hardening rate as a function of plastic strain for the 6 o'clock tube specimens. Using Considere's criterion, the onset of necking occurs between 11.5% and 12.3% plastic strain, regardless of strain rate. This small variation in Considere strain is different from the trend seen in the failure strain, where the elongation to failure increases as the strain rate increases.

Likewise, the trend seen between strain to necking and strain rate for the sheet specimens (Figure 4.31) is different from the strain to failure trend. Using Considere's criterion, the onset of necking occurs at 19.3%, 18.1%, 17.8%, and 15.3% strain at strain rates of 0.003, 0.1, 37, and 100 s^{-1}, respectively. This indicates that the specimen begins to neck earlier as the strain rate increases, whereas the specimens elongate more as the strain rate increases.

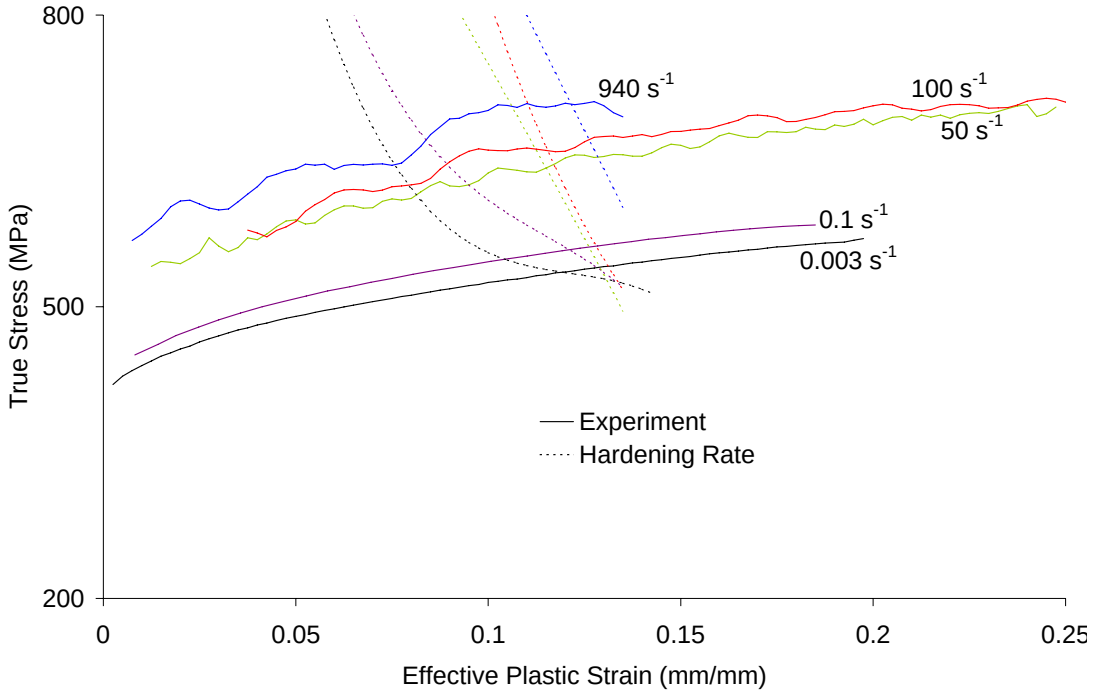

Figure 4.30. True stress and work-hardening rate vs. plastic strain for HSLA350 tube (6 o'clock) at strain rates from 0.003 to 940 s^{-1}

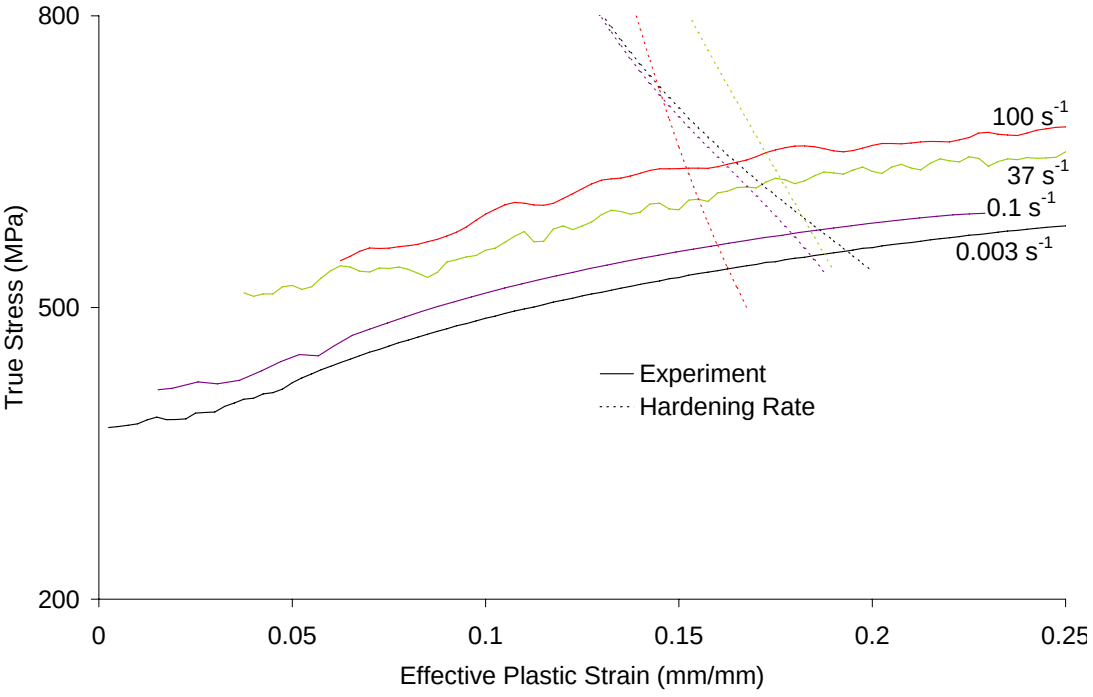

Figure 4.31. True stress and work-hardening rate vs. plastic strain for HSLA350 sheet at strain rates from 0.003 to 100 s^{-1}

4.4 DDQ RESULTS

4.4.1 Strain Rate and Thermal Sensitivity

The strain rate and thermal sensitivity of DDQ for the specimens from the rolling direction of the sheet and the 3 o'clock and 6 o'clock positions of the tube can be seen in the true stress versus effective plastic strain results at all strain rates and temperatures (Figure 4.32 - Figure 4.35). As with the other steels, a positive strain-rate sensitivity is measured. Also, as seen in Figure 4.35, the increase in strength that is associated with an increase in strain rate from 0.003 to 1360 s^{-1} is greater than the decrease in strength that results from a rise in temperature from 21 to 300 °C. This result is different from the results for DP600 and HSLA350, where all of the increase in strength that is associated with a rise in strain rate from 0.003 s^{-1} to around 1250 s^{-1} is approximately equal to the decrease in strength associated with an increase in temperature from 21 to 150 °C.

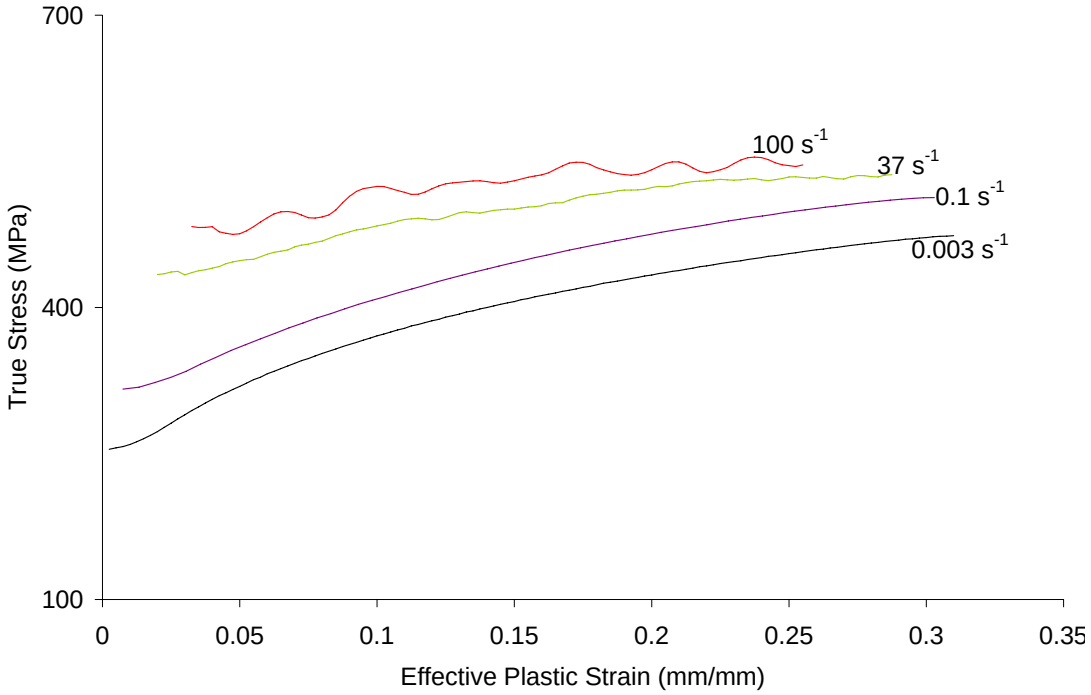

Figure 4.32. True stress vs. effective plastic strain for DDQ sheet specimens at room temperature and strain rates from 0.003 to 100 s^{-1}

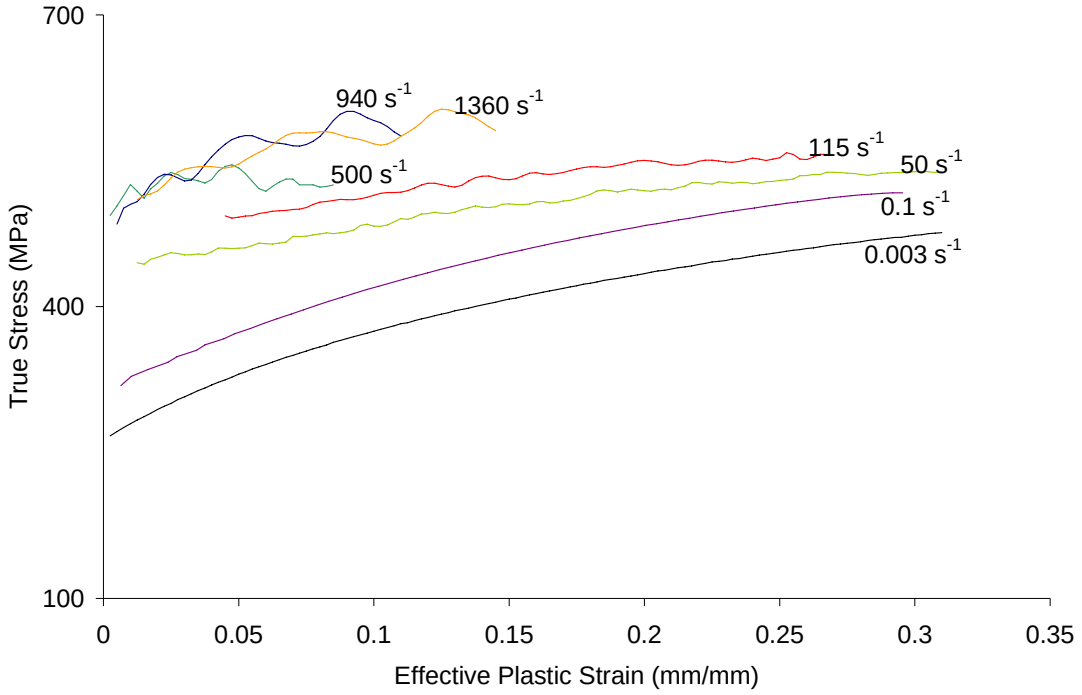

Figure 4.33. True stress vs. effective plastic strain for DDQ tube specimens (3 o'clock) at room temperature and strain rates from 0.003 to 1360 s^{-1}

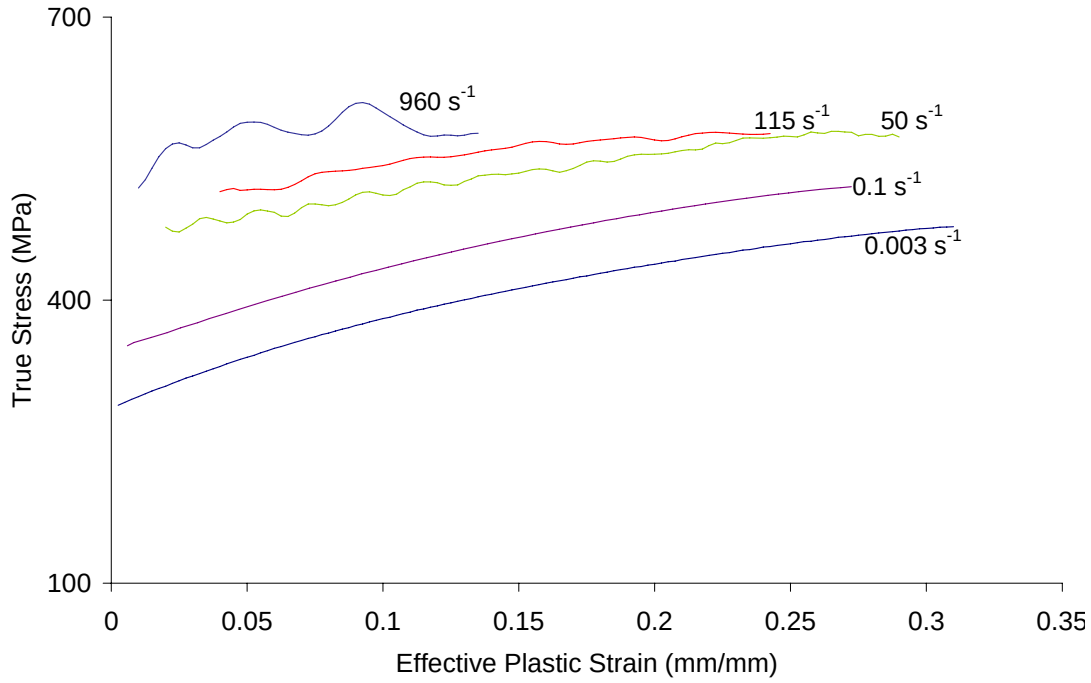

Figure 4.34. True stress vs. effective plastic strain for DDQ tube specimens (6 o'clock) at room temperature and strain rates from 0.003 to 960 s^{-1}

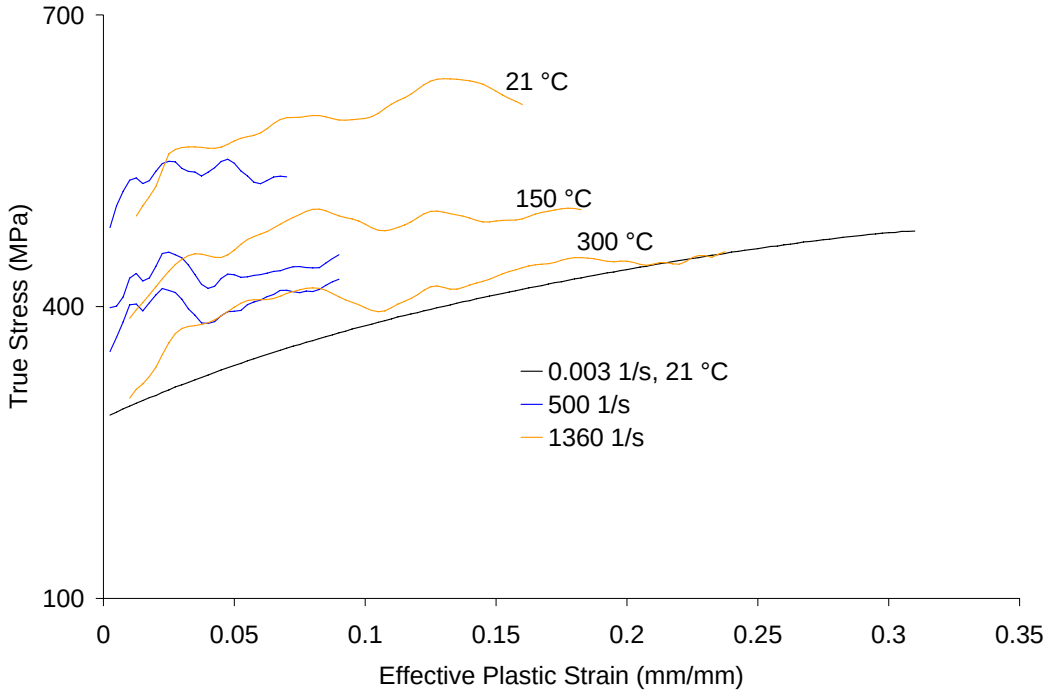

Figure 4.35. True stress vs. effective plastic strain for DDQ tube specimens (6 o'clock) at strain rates of 500 and 1265 s^{-1} and temperatures from 21 to 300 °C

The strain rate sensitivity of the DDQ sheet and tube specimens is illustrated in Figure 4.36, which shows the true stress 10% strain as a function of strain rate at for each experiment that was performed at an initial temperature of 21 °C. At 10% strain, the difference in strength between the sheet specimens and the 6 o'clock tube specimens increases as the strain rate increases, which suggests that the strain rate sensitivity of the sheet and tube are different. This behaviour may be due to scatter in the data. However, at low and intermediate strain rates, the sheet specimens and the 3 o'clock tube specimens have similar strengths, which suggests that the work-hardening that is imparted into the tube during forming affects the strain rate sensitivity of DDQ. As there is no mechanism for a BCC material that would explain this effect, it may be an artifact of testing. At high rates, the difference in strength between the two tube orientations does not appear to be significant.

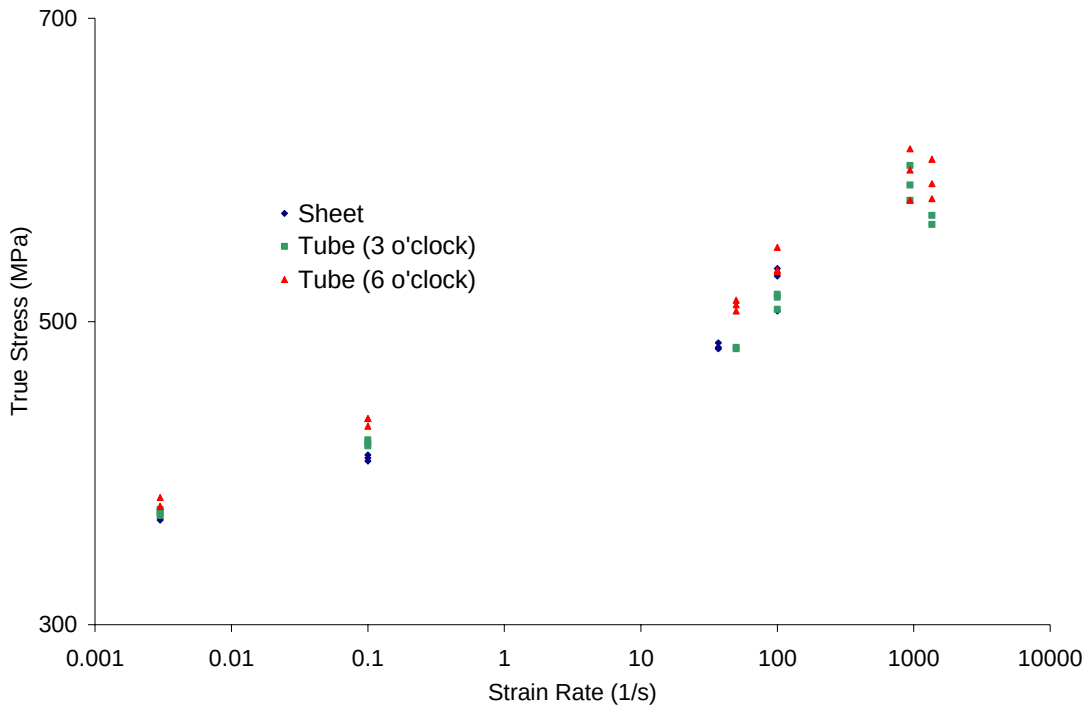

Figure 4.36. True stress vs. strain rate at 10% strain for DDQ

The thermal sensitivity for the 6 o'clock tube specimens can be seen in Figure 4.37, which shows the true stress as a function of the homologous initial testing temperature at 10% plastic strain for the experiments at 1360 s^{-1}. The quasi-static results are also shown to emphasize the decrease in strength that accompanies the rise in temperature.

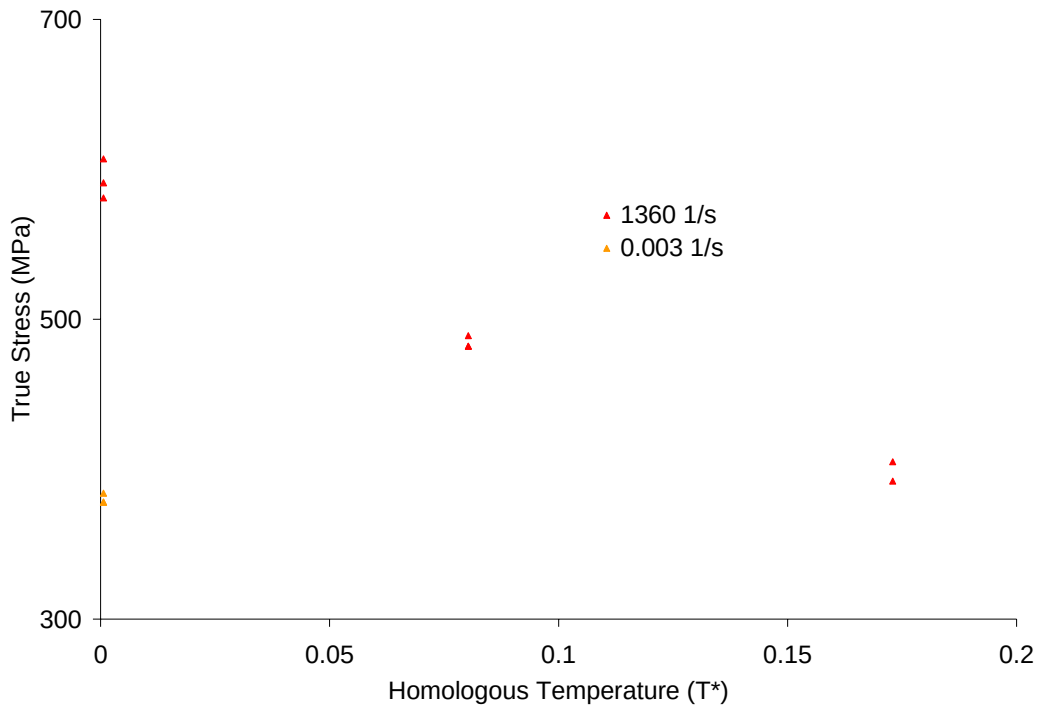

Figure 4.37. True stress vs. homologous temperature at 10% strain for DDQ tube (6 o'clock) specimens tested at 1360 s^{-1}

4.4.2 Upper Yield Stress Effects and Luder's Banding

As with the HSLA350, the DDQ sheet specimens display discontinuous yielding (at less than 1.5% strain), which increases in severity with increasing strain rate. This discontinuous yielding behaviour is not seen in the tube specimens due to the plastic work which has been imparted into them.

For the specimens taken from the sheet, the true stress and plastic strain was only determined for strain rates below 100 s^{-1} (Figure 4.38) because, during the high strain rate experiments, Luder's banding dominates the material behaviour. As seen with the HSLA350 sheet specimens, the presence of Luder's bands results in a time-dependent stress response as opposed to a strain-dependent stress response.

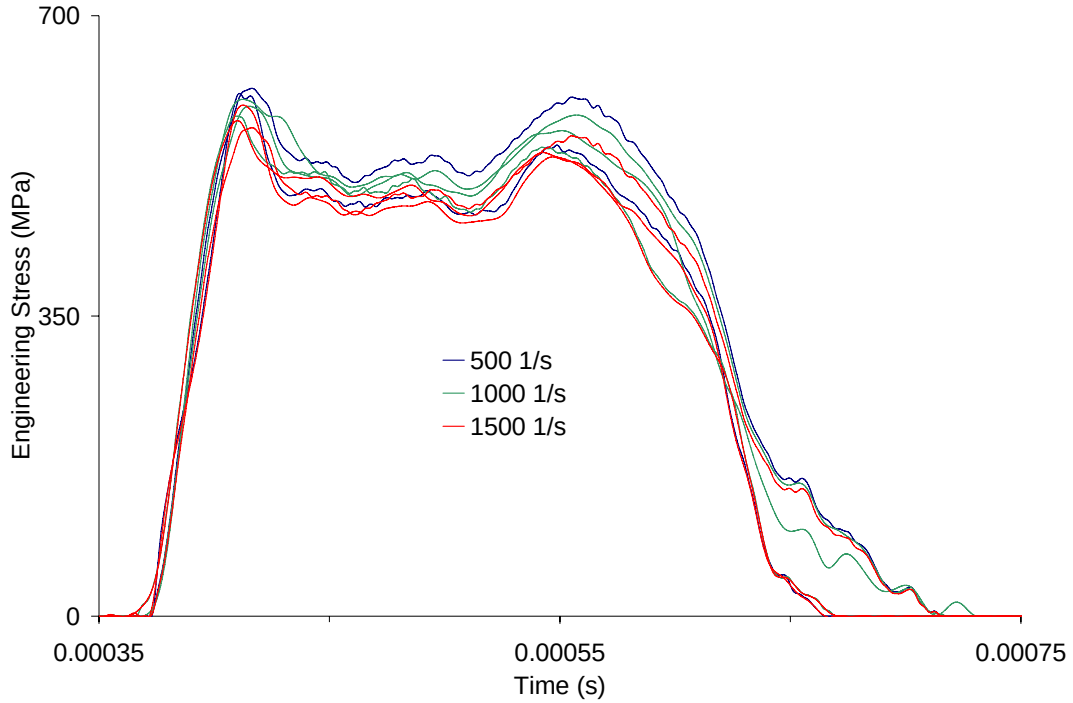

Figure 4.38. Engineering stress vs. time for DDQ sheet specimens at room temperature and nominal strain rates of 500, 1000, and 1500 s^{-1}

At room temperature, the upper yield stress appears to be relatively constant, averaging 596.0 MPa. The Luders stress, which is also relatively constant, is approximately 490 MPa. The time between the rise in stress and the lower yield stress is approximately 61 μs, averaging 61.2, 61.7, and 59.8 μs for the 500, 1000, and 1500 s^{-1} experiments respectively. These times corresponds to average engineering strains of 2.4%, 5.1%, and 7.3%, respectively.

The time required for the Luder's band to propagate across the specimen is relatively constant for each strain rate, with an average duration of 84.3 μs. As with the HSLA350 specimens, the yield stress and Luder's band behaviour account for approximately 72% of the loading duration, which suggests that these results are not useful for constitutive modeling.

As the temperature increases, the time required for the beginning of the Luder's band to start decreases. This can be seen in Figure 4.39, which shows the engineering stress as a

function of time and temperature. For the 1500 s^{-1} experiments, the average time between the rise in stress and the lower yield stress is approximately 59.8 μs at 21 °C. At 150 °C and 300 °C, it takes an average of 43.2 and 37.2 μs, respectively. The time required for the Luder's band to propagate, however, appears to be unchanged. This constant propogation time suggests that the maximum velocity of the Luder's band is not temperature dependent.

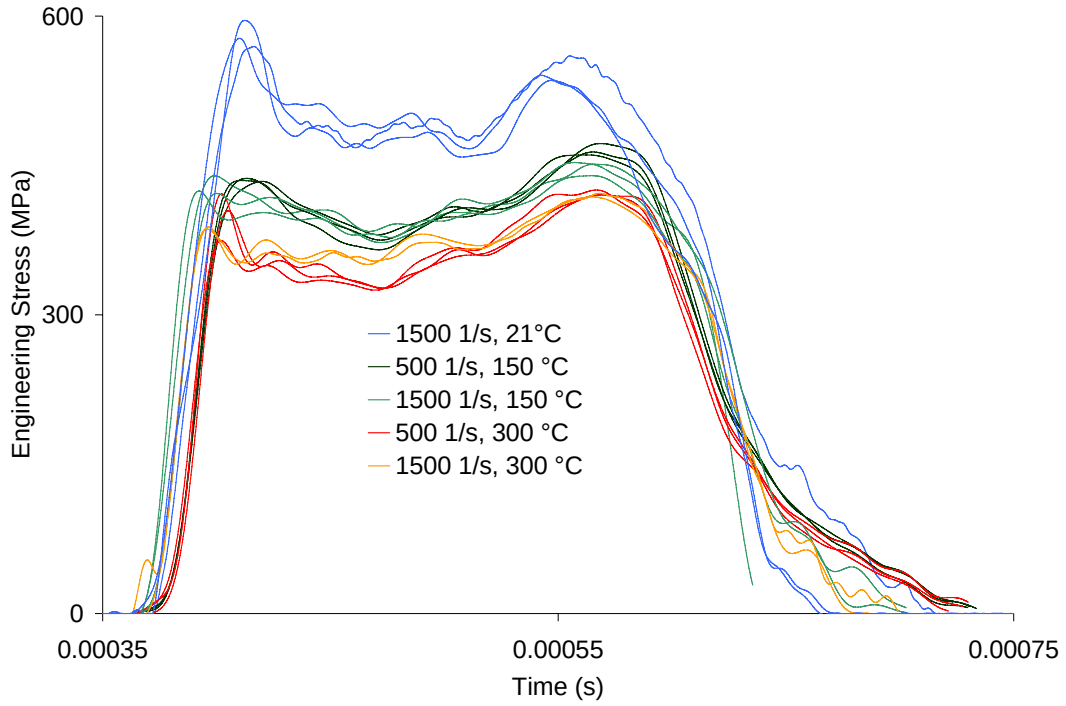

Figure 4.39. Engineering stress vs. time for DDQ sheet specimens at temperatures between 21 and 300 °C and strain rates of 500 and 1500 s^{-1}

The strain rate and temperature sensitivity of the upper and lower yield stress response are shown in Figure 4.40 for the room temperature specimens. It can be seen that both the upper and lower yield stress levels increase dramatically as the strain rate increases up to 500 s^{-1}.

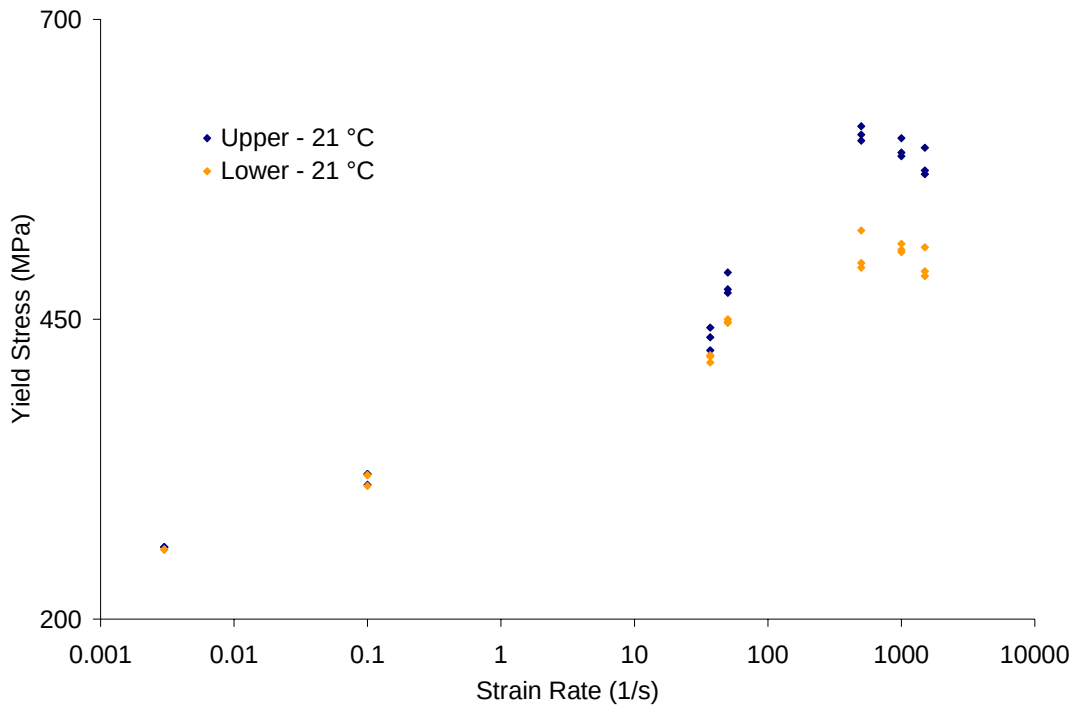

Figure 4.40. Upper and lower yield stress vs. strain rate for DDQ sheet specimens

4.4.3 Tube Forming Effects

The effect of the tube pre-forming operation on the original DDQ material can be seen in Figure 4.41, which shows the response of the sheet and tube specimens (3, 6, and 9 o'clock positions) at 0.003 s^{-1}. The strength of the sheet specimens does not match that of the 3 and 9 o'clock tube specimens until approximately 12% strain. Also of note is that, while there is not a significant difference in strength between the specimens from the 3 and 9 o'clock positions of the tube, the strength of the 3 o'clock specimens lies below the 6 o'clock specimens up to approximately 8% strain. This result suggests that the work-hardening that is imparted to the tube during forming is symmetric but not uniform.

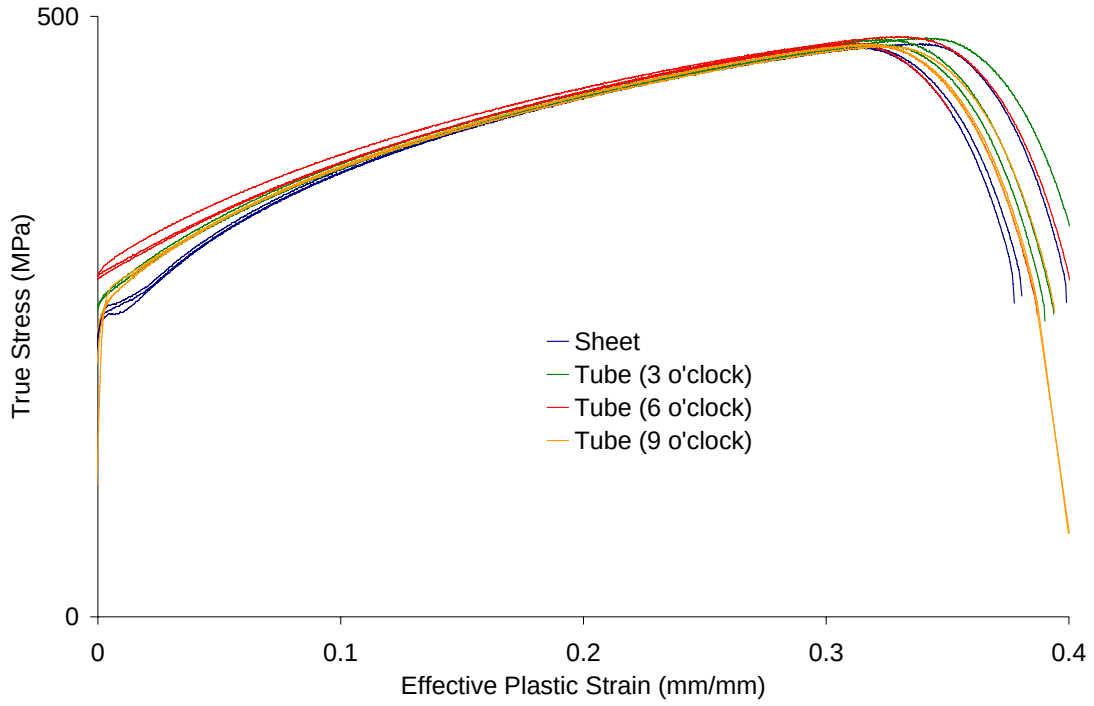

Figure 4.41. Comparison of DDQ sheet and tube behaviour at 0.003 s^{-1}

As the strain rate increases, the difference in strength between the sheet and tube specimens increases. This result can be seen in Figure 4.42, which compares the behaviour of the sheet specimens (Figure 4.32) and 6 o'clock tube specimens (Figure 4.34) at strain rates up to 100 s^{-1}. At 20% strain, the difference between the strength of the sheet and the 6 o'clock tube specimens is approximately 4 MPa at 0.003 s^{-1}, 20 MPa at 0.1 s^{-1}, 34 MPa at 37 s^{-1}, and 28 MPa at 100 s^{-1}.

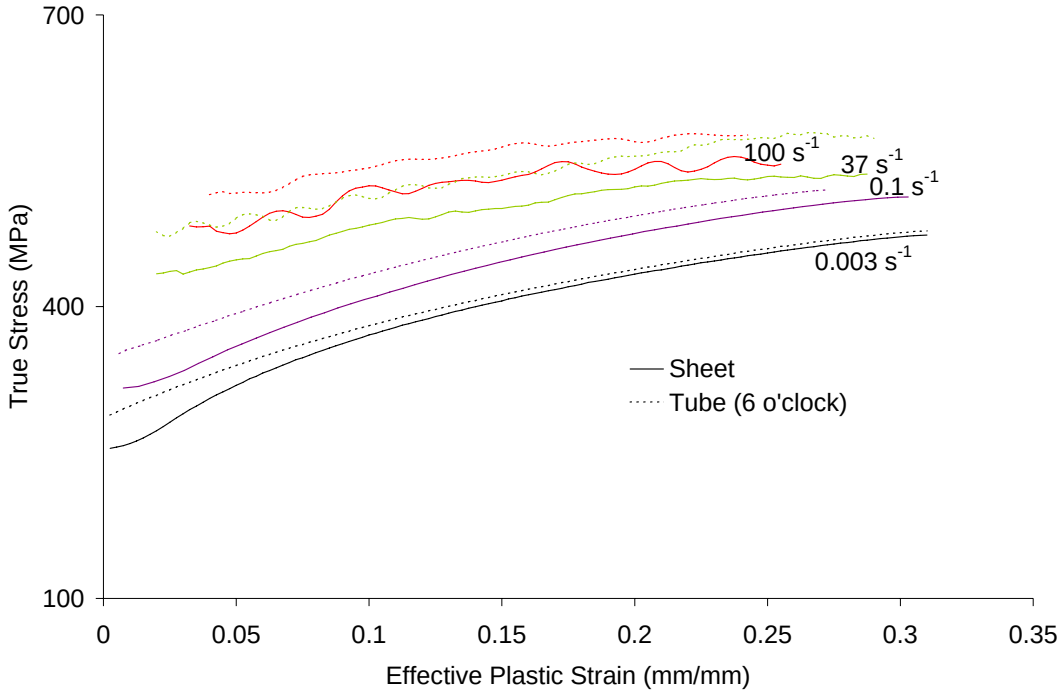

Figure 4.42. Comparison of DDQ sheet and tube (6 o'clock) behaviour at strain rates from 0.003 to 100 s^{-1}

The difference in strength around the perimeter of the tube persists as the strain rate increases up to 100 s-1. The strength of the 3 and 6 o'clock specimens is shown in Figure 4.43. At 20% strain, the difference between the strength of the sheet and the 6 o'clock tube specimens is approximately 3 MPa at 0.003 s^{-1}, 11 MPa at 0.1 s^{-1}, 35 MPa at 37 s^{-1}, and 29 MPa at 100 s^{-1}.

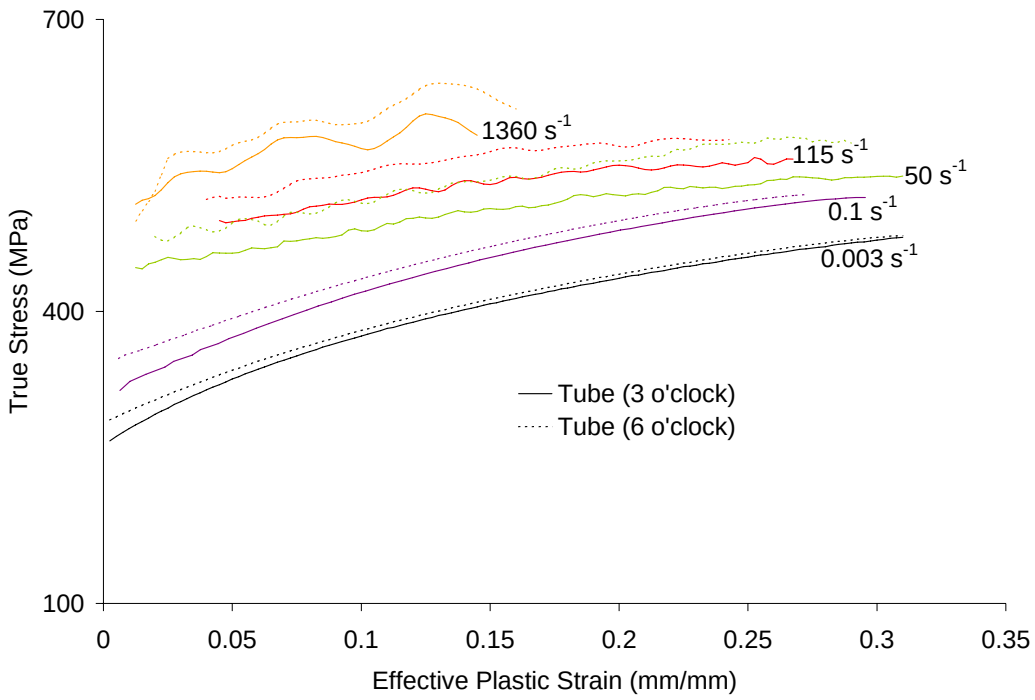

Figure 4.43. Comparison of DDQ 3 o'clock and 6 o'clock tube specimens at strain rates from 0.003 to 1360 s^{-1}

4.4.4 Failure Strain and Reduction in Cross-Sectional Area

The average strain to failure for the sheet and tube specimens is shown in Table 4.3 for strain rates up to 100 s^{-1}. The overall trend is that there is a mild decrease in ductility with increasing strain rate from 0.003 to 100 s^{-1}. This trend can also be seen in Figure 4.44, which shows 6 o'clock tube specimens tested at each strain rate, and Figure 4.45, which shows the failure strain and reduction in cross-sectional area as a function of strain rate for the 6 o'clock tube specimens. The reduction in cross-sectional area follows the same trend with respect to strain rate as the failure strain. The failure strain and reduction in cross-sectional area for the sheet and 3 o'clock tube specimens can be found in Appendix B.

Table 4.3. Percent strain at failure for DDQ sheet and tube

	NOMINAL STRAIN RATE (1/s)			
	0.003	0.1	30	100
Sheet	47.66	43.68	43.04	48.12
Tube (3 o'clock)	48.96	44.97	40.56	45.18
Tube (6 o'clock)	46.53	43.37	46.54	42.32

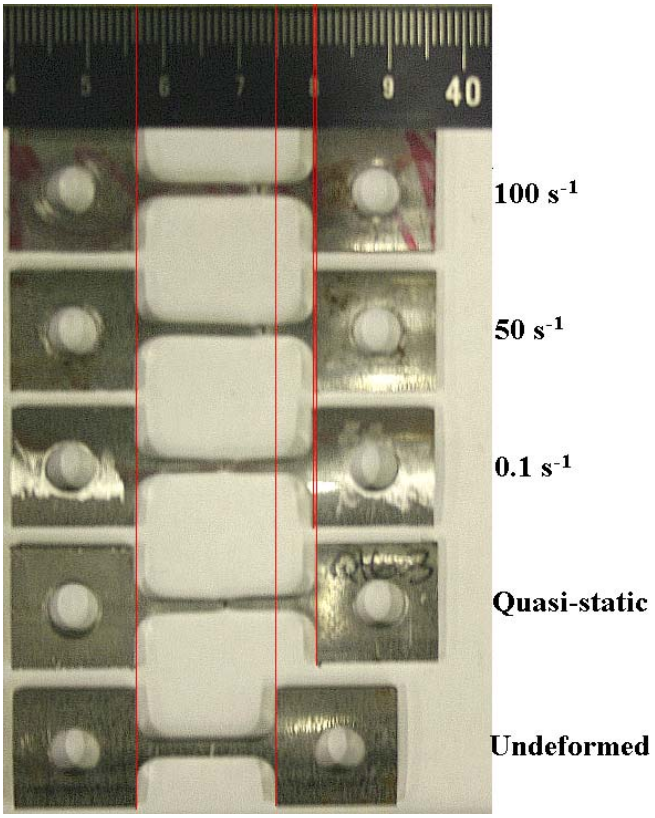

Figure 4.44. Elongation to failure of tested DDQ tube (6 o'clock) specimens

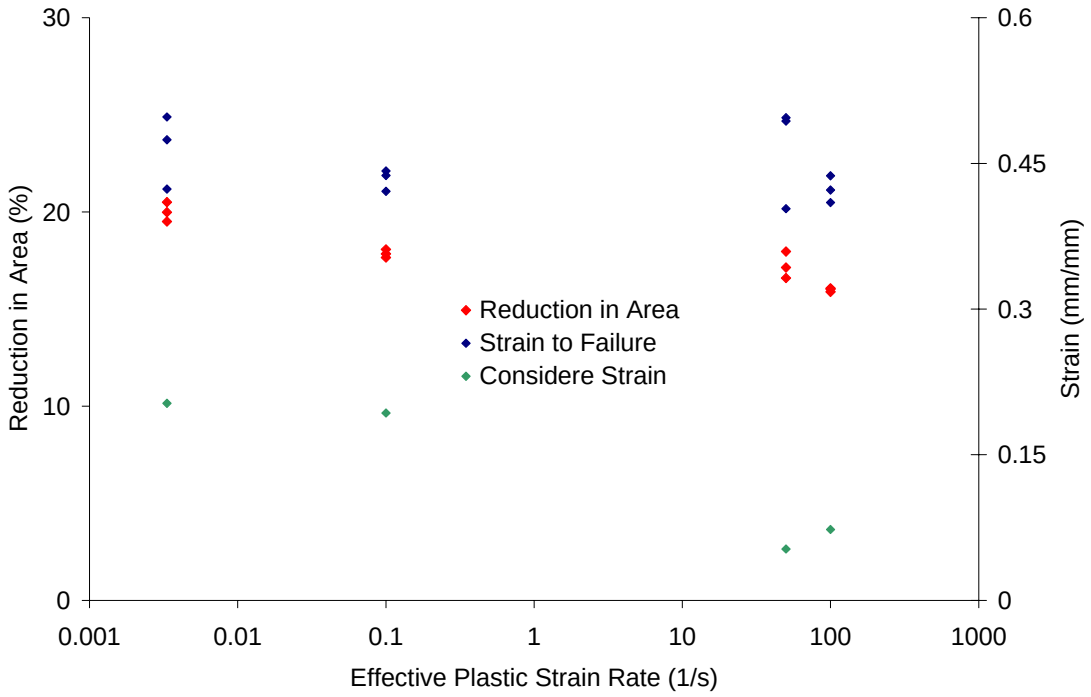

Figure 4.45. Strain to failure and reduction in area of the DDQ tube (6 o'clock) specimens

The relationship between predicted strain at the onset of diffuse necking and strain rate can be seen in Figure 4.46, which shows the true stress and the work-hardening rate as a function of plastic strain for the 6 o'clock tube specimens. Using Considere's criterion, the onset of necking occurs at 20.3% and 19.3% plastic strain for the 0.003 and 0.1 s^{-1} experiments, respectively. At 50 and 115 s^{-1}, the strain at which necking begins drops to 5.3% and 7.3% strain, respectively. This drop in strain is due to the decrease in work-hardening rate with increased strain rate, which can be seen clearly in the work-hardening rate as a function of strain rate and strain (Figure 4.47). The difference between the work-hardening rate at low strain rates and at intermediate strain rates is relatively constant for the DDQ tube specimens.

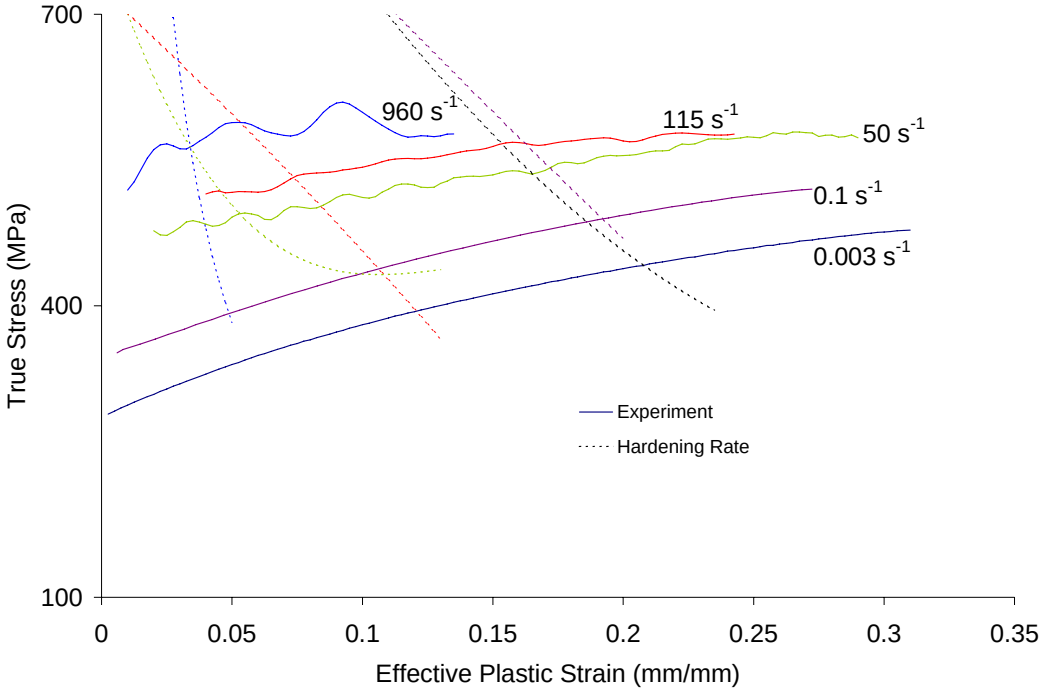

Figure 4.46. True stress and work-hardening rate vs. plastic strain for DDQ tube (6 o'clock) at strain rates from 0.003 to 960 s^{-1}

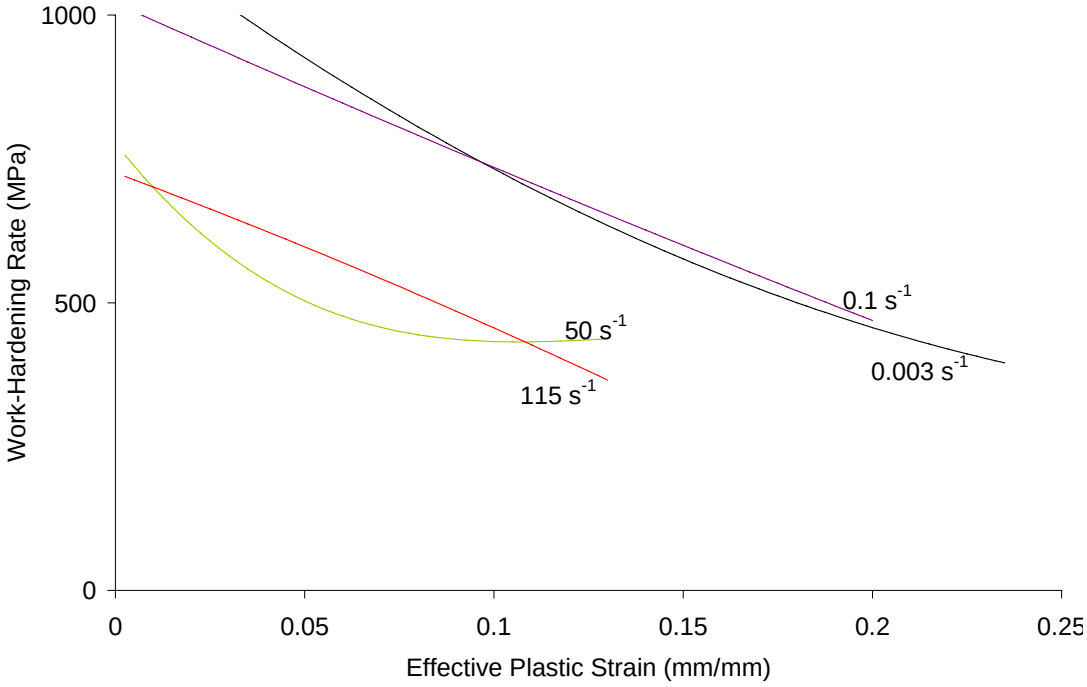

Figure 4.47. Work-hardening rate vs. plastic strain for DDQ tube (6 o'clock) at strain rates from 0.003 to 115 s^{-1}

The same trends are observed in the sheet specimens. The strain at which necking begins decreases as the strain rate increases (Figure 4.48). The onset of necking occurs at 22.1% and 21.1% plastic strain for the 0.003 and 0.1 s^{-1} experiments, respectively. At 37 and 100 s^{-1}, the strain at which necking begins drops to 12.3% and 9.3% strain, respectively. As with the tube, the work-hardening rate decreases as the strain rate increases (Figure 4.49), such that there is a relatively constant difference between the work-hardening rate at low strain rates and at intermediate strain rates for the DDQ sheet specimens.

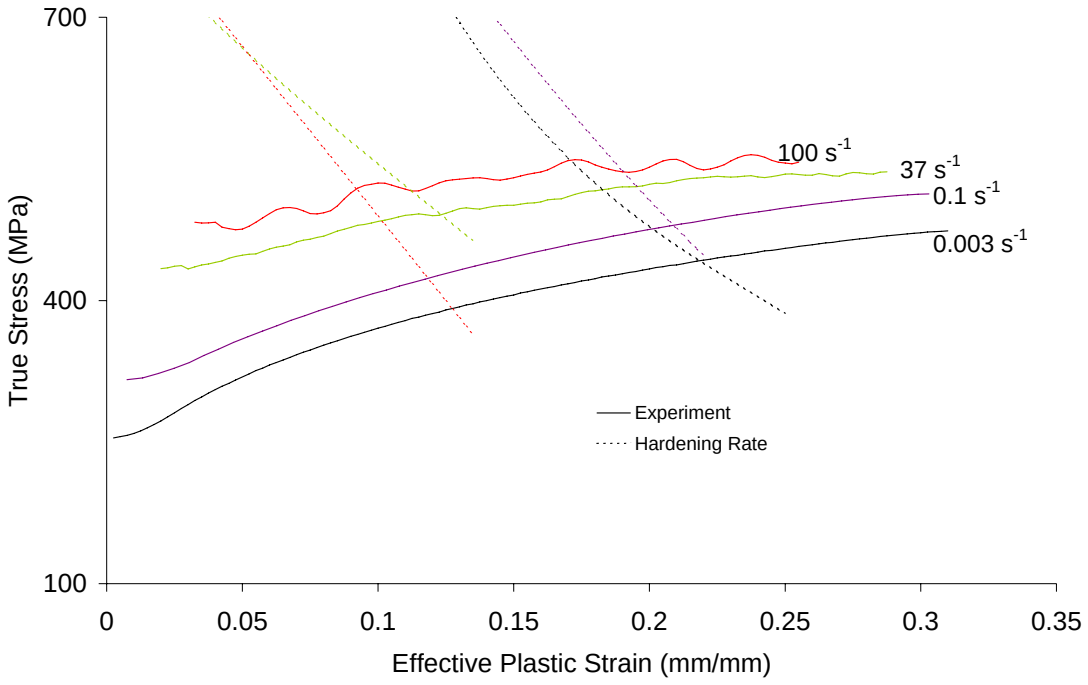

Figure 4.48. True stress and work-hardening rate vs. plastic strain for DDQ sheet at strain rates from 0.003 to 100 s^{-1}

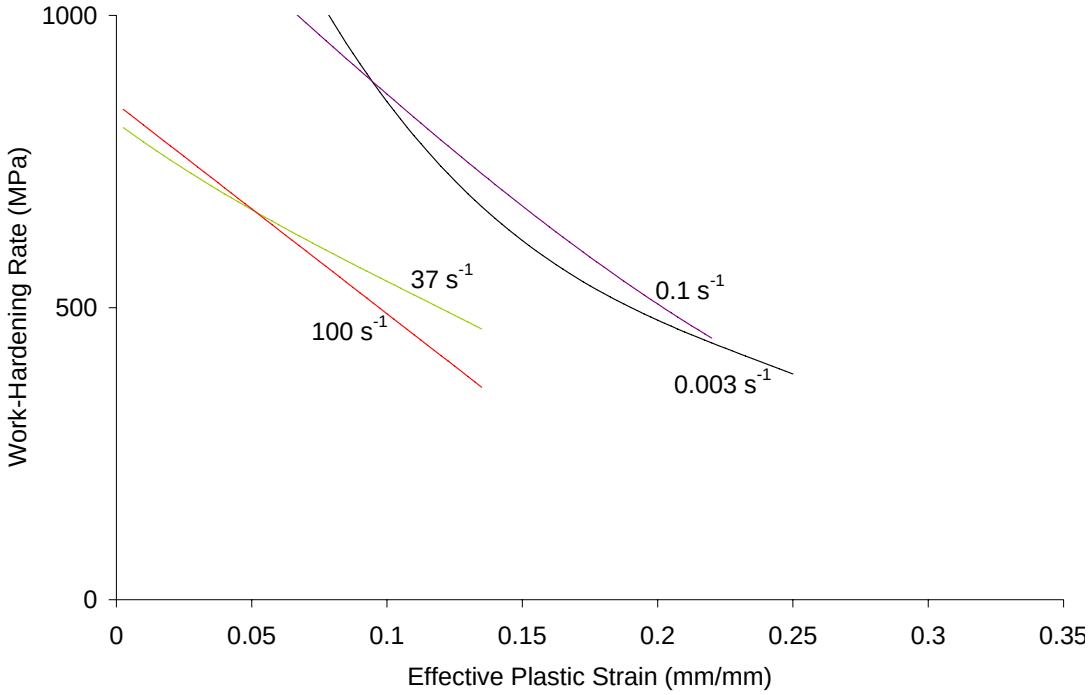

Figure 4.49. Work-hardening rate vs. plastic strain for DDQ sheet at strain rates from 0.003 to 100 s^{-1}

CHAPTER 5

CONSTITUTIVE MODELING

In this chapter, the consitutitve parameters required by the Johnson-Cook [75,76] (Equation 3.1) and Zerilli-Armstrong [78,81] (Equation 3.6) constitutive models are fit to the experimental results. The fits are presented for all three alloys in both sheet and tube form.

5.1 CONSTITUTIVE FITTING PROCEDURE

As seen in Chapter 4, the DDQ and HSLA350 sheet specimens exhibit an upper yield stress that becomes amplified as the strain rate increases. Such a response is not considered in available high strain rate constitutive models such as the Johnson-Cook or Zerilli-Armstrong models. Hence, it was not possible to capture this response for modeling. Fortunately, the tube specimens do not display this response and, therefore, the fits with the Johnson-Cook and Zerilli-Armstrong models are more appropriate.

To model the DDQ and HSLA350 specimens as accurately as possible, the following method was used. First, the 6 o'clock specimens were characterized because, at this orientation, experiments were done at each test condition. From these results, the temperature dependence for each steel was found. Since the temperature sensitivity is not dependent on prior work hardening [80], this result was then used to help characterize the 3 o'clock specimens throughout the complete range of strain rates and temperatures. Characterization of the sheet specimens was performed in a similar manner, but was limited to the data for strain rates up to 100 s^{-1}, which is the highest rate that can be attained before the strong upper/lower yield stress response renders the data unusable. For the tube specimens, in order to characterize the 3 o'clock and 6 o'clock specimens such that some combination of their parameters can be used in future crash models, the

strain rate sensitivity which best describes both sets of data was used. Thus, only the strain-hardening terms vary between the 3 and 6 o'clock fits.

The constitutive parameters for the DP600 specimens were found differently from the DDQ and HSLA350 specimens. Because of the uniform stress-strain behaviour found for all tube locations considered, only one fit was performed for the tube specimens. This situation is ideal for crash simulations since the plastic response of the tube can be considered to be constant around its perimeter. Also, unlike the DDQ and HSLA350 alloys, the DP600 sheet did not display discontinuous yielding at any rates and, thus, the strain rate sensitivity and thermal softening responses for the sheet and tube specimens were characterized independently.

The fitting was done using a non-linear regression technique employed by the SYSTAT statistical software program. In order to obtain an indication of the accuracy of the constitutive fits, R-squared terms were calculated as indicators of "accuracy-of-fit". In addition, a discussion of how well the fits capture the general trends is presented.

5.2 DP600 CONSTITUTIVE FITS

The Johnson-Cook and Zerilli-Armstrong constitutive fits for the DP600 tube specimens are shown in Figure 5.1, Figure 5.2, Figure 5.3, and Figure 5.4. Figure 5.1 (Johnson-Cook) and Figure 5.2 (Zerilli-Armstrong) show the constitutive fits along with the results of the experiments that were performed at an initial temperature of 21 °C. Figure 5.3 (Johnson-Cook) and Figure 5.4 (Zerilli-Armstrong) show the constitutive fits along with the results of the high rate experiments that were performed at elevated temperatures. For the DP600 sheet specimens, the Johnson-Cook constitutive fit is exhibited in Figure 5.5 (21 °C) and Figure 5.7 (elevated temperatures) and the Zerilli-Armstrong constitutive fit is exhibited in Figure 5.6 (21 °C) and Figure 5.8 (elevated temperatures).

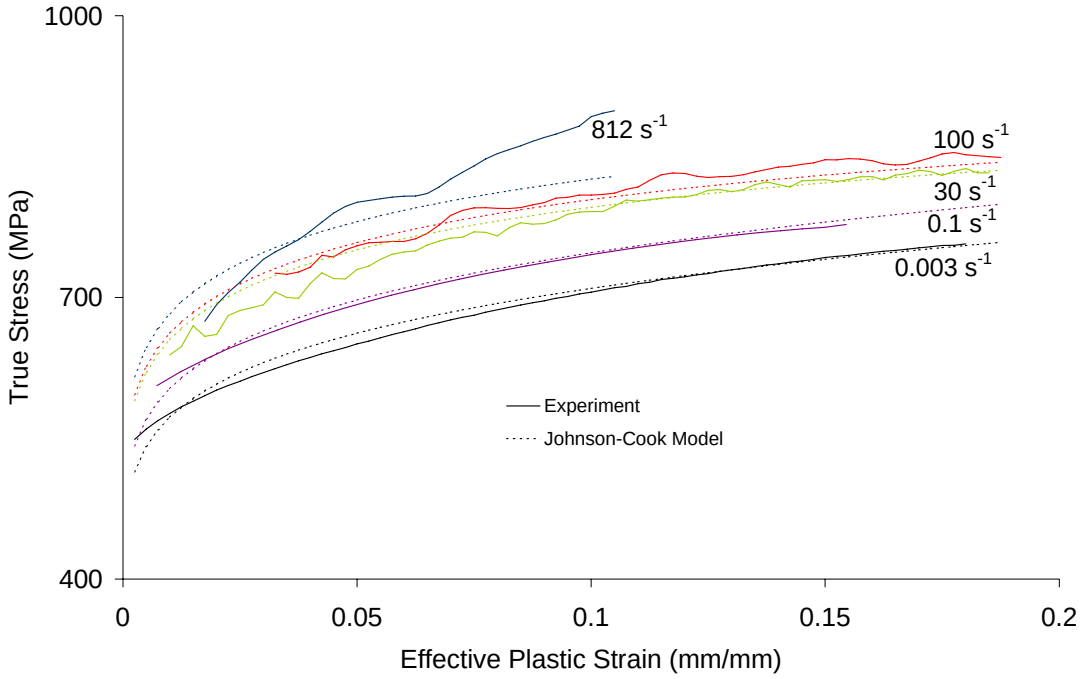

Figure 5.1. DP600 tube ambient temperature results fit with the Johnson-Cook constitutive model

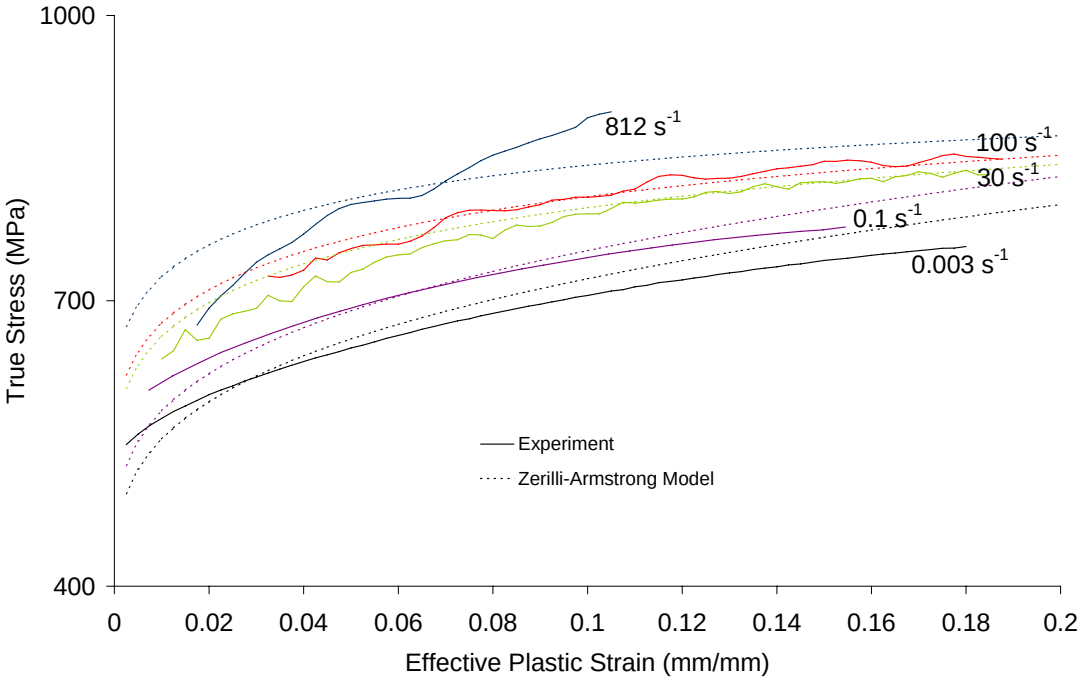

Figure 5.2. DP600 tube ambient temperature results fit with the Zerilli-Armstrong constitutive model

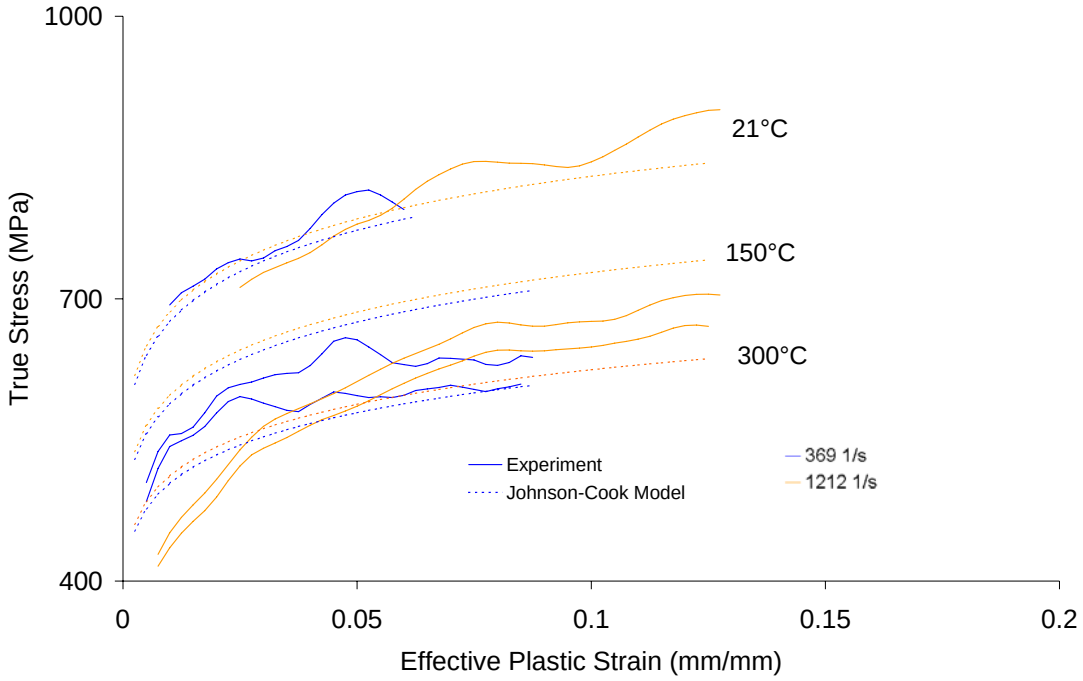

Figure 5.3. DP600 tube elevated temperature results fit with the Johnson-Cook constitutive model

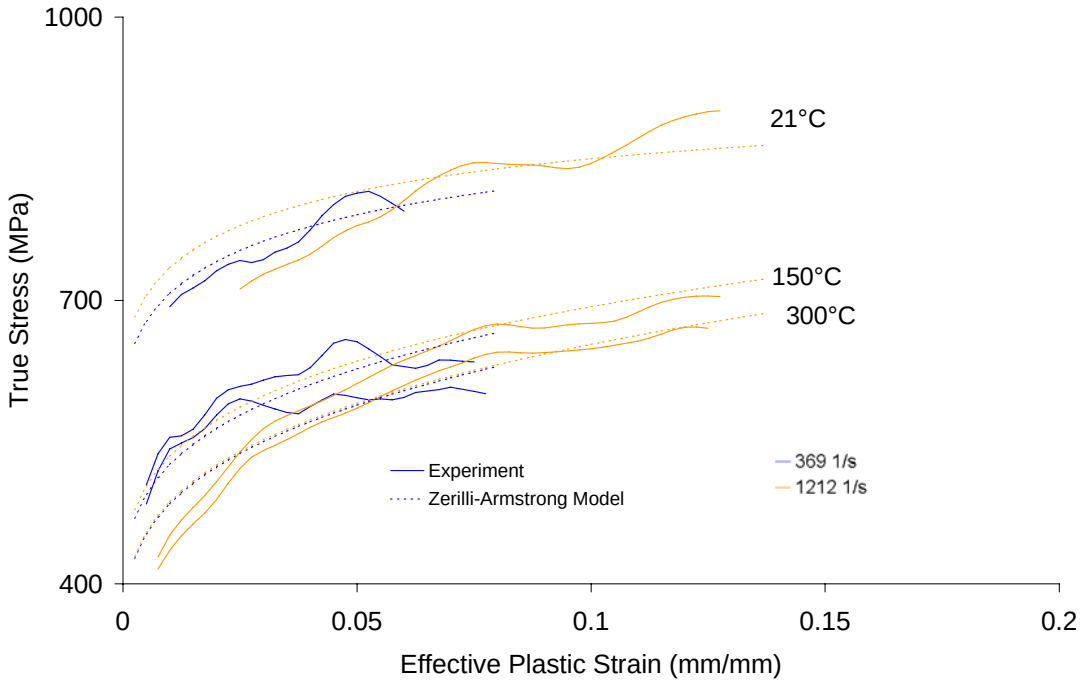

Figure 5.4. DP600 tube elevated temperature results fit with the Zerilli-Armstrong constitutive model

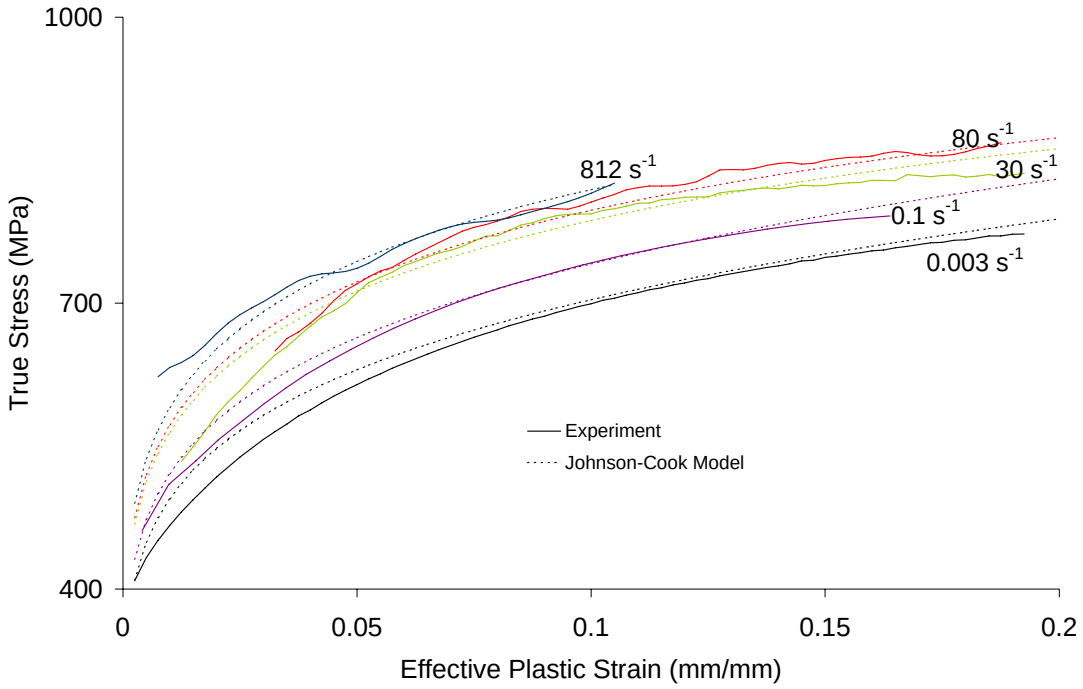

Figure 5.5. DP600 sheet ambient temperature results fit with the Johnson-Cook constitutive model

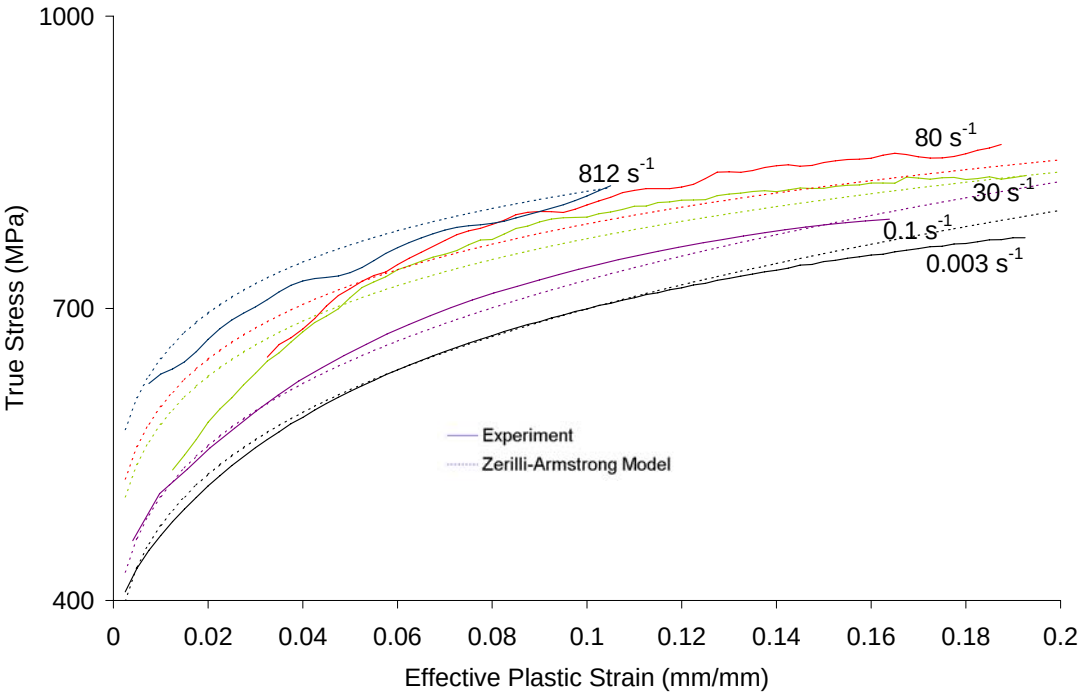

Figure 5.6. DP600 sheet ambient temperature results fit with the Zerilli-Armstrong constitutive model

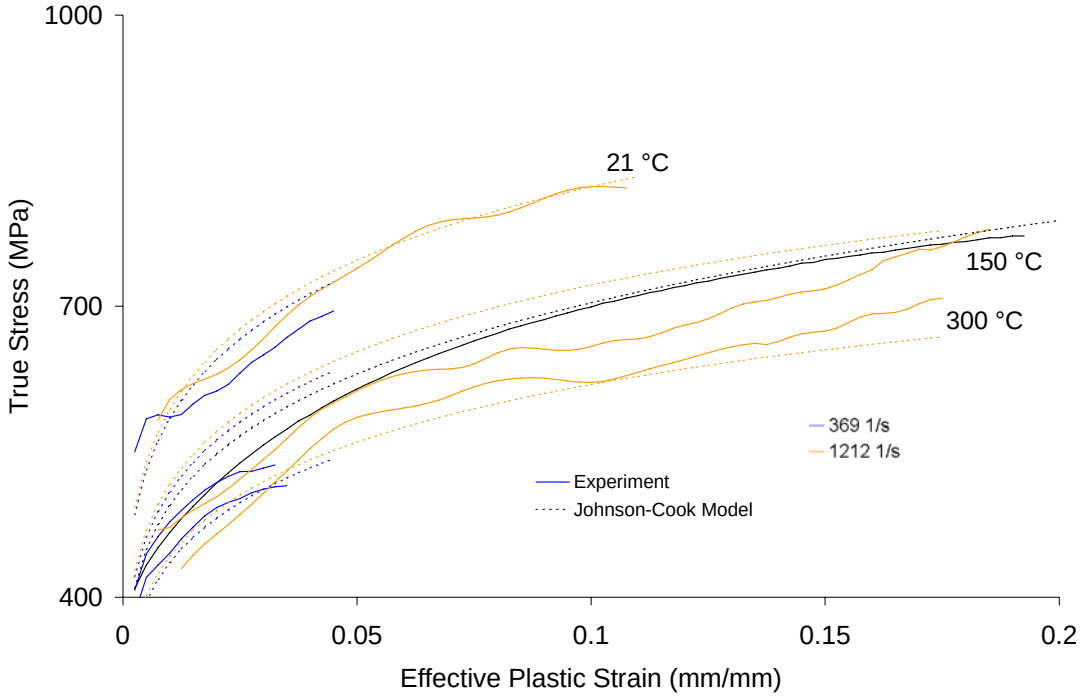

Figure 5.7. DP600 sheet elevated temperature results fit with the Johnson-Cook constitutive model

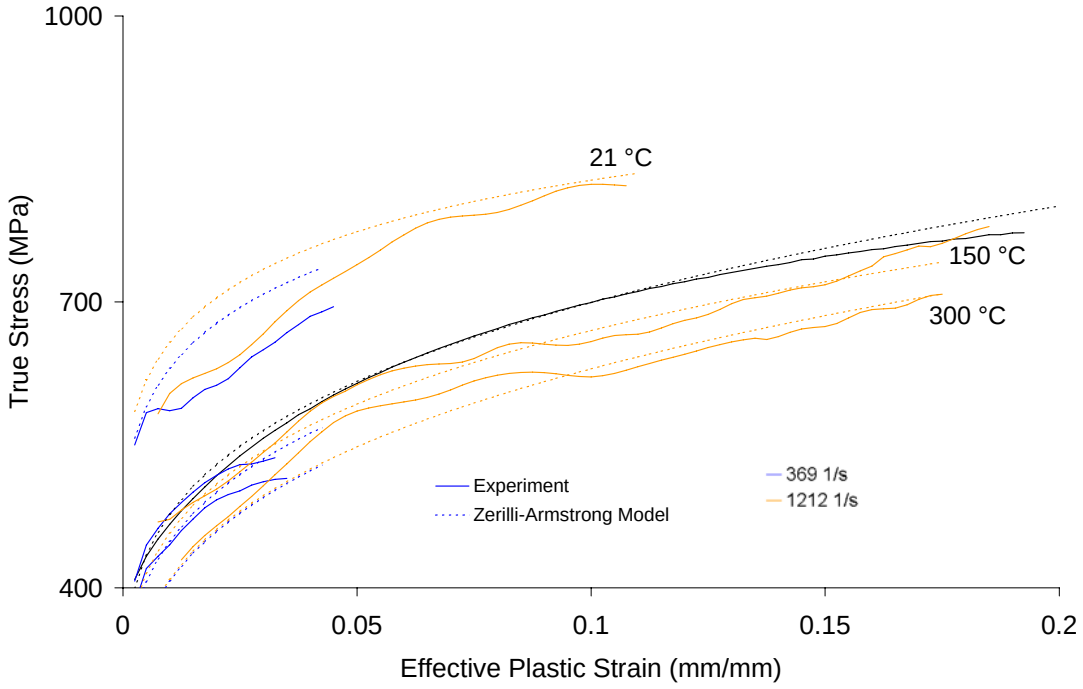

Figure 5.8. DP600 sheet elevated temperature results fit with the Zerilli-Armstrong constitutive model

The constitutive parameters for each fit and model as well as the accuracy of the fits are shown in Table 5.1(Johnson-Cook) and Table 5.2 (Zerilli-Armstrong). The reason that the Johnson-Cook fit is less accurate than the Zerilli-Armstrong fit appears to be related to the elevated temperature experiments. The Johnson-Cook fit does not capture the response at 150 °C as closely as the Zerilli-Armstrong fit. For the other experiments, both models yield very similar results.

The 95% confidence interval is within 8% for the work-hardening terms in the Johnson-Cook fit and within 3% for the strain rate sensitivity and thermal softening terms. For the Zerilli-Armstrong fits, the confidence intervals are quite small relative to the actual terms except for the C_1 term which is roughly 40% of the actual value. This is not concerning, because, in the model, C_1 is multiplied by a very small number (based on the strain rate and temperature) and thus does not have a large effect on the true stress.

Table 5.1. Constitutive parameters for the DP600 averaged curves fit with the Johnson-Cook model

	Johnson-Cook					
	A (MPa)	**B (MPa)**	**n**	**c**	**m**	**R^2**
Sheet	*165*	*968.57*	*0.206*	*0.0145*	*0.868*	***0.955***
(95% confidence)	*±2.89*	*±52.46*	*±0.012*	*±0.002*	*±0.016*	
3 o'clock	*350*	*655.72*	*0.189*	*0.0144*	*0.867*	***0.901***
(95% confidence)	*±25.42*	*±48.47*	*±0.001*			
6 o'clock	*350*	*655.72*	*0.189*	*0.0144*	*0.867*	***0.901***
(95% confidence)	*±25.42*	*±48.47*	*±0.001*	*±0.001*	*±0.025*	

Table 5.2. Constitutive parameters for the DP600 averaged curves fit with the Zerilli-Armstrong model

	Zerilli-Armstrong						
	C_0 (MPa)	**C_1 (MPa)**	**C_3**	**C_4**	**C_5 (MPa)**	**q**	**R^2**
Sheet	*162.81*	*7829.52*	*0.0136*	*0.00032*	*889.21*	*0.288*	***0.976***
(95% confidence)	*±40.21*		*±0.0011*	*Negligible*	*±20.84*	*±0.033*	
3 o'clock	*307.16*	*7829.52*	*0.0138*	*0.00032*	*673.53*	*0.3*	***0.952***
(95% confidence)	*±67.3*				*±39.10*	*±0.073*	
6 o'clock	*307.16*	*7829.52*	*0.0138*	*0.00032*	*673.53*	*0.3*	***0.952***
(95% confidence)	*±67.3*	*±3253*	*±0.0013*	*Negligible*	*±39.10*	*±0.073*	

A source of inaccuracy in fitting the results from the tube specimens is that the work-hardening rate of the specimens tested at high strain rates is much higher than the work-hardening rate of the specimens tested at low and intermediate strain rates (Figure 4.12). As seen in Figure 5.1 and Figure 5.2, this change in work-hardening rate is not captured by either constitutive model. This increase has been seen, to some extent, in the previous work on characterizing dual phase steels [63,64,66]; however, the mechanism that causes this behaviour is unknown. This behaviour is not observed in the results for the sheet specimens, which is why the accuracy of the fits to the sheet results is greater than the accuracy of the fits to the tube results.

5.3 HSLA350 CONSTITUTIVE FITS

The Johnson-Cook and Zerilli-Armstrong constitutive fits for the HSLA350 6 o'clock tube specimens are shown in Figure 5.9 - Figure 5.12. Figure 5.9 (Johnson-Cook) and Figure 5.10 (Zerilli-Armstrong) show the constitutive fits along with the results of the experiments that were performed at an initial temperature of 21 °C. Figure 5.11 (Johnson-Cook) and Figure 5.12 (Zerilli-Armstrong) show the constitutive fits along with the results of the experiments that were performed at elevated temperatures. The fits to the HSLA350 3 o'clock tube specimens are shown in Figure 5.13 (Johnson-Cook) and Figure 5.14 (Zerilli-Armstong). For the HSLA350 sheet specimens, the Johnson-Cook constitutive fit is exhibited in Figure 5.15 and the Zerilli-Armstrong constitutive fit is exhibited in Figure 5.16. The constitutive parameters for each fit and model as well as the accuracy of the fits are shown in Table 5.3 (Johnson-Cook) and Table 5.4 (Zerilli-Armstrong).

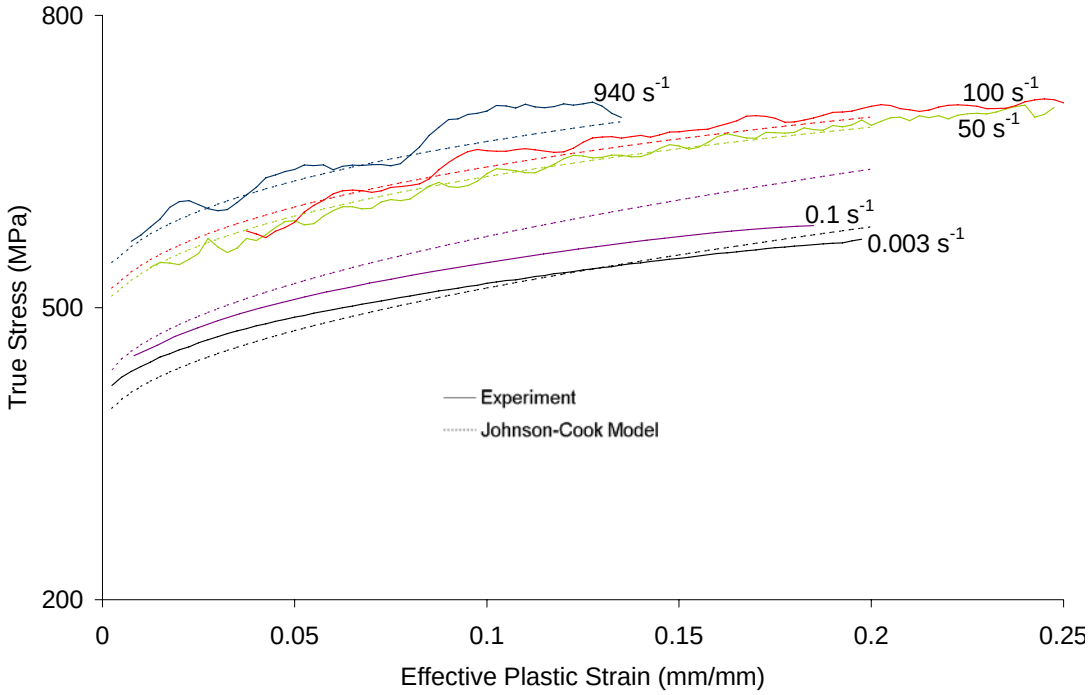

Figure 5.9. HSLA350 tube (6 o'clock) ambient temperature results fit with the Johnson-Cook constitutive model

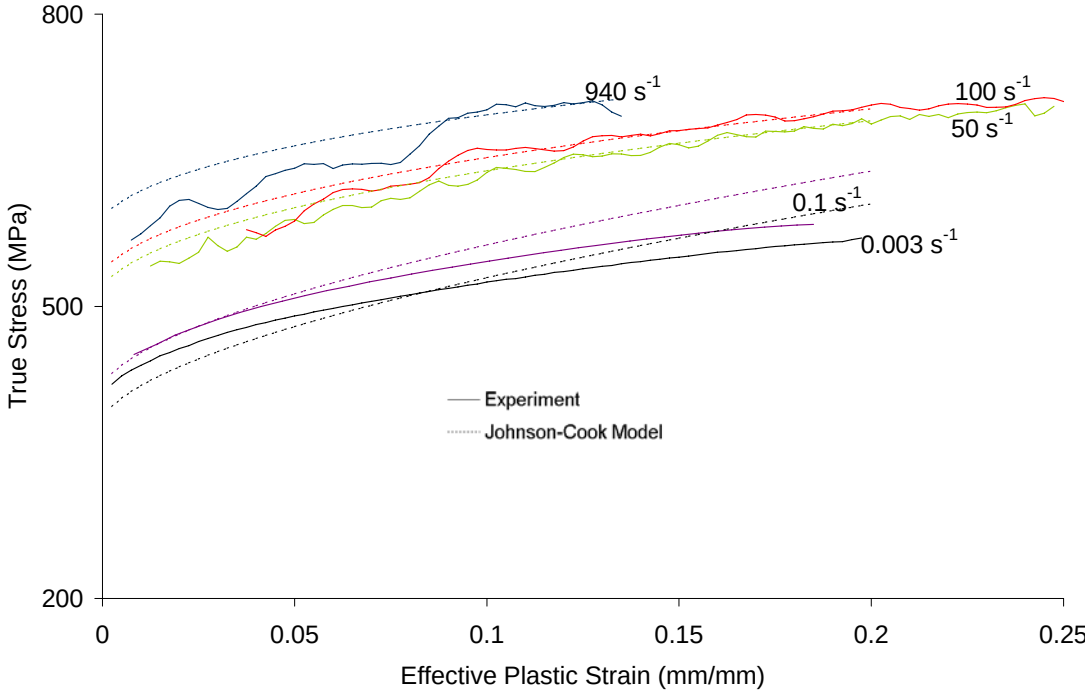

Figure 5.10. HSLA350 tube (6 o'clock) ambient temperature results fit with the Zerilli-Armstrong constitutive model

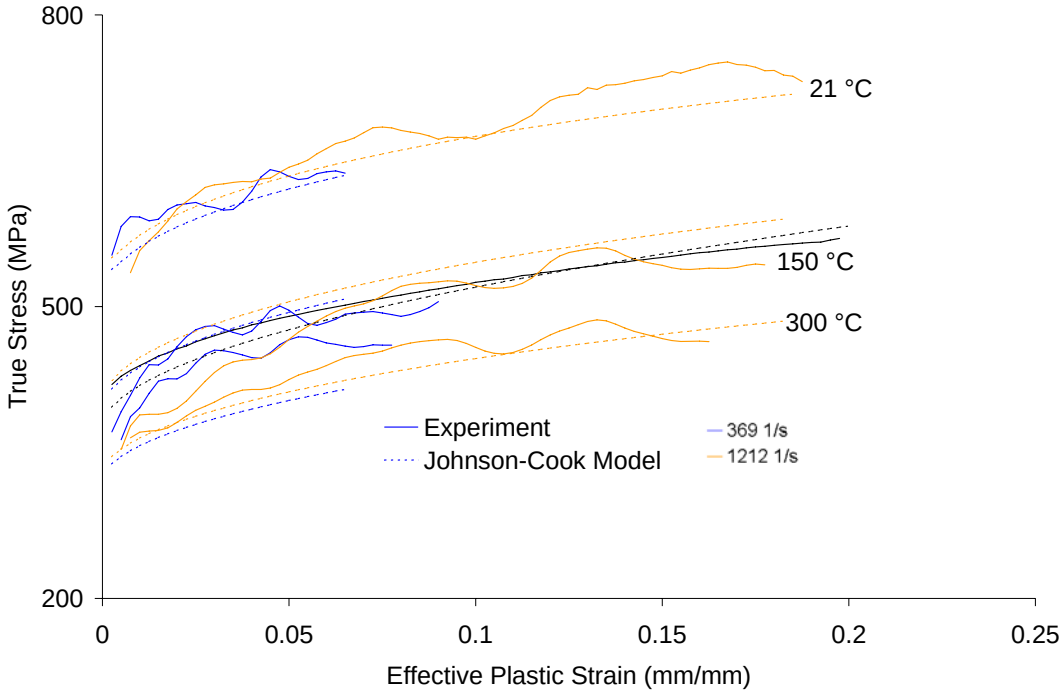

Figure 5.11. HSLA350 tube (6 o'clock) elevated temperature results fit with the Johnson-Cook constitutive model

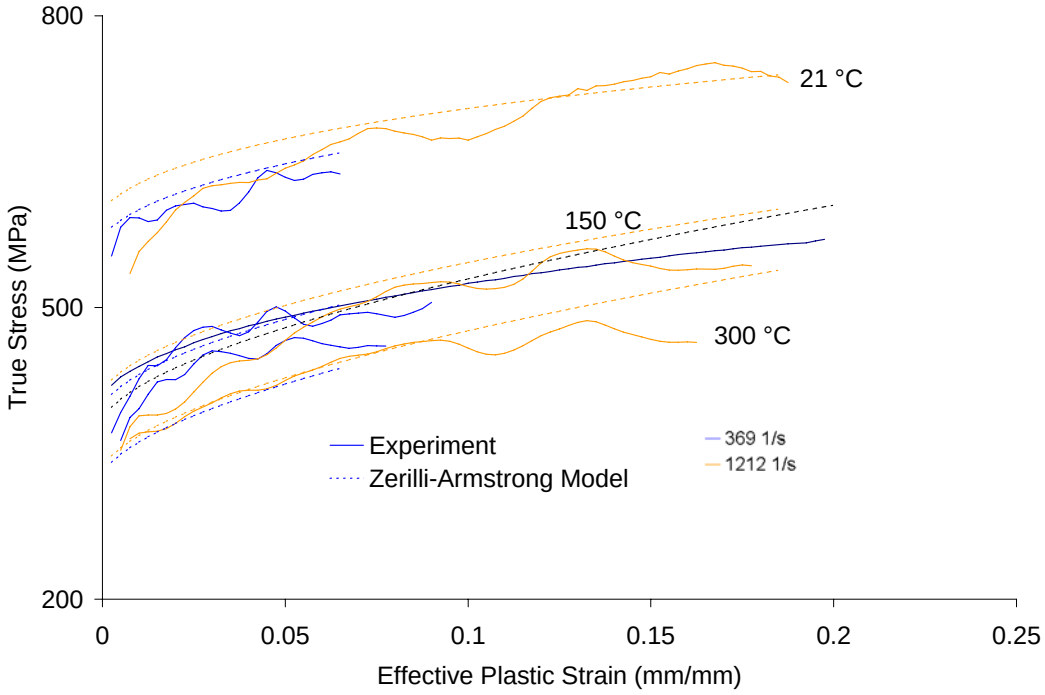

Figure 5.12. HSLA350 tube (6 o'clock) elevated temperature results fit with the Zerilli-Armstrong constitutive model

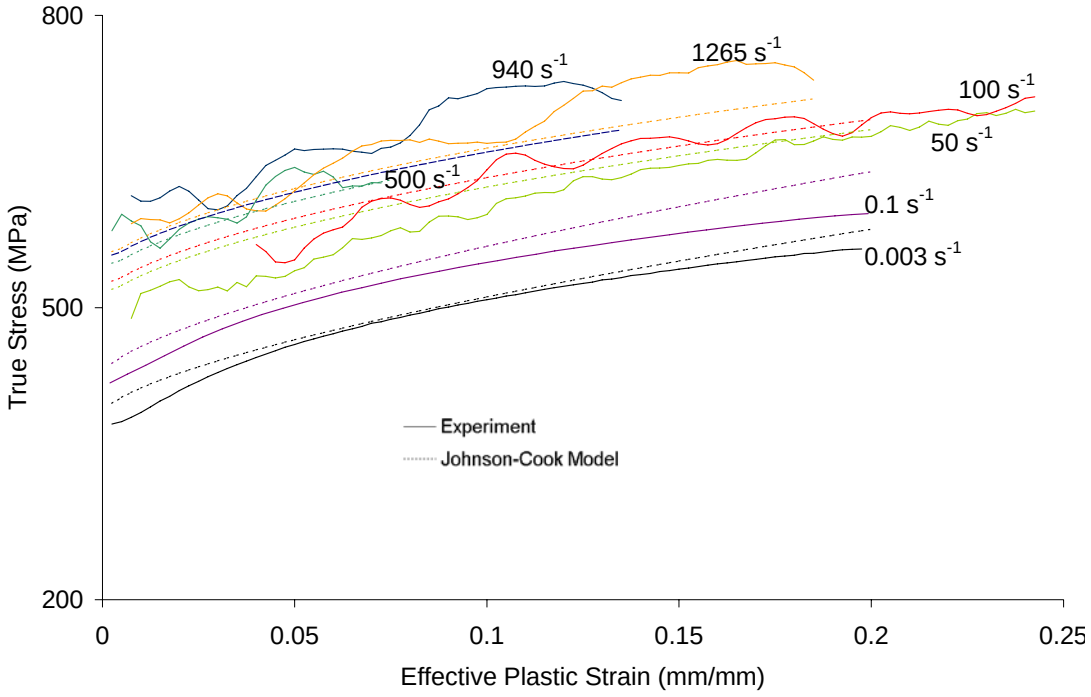

Figure 5.13. HSLA350 tube (3 o'clock) ambient temperature results fit with the Johnson-Cook constitutive model

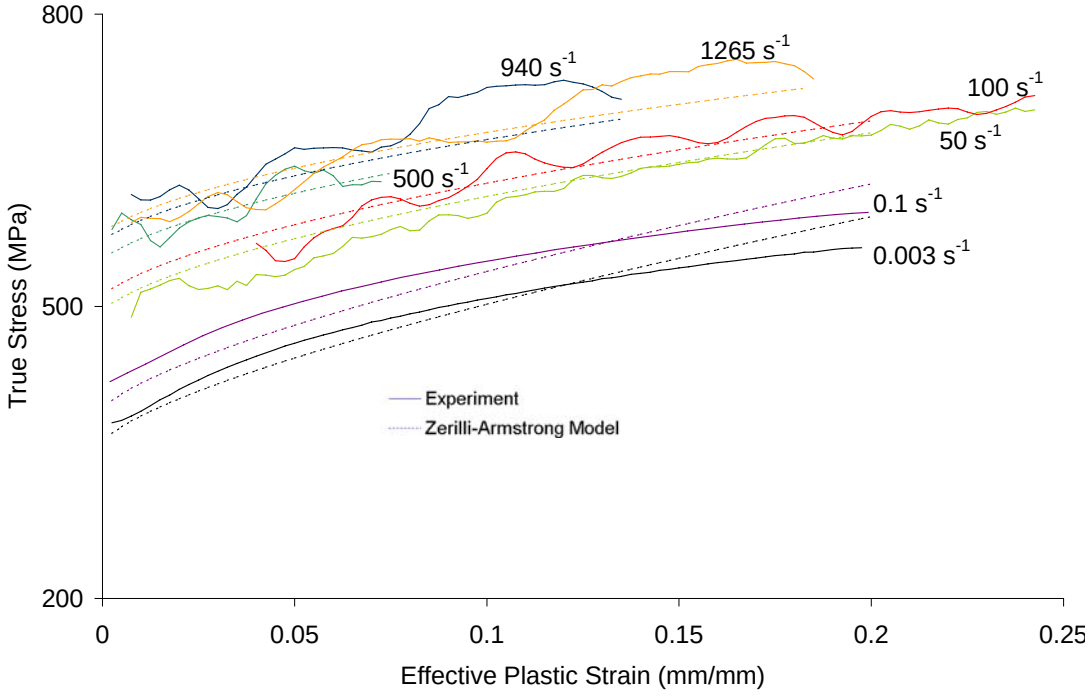

Figure 5.14. HSLA350 tube (3 o'clock) ambient temperature results fit with the Zerilli-Armstrong constitutive model

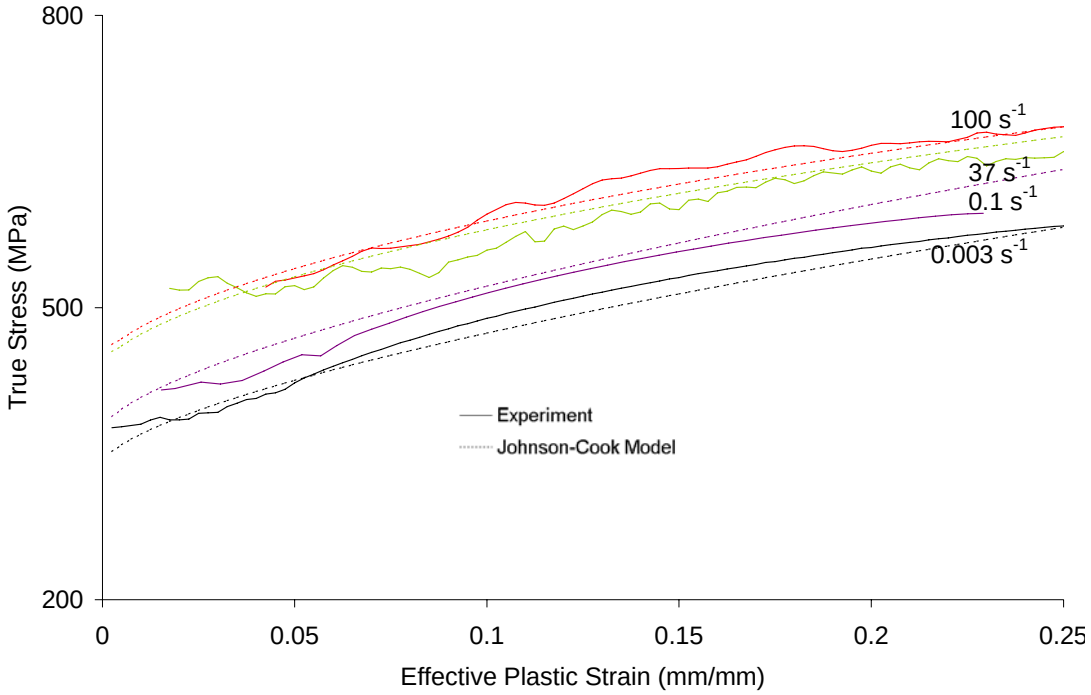

Figure 5.15. HSLA350 sheet ambient temperature results fit with the Johnson-Cook constitutive model

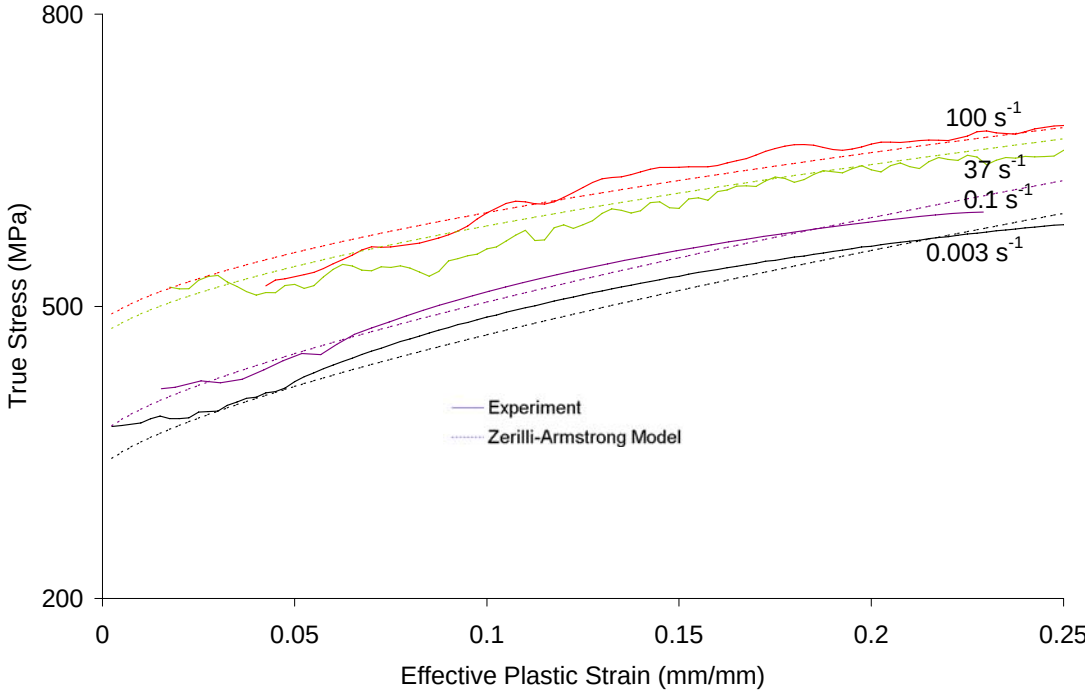

Figure 5.16. HSLA350 sheet ambient temperature results fit with the Zerilli-Armstrong constitutive model

Table 5.3. Constitutive parameters for the HSLA350 averaged curves fit with the Johnson-Cook model

	Johnson-Cook					
	A (MPa)	**B (MPa)**	**n**	**c**	**m**	**R^2**
Sheet	*399.18*	*700.94*	*0.65*	*0.0255*	*0.629*	***0.973***
(95% confidence)	*± 14.39*	*± 30.51*	*± 0.058*			
3 o'clock	*459.35*	*644.67*	*0.662*	*0.0255*	*0.629*	***0.929***
(95% confidence)	*±15.07*	*± 59.03*	*± 0.086*			
6 o'clock	*440.4*	*563.25*	*0.52*	*0.0255*	*0.629*	***0.953***
(95% confidence)	*± 17.04*	*± 28.08*	*± 0.063*	*±0.0008*	*±0.016*	

Table 5.4. Constitutive parameters for the HSLA350 averaged curves fit with the Zerilli-Armstrong model

	Zerilli-Armstrong						
	C_0 (MPa)	**C_1 (MPa)**	**C_3**	**C_4**	**C_5 (MPa)**	**q**	**R^2**
Sheet	*244.37*	*2592.32*	*0.0096*	*0.00032*	*696.85*	*0.706*	***0.976***
(95% confidence)	*± 11.45*				*± 33.56*	*± 0.057*	
3 o'clock	*269.57*	*2592.32*	*0.0096*	*0.00032*	*722.98*	*0.703*	***0.954***
(95% confidence)	*± 10.99*				*± 51.61*	*± 0.065*	
6 o'clock	*291.31*	*2592.32*	*0.0096*	*0.00032*	*584.48*	*0.594*	***0.956***
(95% confidence)	*± 20.18*	*± 727.14*	*± 0.0012*	*Negligible*	*± 37.12*	*± 0.063*	

In the case of the HSLA350 specimens, both constitutive models are equally adept at capturing the material behaviour. Also, because the work-hardening rate is not sensitive to strain rate, the constitutive fits are better for the HSLA350 tube specimens than for the DP600 tube specimens, particularly with the Johnson-Cook fit. This is illustrated in Figure 5.9 where, except for the data at 0.003 and 0.1 s^{-1}, the work-hardening rate of the specimens is matched by the model quite accurately, which implies that the Johnson-Cook model is capturing the thermal softening behaviour well; the similarity between the fit and the thermal softening is confirmed in the fit of the elevated temperature experiments (Figure 5.11). The Zerilli-Armstrong fits, shown in Figure 5.12, capture this behaviour as well. For both models, it appears that the results are captured accurately except for the experiments at 0.1 s^{-1}. For crash models, this should not have a significant effect.

The majority of the inaccuracy of the fits seems to be associated with the results of the experiments conducted at 0.1 s^{-1}. These results are only captured adequately in the fits to the sheet data (Figure 5.15 and Figure 5.16) because the TSHB experiments were not considered, which presented less of a challenge for fitting.

5.4 DDQ CONSTITUTIVE FITS

The Johnson-Cook and Zerilli-Armstrong constitutive fits for the DDQ 6 o'clock tube specimens are shown in Figure 5.17 - Figure 5.20. Figure 5.17 (Johnson-Cook) and Figure 5.18 (Zerilli-Armstrong) show the constitutive fits along with the results of the experiments that were performed at an initial temperature of 21 °C. Figure 5.19 (Johnson-Cook) and Figure 5.20 (Zerilli-Armstrong) show the constitutive fits along with the results of the experiments that were performed at elevated temperatures. The fits to the DDQ 3 o'clock tube specimens are shown in Figure 5.21 (Johnson-Cook) and Figure 5.22 (Zerilli-Armstrong). For the DDQ sheet specimens, the Johnson-Cook constitutive fit is exhibited in Figure 5.23 and the Zerilli-Armstrong constitutive fit is exhibited in Figure 5.24. The constitutive parameters for each fit and model as well as the accuracy of the fits are shown inTable 5.5 (Johnson-Cook) and Table 5.6 (Zerilli-Armstrong).

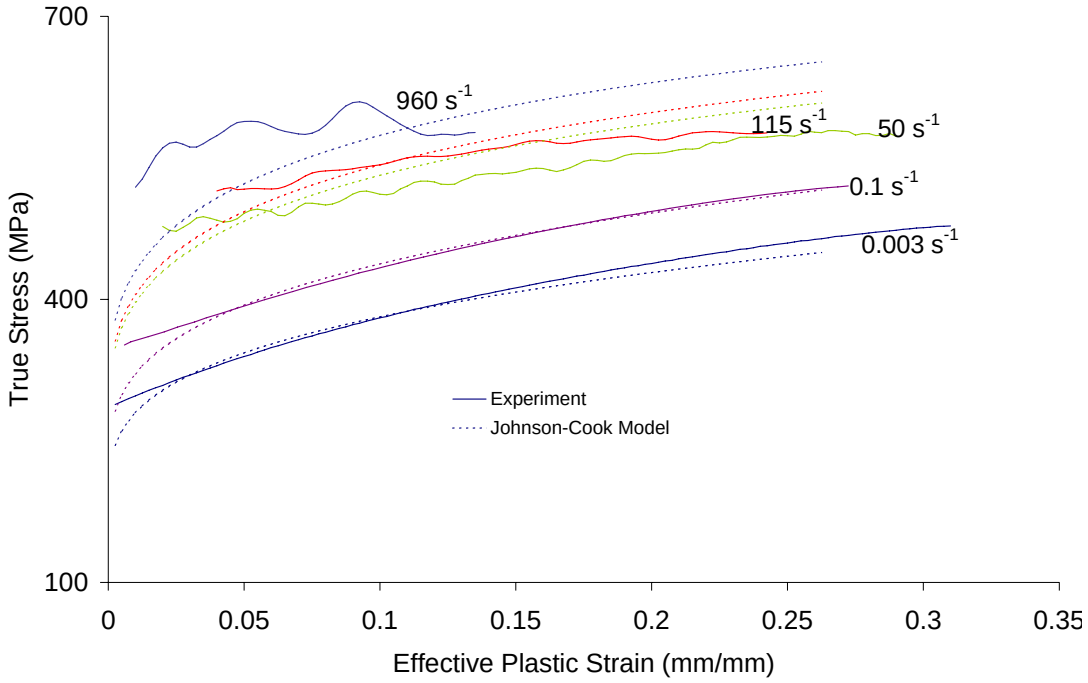

Figure 5.17. DDQ tube (6 o'clock) ambient temperature results fit with the Johnson-Cook constitutive model

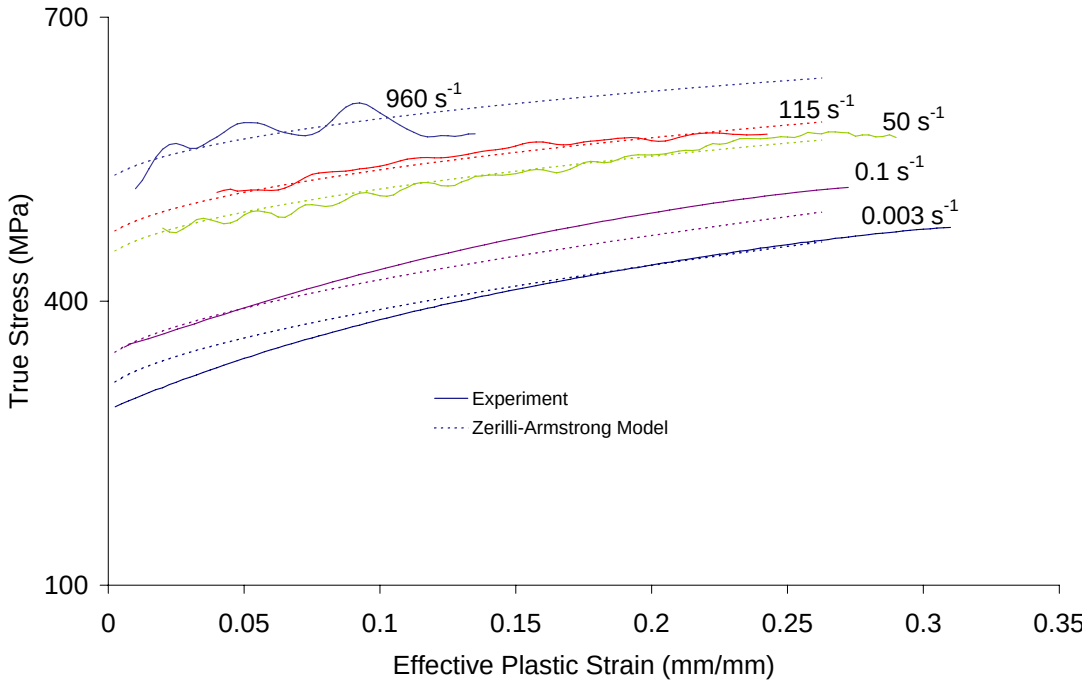

Figure 5.18. DDQ tube (6 o'clock) ambient temperature results fit with the Zerilli-Armstrong constitutive model

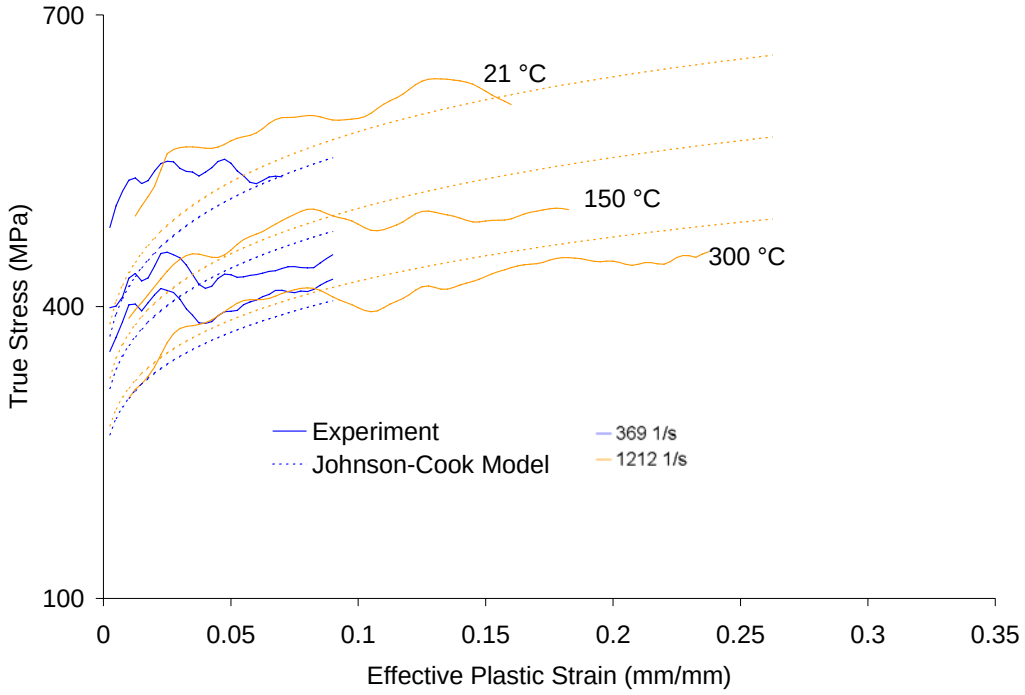

Figure 5.19. DDQ tube (6 o'clock) elevated temperature results fit with the Johnson-Cook constitutive model

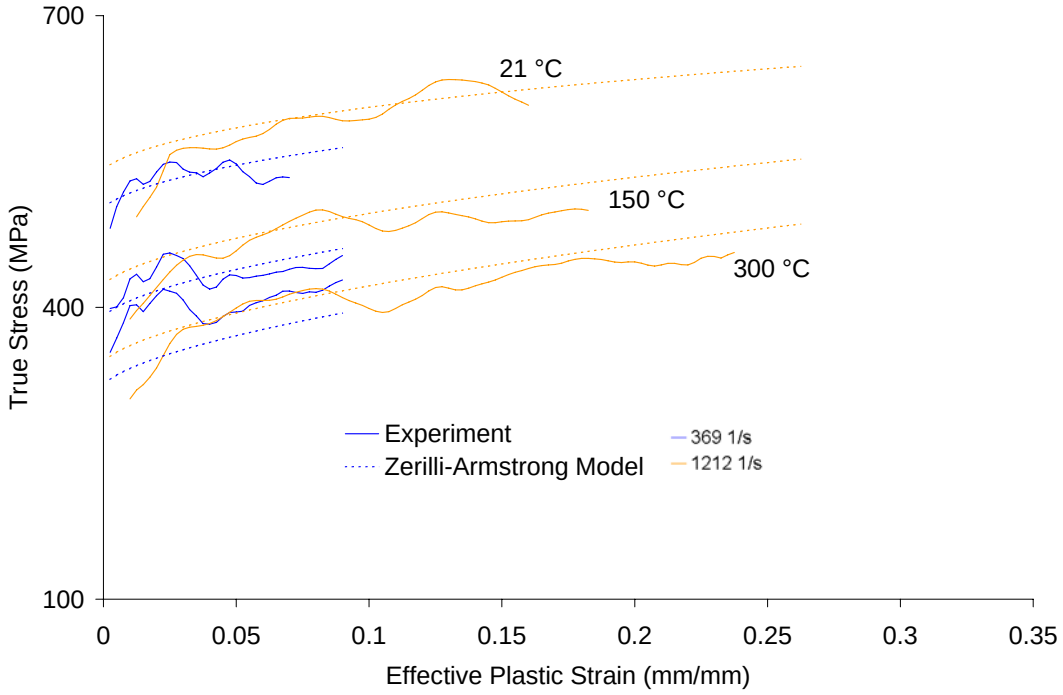

Figure 5.20. DDQ tube (6 o'clock) elevated temperature results fit with the Zerilli-Armstrong constitutive model

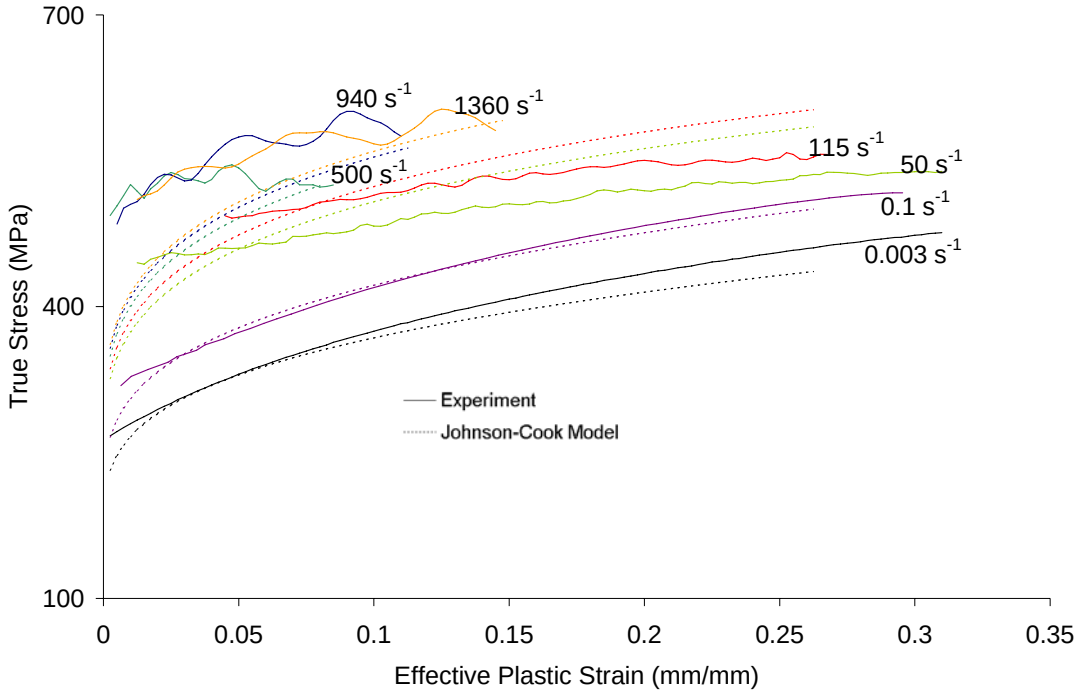

Figure 5.21. DDQ tube (3 o'clock) ambient temperature results fit with the Johnson-Cook constitutive model

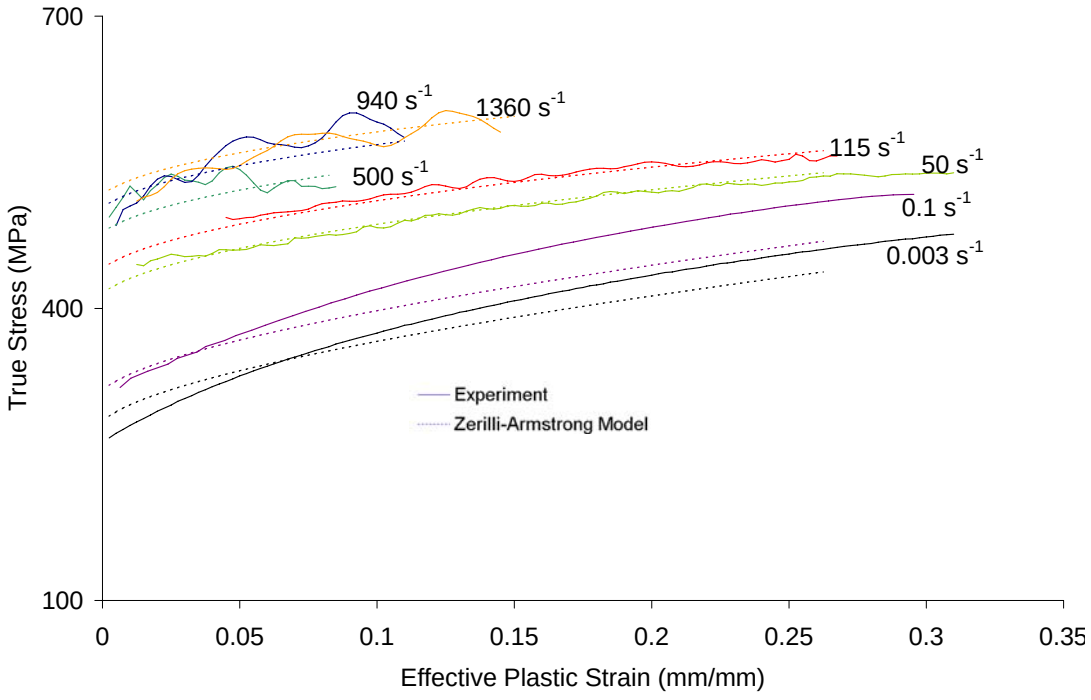

Figure 5.22. DDQ tube (3 o'clock) ambient temperature results fit with the Zerilli-Armstrong constitutive model

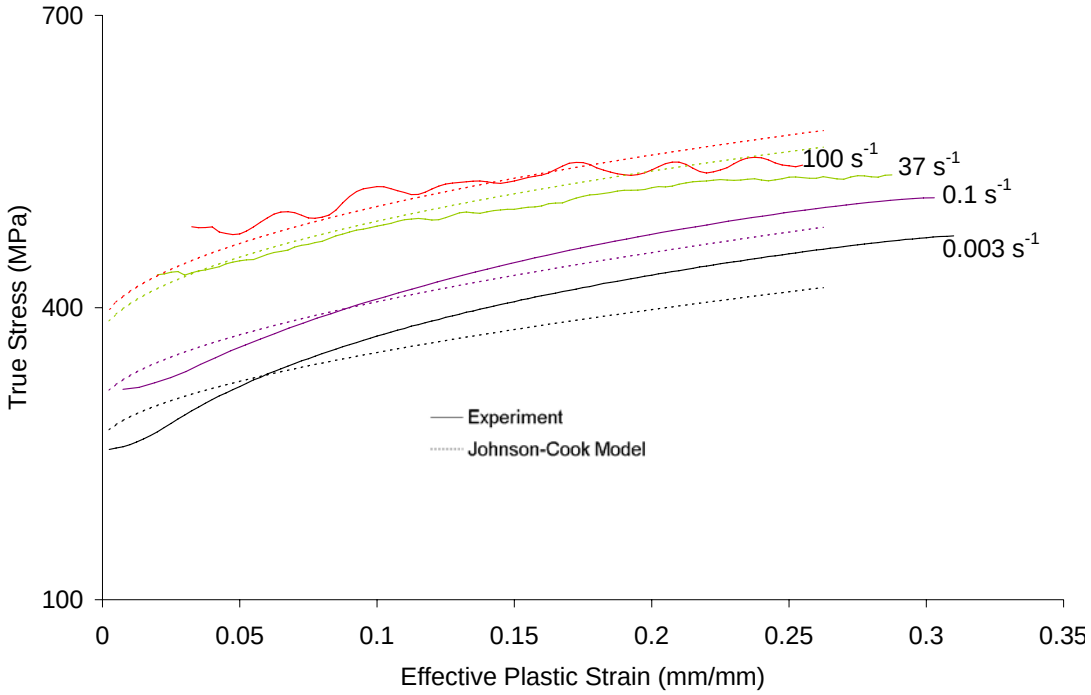

Figure 5.23. DDQ sheet ambient temperature results fit with the Johnson-Cook constitutive model

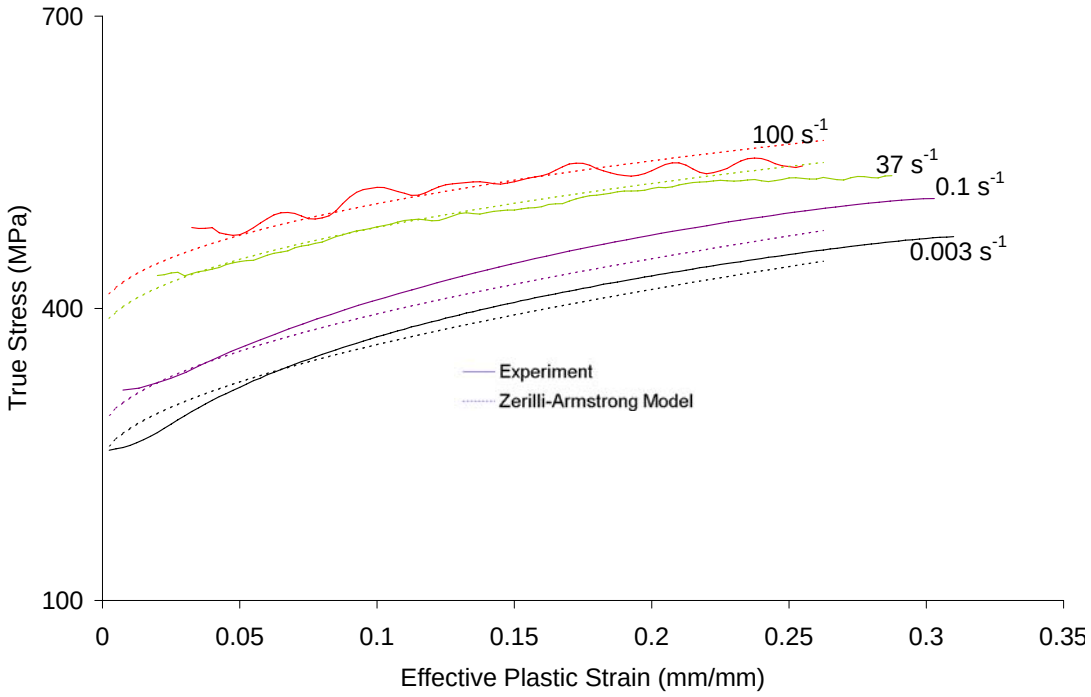

Figure 5.24. DDQ sheet ambient temperature results fit with the Zerilli-Armstrong constitutive model

Table 5.5. Constitutive parameters for the DDQ averaged curves fit with the Johnson-Cook model

	Johnson-Cook					
	A (MPa)	**B (MPa)**	**n**	**c**	**m**	**R^2**
Sheet	*330.19*	*423.18*	*0.575*	*0.0346*	*0.822*	***0.912***
(95% confidence)	*± 26.22*	*± 33.29*	*± 0.132*			
3 o'clock	*205.99*	*521.36*	*0.3*	*0.0346*	*0.822*	***0.804***
(95% confidence)	*±2.901*	*± 23.65*	*± 0.02*			
6 o'clock	*222.94*	*507.59*	*0.3*	*0.0346*	*0.822*	***0.854***
(95% confidence)	*± 32.05*	*± 28.42*	*± 0.02*	*±0.0013*	*±0.014*	

Table 5.6. Constitutive parameters for the DDQ averaged curves fit with the Zerilli-Armstrong model

	Zerilli-Armstrong						
	C_0 (MPa)	**C_1 (MPa)**	**C_3**	**C_4**	**C_5 (MPa)**	**q**	**R^2**
Sheet	*181.89*	*946.3*	*0.00688*	*0.00041*	*433.88*	*0.563*	***0.963***
(95% confidence)	*± 15.75*				*± 18.95*	*± 0.074*	
3 o'clock	*218.87*	*946.3*	*0.00688*	*0.00041*	*364.05*	*0.632*	***0.948***
(95% confidence)	*± 1.52*				*± 22.08*	*± 0.067*	
6 o'clock	*244.09*	*946.3*	*0.00688*	*0.00041*	*364.05*	*0.632*	***0.954***
(95% confidence)	*± 14.38*	*± 70.32*	*± 0.0004*	*± 0.00002*	*± 20.19*	*± 0.065*	

It is evident from these fits that the Zerilli-Armstrong model provides a better fit to the data than the Johnson-Cook model. This improved fit can be seen by comparing from - Figure 5.17 and Figure 5.18, from which it is concluded that the Zerilli-Armstrong model provides a much closer estimation than the Johnson-Cook model of the thermal softening that is associated with the drop in work-hardening rate from the low strain rate experiments to the intermediate strain rate experiments. The Zerilli-Armstrong fit also captures the behaviour of the DDQ specimens at elevated temperatures more closely than the Johnson-Cook model (Figure 5.19 and Figure 5.20).

The accuracy of the fits to the 3 o'clock tube specimen behaviour is slightly lower than for the 6 o'clock tube specimen fits for both constitutive models. The reason for this lower accuracy appears to be related to the work hardening which is imparted into the tube during forming. As illustrated in Figure 4.36 and Figure 4.43, the measured strain

rate sensitivity of the 3 o'clock and 6 o'clock tube specimens does not appear to be identical. Thus, when assigning a common strain rate sensitivity to the tube specimens, inaccuracy is inevitable; in this case, the inaccuracy is reflected in the lower quality of the fit to the 3 o'clock tube specimen results.

The fits to the DDQ sheet specimens were more accurate than the fits to the DDQ tube specimens. As with the HSLA350 results, this is misleading because, for the sheet specimens, the TSHB experiments were not considered; hence, only four averaged curves were used for the fit rather than seven or eleven for the tube specimens.

CHAPTER 6

NUMERICAL MODELING

In order to verify that the constitutive models are fit correctly to the data, finite element models of the IFWI and TSHB experiments were created. These models were then run to confirm whether the specimen load-displacement response could be reproduced. Such confirmation would lend confidence to the use of the Johnson-Cook and Zerilli-Armstrong constitutive fits in future simulation of automobile crash events. The finite element models were created using Hypermesh [99] and were solved using LS-Dyna [100].

There is an additional motivation for creating the IFWI model. In Chapter 2, a method for minimizing the oscillations in the force measurements while reaching a constant strain rate at the smallest possible strain was developed using analytical and experimental techniques. A numerical model which confirms the experimental results would further validate the testing method.

6.1 FINITE ELEMENT MODEL OF THE IFWI EXPERIMENT

The finite element model of the IFWI, along with a enlarged view of the specimen mesh, can be seen in Figure 6.1. For this simulation, the lower grip, upper grip, specimen, and load cell are modeled. The striker, silicon pads, and extra mass are not modeled for three reasons. The first reason is that, rather than modeling the striker and assigning it a displacement-time profile or initial velocity as the input for the model, a displacement-time profile can be assigned directly to the lower grip, since the lower grip displacement is measured by the ELVS during the experiment. This greatly increases the computational efficiency of the simulation. The second reason is that, due to the penalty stiffness method that is employed in LS-Dyna to deal with the contact between two

surfaces, significant high-frequency oscillations can be created at the contact interface [101]. If the striker is not modeled, these oscillations do not have to be accounted for. The last reason is that the silicon pads would need to be characterized if they were included. Such characterization was considered beyond the scope of this work.

In order to verify that the experimental values can be reproduced, the measured displacement-time profile of a DP600 sheet specimen (Figure 6.2) was used as the boundary input for the motion of the lower grip and the resultant force was obtained from an element in the load cell. This force was then compared to the experimentally measured force (Figure 6.3).

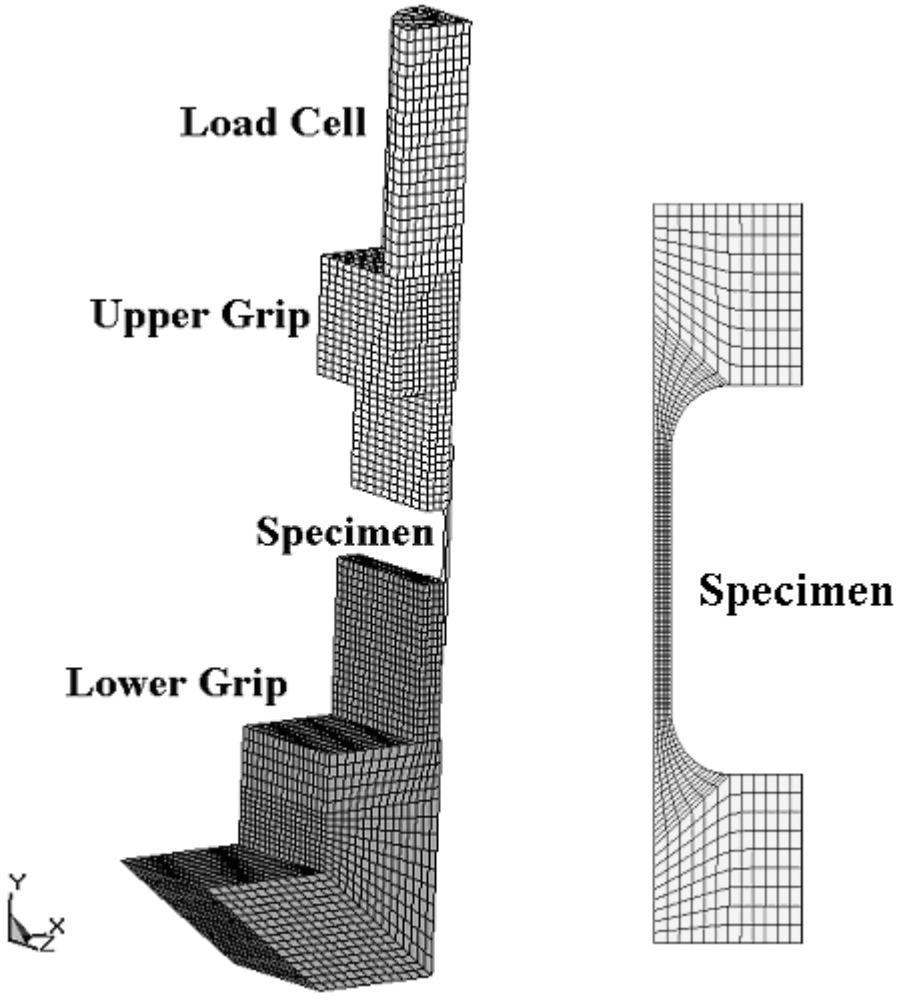

Figure 6.1. Mesh of the IFWI finite element model

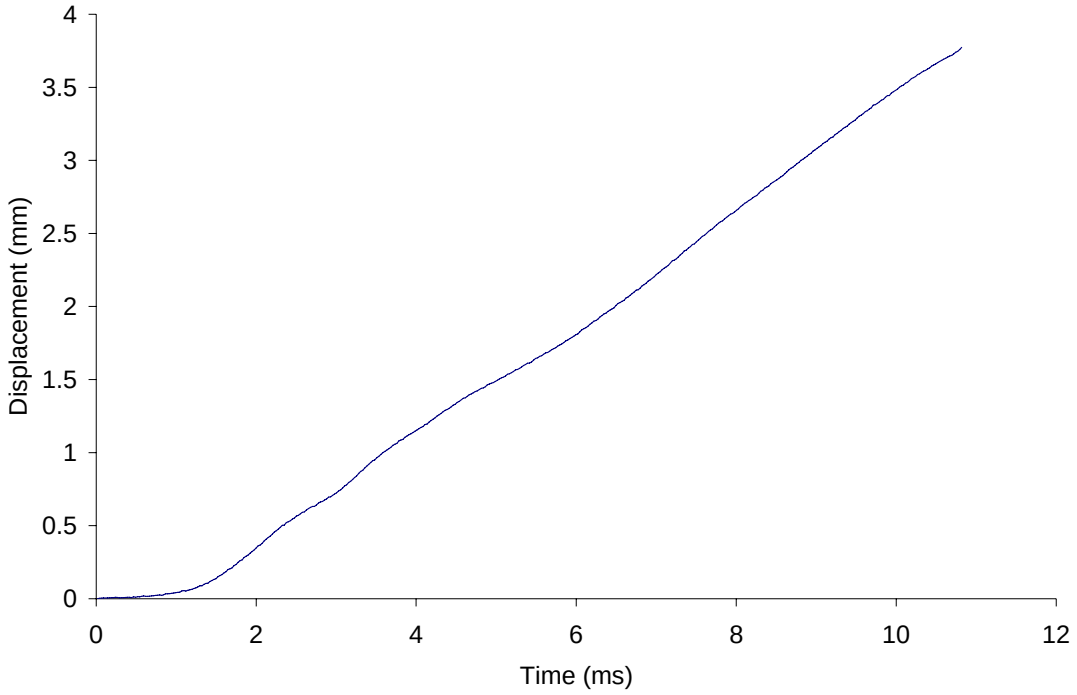

Figure 6.2. Displacement profile of the lower grip during a 30 s^{-1} experiment on DP600 sheet.

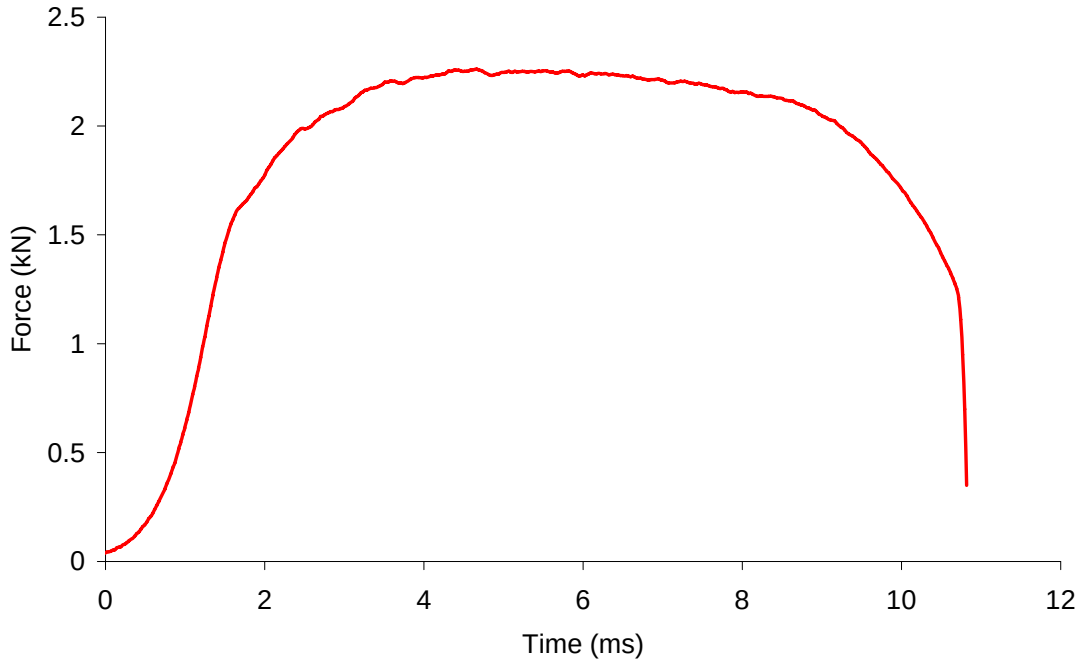

Figure 6.3. Force versus time measured during a 30 s^{-1} experiment on a DP600 sheet specimen.

Each of the four components were meshed using fully integrated brick elements (element type 1). The lower grip, upper grip, specimen, and load cell contain 8245, 1950, 2550, and 1008 elements respectively. The lower grip, upper grip, and load cell were modeled as elastic materials; the lower grip as titanium, the upper grip as steel and load cell as a piezoelectric material. The elastic modulus and density of the load cell were set to match the natural frequency of the load cell (2.807 kHz). This was done using equation 6.1, where E is the elastic modulus, L is the length, and ρ is the density of the load cell. The specimen was modeled using both the Johnson-Cook and Zerilli-Armstrong material models with the constitutive parameters fit to the DP600 sheet results. The complete LS-Dyna input deck is given in Appendix C.

$$\omega_n = \sqrt{\frac{k}{m}} = \sqrt{\frac{E}{L^2 \rho}} \qquad (6.1)$$

The model was run for a duration of 15 ms, which corresponds to the approximate duration of the experiment. The base units of mm, ms, and grams were used, which means that the force was calculated in Newtons and the stress was calculated in MPa. The reference strain rate in the constitutive models was 0.001 ms^{-1} because of the unit system.

A quarter-model was used to take advantage of the symmetric nature of the experiment. In order to accomplish this, the model was cut in half twice; once along the XY-plane and once along the YZ-plane (Figure 6.1) and standard symmetry conditions were prescribed. The nodes at the upper most point of the load cell (where Y is greatest), were completely fixed.

6.2 IFWI FINITE ELEMENT MODEL RESULTS

In order to assess whether the experimental results can be reproduced, the force in the simulated load cell must match the force measured in the experiment. The level of agreement can be seen in Figure 6.4, where the experimental and numerical stress versus time values are shown. It can be seen that the experimental and numerical results match reasonably well. The numerical model incorporating the Zerilli-Armstrong constitutive equation predicts a stress which is slightly smaller than the corresponding model using the Johnson-Cook constitutive equation and the experimental results. This is expected, given that the stress predicted by the Zerilli-Armstrong model is smaller at 30 s^{-1} than the others (Figure 5.5 and Figure 5.6). There are also some slight differences in the rise time of the predicted and measured response, possibly due to neglecting the RTV silicon pads in the models. This should be verified in future work. However, from these results, it can be concluded that the experimental predictions are accurate and that the constitutive models are being used correctly.

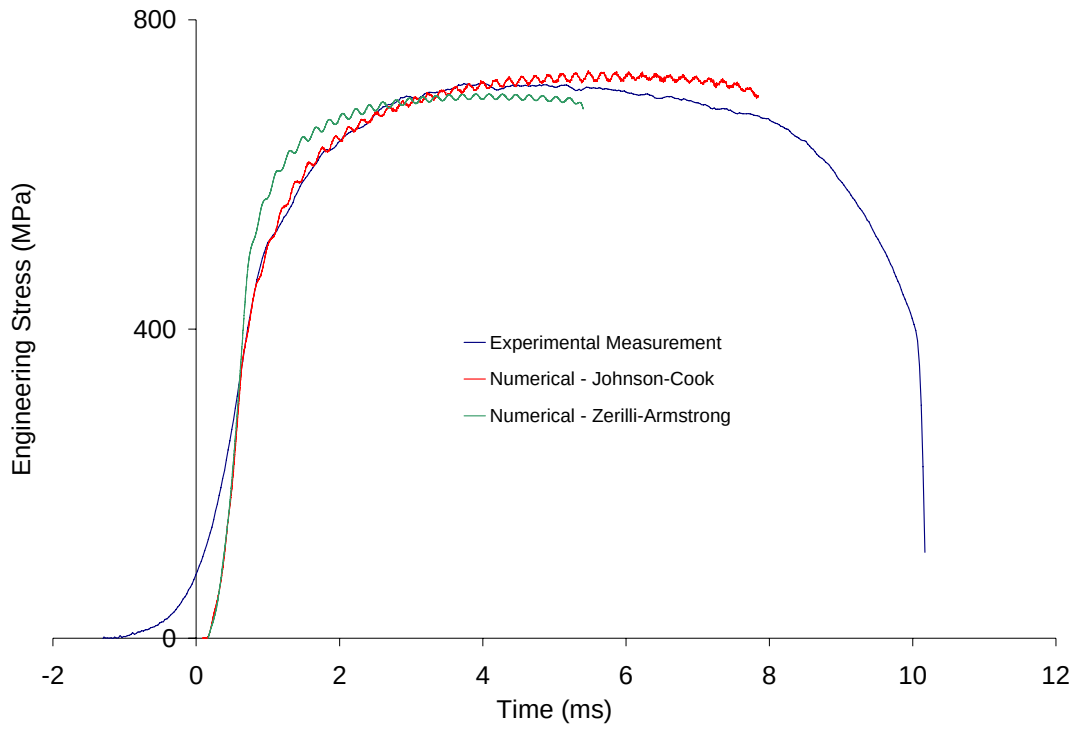

Figure 6.4. Stress vs. time for IFWI experimental measurements and numerical calculations

The other important aspect of the model is to validate the experimental method for minimizing the oscillations in the measured force signal, as outlined in Chapter 2. In order to accomplish this, the numerical force-time response of the specimen should correspond to the analytically determined result.

The initial portion (time < 0.5 ms) of the experimental and numerical force-time response is different, yet they both result from the same displacement-time input conditions. The difference in shape likely occurs because the RTV silicon pads are not modeled.

As seen in Chapter 2, the shape of the initial rise in force affects the amplitude of the oscillations in the data. From the IFWI model, it can be seen that the amplitude of the initial rise behaviour is equal to the amplitude of the oscillations throughout the experiment. This is shown in Figure 6.5, where the amplitude of the theoretical function (0.0085 kN) matches the amplitude of the oscillations in the rest of the force – time response.

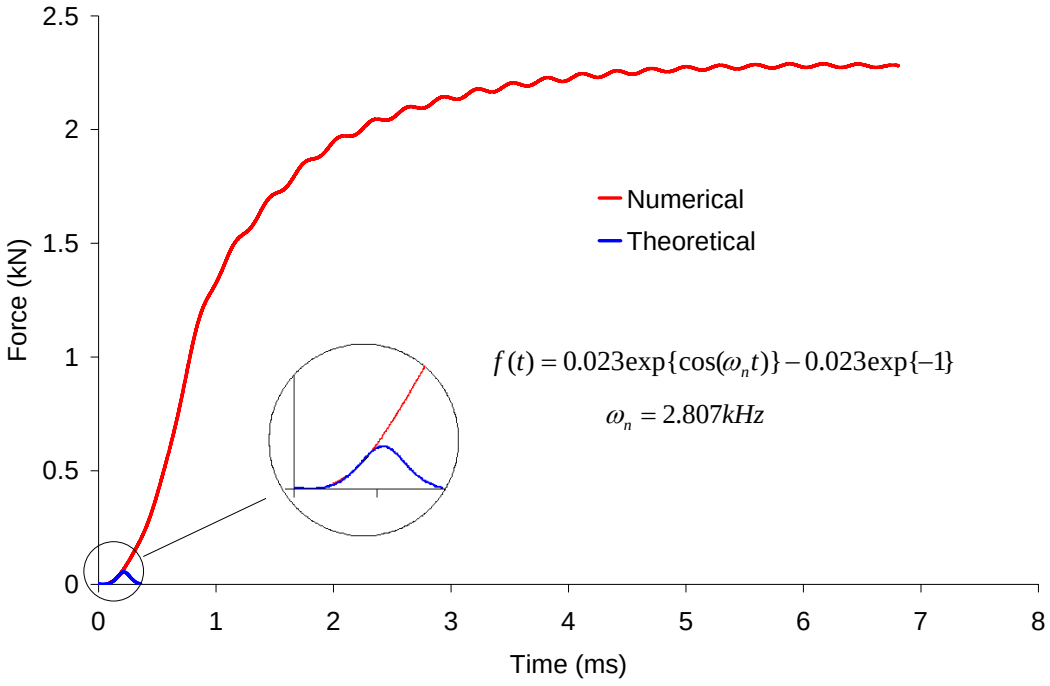

Figure 6.5. Force vs. time for the numerical and theoretical predictions of the IFWI experimental results

In Chapter 3, the apparent elastic modulus found during the intermediate and high rate experiments was discussed. It was found that the elastic modulus of the specimen was significantly smaller during IFWI experiments than during the low strain rate experiments. This drop in elastic modulus is a testing artifact, and should not be used to determine constitutive data. Evidence of this is shown in Figure 6.6, where the engineering stress – strain results calculated from the numerical model are plotted. The elastic modulus from the model was found to be 102.5 GPa. To calculate the plastic strain for this result, the engineering strain would have to be offset by 0.21%.

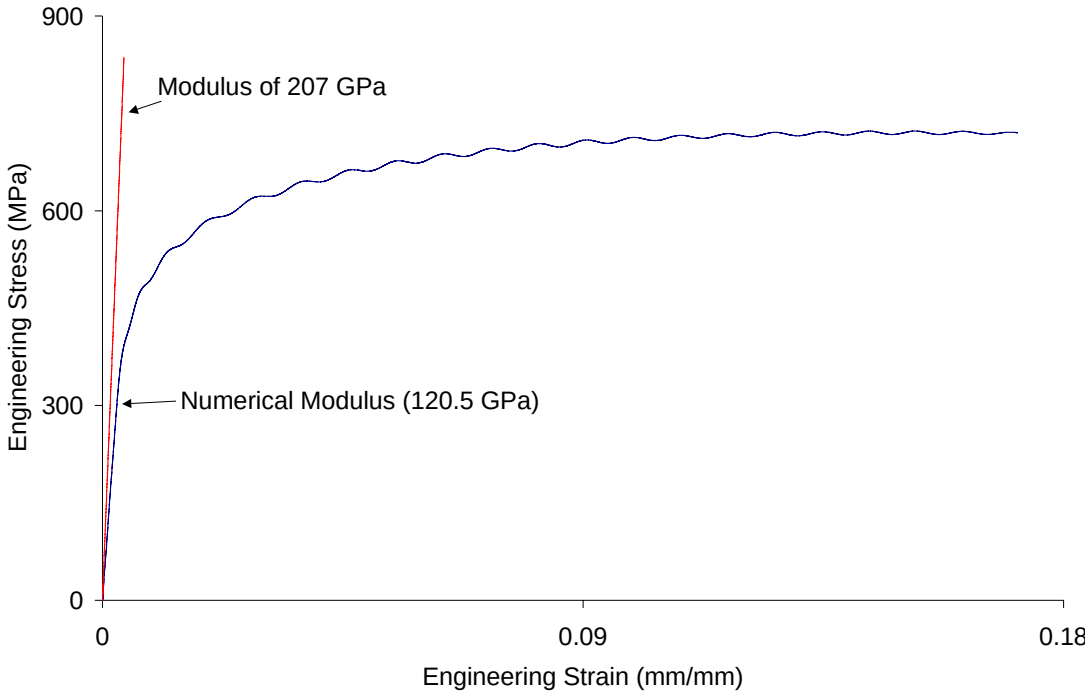

Figure 6.6. Comparison of the numerically determined and actual elastic modulus

6.3 FINITE ELEMENT MODEL OF THE TSHB EXPERIMENT

The finite element model of the TSHB is shown in Figure 6.7. A magnified view of the specimen and bars is shown in Figure 6.8, a magnified view of the specimen mesh is shown in Figure 6.9, and a cross-section of the bar mesh is shown in Figure 6.10. For simulation purposes, only the incident bar, specimen, and transmitted bar are modeled.

Rather than model the striker and end-cap (and deal with the aforementioned contact issues), the nodes at the free end of the incident bar (labeled as the boundary node set in Figure 6.7) were assigned a velocity-time profile that was derived from the experimental results of the tests on a DP600 sheet specimen at 812 s^{-1}. This profile can be seen in Figure 6.11, where the velocity rises to a relatively constant value of 6.15 mm/ms. The duration of the boundary velocity condition is about 0.258 ms, which is the duration of the incident and reflected pulse.

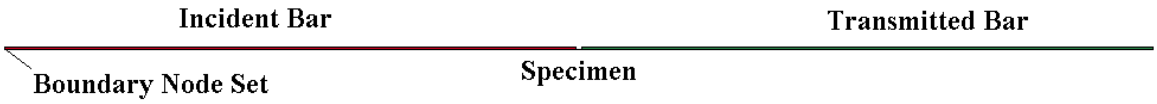

Figure 6.7. TSHB finite element model

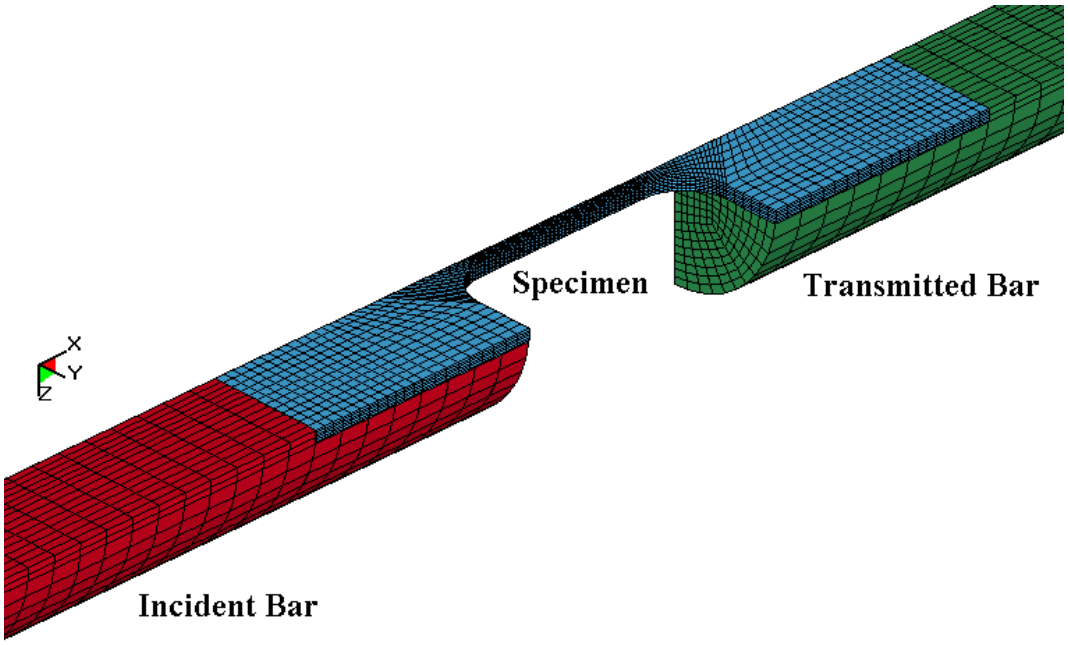

Figure 6.8. Magnified view of the TSHB model at the specimen-bar interfaces

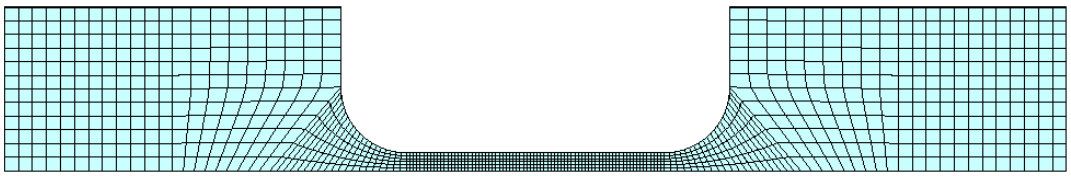

Figure 6.9. Specimen mesh

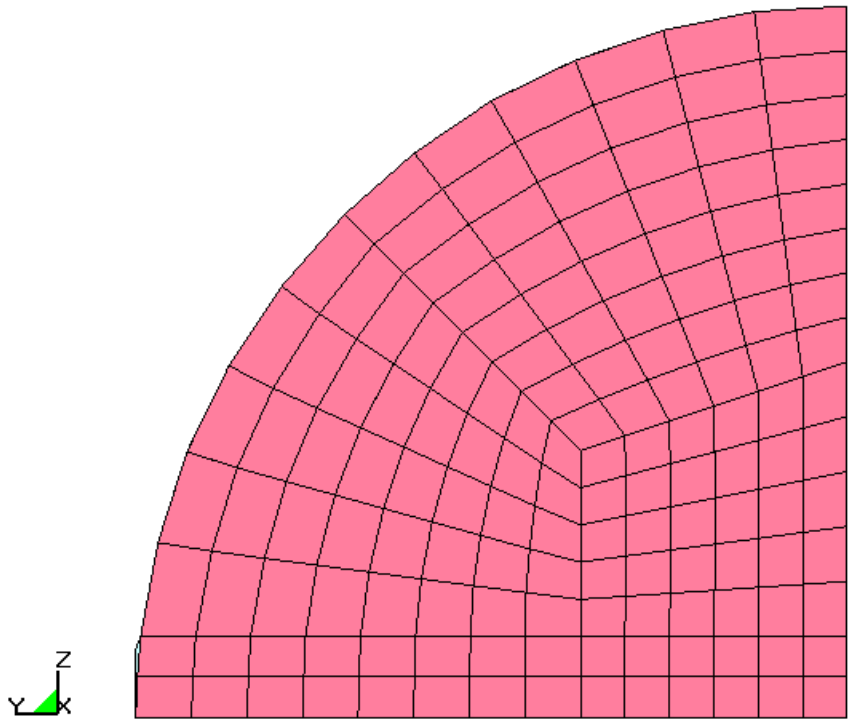

Figure 6.10. Mesh of the incident and transmitted bar cross-section

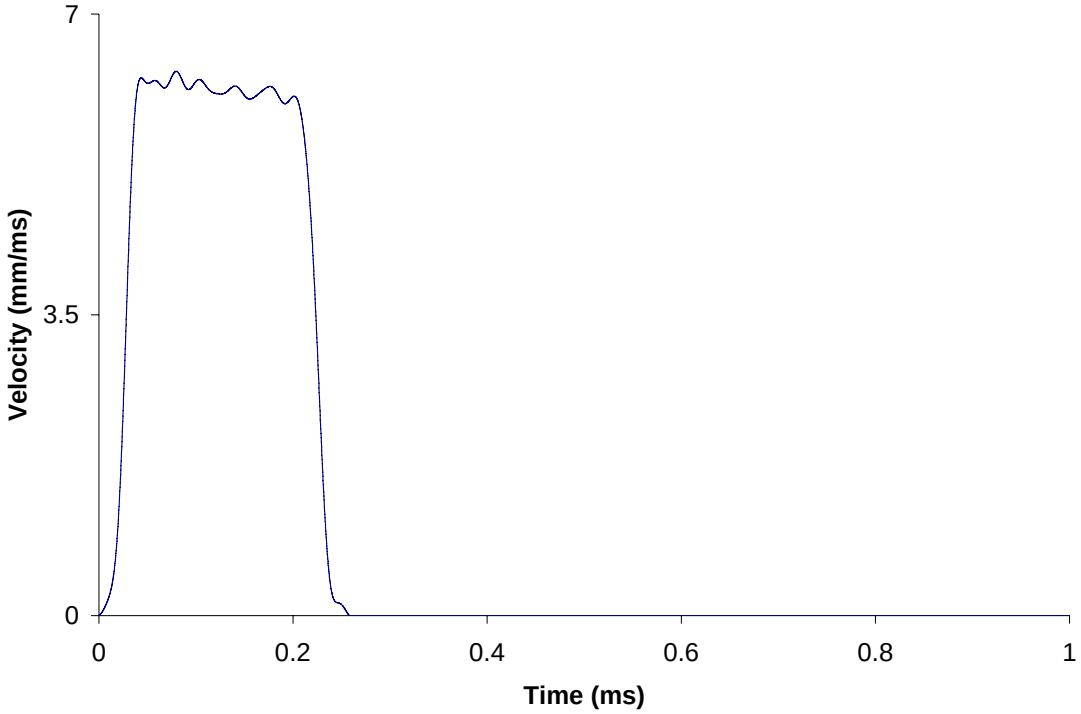

Figure 6.11. Velocity-time input for the TSHB boundary nodes

As with the IFWI model, all of the components are meshed using brick elements. The incident and transmitted bar are each modeled using 150,594 elements. Each element has a length of 2 mm. The specimen is meshed with 2,550 elements, which is the same as in the IFWI model. The model was run for a duration of 1 ms, corresponding to the duration of the experiment.

The incident and transmitted bar are characterized as elastic with the density and elastic modulus of Al 6061. The specimen was modeled using the Johnson-Cook and Zerilli-Armstrong constitutive parameters for the DP600 sheet specimens.

As with the IFWI, a quarter-model was used to take advantage of the symmetric nature of the experiment. Because neither of the bars are fixed in the experiment, no constraints are imposed in the axial direction of the bars (other than the prescribed velocity at the end of the incident bar).

6.4 TSHB FINITE ELEMENT MODEL RESULTS

In order to validate the experimental results, the incident, reflected, and transmitted waves from the numerical model should match those measured during the experiment. The incident wave time history is a direct function of the prescribed velocity at the end of the incident bar. It is the reflected and transmitted waves that will depend on the specimen properties and constitutive model.

The measured and predicted incident and reflected waves can be seen in Figure 6.12. The transmitted waves are shown in Figure 6.13. Excellent agreement is seen between the two incident waves, which confirms that the prescribed boundary condition is accurate.

The magnitude of the predicted reflected wave using both models is larger than that measured in the experiments. Based on TSHB theory (Equations 1.4-1.6), this discrepancy implies that the strain rate generated in the simulation will exceed that in the actual experiment. The reason for this discrepancy is largely due to the small difference in magnitude between the experimental and numerical incident waves. Sources of momentum loss in the experiments (friction between the incident bar and bushings, wave dispersion, etc.) may also contribute to the discrepancy.

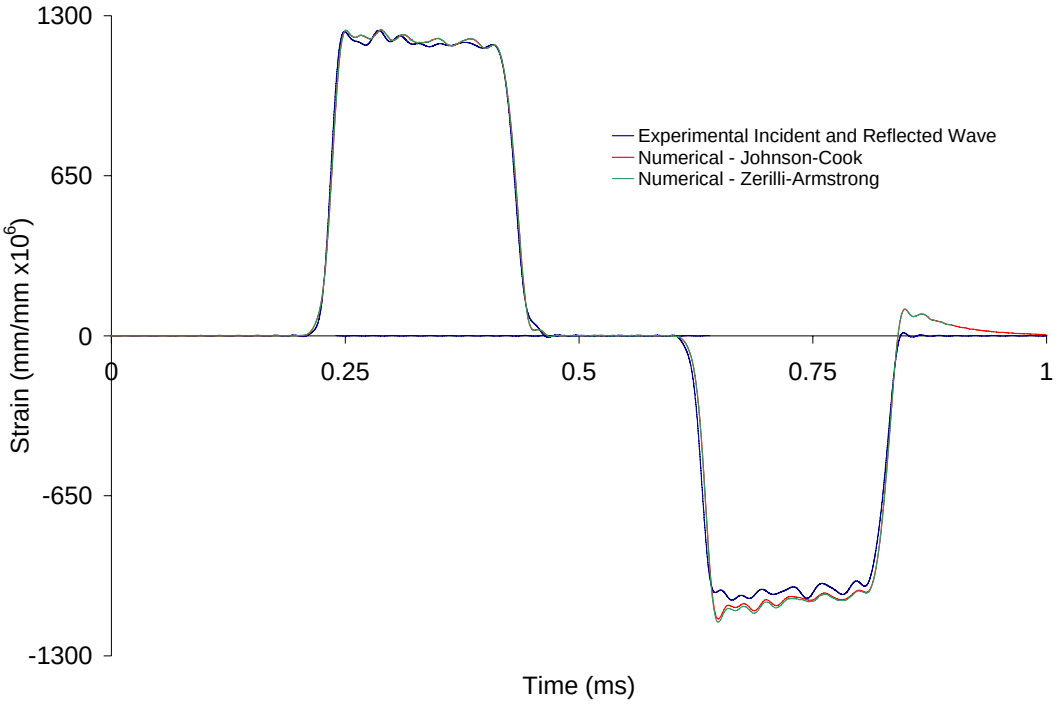

Figure 6.12. Measured and predicted waves: incident and reflected wave

The measured and predicted transmitted waves match relatively closely as well, suggesting that the numerical model accurately predicts the experimental results. The close match between the experiment and model is expected, since the material behaviour was fit closely by both constitutive models (Figure 5.5 and Figure 5.6)

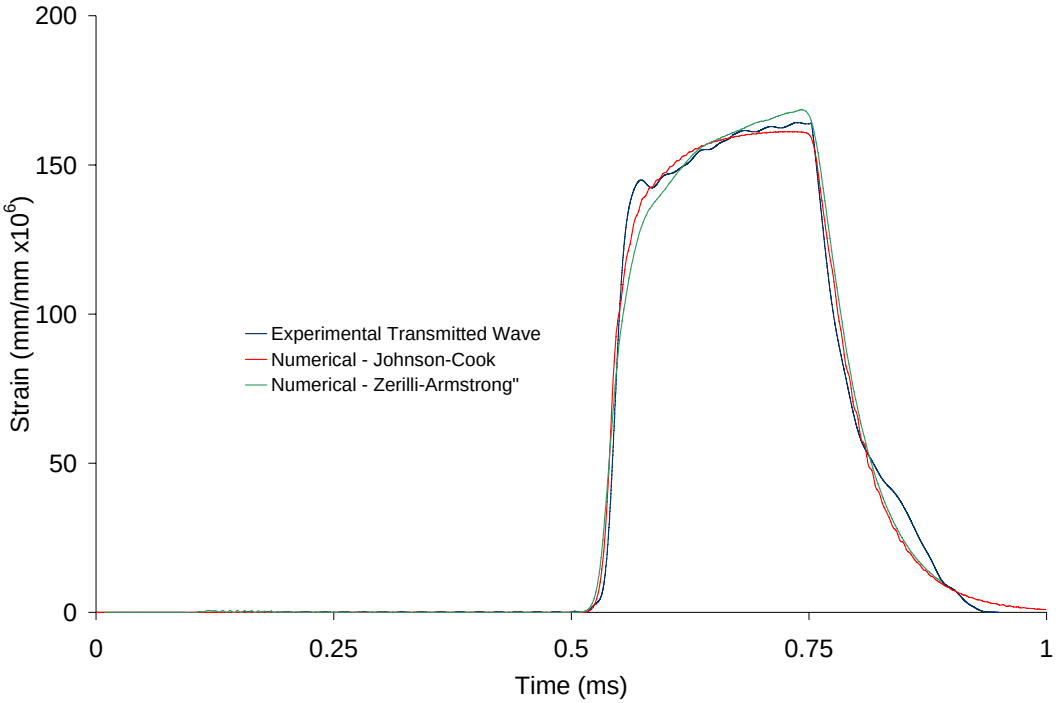

Figure 6.13. Measured and predicted waves: transmitted wave

Due to conservation of momentum, the transmitted and reflected waves should sum to equal the incident wave. The sum of the predicted reflected and transmitted waves, along with the predicted incident wave is shown in Figure 6.14 for the model that used the Zerilli-Armstrong equation. In general, however, there is excellent agreement between the model and the experiment, suggesting that the constitutive model has been applied correctly.

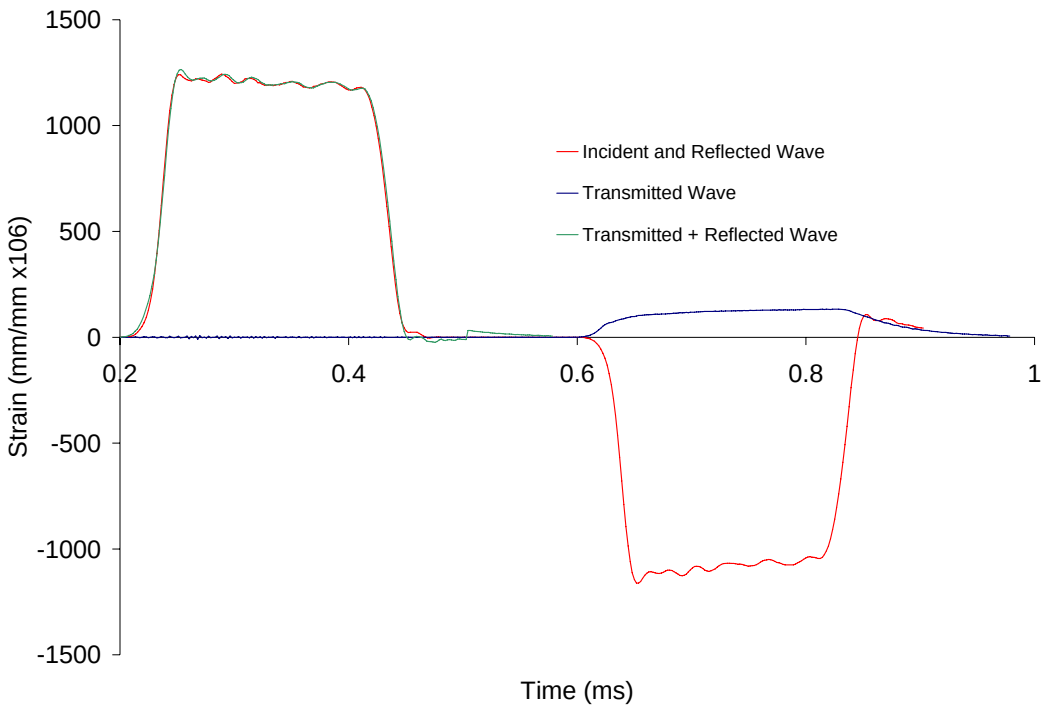

Figure 6.14. Comparison of the predicted incident wave with the added transmitted and reflected waves using the Zerilli-Armstrong constitutive model

Another point to consider is that, during the experiment, the specimen did not fail during the first loading pulse. This was also predicted in the model, as seen in Figure 6.15, even though failure was not considered in the constitutive model. No necking is observed in the specimen during the unloading portion of the pulse (after 0.225 ms have elapsed).

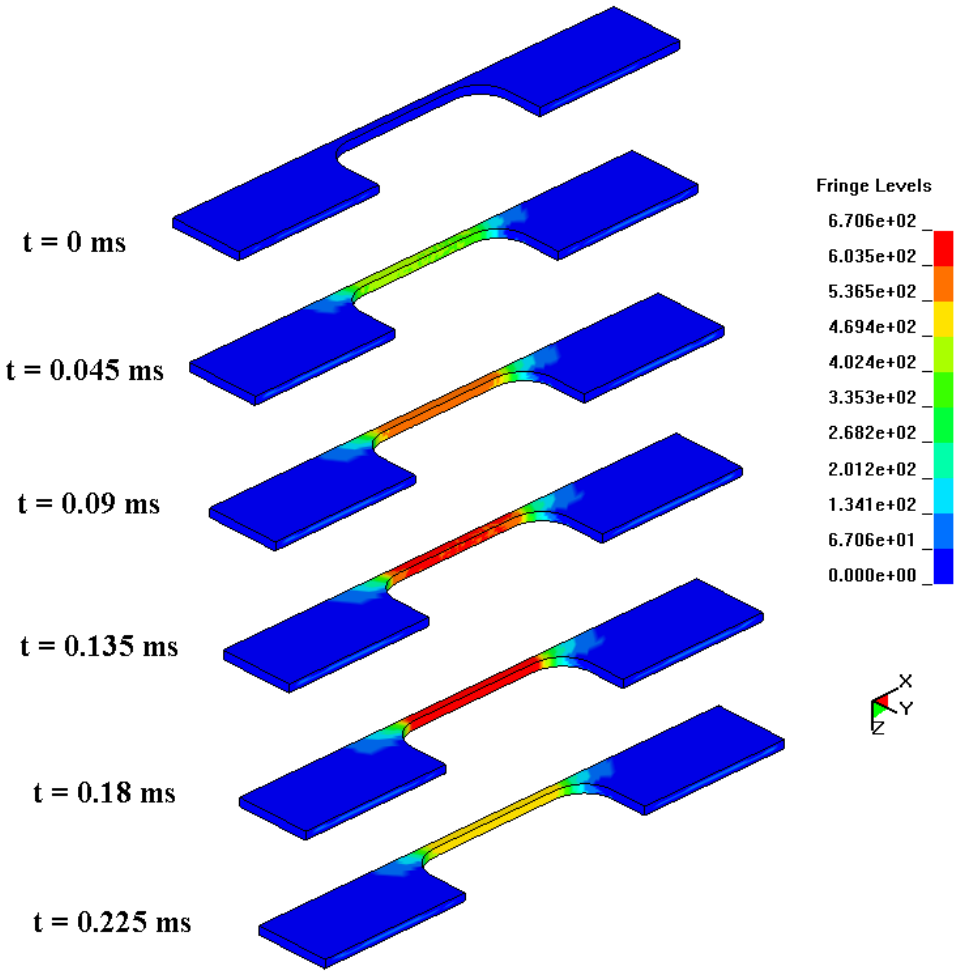

Figure 6.15. Predicted stress levels in the TSHB specimen

CHAPTER 7

DISCUSSION

In order to carry out the experiments at intermediate strain rates, an experimental method was developed using an IFWI. The crux of this method is to obtain uniaxial tensile strengths of the test specimens at as constant a strain rate as possible while ensuring that the strength measurements were not obscured by transient oscillations. Minimization of the transient oscillations was achieved by using pads made of RTV silicon to dampen the impact of the striker on the lower grip. A similar method was employed by Hsiao and Molina [35] for obtaining IFWI force measurements. The minimum acceptable thickness of the pads, corresponding to the minimum strain at which a constant strain rate is reached, was determined experimentally.

For the HSLA350 and DDQ sheet specimens, the magnitude of the transient oscillations was greater than for the other specimens because of the large upper-to-lower yield stress ratio seen in the results of the intermediate strain rate experiments. The sudden drop in strength from the upper to lower yield stress caused a discontinuous input to the load cell, which caused the load cell measurements to oscillate about the actual value. This behaviour was not observed in the DP600 sheet specimens or any of the tube specimens. The effect of discontinuous inputs on IFWI force measurements is discussed in greater detail by Williams and Adams [50].

The upper yield stress, seen in the HSLA350 and DDQ sheet specimens, was amplified tremendously in the TSHB experiments. This effect is similar to that seen in the results of Xue *et al.* [27], Nemat-Nasser [20], and Bassim [26] for experiments on HSLA steels. Nemat-Nasser speculated that the amplified yield stress might be due to dynamic strain aging. In the current work, the upper yield stress and discontinuous yielding accounted for over 70% of the TSHB experiment duration, which rendered the results unusable for constitutive modeling. The other trend seen for these specimens in the TSHB

experiments is that the time that is necessary for the Luder's band to propogate across the gauge length of the specimen does not change as the strain rate changes. This trend suggests that the maximum velocity of the Luder's band was reached.

Constitutive parameters for both the Johnson-Cook and Zerilli-Armstrong models were determined based on the results of all of the steels in both sheet and tube form. It was found that the accuracy of the fit using the Zerilli-Armstrong model was generally superior to that of the Johnson-Cook model fit. The reason for the difference in accuracy is that the Johnson-Cook model was less able to capture the thermal softening behaviour of the steels, with the exception to this being the HSLA350 response. The parameters for both models fit the HSLA350 results with the same accuracy. The fits for the tube specimens of each steel were applied successfully by Grantab [93] in modeling the crash behaviour of hydroformed subframe axial crush rails.

A positive strain rate sensitivity was obtained for each of the steels considered in this research (Figure 7.1). It was found that, as the strength of the steel increased, the strain rate sensitivity decreased. For an increase in strain rate from 0.003 to 100 s^{-1}, the corresponding increase in strength at 10% strain was found to be approximately 170, 130, and 110 MPa for DDQ, HSLA350, and DP600, respectively.

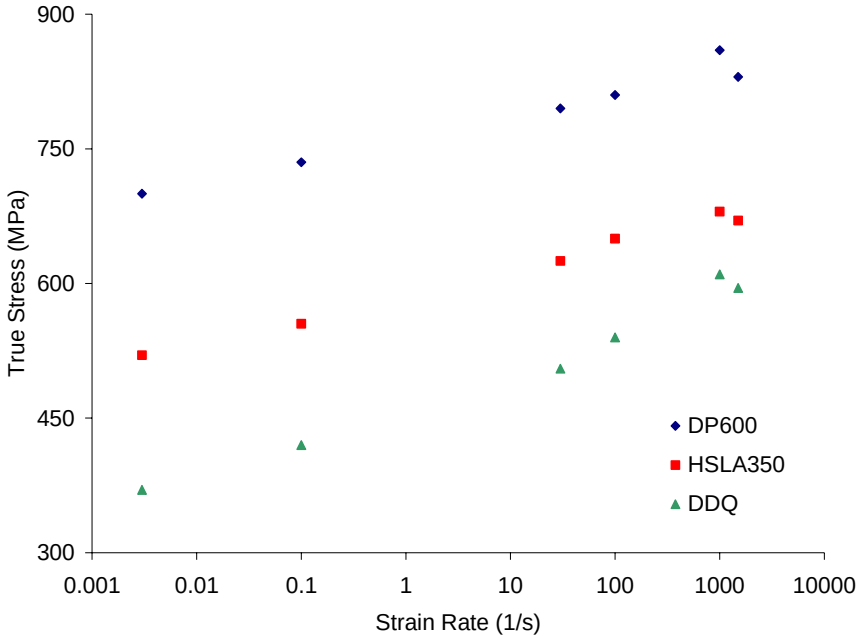

Figure 7.1. Strain rate sensitivity of each steel for the 6 o'clock tube specimens

The thermal sensitivity was obtained for each steel as well, however no correlation was seen between strength and thermal sensitivity (Figure 7.2). For a rise in temperature from 21 to 300 °C, the loss in strength at 10% strain was found to be 200, 225, and 195 MPa for DDQ, HSLA350, and DP600, respectively.

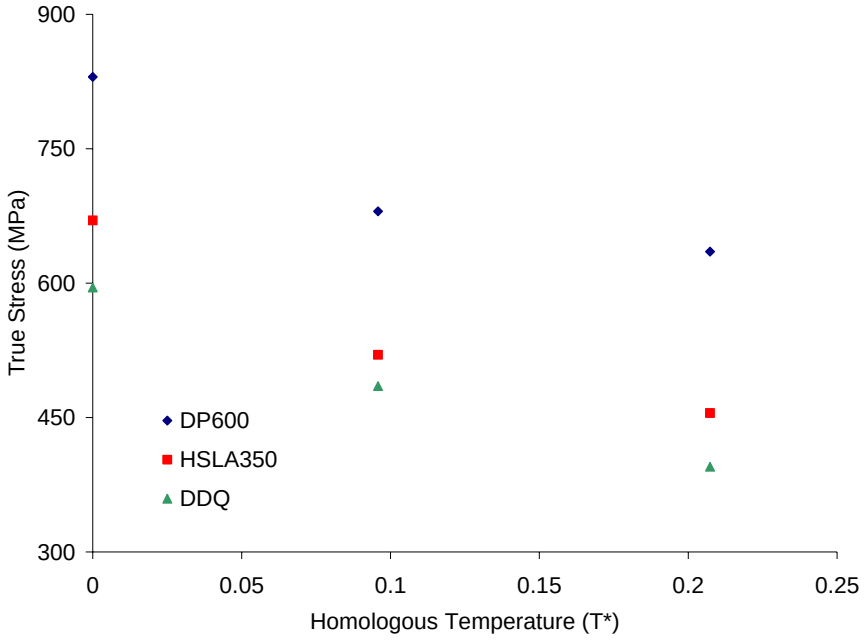

Figure 7.2. Thermal sensitivity of each steel (6 o'clock tube specimens) at a nominal strain rate of 1500 s^{-1}

An important aspect of high strain rate deformation is the temperature rise that occurs at near-adiabatic conditions. To illustrate this effect, Figure 7.3 shows the temperature rise for the 6 o'clock tube specimens of each material at 20% strain. The associated drop in strength predicted by the Johnson-Cook temperature sensitivity. The temperature rise at 100 s^{-1}, for example, is 35.7, 26.8, and 19.2 °C for the DP600, HSLA350, and DDQ specimens, respectively. This increase in temperature is proportional to the strength of the steel (Equation 3.4). The associated loss in strength, however, is 43.2, 68.9, and 23.8 MPa for the DP600, HSLA350, and DDQ specimens, respectively. This drop in strength highlights the importance of accounting for thermal softening in high strain rate experiments.

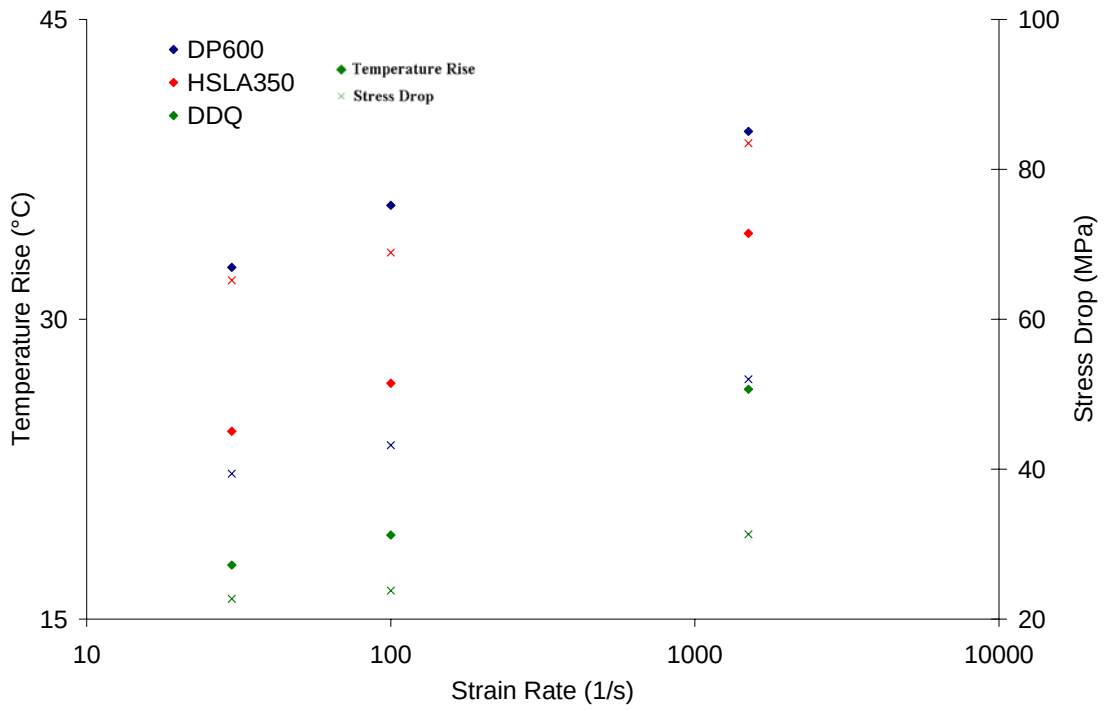

Figure 7.3. Temperature rise and corresponding stress drop at 20% strain for all steels

For all of the alloys, a difference in the stress-strain behaviour was seen between the sheet and tube specimens, due to the plastic work that was imparted during forming of the tube. In each case, the stength of the sheet specimens was initially less than that of the tube specimens, but the two strengths converged as the strain increased. This took place at roughly 10%, 20%, and 12% strain for the DP600, HSLA350, and DDQ specimens, respectively.

For DP600, this trend of converging strengths was observed to remain relatively unchanged as the strain rate increased up to 100 s^{-1}. At high strain rates, the stress-strain response of the tube specimens diverged from that of the sheet specimens, due to an increase in work-hardening rate. An increase in work-hardening rate as strain rate increases has been observed by Beynon *et al.* [15,16], Schael [17], and Tarigopula [18]. Unfortunately, none of these authors speculate about the origin of this effect. In addition to this effect, it was found that the strength of the DP600 tube specimens was the same at all positions around the circumference of the tube for all strain rates.

For the HSLA350 and DDQ specimens, in addition to the difference in stress-strain response of the sheet and tube specimens, there was a difference in stress-strain response of the tube specimens taken from the 3 o'clock and 6 o'clock orientations of the tube. It was also found that the response of the tube specimens was symmetric, but not uniform, around the perimeter of the tube.

For all specimens, strain-to-failure and strain-to-necking were determined at strain rates up to 100 s^{-1}. The failure strain was found from the engineering stress – strain results and was defined as the strain at which the specimen could no longer support any load. The strain-to-necking was found using Considere's criterion for tensile instability.

For each steel, a drop in ductility was seen as the strain rate increased from 0.003 to 0.1 s^{-1}. As the strain rate increased further, the ductility of the HSLA350 increased markedly, while the ductility of the DDQ and DP600 remained relatively constant. These trends have not been seen previously for dual phase steels or HSLA steels. Beynon et al. [15,16] and Schael [17] both noted a drop in ductility (3-5% strain) for a rise in strain rate from 0.003 to 400 s^{-1} for DP500, DP600, and DP800 steels. For HSLA65, Nemat-Nasser [26] observed a decrease in ductility (approximately 10%) when increasing the strain rate from 0.003 to 3000 s^{-1}.

The onset of diffuse necking dropped (3-4% strain) for DP600 and HSLA350 specimens as the strain rate increased from 0.003 to 100 s^{-1}. For DDQ specimens, the onset of diffuse necking dropped by 14% strain from the low to intermediate strain rate tests, due to a drop in work-hardening rate as the strain rate increased.

Numerical models of both the IFWI and TSHB experiments were created to assess whether the experimental results could be reproduced numerically and to ensure that both the Johnson-Cook and Zerilli-Armstrong constitutive models were properly applied in the simulations. For this assessment, the experiments and constitutive parameters of the DP600 sheet specimens were used. It was found that the predicted and measured force-

time responses matched quite closely for each of the models (one using the Johnson-Cook parameters for the specimen and the other using the Zerilli-Armstrong parameters). This comparison has confirmed that the experimental results can be reproduced and that the constitutive models were applied properly.

To satisfy the criteria for the TSHB model, it was essential for the model to match the measured incident, reflected, and transmitted waves. Each wave was reproduced quite closely by both models (one using the Johnson-Cook parameters for the specimen and the other using the Zerilli-Armstrong parameters). This further confirmed that the constitutive equations were applied properly in the models.

Future research should consider study of the upper yield stress and Luder's banding in the HSLA350 and DDQ specimens in the TSHB experiment. Use of high speed photography and possibly a 'stress coating', similar to the one used by Kyriakides *et al.* [90], would allow for visualization of the Luder's band as it propogates across the specimen. This work would aid in creating a foundation for developing a constitutive model that can account for these effects. Future work should also further consider the metallography of the specimens at the point of fracture. This may offer insight into the failure mechanisms and trends that were observed for the necking and failure strain.

CHAPTER 8

CONCLUSIONS AND FUTURE WORK

8.1 CONCLUSIONS

From this body of work, several conclusions can be drawn:

- Each of the steels tested display a positive strain rate sensitivity over the complete range of strain rates. For an increase in strain rate from 0.003 to 100 s^{-1}, the corresponding increase in strength at 10% strain was found to be approximately 170, 130, and 110 MPa for DDQ, HSLA350, and DP600, respectively.
- Each steel displayed a thermal softening response. For a rise in temperature from 21 to 300 °C, the loss in strength at 10% strain was found to be 200, 225, and 195 MPa for DDQ, HSLA350, and DP600, respectively.
- For each steel a substantial difference in strength was seen between the sheet and tube specimens at low strains. As the strain increased, the difference between the sheet and tube specimen responses decreased.
- An upper yield stress and discontinuous yielding were observed in the HSLA350 and DDQ sheet specimens and both increased in magnitude as the strain rate increased. This effect was so strong in the TSHB experiments that very little uniform strain could be observed.
- The experimental results were better fit with parameters from the Zerilli-Armstrong constitutive model than the Johnson-Cook constitutive model.
- Numerical simulations, using both constitutive models, confirmed that the material response was accurately captured by the IFWI and TSHB models and that the constitutive models were applied properly to the experimental data.

8.2 FUTURE WORK

The following future research should be considered:

The mechanism for the increasing amplitude of the upper yield stress with increasing strain rate and the time dependence of the Luder's band at high strain rates, seen in the DDQ and HSLA350 sheet specimens, was not determined in this research. Future work should investigate this behaviour with an aim to developing an appropriate constitutive model.

Metallographic examinations of the specimens at the fracture surface should be completed. This work would aid in determining the failure mechanisms, such that a damage model could be incorporated into the constitutive equations, allowing for more accurate predictions of failure strain.

Finally, a difference between the rise time for the force in the predicted and measured force-time response in the IFWI model was seen. The most likely reason for this difference is that the RTV silicon pads are not modeled. To confirm that this is the case, and to aid in future IFWI modeling, the RTV silicon pads should be modeled.

REFERENCES

[1] W.J. Nam and C.M. Bae, Microstructural evolution and its relation to mechanical properties in a drawn dual-phase steel, Journal of Materials Science, Volume 34, 1999, 5661-5668

[2] S.J. Barnard, G.D.W. Smith, M. Sarikaya and G. Thomas, Carbon atom distribution in a dual phase steel: an atom probe study, Scripta Metallurgica, Volume 15, 1981, 387-392

[3] D.K. Mondal and R.M. Dey, Effect of grain size on the microstructure and mechanical properties of a C-Mn-V dual-phase steel, Materials Science and Engineering, Volume A149, 1992, 173-181

[4] G. S. Huppi, D. K. Matlock and G. Krauss, An evaluation of the importance of epitaxial ferrite in dual-phase steel microstructures, Scripta Metallurgica, Volume 14, Issue 11, November 1980, 1239-1243.

[5] R.O. Rocha, T.M.F. Melo, E.V. Pereloma and D.B. Santos, Microstructural evolution at the initial stages of continuous annealing of cold rolled dual-phase steel, Materials Science and Engineering, Volume A391, 2005, 296-304

[6] M. Erdogan and R. Priestner, Effect of epitaxial ferrite on yielding and plastic flow in dual phase steel in tension and compression, Materials Science and Technology, Volume 15, Issue 11, November 1999, 1273-1284

[7] M. Sarwar and R. Priestner, Influence of ferrite-martensite microstructural morphology on tensile properties of dual-phase steel, Journal of Materials Science, Volume 31, 1996, 2091-2095

[8] Richard D. Lawson, David K. Matlock and George Krauss, An etching technique for microalloyed dual-phase steels, Metallography, Volume 13, Issue 1, February 1980, Pages 71-87.

[9] U. Liedl, S. Traint and E.A. Werner, An unexpected feature of the stress-strain diagram of dual-phase steel, Computational Materials Science, Volume 25, 2002, 122-128

[10] W.R. Cribb and M. Rigsbee, Structure and Properties of Dual-Phase Steels, ed. A.T. Davenport, Warrendale, Pennsylvania, 1979

[11] H. Fischmeister and B. Karlsson, Plastizitatseigenschaften grob-zweiphasiger Werkstoffe, Z. Metallkunde, 1977, 311-327

[12] M. Erdogan and R. Priestner, Effect of martensite content, its dispersion, and epitaxial ferrite content on Baushinger behaviour of dual phase steel, Materials Science and Technology, Volume 18, Issue 4, April 2002, 369-376

[13] Y. Sakuma, D.K. Matlock and G. Krauss, Intercritically annealed and isothermally transformed 0.15 pct C steels: Part 1. transformation, microstructure, and room-temperature mechanical properties, Metallurgical Transactions of the ASME, Volume 23A, April 1992, 1221-1231

[14] G.T. Hahn, Model for yielding with special reference to yield-point phenomena of iron and related BCC metals, Acta Metallurgica, Volume 10, 1962, 727-738

[15] N.D. Beynon, T.B. Jones and G. Fourlaris, Effect of high strain rate deformation on microstructure of strip steels tested under dynamic tensile conditions, Materials Science and technology, Volume 21, Issue 1, 2005, 103-112

[16] N.D. Beynon, S. Oliver, T.B. Jones and G. Fourlaris, Tensile and work hardening properties of low carbon dual phase strip steels at high strain rates, Materials Science and technology, Volume 21, Issue 7, 2005, 771-778

[17] W. Bleck and I. Schael, Determination of crash-relevant material parameters by dynamic tensile tests, Steel Research, Volume 71, Issue 5, May 2000, 173-178

[18] V. Tarigopula, M. Langseth, O.S. Hopperstad, A.H. Clausen, Axial crushing of thin-walled high-strength steel sections, International Journal of Impact Engineering, Volume 32, 2006, 847-882

[19] A.A. Gorni and P.R. Mei, Development of alternative as-rolled alloys to replace quenched and tempered steels with tensile strength in the range of 600-800 MPa, Journal of Materials Processing Technology, Volume 162-163, 2005, 298-303

[20] S. Nemat-Nasser and W.G. Guo, Thermomechanical response of HSLA-65 steel plates: experiments and modeling, Mechanics of Materials, Volume 37, 2005, 379-405

[21] J. Kilber and I. Schindler, Recrystallization/precipitation behaviour in microalloyed steels, Journal of Materials Processing Technology, Volume 60, 1996, 597-602

[22] E.V. Pereloma, B.R. Crawford and P.D. Hodgson, Strain-induced precipitation behaviour in hot rolled strip steel, Materials Science and Engineering A299, 2001, 27-37

[23] S.K. Dhua, D. Mukerjee and D.S. Sarma, Influence of tempering on the microstructure and mechanical properties of HSLA-100 steel plate, Metallurgy Transactions A 32A, 2259-2270.

[24] L. Holappa, V. Ollinainen and W. Kasprzak, The effect of silicon and vanadium alloying elements on the microstructure of air cooled forged HSLA steels, Journal of Materials Processing Technology, Volume 109, 2001, 78-82

[25] P.C.M Rodrigues, E.V. Pereloma and D.B. Santos, Mechanical properties of an HSLA bainitic steel subjected to controlled rolling with accelerated cooling, Materials Science and Engineering, Volume A283, 2000, 136-143

[26] M.N. Bassim and N. Panic, High strain rate effects on the strain of alloy steels, Journal of Materials Processing Technology, Volume 92-93, 1999, 481-485

[27] Q. Xue, D. Benson, M.A. Meyers, V.F. Nesterenko and E.A. Olevsky, Constitutive response of welded HSLA 100 steel, Materials Science and Engineering A354, 2003, 166-179

[28] D.L. Baragar, The high temperature and high strain-rate behaviour of a plain carbon and an HSLA steel, Journal of Mechanical Working Technology, Volume 14, 1987, 295-307

[29] R. Fernie and N.A. Warrior, Impact test rigs for high strain rate tensile and compressive testing of composite materials, Technical note, Strain, Volume 38, 2002, 69-73

[30] W. Abramowicz and N. Jones, Transition from initial global bending to progressive buckling of tubes loaded statically and dynamically, International Journal of Impact Engineering, Volume 19, 1997, 415-437

[31] W. Abramowicz and N. Jones, Dynamic progressive buckling of circular and square tubes, International Journal of Impact Engineering, Volume 4, 1986, 243-270

[32] S.F. Lee and G.M. Swallowe, Direct measurement of high rate stress-strain curves using instrumented falling weight and high-speed photography, Imaging Science Journal, Volume 52, 2004, 193-201

[33] G.M. Swallowe and S.F. Lee, A study of the mechanical properties of PMMA and PS at strain rates of 10^{-4} to 10^{3} s^{-1} over the temperature range 293-363 K, Journal de Physique IV, Volume 110, 2003, 33-38

[34] S.M. Walley, D. Xing and J.E. Field, Mechanical properties of three transparent polymers in compression at a very high rate of strain, Impact and Dynamic Fracture of Polymers and Composites, 1995, 289-303

[35] H.M. Hsiao and I.M. Daniel, Strain rate behaviour of composite materials, Composites Part B, Volume 29B, 1998, 521-533

[36] A.G. Salvi, A.M. Waas and A. Caliskan, Specimen size effects in the off-axis compression test of unidirectional carbon fiber tow composites, Composites Science and Technology, Volume 64, January 2004, 83-97

[37] L.A. Fasce, V. Pettarin, R. Seltzer and P.M. Frontini, Evaluation of Impact Fracture Toughness of Polymeric Materials by Means of the J-Integral Approach, Polymer Engineering and Science, Volume 43, May 2003, 1081-1095

[38] Z.H.M. Ishak and J.P. Berry, Impact properties of short carbon fiber reinforced nylon 6.6, Polymer Engineering & Science, Volume 33, 1483-1488

[39] M. Sanchez-Soto, A.B. Martinez, O.O. Santana and A. Gordillo, On the application of a damped model to the falling weight impact characterization of glass beads-polystyrene composites, Journal of applied polymer science, Volume 93, 2004, 1271-1284

[40] S. Jose, S. Thomas, E. Lievana and J. Karger-Kocsis, Morphology and mechanical properties of polyamide 12 blends with Styrene/Ethylene–Butylene/Styrene rubbers with and without maleation, Journal of Applied Polymer Science, Volume 95, 2005, 1376–1387

[41] S.C. Tjong, J.S. Shen and R.K.Y Li, Morphological behaviour and instrumented dart impact properties of /3-crystalline-phase polypropylene, Polymer, Volume 37, 1996, 2309-2316

[42] J. Karger-Kocsis, D.E. Mouzakis, G.W. Ehrenstein and J. Varga, Instrumented tensile and falling weight impact response of injection-molded a- and b-phase polypropylene homopolymers with various melt flow indices, Journal of Applied Polymer Science, Volume 73, 1999, 1205-1214

[43] J.I. Velasco, A.B. Martinez, D. Arencon, M.A. Rodriguez-Perez and J.A. De Saja, Application of instrumented falling dart impact to the mechanical characterization of thermoplastic foams, Journal of Material Science, Volume 34, 1999, 431-438

[44] G.J. Molina and Y.M. Haddad, Acousto-ultrasonics approach to the characterization of impact properties of a class of engineering materials, International Journal of Pressure Vessels and Piping, Volume 67, 1996, 307-315

[45] P.S. Song, J.C. Wu, S. Hwang and B.C. Sheu, Statistical analysis of impact strength and strength reliability of steel-polypropylene hybrid fiber-reinforced concrete, Construction and Building Materials, Volume 19, 2005, 1-9

[46] T. Nicholas, Tensile testing of materials at high rates of strain, Experimental Mechanics, Volume 21, 1981, 177-185.

[47] H.S. Shin, H.M. Lee and M.S. Kim, Impact tensile behaviour of 9% nickel steel at low temperature, International Journal of Impact Engineering, Volume 24, 2000, 571-581

[48] A.P. Mouritz, Failure mechanisms of mild steel bolts under different loading rates, International Journal of Impact Engineering, Volume 15, 1994, 311-324

[49] P.J. Cain, Digital filtering of impact data, ASTM STP, 1987, 81-102

[50] J.G. Williams and G.C. Adams, The analysis of instrumented impact tests using a mass-spring model, International Journal of Fracture, Volume 33, 1987, 209-222

[51] M.S. Found, I.C. Howard and A.P. Paran, Interpretation of signals from dropweight impact tests, Composite Structures, Volume 42, 1998, 353-363

[52] J.M. Lifshitz, F. Gov, M. Gandelsman, Instrumented low-velocity impact of CFRP beams, International Journal of Impact Engineering, 1995, Volume 16, 201-215

[53] D.J. Inman, Engineering Vibration, 2nd Edition, Prentice Hall, New Jersey, 2001, 177-183

[54] E. Roos and U. Mayer, Progress in testing sheet material at high strain rates, Journal de Physique IV, Volume 110, 2003, 495-500

[55] G.H. Majzoobi, F.F. Saniee and M. Bahrami, A tensile impact apparatus for characterization of fibrous composites at high strain rates, Journal of Materials Processing Technology, Volume 162-163, 2005, 76-82

[56] B. Hopkinson, A method of measuring the pressure produced in the detonation of high explosives or by the impact of bullets, Philosophical Transactions of the Royal Society of London Series A, Volume 213, 1914, 437-456

[57] H. Kolsky, An investigation of the mechanical properties of materials at very high rates of loading, Proceedings of the Physical Society of London, Volume 62B, 1949, 676-700

[58] G.T. Gray III, Classic split-Hopkinson pressure bar testing, technical note, Los Alamos National Laboratory, 2000

[59] L.D. Bertholf and C.H. Karnes, Two-dimensional analysis of the split Hopkinson pressure bar system, Journal of Mechanics and Physics of Solids, Volume 23, 1974, 1-19

[60] U.S. Lindholm and L. M. Yeakley, High strain-rate testing: tension and compression, Experimental Mechanics, Volume 8, 1968, 1-9

[61] U.S. Lindholm, Some experiments with the split hopkinson pressure bar, Journal of the Mechanics and Physics of Solids, Volume 12, 1964, 317-335

[62] P.S. Follansbee and C. Frantz, Wave propagation in the split Hopkinson pressure bar, Journal of Engineering Materials and Technology, Volume 105, January 1983, 61-66

[63] L. Pochhammer, About the initiation of the velocities of small oscillations in unbounded isotropic circular cylinders, Journal Reine Angew Mathematica, Volume 81, 1876, 324-336

[64] C. Chree, The equations of an isotropic elastic solid in polar and cylindrical co-ordinates: their solution and application, Transactions of the Cambridge Philosophical Society, Volume 41, 1889, 250-369

[65] R.M. Davies, A critical study of the Hopkinson pressure bar, Philosophical Transactions of the Royal Society of London Series A, Volume 240, 1948, 375-457

[66] C.P. Salisbury, Spectral analysis of wave propagation through a polymeric Hopkinson bar. Masters of Applied Science thesis, University of Waterloo, 2001.

[67] W. Chen, B. Song, D.J. Frew and M.J. Forrestal, Dynamic small strain measurements of a metal specimen with a split Hopkinson pressure bar, Techical Note, Society for Experimental Mechanics, Volume 43, March 2003, 20-23

[68] T. Nicholas, *Material Behavior at High Strain Rates*, Ch. 8 in: Impact Dynamics, Zukas, J.A. (Ed.), John Wiley & Sons, Inc., New York, 1982.

[69] Y. Li and K.T. Ramesh, An optical technique for measurement of material properties in the tension Kolsky bar, International Journal of Impact Engineering, In Press, 2005

[70] G.H. Staab and A. Gilat, A direct-tension split Hopkinson bar for high strain-rate testing, Journal of Experimental Mechanics, Volume 31, 1991, 232-235

[71] J. Rodriguez, C. Navarro and V. Sanchez-Galvez, Numerical assessment of the dynamic tension test using the split Hopkinson bar, Journal of Testing Evaluation, Volume 22, 1994, 335-342

[72] G. Haugou, E. Markiewicz and J. Fabis, On the use of the non direct tensile loading on a classical split Hopkinson bar apparatus dedicated to sheet metal specimen characterization, Journal of Impact Engineering, Volume 32, May 2006, 778-798

[73] H. Huh, W.J. Kang and S.S. Han, A Tension Split Hopkinson Bar for Investigating the Dynamic Behavior of Sheet Metals, Journal of Experimental Mechanics, Volume 42, March 2002, 8-17

[74] H. Zhao and G. Gary, The testing and behaviour modeling of sheet metals at strain rates from 10^{-4} to 10^{4} s^{-1}, Materials Science and Engineering, Volume A207, 1996, 46-50

[75] G. R. Johnson and W. H. Cook, A constitutive model and data for metals subjected to large strains, high strain-rates and high temperatures. Proc. 7th Int. Symposium on Ballistics, 1983, 541-547.

[76] G.R. Johnson and W.H. Cook, Fracture characteristics of three metals subjected to various strains, strain rates, temperatures and pressures, Engineering Fracture Mechanics, Volume 21, 1985, 31-48.

[77] G.T. Gray III, S.R. Chen, W. Wright and M.F. Lopez, Constitutive equations for annealed metals under compression at high strain rates and high temperatures, Report LA-12669-MS, Los Alamos National Laboratory, 1994

[78] F.J. Zerilli and R.W. Armstrong, Dislocation-mechanics-based constitutive relations for material dynamics calculations, Journal of Applied Physics, Volume 61, 1987, 1816-1825

[79] W.K. Rule and S.E. Jones, A revised form for the Johnson-Cook strength model, International Journal of Impact Engineering, Volume 21, September 1998, 609-624

[80] W.J. Kang, S.S. Cho, H. Huh and D.T. Chung, Modified Johnson-Cook model for vehicle body crashworthiness simulation, International Journal of Vehicle Design, Volume 21, 1999, 424-435

[81] F.J. Zerilli and R.W. Armstrong, Dislocation-mechanics-based constitutive relations for material dynamics modeling: slip and deformation twinning in iron, Shock Waves in Condensed Matter, 1987, 273-276

[82] Z.S. Basinski, Thermally activated glide in face-centred cubic metals and its application to the theory of strain hardening, Philosophical Magazine, Volume 4, 1959, 393-432

[83] E. Orowan, Problems of plastic gliding, Proceedings of the Physical Society, Volume 52, 1940, 8-22

[84] Y.M. Gupta, G.E. Duvall and G.R. Fowles, Dislocation mechanisms for stress relaxation in shocked LiF, Journal of Applied Physics, Volume 46, 1975, 532-546

[85] M.A. Meyers and K.K. Chawla, Mechanical Behaviour of Materials, Prentice Hall, New Jersey, 1999

[86] J.D. Campbell and W.G. Ferguson, Temperature and Strain-Rate Dependence of the Shear Strength of Mild Steel, Philosophical Magazine, Volume 21, 1970, 63-82

[87] R.W. Armstrong and F.J. Zerilli, Dislocation mechanics aspects of plastic instability and shear banding, Mechanics of Materials, Volume 17, 1994, 319-327

[88] N.J. Petch, Theory of the yield point and of strain-ageing in steel, in: J.A. Charles and G.C. Smith, editors, Advances in Physical Metallurgy, Institute of Metals, London

[89] A.H. Cottrell and B.A. Bilby, Dislocation theory of yielding and strain ageing of iron, Proceedings of the Physical Society of London Section A, Volume 62, 1949, 49-62

[90] S. Kyriakides and J.E. Miller, On the propagation of Luders bands in steel strips, Journal of Applied Mechanics, Volume 67, December 2000, 645-654

[91] W.G. Johnston and J.J. Gilman, Dislocation velocities, dislocation densities, and plastic flow in lithium fluoride crystals, Journal of Applied Physics, Volume 30, 1959, 129-144

[92] H. Neuhauser and A. Hampel, Observation of Luders bands in single-crystals, Scripta Metallurgica et Materialia, Volume 29, 1993, 1151-1157

[93] R. Grantab, Interaction Between Forming and Crashworthiness of Advanced High Strength Steel S-Rails . Masters of Applied Science thesis, University of Waterloo, 2006.

[94] R. Smerd, S. Winkler, C. Salisbury and M.J. Worswick, High strain rate tensile testing of automotive aluminum alloy sheet, International Journal of Impact Engineering, In Press

[95] Bailey SJ, Baldini NC, Barkley EI, Peters KA, Rosiak JL, Simms ST, et al., editors. Annual book of ASTM standards: metals—mechanical testing; elevated and low temperature tests; metallography. West Conshohocken, PA: ASTM International; 2003. p. 61–82.

[96] D. MacDougall, Determination of the Plastic Work Converted to Heat Using Radiometry, Experimental Mechanics, Vol. 40, No. 3, 2000, pp. 298-306.

[97] R.O. Smerd, Constitutive Behaviour of Aluminum Alloy Sheet at High Strain Rates, Masters of Applied Science thesis, University of Waterloo, 2005.

[98] L. Weber, M. Kouzeli, C. San Marchi and A. Mortensen, On the Use of Considere's Criterion in Tensile Testing of Materials Which Accumulate Internal Damage. Scripta Materialia, Vol. 41, No. 5, 1999, pp. 549-551.

[99] Altair Hypermesh v. 5.1, Troy, Michigan

[100] J.O. Hallquist, 2003. LS-Dyna – Keyword Users Manual, version 970. Livermore Software Technology Corporation.

[101] M.J. Worsick, ME 725 course notes: advanced topics in stress analysis, forming, impact, and modeling, University of Waterloo, 2005

APPENDIX A

Specimen Data and Engineering Stress-Strain Results for all Specimens

Steel	Sheet/Tube Position	Initial Gauge Dimensions (mm) Length	Width	Thickness	Strain Rate (1/s) Nominal	Achieved	Initial Temp (°C)	Strain Offset
DP600	Sheet	50.8	12.72	1.82	0.0033	0.003	21	0
		50.8	12.72	1.83	0.0033	0.003	21	0
		50.8	12.71	1.83	0.0033	0.003	21	0
		12.5	1.75	1.84	0.0033	0.003	21	0.0224
		12.5	1.84	1.83	0.0033	0.003	21	0.0096
		12.5	1.81	1.85	0.0033	0.003	21	0.0098
		12.5	1.70	1.84	0.1	0.1	21	0.0056
		12.5	1.70	1.83	0.1	0.1	21	0.0208
		12.5	1.71	1.84	0.1	0.1	21	0.0120
		12.5	1.72	1.83	30	30	21	0.0066
		12.5	1.70	1.84	30	30	21	0.0066
		12.5	1.82	1.84	30	30	21	0.0066
		12.5	1.77	1.81	100	80	21	0.0064
		12.5	1.76	1.83	100	80	21	0.0064
		12.5	1.76	1.83	100	80	21	0.0164
		12.5	1.70	1.85	500	369	21	0.0050
		12.5	1.70	1.85	500	369	21	0.0050
		12.5	1.69	1.83	500	369	21	0.0050
		12.5	1.77	1.80	1000	812	21	0.0180
		12.5	1.72	1.83	1000	812	21	0.0070
		12.5	1.73	1.83	1000	812	21	0.0040
		12.5	1.72	1.84	1500	1212	21	0.0200
		12.5	1.74	1.84	1500	1212	21	0.0200
		12.5	1.71	1.84	1500	1212	21	0.0150
		12.5	1.74	1.85	500	369	150	0.0053
		12.5	1.72	1.84	500	369	150	0.0053
		12.5	1.73	1.85	500	369	150	0.0053
		12.5	1.75	1.85	1500	1212	150	0.0025
		12.5	1.73	1.85	1500	1212	150	0.0025
		12.5	1.73	1.85	1500	1212	150	0.0120
		12.5	1.71	1.85	500	369	300	0.0053
		12.5	1.72	1.85	500	369	300	0.0053
		12.5	1.76	1.84	500	369	300	0.0053
		12.5	1.73	1.85	1500	1212	300	0.0120
		12.5	1.75	1.85	1500	1212	300	0.0175
		12.5	1.72	1.85	1500	1212	300	0.0180

Steel	Sheet/Tube Position	Initial Gauge Dimensions (mm) Length	Width	Thickness	Strain Rate (1/s) Nominal	Achieved	Initial Temp (°C)	Strain Offset
DP600	3 o'clock	50.8	12.72	1.86	0.0033	0.003	21	0
		50.8	12.72	1.87	0.0033	0.003	21	0
		50.8	12.71	1.86	0.0033	0.003	21	0
		12.5	1.72	1.86	0.0033	0.003	21	0.0056
		12.5	1.72	1.86	0.0033	0.003	21	0.0208
		12.5	1.72	1.87	0.0033	0.003	21	0.0120
		12.5	1.73	1.85	0.1	0.1	21	0.0110
		12.5	1.77	1.87	0.1	0.1	21	0.0080
		12.5	1.75	1.86	0.1	0.1	21	0.0110
		12.5	1.71	1.84	30	37	21	0.0080
		12.5	1.72	1.86	30	37	21	0.0190
		12.5	1.72	1.86	30	37	21	0.0210
		12.5	1.72	1.86	100	95	21	0.0100
		12.5	1.72	1.87	100	95	21	0.0060
		12.5	1.73	1.85	100	95	21	0.0060
		12.5	1.77	1.87	500	369	21	0.0100
		12.5	1.75	1.86	500	369	21	0.0080
		12.5	1.73	1.86	500	369	21	0.0080
		12.5	1.74	1.86	1000	812	21	0.0140
		12.5	1.74	1.86	1000	812	21	0.0140
		12.5	1.74	1.85	1000	812	21	0.0110
		12.5	1.74	1.87	1500	1212	21	0.0120
		12.5	1.73	1.86	1500	1212	21	0.0120
		12.5	1.73	1.87	1500	1212	21	0.0260

Steel	Sheet/Tube Position	Initial Gauge Dimensions (mm) Length	Width	Thickness	Strain Rate (1/s) Nominal	Achieved	Initial Temp (°C)	Strain Offset
DP600	6 o'clock	50.8	12.72	1.84	0.0033	0.003	21	0
		50.8	12.71	1.84	0.0033	0.003	21	0
		50.8	12.71	1.84	0.0033	0.003	21	0
		12.5	1.73	1.84	0.0033	0.003	21	0.0200
		12.5	1.74	1.83	0.0033	0.003	21	0.0270
		12.5	1.75	1.83	0.0033	0.003	21	0.0176
		12.5	1.73	1.83	0.1	0.1	21	0.0168
		12.5	1.73	1.83	0.1	0.1	21	0.0240
		12.5	1.73	1.83	0.1	0.1	21	0.0144
		12.5	1.72	1.86	30	37	21	0.0110
		12.5	1.73	1.85	30	37	21	0.0080
		12.5	1.74	1.87	30	37	21	0.0110
		12.5	1.72	1.85	100	95	21	0.0100
		12.5	1.73	1.89	100	95	21	0.0060
		12.5	1.71	1.86	100	95	21	0.0060
		12.5	1.74	1.86	500	369	21	0.0075
		12.5	1.75	1.87	500	369	21	0.0101
		12.5	1.73	1.88	500	369	21	0.0075
		12.5	1.73	1.87	1000	812	21	0.0180
		12.5	1.74	1.86	1000	812	21	0.0160
		12.5	1.73	1.85	1000	812	21	0.0136
		12.5	1.73	1.87	1500	1212	21	0.0220
		12.5	1.74	1.87	1500	1212	21	0.0162
		12.5	1.73	1.88	1500	1212	21	0.0112
		12.5	1.72	1.86	500	369	150	0.0059
		12.5	1.72	1.86	500	369	150	0.0055
		12.5	1.72	1.86	500	369	150	0.0063
		12.5	1.72	1.87	1500	1212	150	0.0220
		12.5	1.73	1.85	1500	1212	150	0.0160
		12.5	1.77	1.87	1500	1212	150	0.0155
		12.5	1.75	1.86	500	369	300	0.0063
		12.5	1.73	1.86	500	369	300	0.0059
		12.5	1.74	1.86	500	369	300	0.0059
		12.5	1.74	1.86	1500	1212	300	0.0194
		12.5	1.74	1.85	1500	1212	300	0.0155
		12.5	1.74	1.87	1500	1212	300	0.0160

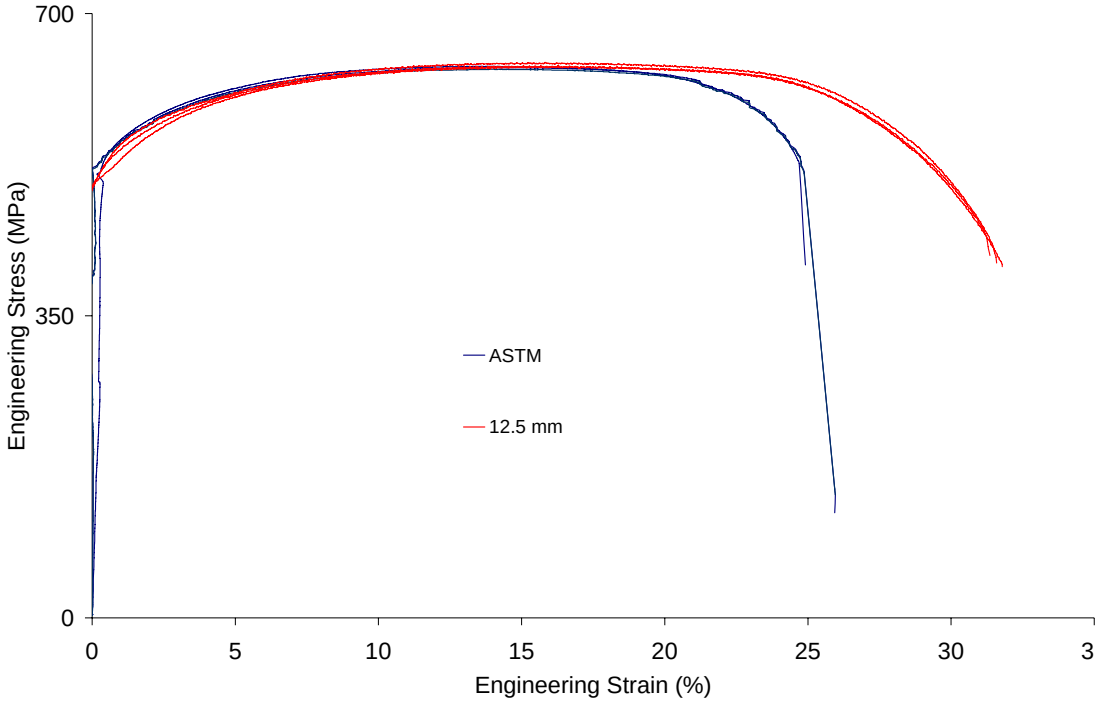

Figure A.1. Engineering stress vs. engineering strain of DP600 tube (3 o'clock) at $0.0033s^{-1}$

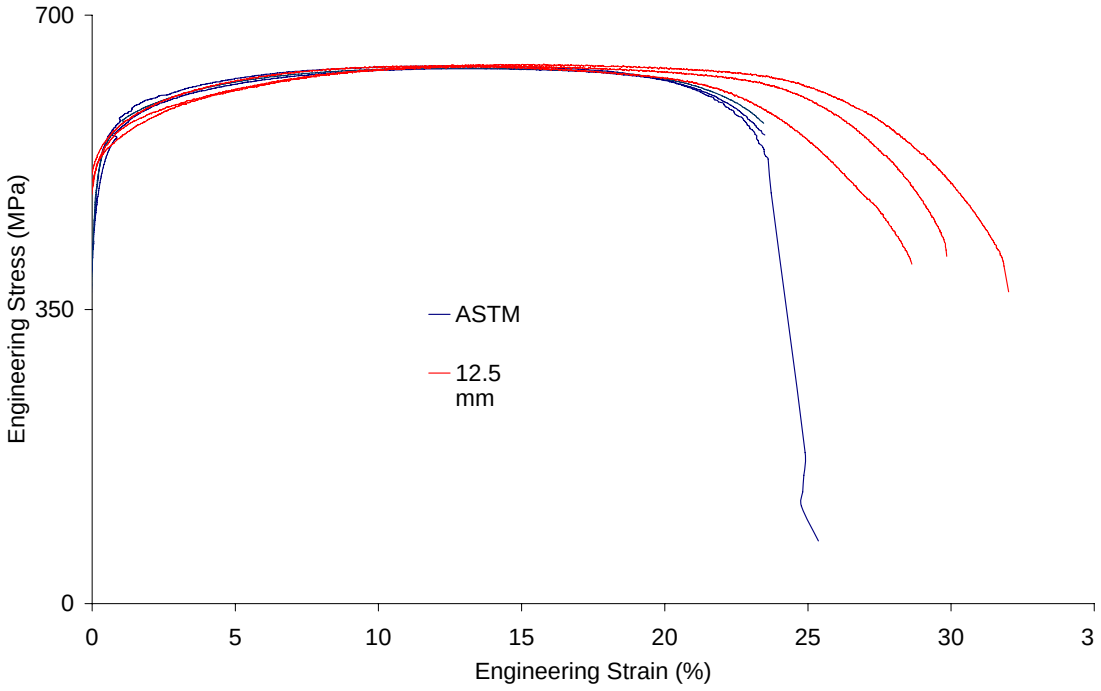

Figure A.2. Engineering stress vs. engineering strain of DP600 tube (6 o'clock) at $0.0033s^{-1}$

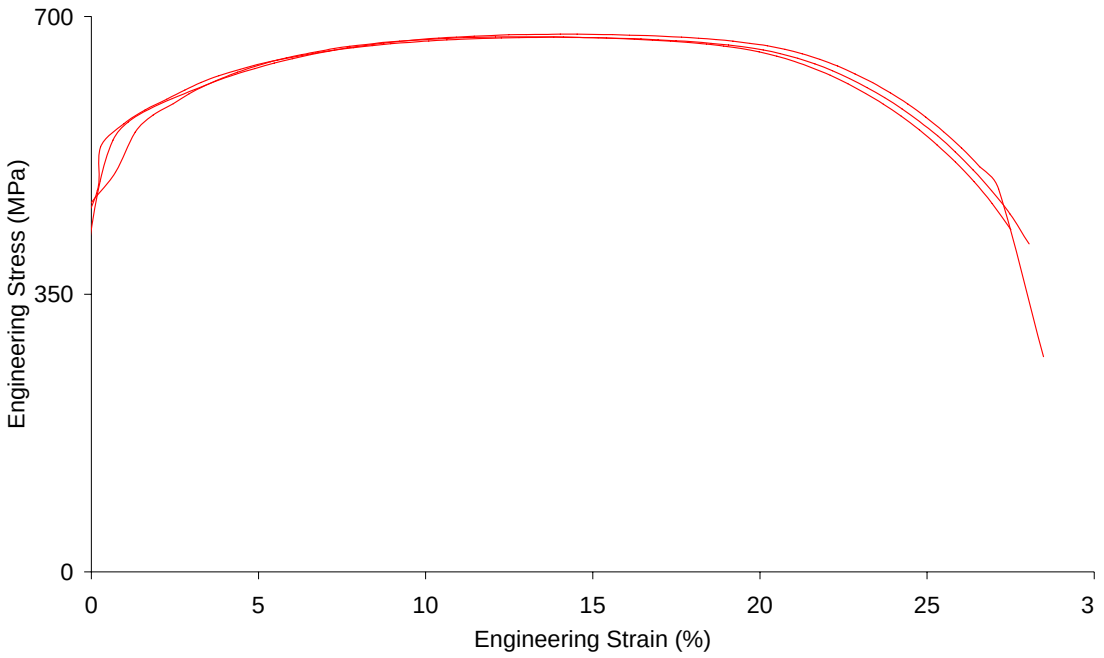

Figure A.3. Engineering stress vs. engineering strain of DP600 tube (3 o'clock) at $0.1s^{-1}$

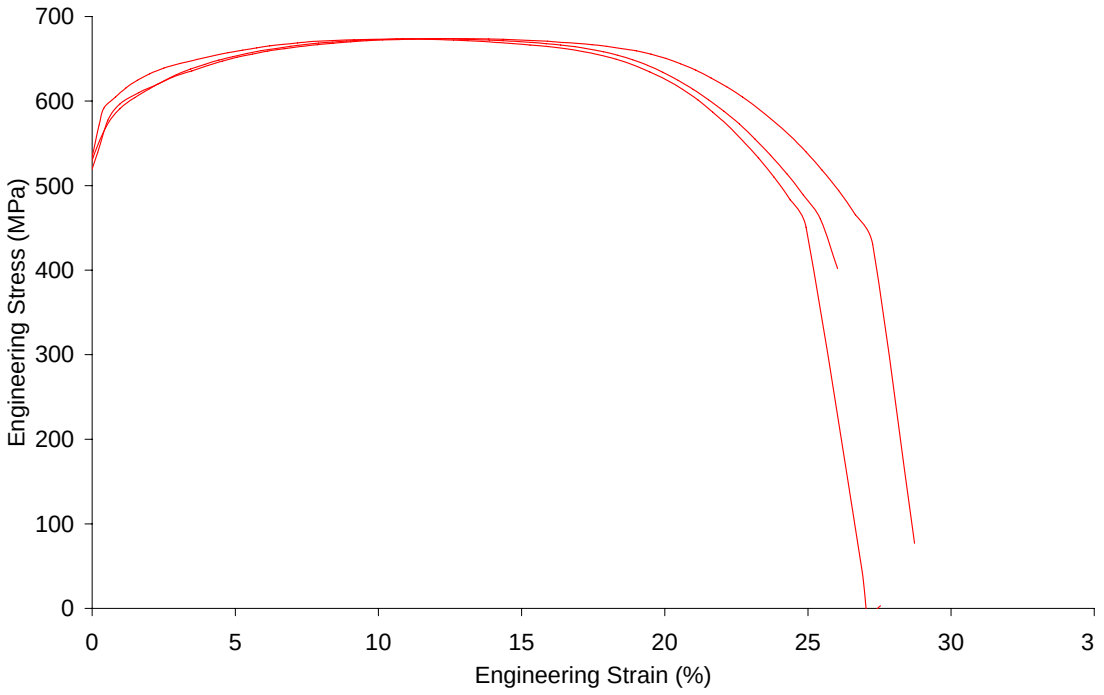

Figure A.4. Engineering stress vs. engineering strain of DP600 tube (6 o'clock) at $0.1s^{-1}$

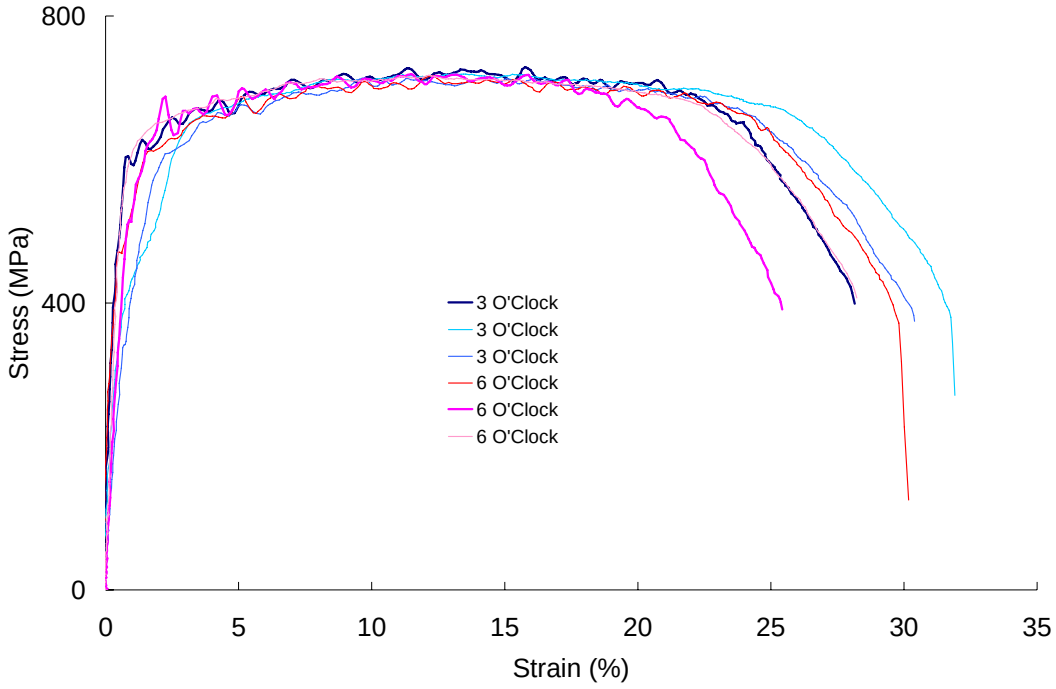

Figure A.5. Engineering stress vs. engineering strain of DP600 tube at $37s^{-1}$

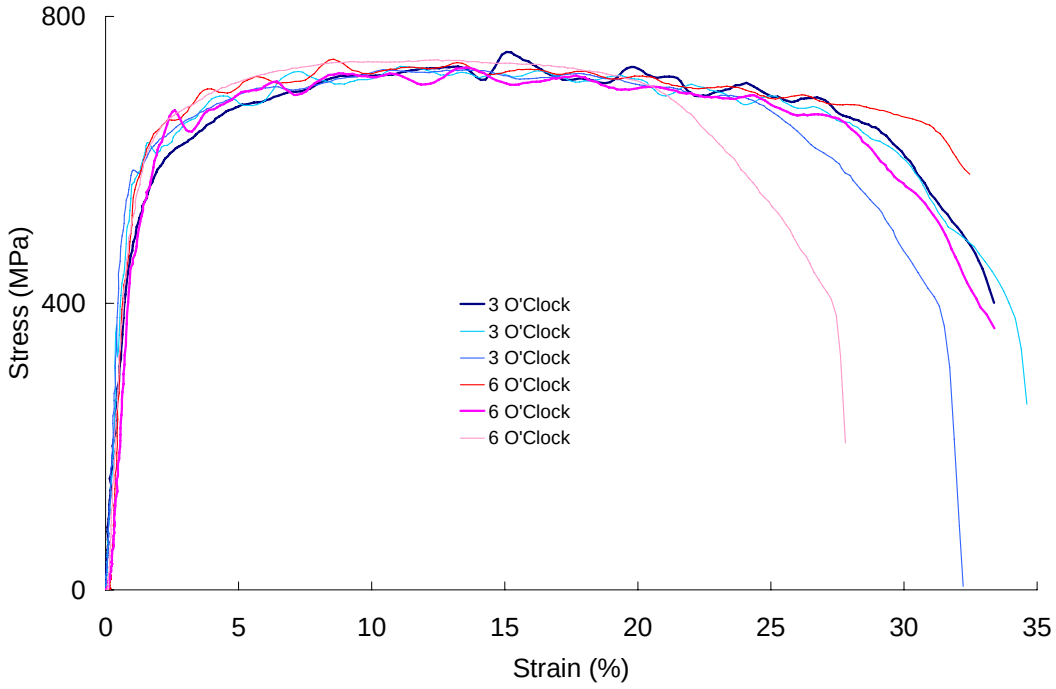

Figure A.6. Engineering stress vs. engineering strain of DP600 tube at $95s^{-1}$

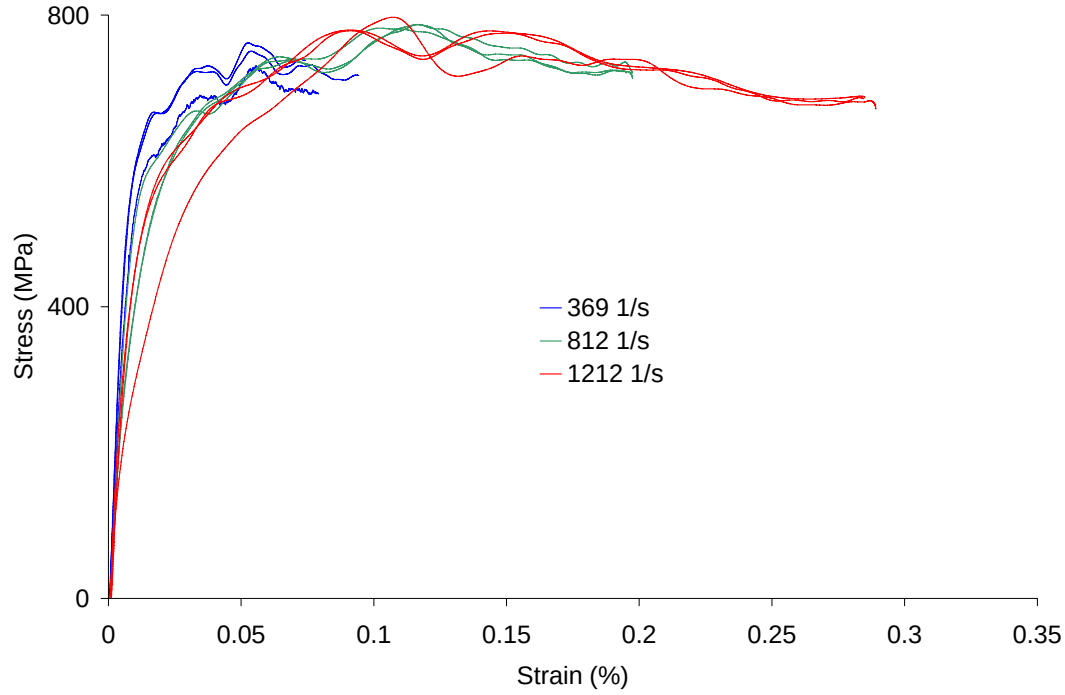

Figure A.7. Engineering stress vs. strain of DP600 tube (3 o'clock) at high rates

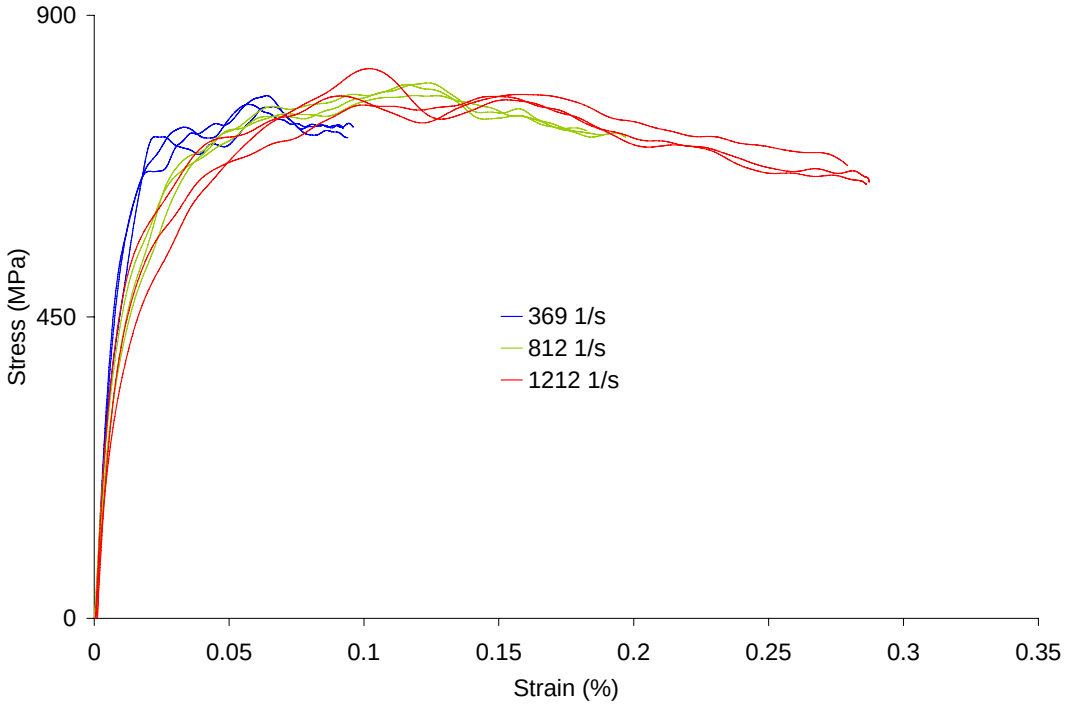

Figure A.8. Engineering stress vs. strain of DP600 tube (6 o'clock) at high rates

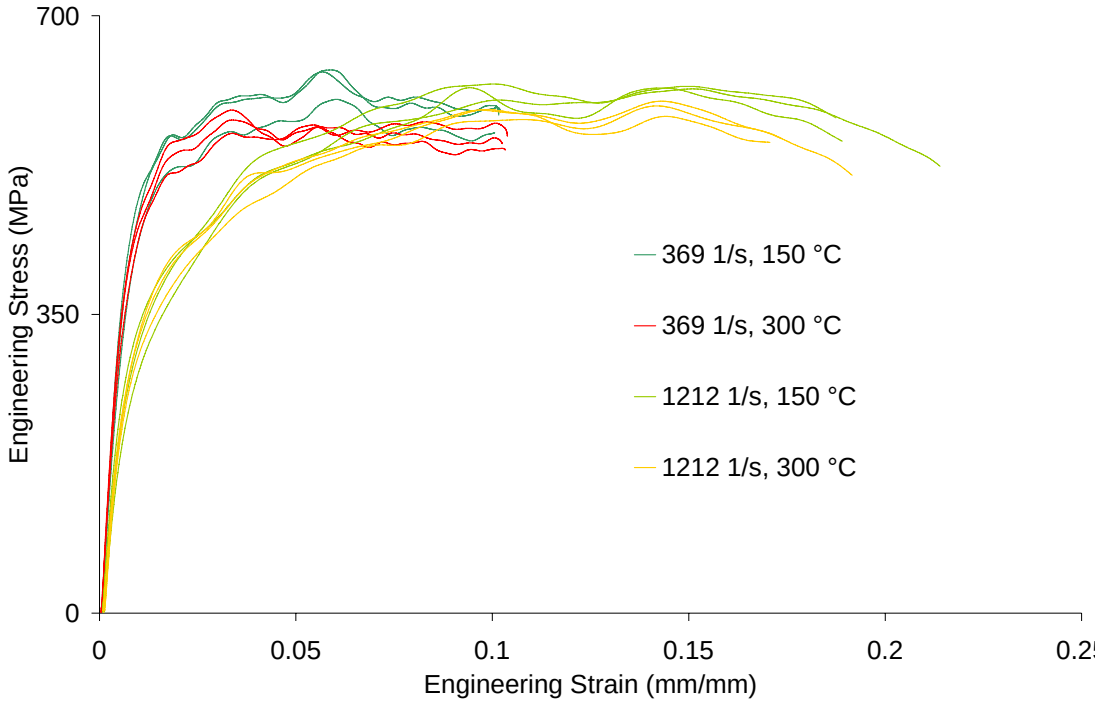

Figure A.9. Engineering stress vs. strain of DP600 tube (6 o'clock) at high temperatures

Steel	Sheet/Tube Position	Initial Gauge Dimensions (mm) Length	Width	Thickness	Strain Rate (1/s) Nominal	Achieved	Initial Temp (°C)	Strain Offset
HSLA350	Sheet	50.8	12.72	1.83	0.0033	0.003	21	0
		50.8	12.72	1.82	0.0033	0.003	21	0
		50.8	12.71	1.84	0.0033	0.003	21	0
		12.5	1.73	1.85	0.0033	0.003	21	0.0025
		12.5	1.74	1.85	0.0033	0.003	21	0.0025
		12.5	1.72	1.83	0.0033	0.003	21	0.0120
		12.5	1.73	1.80	0.1	0.1	21	0.0053
		12.5	1.71	1.83	0.1	0.1	21	0.0053
		12.5	1.74	1.83	0.1	0.1	21	0.0053
		12.5	1.75	1.82	30	37	21	0.0120
		12.5	1.76	1.81	30	37	21	0.0175
		12.5	1.74	1.83	30	37	21	0.0180
		12.5	1.74	1.83	100	100	21	0.0210
		12.5	1.76	1.86	100	100	21	0.0100
		12.5	1.73	1.81	100	100	21	0.0060
		12.5	1.71	1.85	500	N/A	21	0.0060
		12.5	1.72	1.85	500	N/A	21	0.0100
		12.5	1.76	1.84	500	N/A	21	0.0080
		12.5	1.73	1.85	1000	N/A	21	0.0090
		12.5	1.75	1.85	1000	N/A	21	0.0120
		12.5	1.72	1.85	1000	N/A	21	0.0115
		12.5	1.72	1.83	1500	N/A	21	0.0050
		12.5	1.72	1.85	1500	N/A	21	0.0090
		12.5	1.73	1.84	1500	N/A	21	0.0120
		12.5	1.77	1.83	500	N/A	150	0.0053
		12.5	1.75	1.84	500	N/A	150	0.0056
		12.5	1.73	1.83	500	N/A	150	0.0081
		12.5	1.74	1.84	1500	N/A	150	0.0095
		12.5	1.74	1.84	1500	N/A	150	0.0114
		12.5	1.74	1.81	1500	N/A	150	0.0125
		12.5	1.74	1.83	500	N/A	300	0.0075
		12.5	1.73	1.83	500	N/A	300	0.0072
		12.5	1.73	1.82	500	N/A	300	0.0064
		12.5	1.73	1.81	1500	N/A	300	0.0091
		12.5	1.71	1.84	1500	N/A	300	0.0128
		12.5	1.74	1.81	1500	N/A	300	0.0136

Steel	Sheet/Tube Position	Initial Gauge Dimensions (mm) Length	Width	Thickness	Strain Rate (1/s) Nominal	Achieved	Initial Temp (°C)	Strain Offset
HSLA350	3 o'clock	50.8	12.81	1.82	0.0033	0.003	21	0
		50.8	12.74	1.81	0.0033	0.003	21	0
		50.8	12.71	1.81	0.0033	0.003	21	0
		12.5	1.73	1.81	0.0033	0.003	21	0.0223
		12.5	1.77	1.82	0.0033	0.003	21	0.0112
		12.5	1.75	1.83	0.0033	0.003	21	0.0098
		12.5	1.73	1.84	0.1	0.1	21	0.0046
		12.5	1.74	1.82	0.1	0.1	21	0.0217
		12.5	1.74	1.82	0.1	0.1	21	0.0038
		12.5	1.76	1.81	30	50	21	0.0011
		12.5	1.73	1.82	30	50	21	0.0082
		12.5	1.74	1.81	30	50	21	0.0049
		12.5	1.73	1.84	100	100	21	0.0065
		12.5	1.73	1.84	100	100	21	0.0092
		12.5	1.74	1.82	100	100	21	0.0165
		12.5	1.72	1.83	500	500	21	0.0100
		12.5	1.72	1.84	500	500	21	0.0062
		12.5	1.73	1.83	500	500	21	0.0071
		12.5	1.77	1.84	1000	940	21	0.0120
		12.5	1.75	1.84	1000	940	21	0.0070
		12.5	1.73	1.81	1000	940	21	0.0070
		12.5	1.74	1.83	1500	1265	21	0.0150
		12.5	1.74	1.83	1500	1265	21	0.0132
		12.5	1.74	1.85	1500	1265	21	0.0111

Steel	Sheet/Tube Position	Initial Gauge Dimensions (mm) Length	Width	Thickness	Strain Rate (1/s) Nominal	Achieved	Initial Temp (°C)	Strain Offset
HSLA350	6 o'clock	50.8	12.69	1.84	0.0033	0.003	21	0
		50.8	12.76	1.81	0.0033	0.003	21	0
		50.8	12.74	1.82	0.0033	0.003	21	0
		12.5	1.71	1.83	0.0033	0.003	21	0.0215
		12.5	1.72	1.83	0.0033	0.003	21	0.0086
		12.5	1.74	1.83	0.0033	0.003	21	0.0098
		12.5	1.73	1.82	0.1	0.1	21	0.0056
		12.5	1.76	1.84	0.1	0.1	21	0.0197
		12.5	1.73	1.82	0.1	0.1	21	0.0143
		12.5	1.73	1.80	30	50	21	0.0049
		12.5	1.77	1.81	30	50	21	0.0037
		12.5	1.72	1.81	30	50	21	0.0120
		12.5	1.73	1.83	100	100	21	0.0118
		12.5	1.74	1.83	100	100	21	0.0063
		12.5	1.72	1.83	100	100	21	0.0072
		12.5	1.71	1.82	500	500	21	0.0101
		12.5	1.74	1.84	500	500	21	0.0075
		12.5	1.73	1.81	500	500	21	0.0180
		12.5	1.73	1.84	1000	940	21	0.0160
		12.5	1.77	1.84	1000	940	21	0.0136
		12.5	1.73	1.84	1000	940	21	0.0220
		12.5	1.76	1.83	1500	1265	21	0.0120
		12.5	1.74	1.83	1500	1265	21	0.0165
		12.5	1.73	1.83	1500	1265	21	0.0180
		12.5	1.72	1.83	500	500	150	0.0066
		12.5	1.73	1.82	500	500	150	0.0066
		12.5	1.74	1.84	500	500	150	0.0072
		12.5	1.75	1.82	1500	1265	150	0.0120
		12.5	1.73	1.83	1500	1265	150	0.0165
		12.5	1.73	1.81	1500	1265	150	0.0212
		12.5	1.74	1.82	500	500	300	0.0066
		12.5	1.72	1.84	500	500	300	0.0066
		12.5	1.74	1.83	500	500	300	0.0086
		12.5	1.74	1.81	1500	1265	300	0.0204
		12.5	1.75	1.83	1500	1265	300	0.0110
		12.5	1.73	1.83	1500	1265	300	0.0100

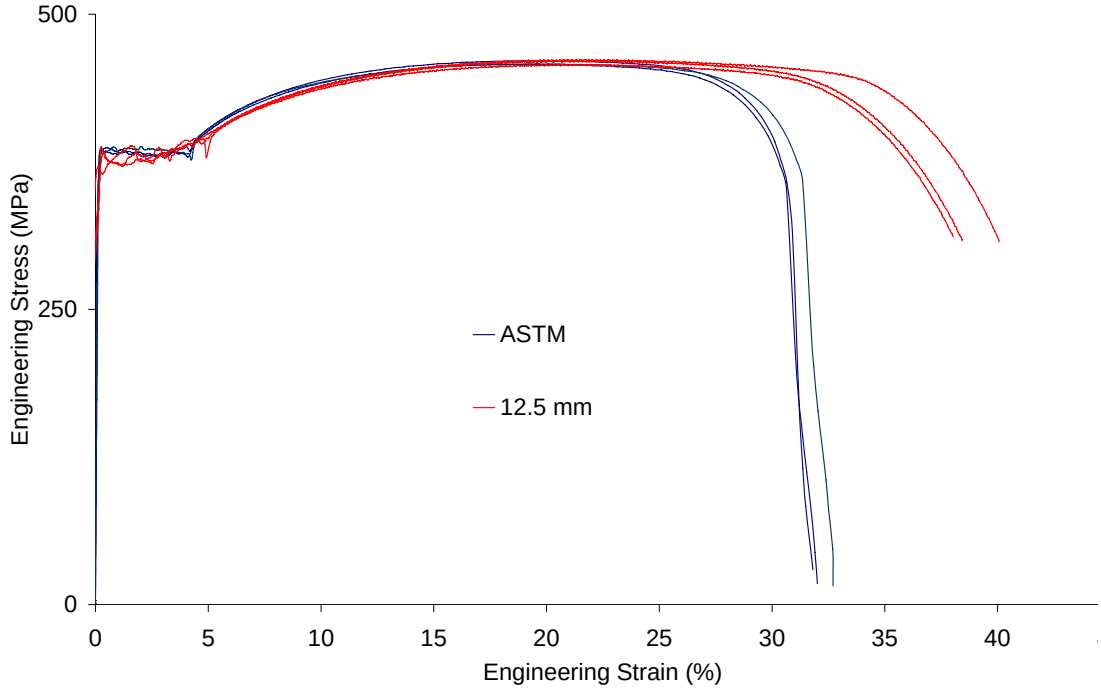

Figure A.10. Engineering stress vs. engineering strain of HSLA350 sheet at $0.0033s^{-1}$

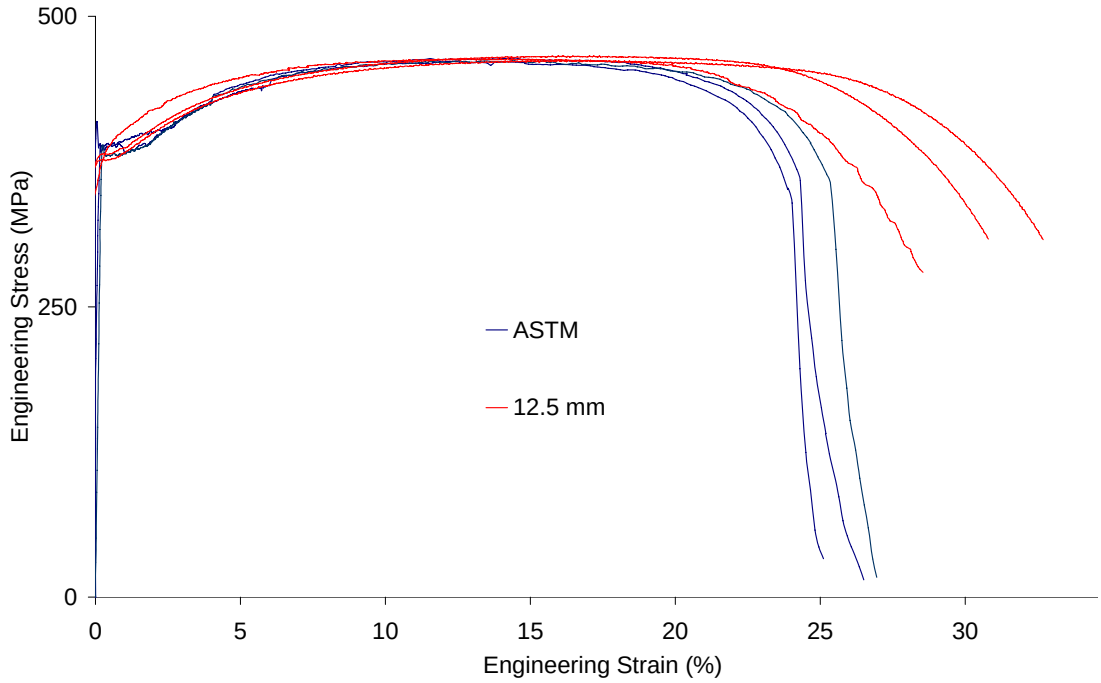

Figure A.11. Engineering stress vs. strain of HSLA350 tube (3 o'clock) at $0.0033s^{-1}$

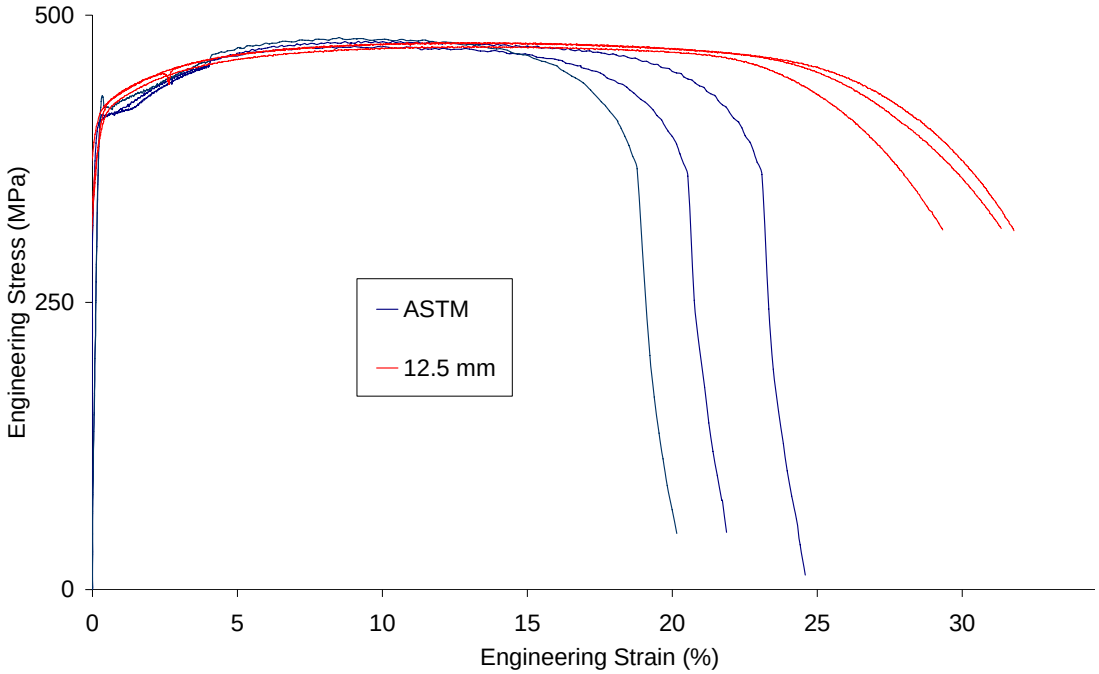

Figure A.12. Engineering stress vs. strain of HSLA350 tube (6 o'clock) at $0.0033s^{-1}$

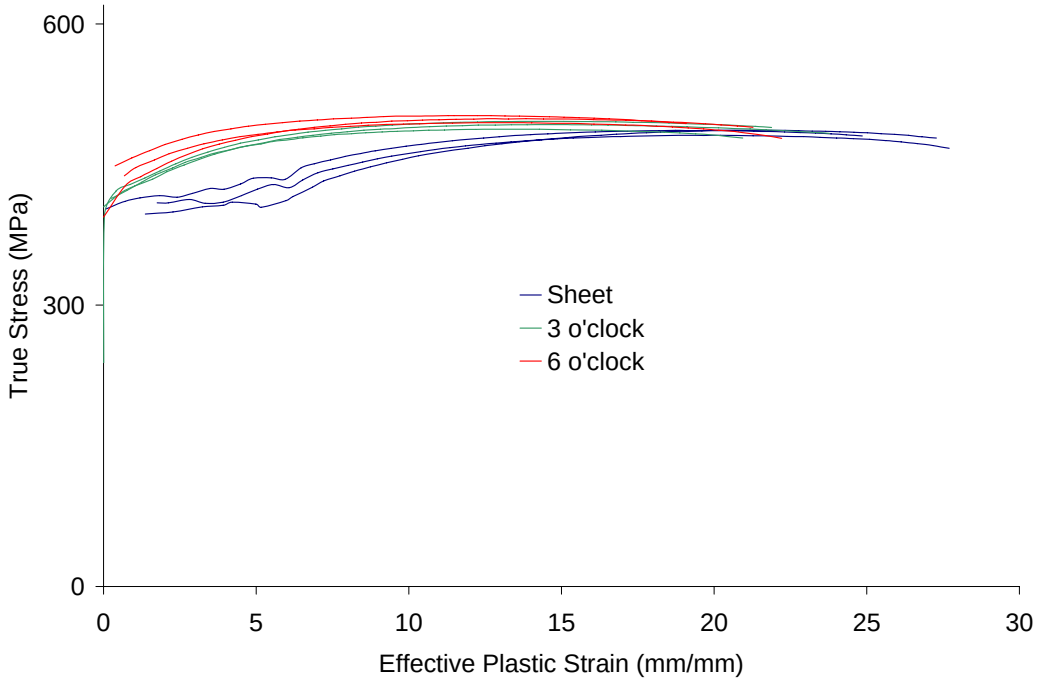

Figure A.13. Engineering stress vs. strain of HSLA350 sheet and tube at $0.1s^{-1}$

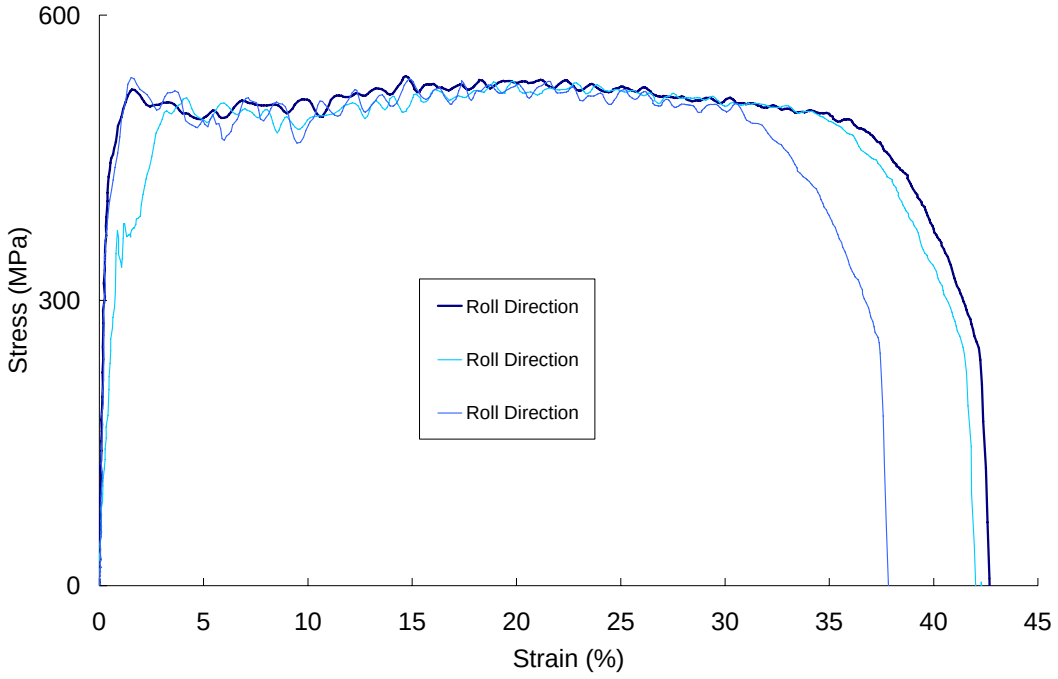

Figure A.14. Engineering stress vs. engineering strain of HSLA350 sheet at $37s^{-1}$

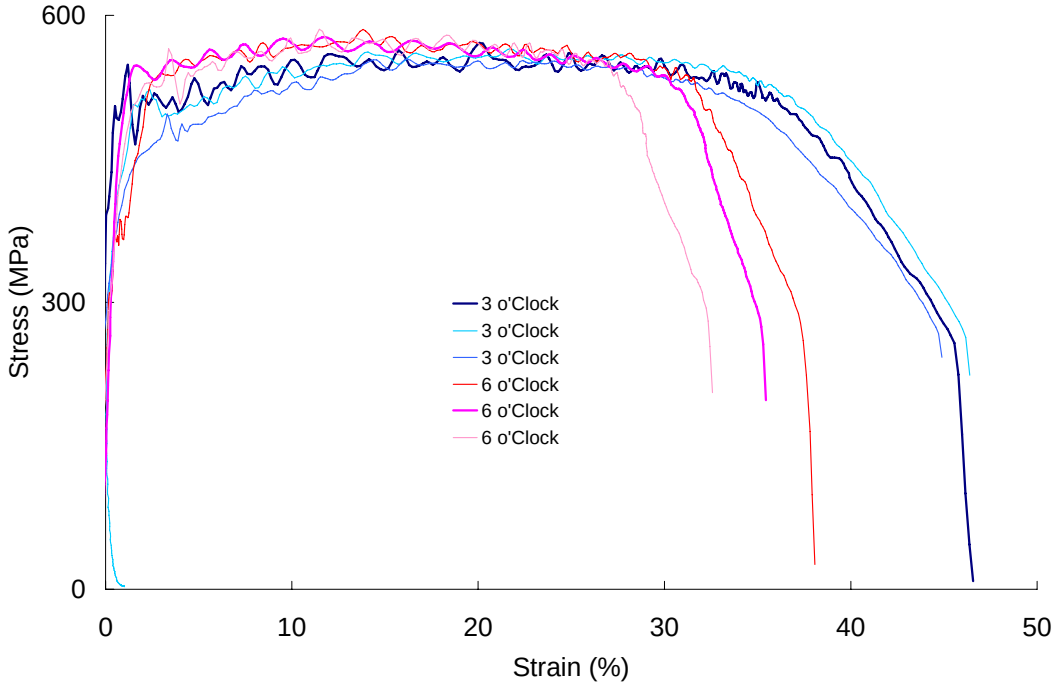

Figure A.15. Engineering stress vs. engineering strain of HSLA350 tube at $50s^{-1}$

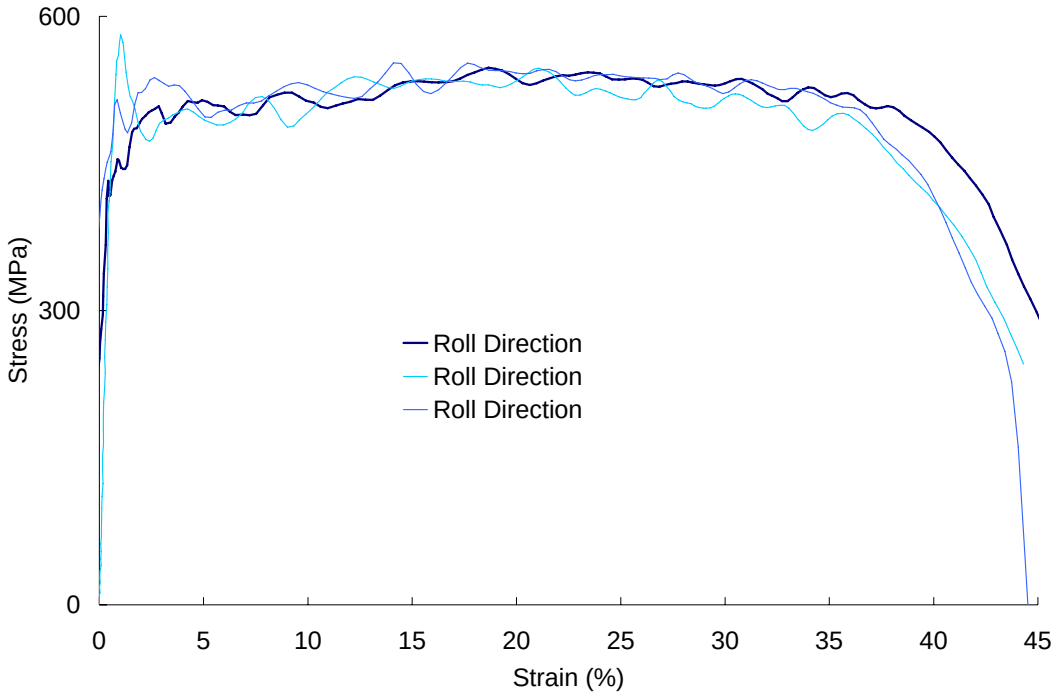

Figure A.16. Engineering stress vs. engineering strain of HSLA350 sheet at $100s^{-1}$

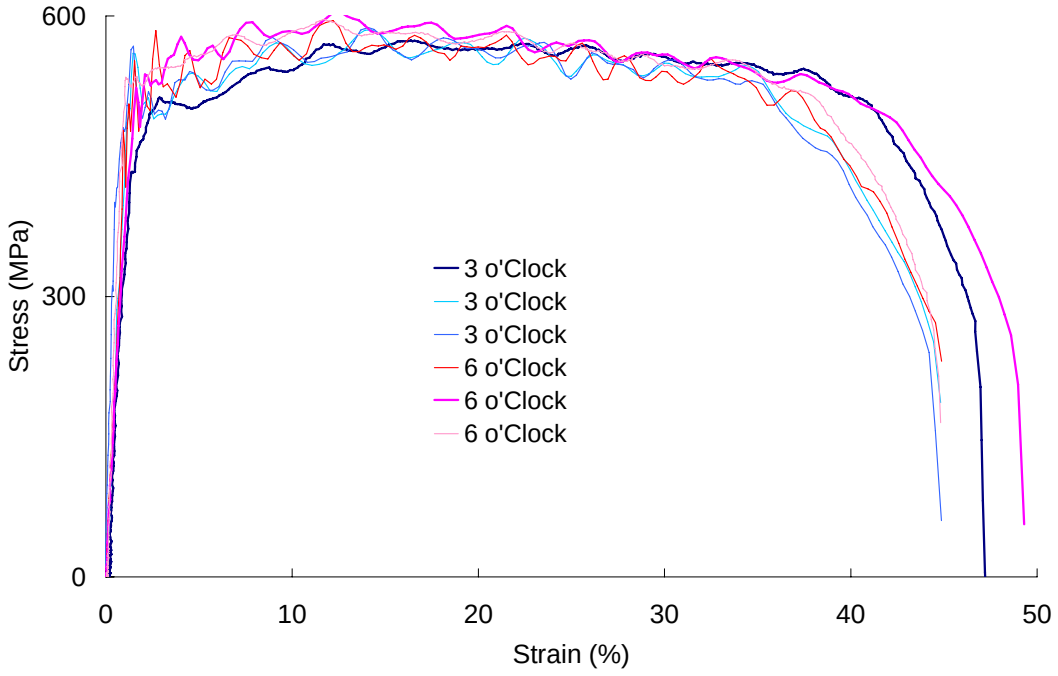

Figure A.17. Engineering stress vs. engineering strain of HSLA350 tube at $100s^{-1}$

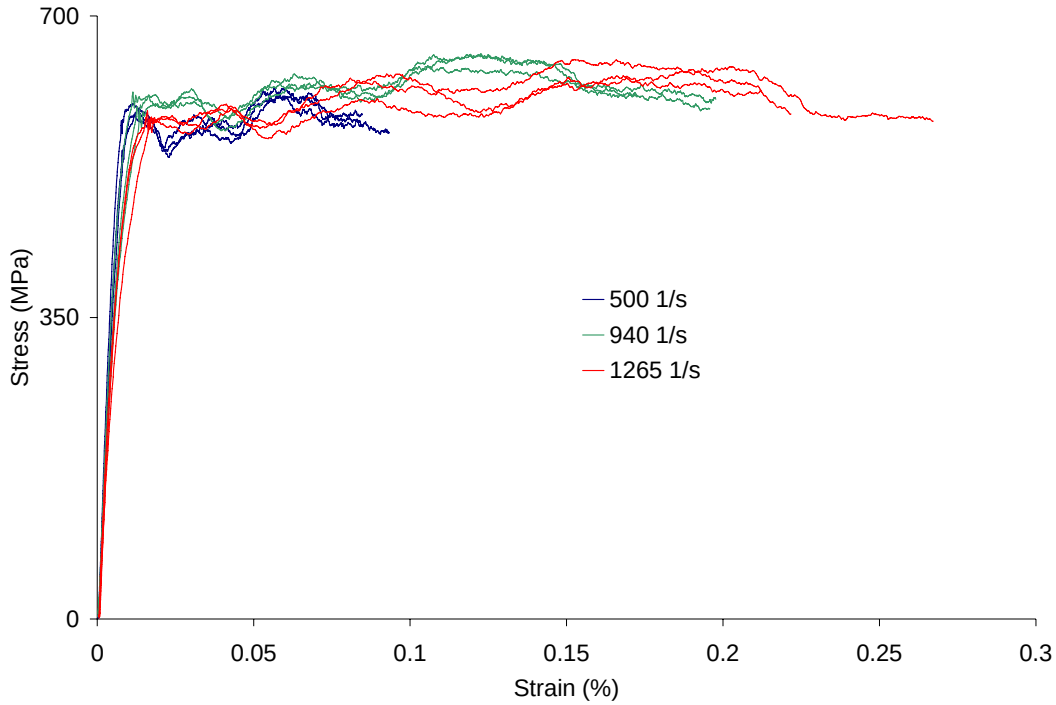

Figure A.18. Engineering stress vs. strain of HSLA350 tube (3 o'clock) at high rates

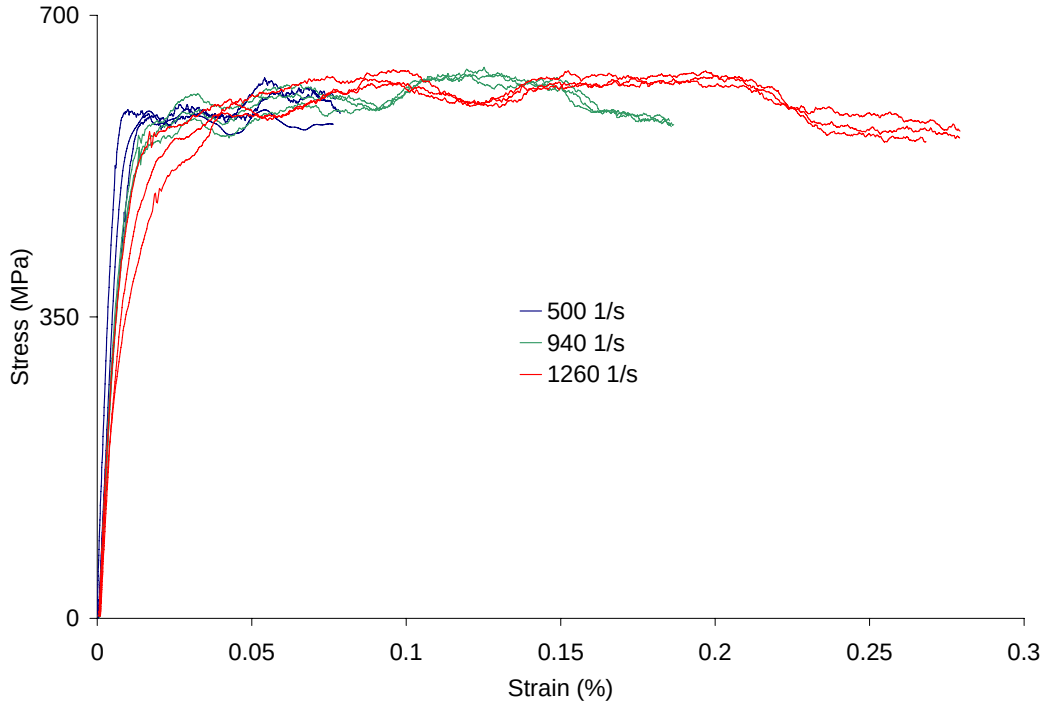

Figure A.19. Engineering stress vs. strain of HSLA350 tube (6 o'clock) at high rates

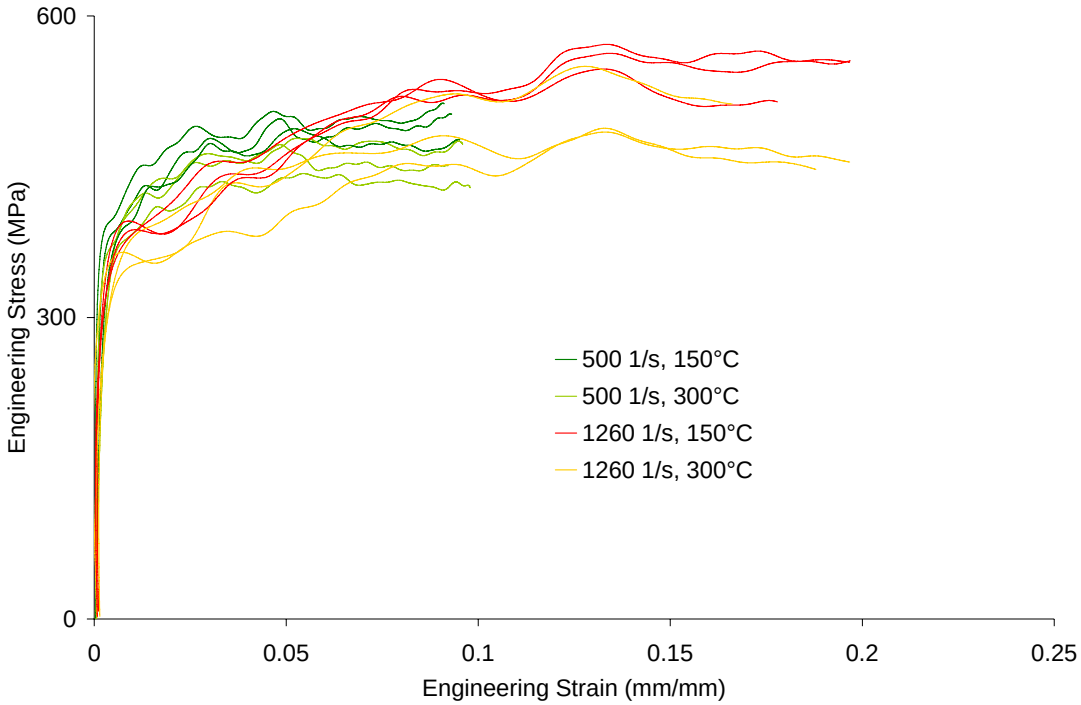

Figure A.20. Engineering stress vs. strain of HSLA350 tube at high temperatures

Steel	Sheet/Tube Position	Initial Gauge Dimensions (mm) Length	Width	Thickness	Strain Rate (1/s) Nominal	Achieved	Initial Temp (°C)	Strain Offset
DDQ	Sheet	50.8	12.72	1.88	0.0033	0.003	21	0
		50.8	12.68	1.87	0.0033	0.003	21	0
		50.8	12.74	1.86	0.0033	0.003	21	0
		12.5	1.77	1.86	0.0033	0.003	21	0.0211
		12.5	1.75	1.84	0.0033	0.003	21	0.0087
		12.5	1.73	1.86	0.0033	0.003	21	0.0086
		12.5	1.74	1.85	0.1	0.1	21	0.0045
		12.5	1.74	1.87	0.1	0.1	21	0.0208
		12.5	1.77	1.86	0.1	0.1	21	0.0087
		12.5	1.76	1.87	30	37	21	0.0087
		12.5	1.76	1.85	30	37	21	0.0088
		12.5	1.75	1.86	30	37	21	0.0094
		12.5	1.77	1.87	100	100	21	0.0072
		12.5	1.75	1.86	100	100	21	0.0101
		12.5	1.73	1.86	100	100	21	0.0075
		12.5	1.74	1.86	500	N/A	21	0.0180
		12.5	1.74	1.87	500	N/A	21	0.0160
		12.5	1.76	1.85	500	N/A	21	0.0070
		12.5	1.73	1.87	1000	N/A	21	0.0070
		12.5	1.74	1.86	1000	N/A	21	0.0150
		12.5	1.73	1.84	1000	N/A	21	0.0132
		12.5	1.73	1.86	1500	N/A	21	0.0136
		12.5	1.74	1.86	1500	N/A	21	0.0220
		12.5	1.73	1.86	1500	N/A	21	0.0162
		12.5	1.73	1.87	500	N/A	150	0.0112
		12.5	1.74	1.85	500	N/A	150	0.0059
		12.5	1.72	1.87	500	N/A	150	0.0055
		12.5	1.74	1.86	1500	N/A	150	0.0063
		12.5	1.74	1.86	1500	N/A	150	0.0084
		12.5	1.75	1.86	1500	N/A	150	0.0053
		12.5	1.72	1.86	500	N/A	300	0.0025
		12.5	1.74	1.85	500	N/A	300	0.0025
		12.5	1.73	1.87	500	N/A	300	0.0120
		12.5	1.76	1.86	1500	N/A	300	0.0153
		12.5	1.73	1.84	1500	N/A	300	0.0154
		12.5	1.73	1.85	1500	N/A	300	0.0114

Steel	Sheet/Tube Position	Initial Gauge Dimensions (mm) Length	Width	Thickness	Strain Rate (1/s) Nominal	Achieved	Initial Temp (°C)	Strain Offset
DDQ	3 o'clock	50.8	12.74	1.84	0.0033	0.003	21	0
		50.8	12.77	1.84	0.0033	0.003	21	0
		50.8	12.73	1.85	0.0033	0.003	21	0
		12.5	1.73	1.87	0.0033	0.003	21	0.0120
		12.5	1.74	1.85	0.0033	0.003	21	0.0173
		12.5	1.75	1.87	0.0033	0.003	21	0.0143
		12.5	1.74	1.86	0.1	0.1	21	0.0220
		12.5	1.75	1.86	0.1	0.1	21	0.0160
		12.5	1.72	1.86	0.1	0.1	21	0.0155
		12.5	1.77	1.86	30	50	21	0.0076
		12.5	1.76	1.83	30	50	21	0.0121
		12.5	1.76	1.88	30	50	21	0.0112
		12.5	1.74	1.86	100	115	21	0.0057
		12.5	1.76	1.87	100	115	21	0.0120
		12.5	1.73	1.88	100	115	21	0.0168
		12.5	1.74	1.87	500	500	21	0.0180
		12.5	1.73	1.86	500	500	21	0.0210
		12.5	1.73	1.85	500	500	21	0.0142
		12.5	1.74	1.87	1000	940	21	0.0060
		12.5	1.72	1.87	1000	940	21	0.0070
		12.5	1.72	1.88	1000	940	21	0.0112
		12.5	1.73	1.86	1500	1360	21	0.0059
		12.5	1.77	1.86	1500	1360	21	0.0055
		12.5	1.75	1.86	1500	1360	21	0.0063

Steel	Sheet/Tube Position	Initial Gauge Dimensions (mm) Length	Width	Thickness	Strain Rate (1/s) Nominal	Achieved	Initial Temp (°C)	Strain Offset
DDQ	6 o'clock	50.8	12.71	1.84	0.0033	0.003	21	0
		50.8	12.68	1.81	0.0033	0.003	21	0
		50.8	12.77	1.82	0.0033	0.003	21	0
		12.5	1.72	1.84	0.0033	0.003	21	0.0066
		12.5	1.73	1.83	0.0033	0.003	21	0.0055
		12.5	1.77	1.83	0.0033	0.003	21	0.0063
		12.5	1.75	1.83	0.1	0.1	21	0.0078
		12.5	1.71	1.83	0.1	0.1	21	0.0046
		12.5	1.72	1.82	0.1	0.1	21	0.0097
		12.5	1.74	1.84	30	50	21	0.0076
		12.5	1.73	1.84	30	50	21	0.0076
		12.5	1.74	1.84	30	50	21	0.0076
		12.5	1.72	1.84	100	115	21	0.0082
		12.5	1.73	1.83	100	115	21	0.0047
		12.5	1.74	1.83	100	115	21	0.0068
		12.5	1.72	1.83	500	500	21	0.0101
		12.5	1.71	1.83	500	500	21	0.0165
		12.5	1.74	1.82	500	500	21	0.0122
		12.5	1.73	1.84	1000	940	21	0.0074
		12.5	1.73	1.82	1000	940	21	0.0062
		12.5	1.77	1.83	1000	940	21	0.0120
		12.5	1.73	1.81	1500	1360	21	0.0068
		12.5	1.76	1.82	1500	1360	21	0.0071
		12.5	1.74	1.84	1500	1360	21	0.0068
		12.5	1.73	1.83	500	500	150	0.0068
		12.5	1.72	1.84	500	500	150	0.0101
		12.5	1.73	1.82	500	500	150	0.0165
		12.5	1.74	1.83	1500	1360	150	0.0120
		12.5	1.75	1.84	1500	1360	150	0.0165
		12.5	1.73	1.83	1500	1360	150	0.0180
		12.5	1.74	1.84	500	500	300	0.0066
		12.5	1.73	1.84	500	500	300	0.0060
		12.5	1.73	1.81	500	500	300	0.0075
		12.5	1.74	1.83	1500	1360	300	0.0101
		12.5	1.72	1.82	1500	1360	300	0.0165
		12.5	1.74	1.82	1500	1360	300	0.0212

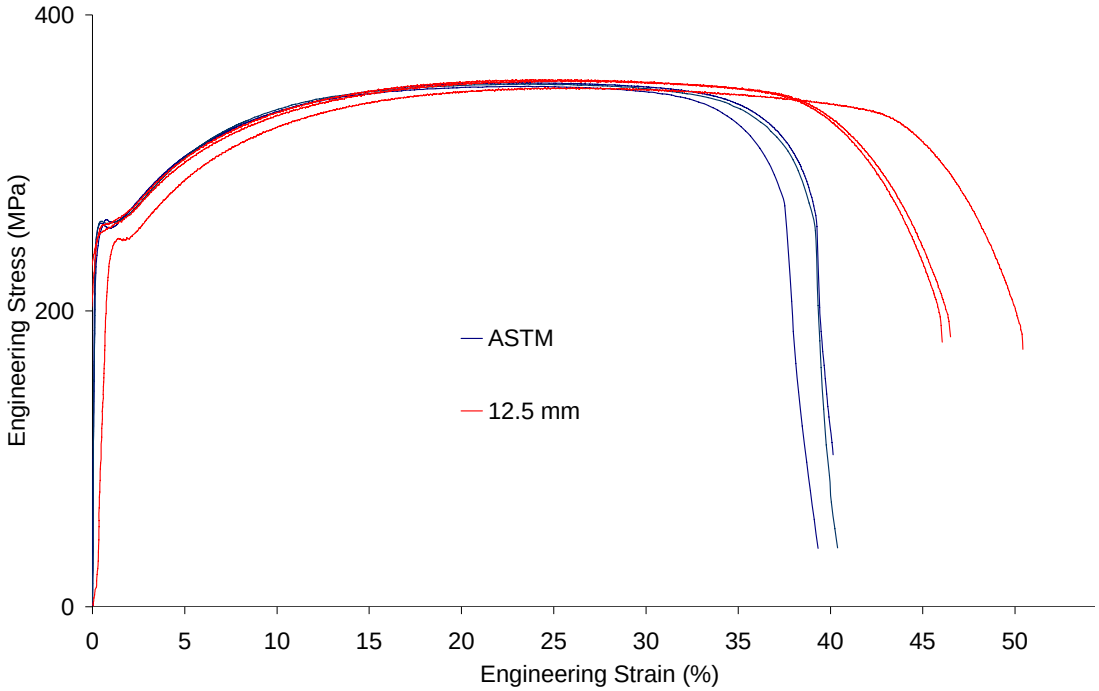

Figure A.21. Engineering stress vs. engineering strain of DDQ sheet at 0.0033s^{-1}

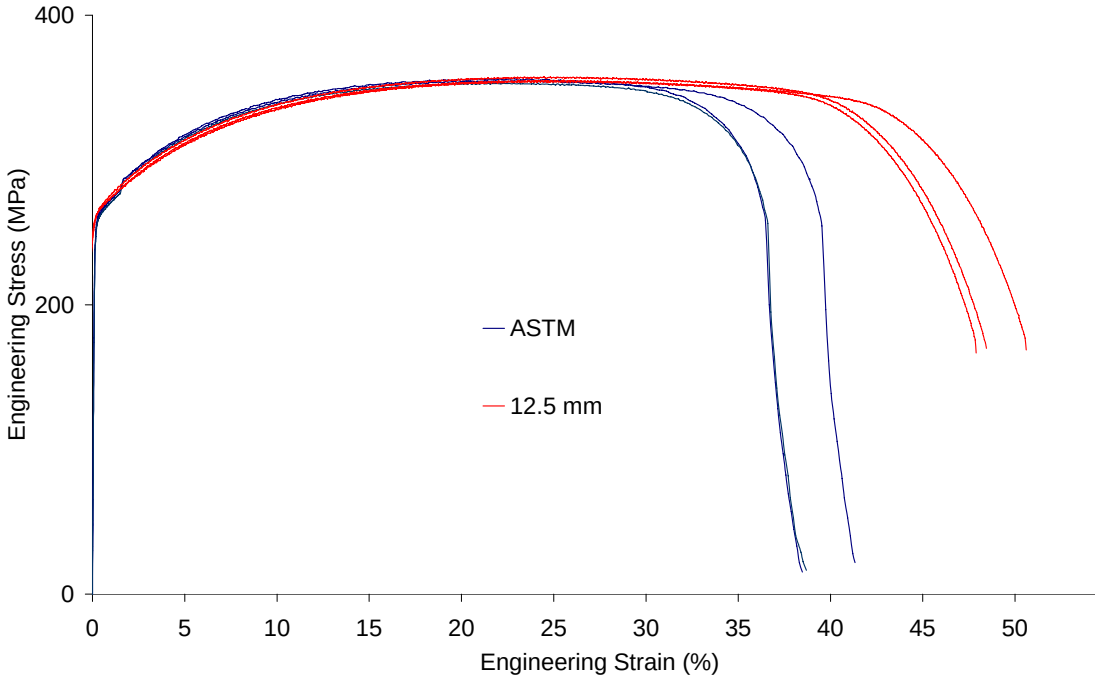

Figure A.22. Engineering stress vs. strain of DDQ tube (3 o'clock) at 0.0033s^{-1}

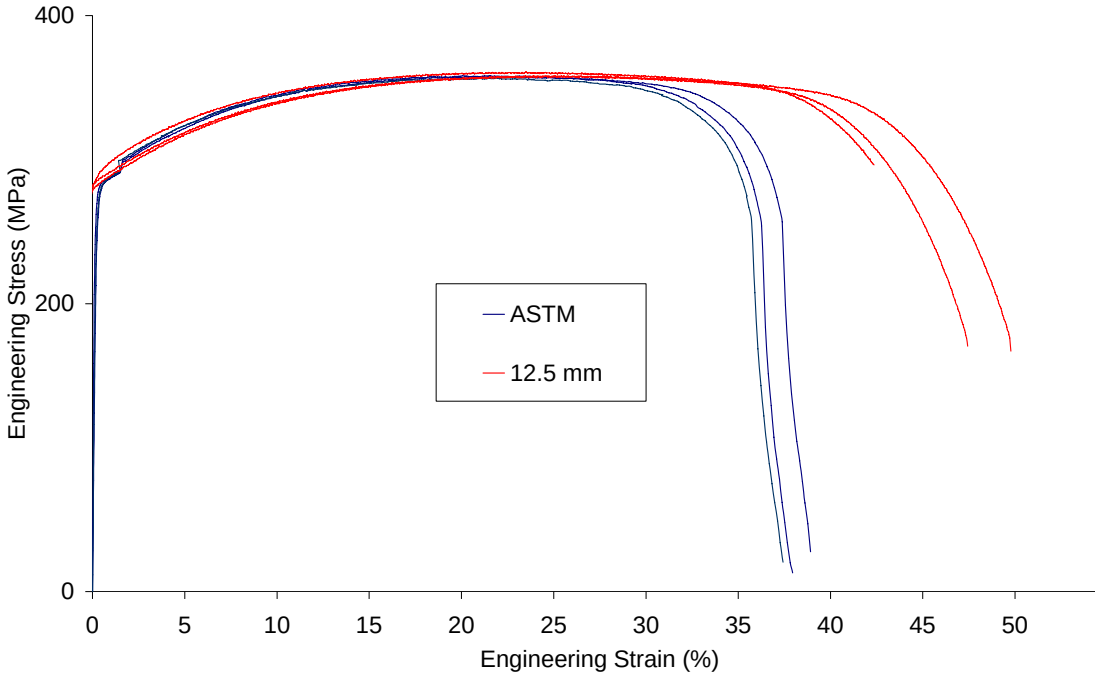

Figure A.22. Engineering stress vs. strain of DDQ tube (6 o'clock) at $0.0033s^{-1}$

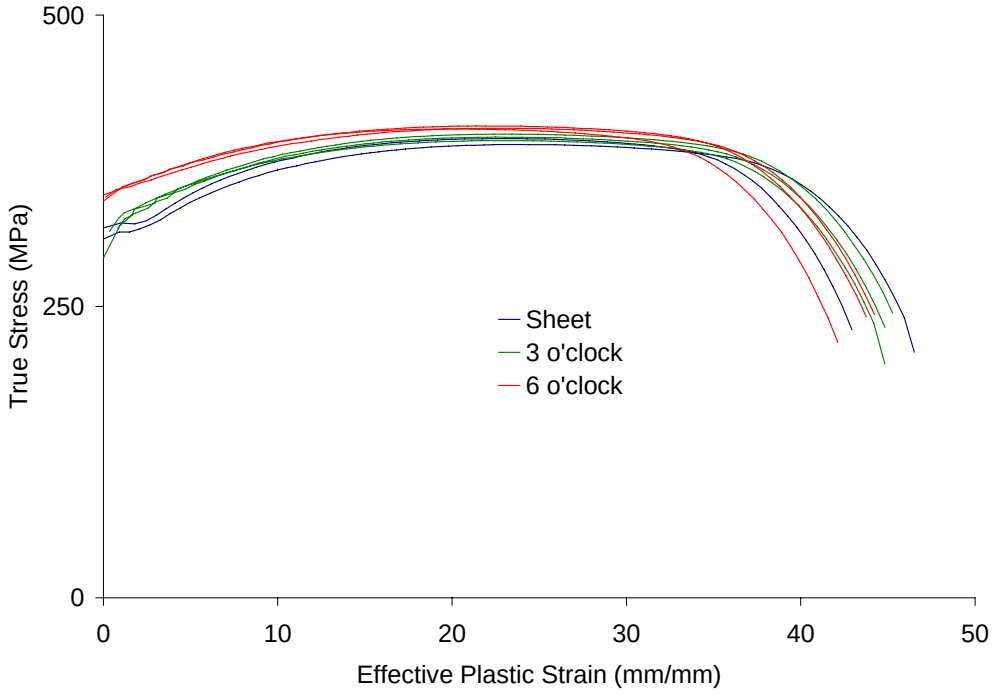

Figure A.23. Engineering stress vs. strain of DDQ sheet and tube at $0.1s^{-1}$

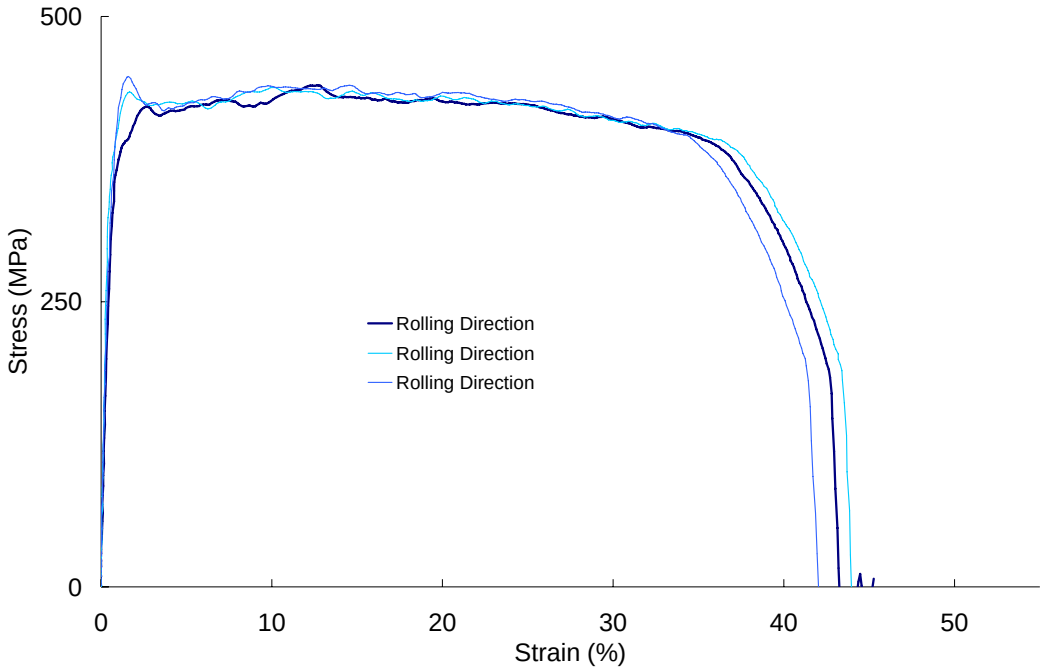

Figure A.24. Engineering stress vs. engineering strain of DDQ sheet at $37s^{-1}$

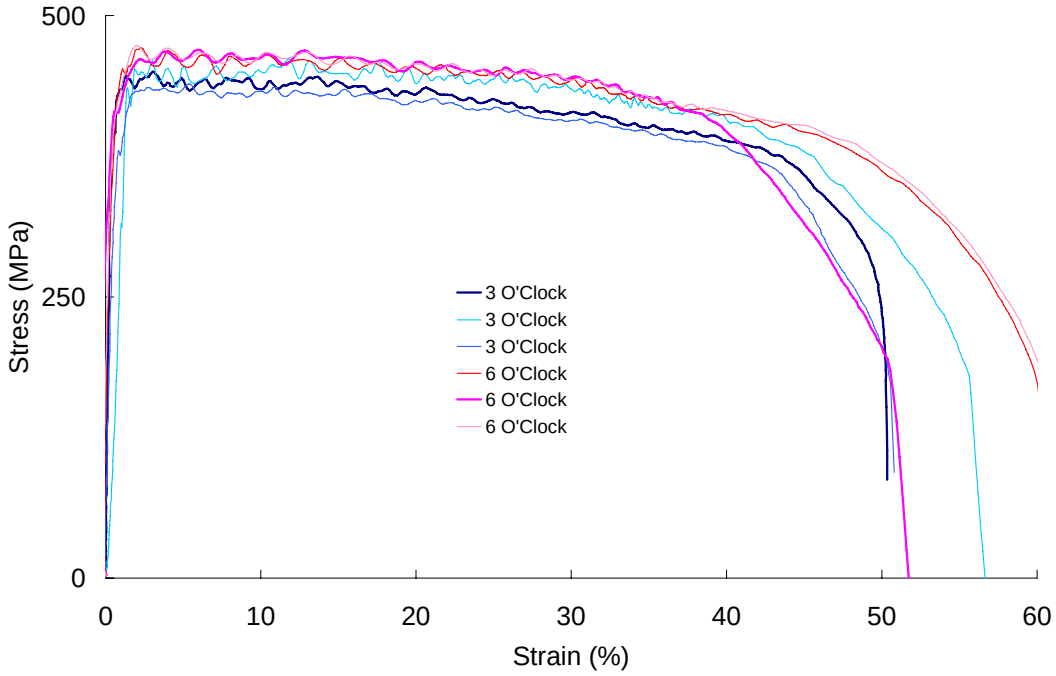

Figure A.25. Engineering stress vs. engineering strain of DDQ tube at $50s^{-1}$

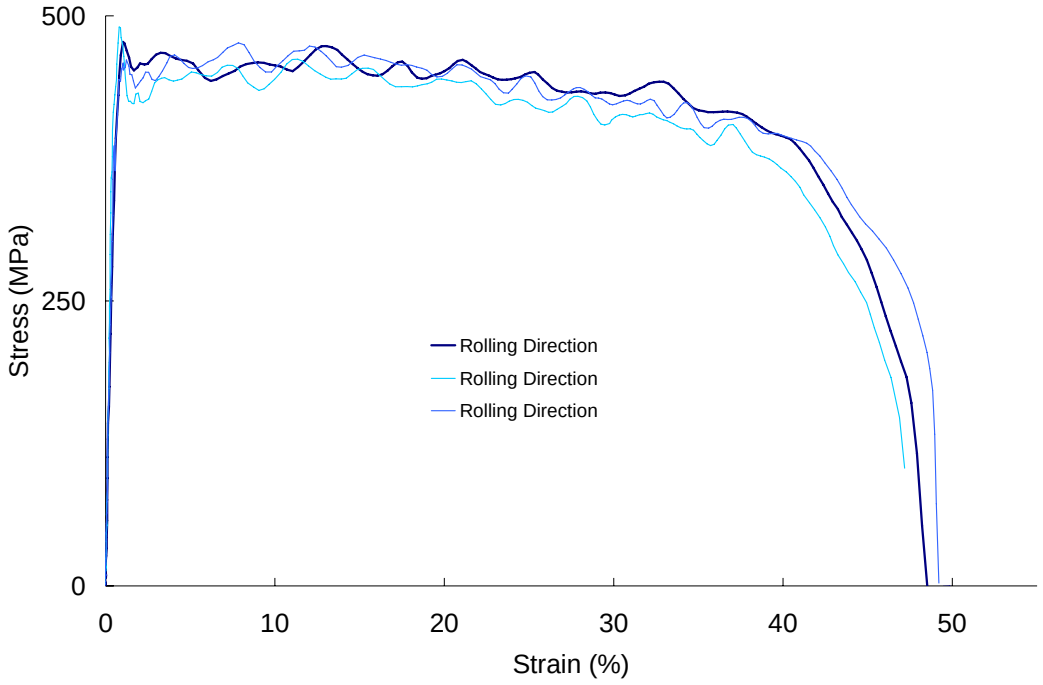

Figure A.26. Engineering stress vs. engineering strain of DDQ sheet at $100s^{-1}$

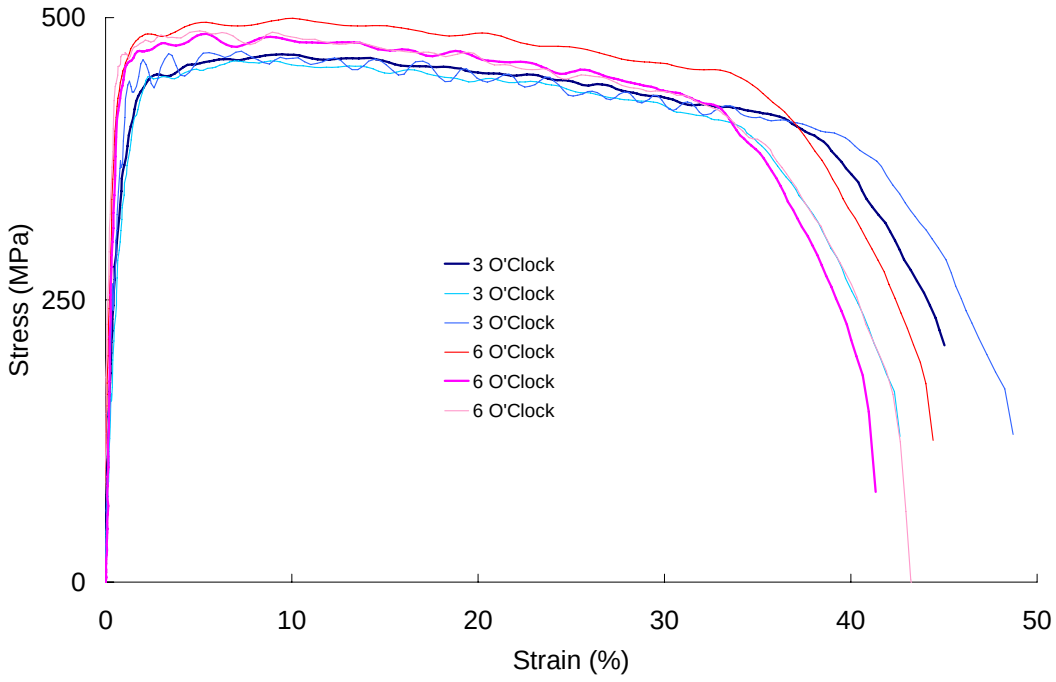

Figure A.27. Engineering stress vs. engineering strain of DDQ tube at $100s^{-1}$

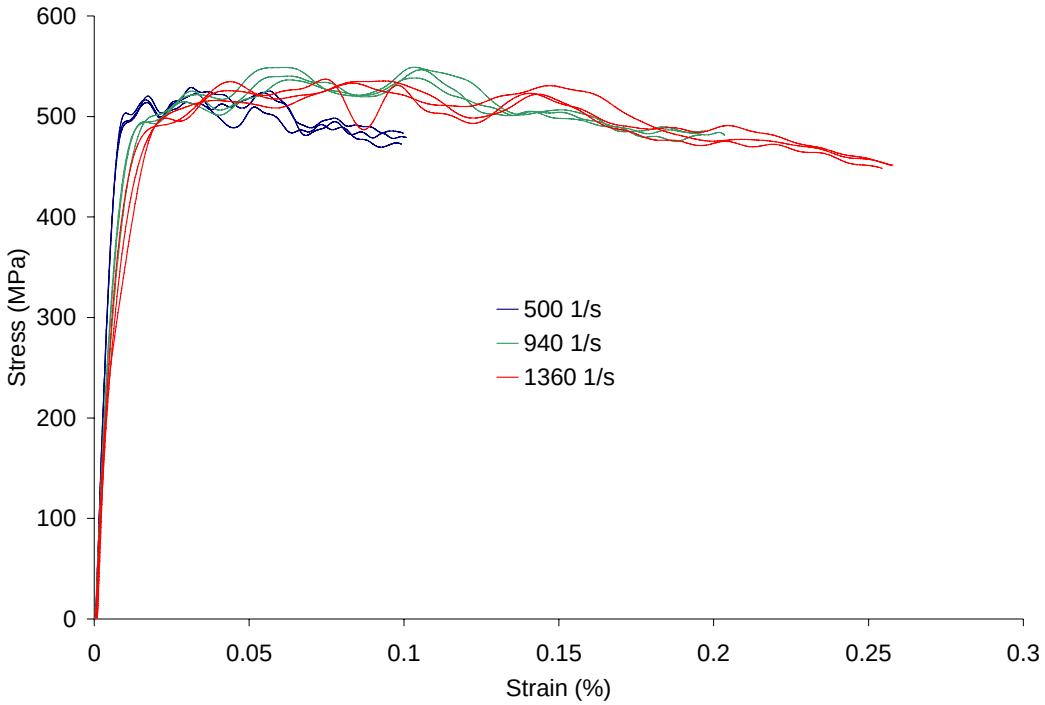

Figure A.28. Engineering stress vs. strain of DDQ tube (3 o'clock) at high rates

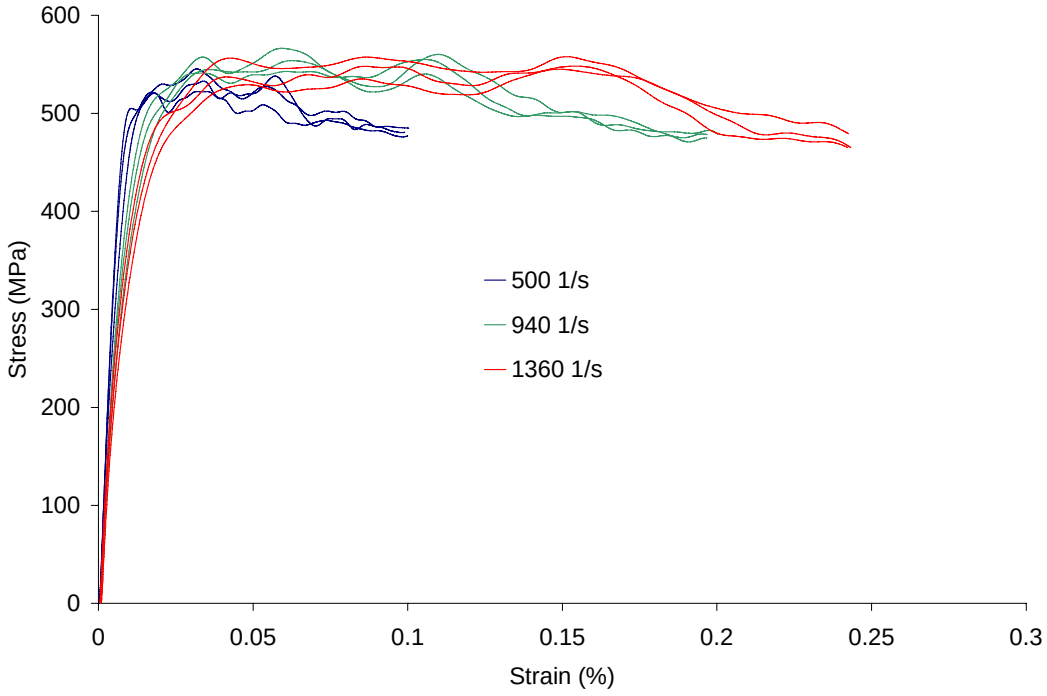

Figure A.29. Engineering stress vs. strain of DDQ tube (6 o'clock) at high rates

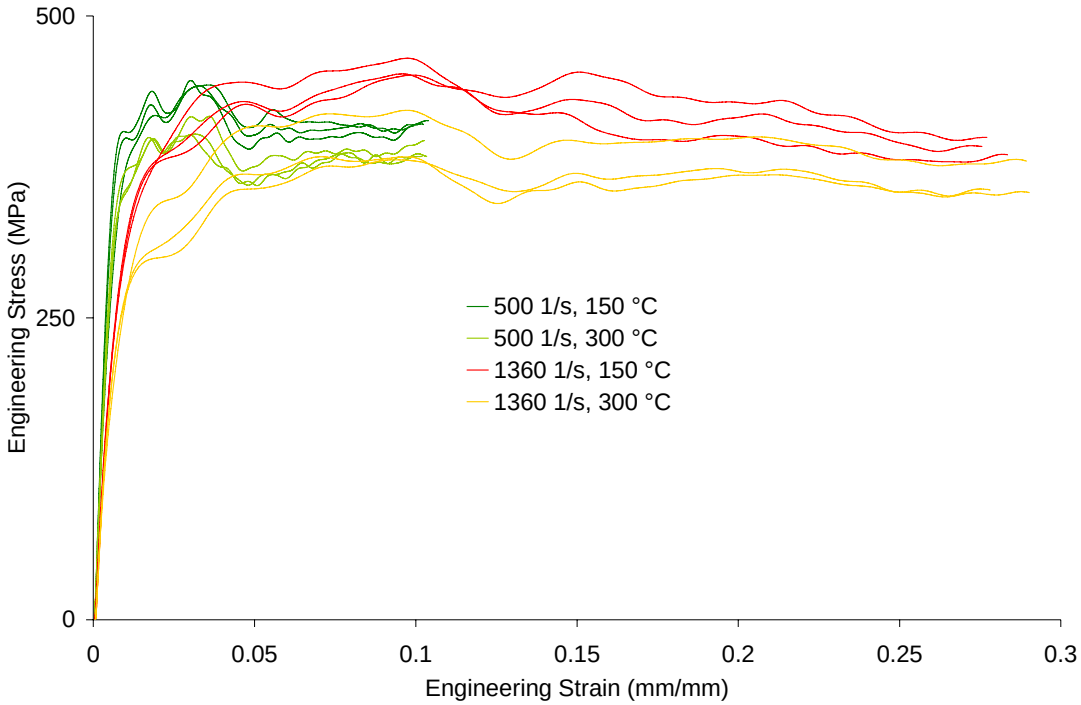

Figure A.29. Engineering stress vs. strain of DDQ tube at high temperatures

APPENDIX B

Strain-to-Failure for Sheet and Tube (3 o'clock) Specimens

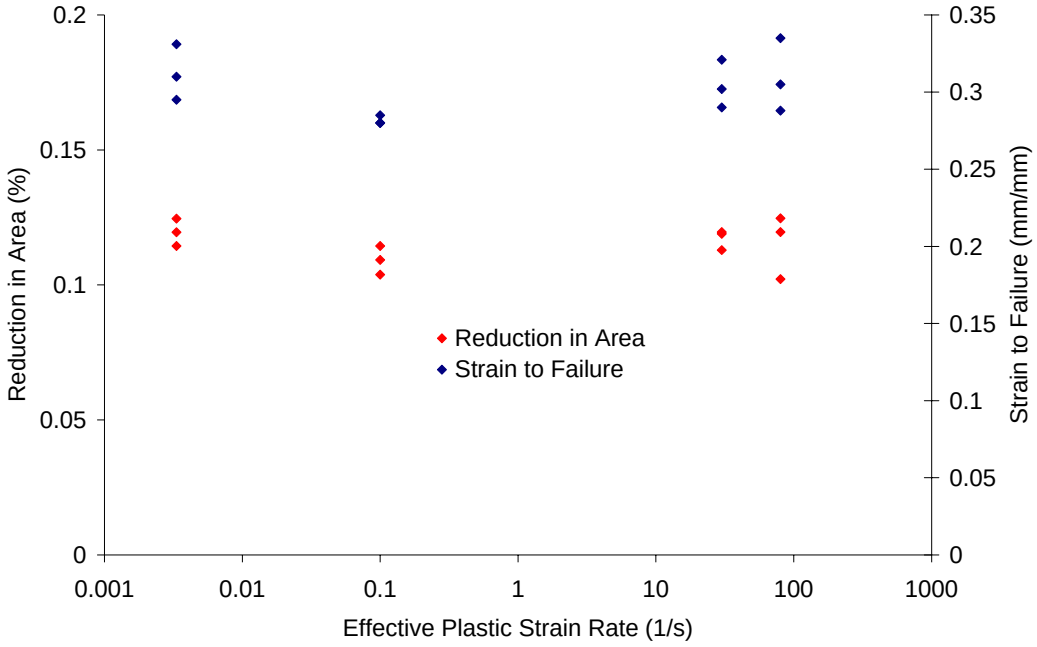

Figure B.1. Strain to Failure and Reduction in Area of DP600 sheet specimens

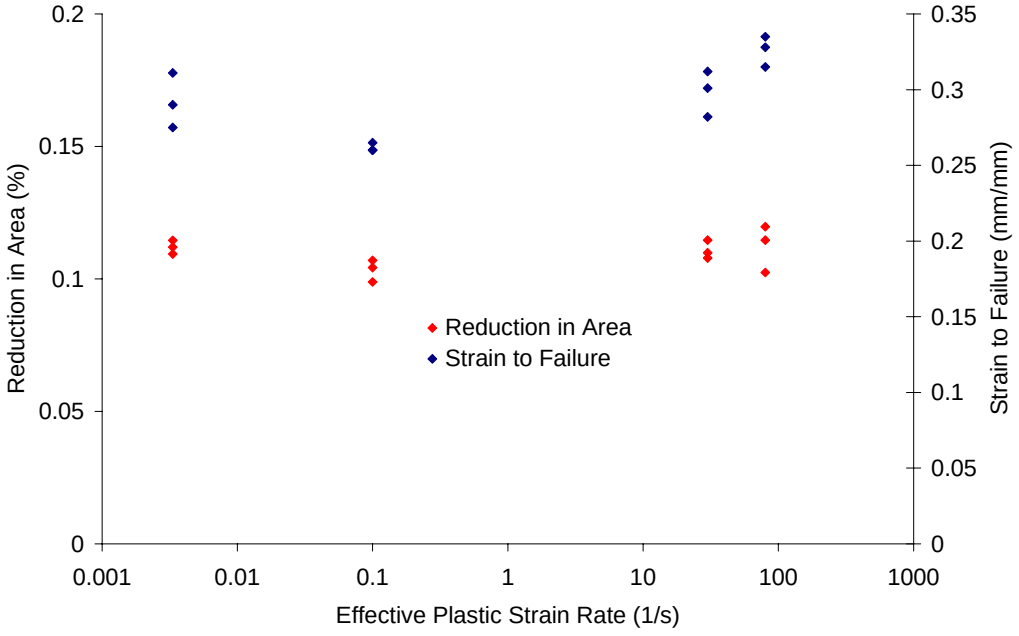

Figure B.2. Strain to Failure and Reduction in Area of DP600 tube (3 o'clock) specimens

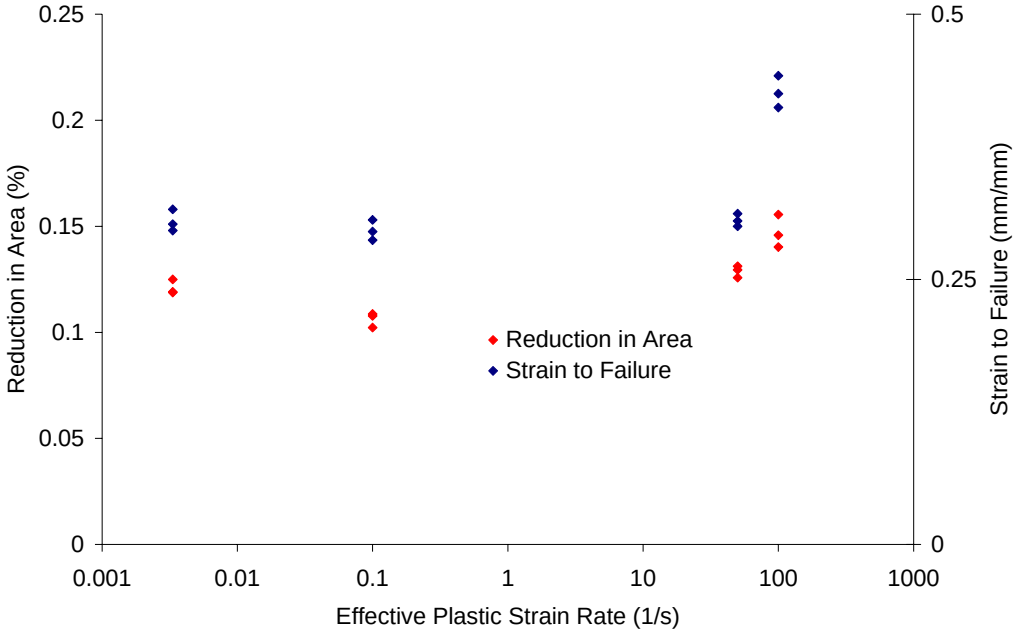

Figure B.3. Strain to Failure and Reduction in Area of HSLA350 sheet specimens

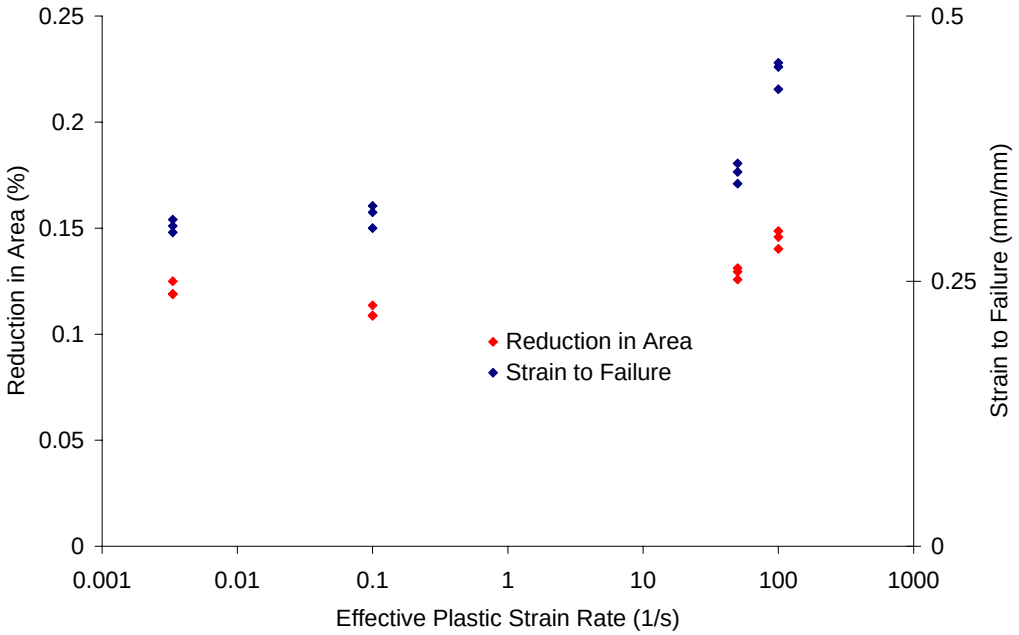

Figure B.4. Failure Strain and Reduction in Area of HSLA350 tube (3 o'clock) specimens

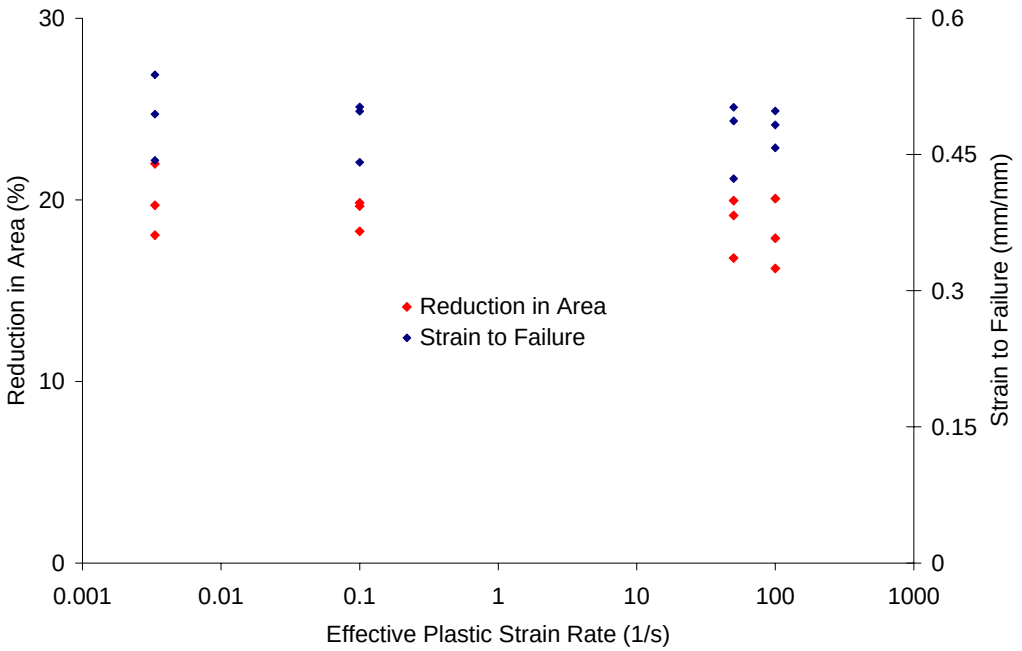

Figure B.5. Strain to Failure and Reduction in Area of DDQ sheet specimens

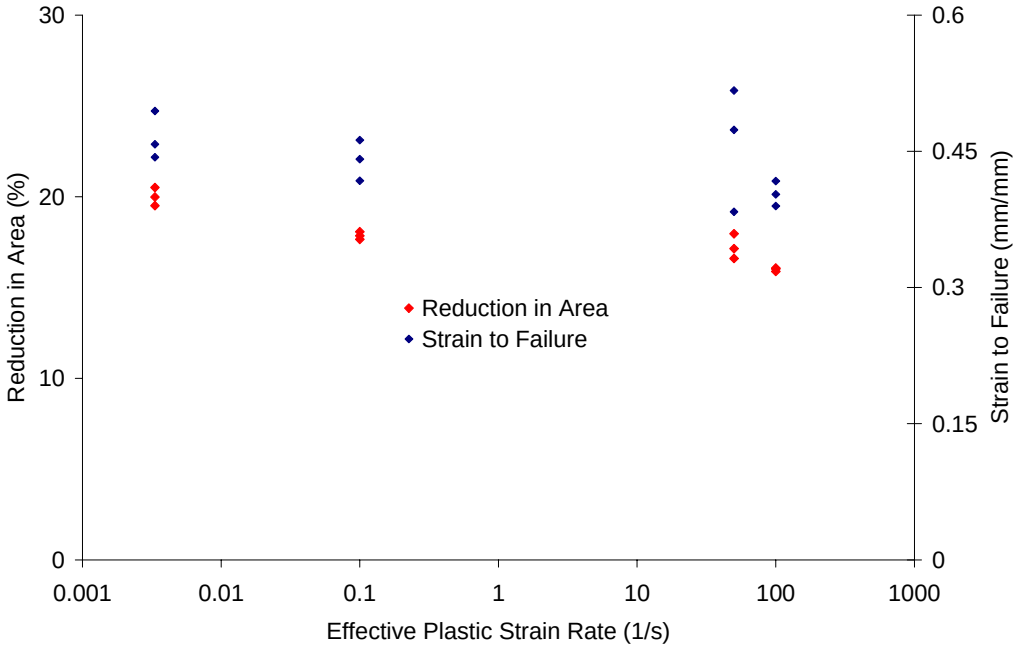

Figure B.6. Failure Strain and Reduction in Area of DDQ tube (3 o'clock) specimens

APPENDIX C

LS-Dyna Deck for the IFWI simulation using the Johnson-Cook Constitutive Model

```
*KEYWORD 25000000
$
*TITLE
Single pulse failure
$
$ User supplied input:
$
$
$ User supplied input:
$
$---+----1----+----2----+----3----+----4----+----5----+----6----+----7-
---+----8
$
$ N-mm-ms-g-MPa
$
$ Optional Control Cards that have been modified.
$
$---+----1----+----2----+----3----+----4----+----5----+----6----+----7-
---+----8
$
*CONTROL_BULK_VISCOSITY
$       Q1        Q2      TYPE
       .1,        0.01,      1
*CONTROL_TERMINATION
$ Time (in millisec) that the simulation stops after.
$   ENDTIM    ENDCYC     DTMIN    ENDNEG    ENDMAS
        15         0
$
$
*CONTROL_HOURGLASS
$ Change the default hourglass control to a Flanagan-Belytschko with
exact volum
$ integration... recommended for large deformations
$      IHQ        QH
         3     0.100
$
$
*CONTROL_CONTACT
$ Allow the Shell thickness to be considered in surface to surface and
node to
$ surface type contacts.
$   SLSFAC    RWPNAL    ISLCHK    SHLTHK    PENOPT    THKCHG     ORIEN
     0.010     0.000         2         1         4         1         1
$   USRSTR    USRFAC     NSBCS    INTERM    XPENEN
         0         0        10         0     4.000
$
*CONTROL_ENERGY
$ Used to allow hourglass energy to be calculated and stored in the
$ GLSTAT and MATSUM ASCII files
$     HGEN      RWEN    SLNTEN     RYLEN
         2         2         2         1
$
```

```
$
$---+----1----+----2----+----3----+----4----+----5----+----6----+----7-
---+----8
$
$ ASCII and LS TAURUS output
$
$---+----1----+----2----+----3----+----4----+----5----+----6----+----7-
---+----8
$
*DATABASE_RCFORC
$       DT
 0.100E+00
$
*DATABASE_RBDOUT
$       DT
 0.0250+00
$
*DATABASE_GLSTAT
$       DT
 0.0250+00
$
*DATABASE_BNDOUT
$       DT
 0.0250+00
$
$
$
$
*DATABASE_BINARY_D3PLOT
$  DT/CYCL      LCDT    NOBEAM
 0.100E+00
$
*DATABASE_EXTENT_BINARY
$    NEIPH     NEIPS    MAXINT    STRFLG    SIGFLG    EPSFLG    RLTFLG
ENGFLG
         5         0         7         1         1         1         1
1
$   CMPFLG    IEVERP    BEAMIP     DCOMP      SHGE     STSSZ
         0         0         0         2         0         0
$
$
$---+----1----+----2----+----3----+----4----+----5----+----6----+----7-
---+----8
$
$ Parts
$
$---+----1----+----2----+----3----+----4----+----5----+----6----+----7-
---+----8
$
*PART
Specimen
$      PID     SECID       MID     EOSID      HGID      GRAV    ADPOPT
         2         1         3         0
$
*PART
lowerjaw
$      PID     SECID       MID     EOSID      HGID      GRAV    ADPOPT
```

```
         1         1         1         0
$
*PART
upperjaw
$      PID     SECID       MID     EOSID      HGID      GRAV    ADPOPT
         3         1         1         0
$
*PART
loadcell
$      PID     SECID       MID     EOSID      HGID      GRAV    ADPOPT
         4         1         4         0
$
$
$---+----1----+----2----+----3----+----4----+----5----+----6----+----7-
---+----8
$
$ material/section data
$
$---+----1----+----2----+----3----+----4----+----5----+----6----+----7-
---+----8
$
$
*MAT_ELASTIC
$      MID        RO         E        PR         K         N       SRC
SRP
         1 4.420E-03    120000      0.31
$
$*MAT_ELASTIC
$      MID        RO         E        PR         K         N       SRC
SRP
$         2   1.15e-3      4134      0.35
$
$----- MATERIAL MODEL FOR SAMPLE-----------------------------------------
----
*MAT_USER_DEFINED_MATERIAL_MODELS
$      MID        R0        MT       LMC       NHV    IORTHO     IBULK
IG
         3,  7.83E-03,      49,       27,        5,        0,         9,
1
$    IVECT     IFAIL
         0,        1
$       G0         A         B         N         C         M
78.74E+03,   165.00,   968.57,    00.206,     0.0144,    0.867
$       BK      TREF      EREF     TMELT     ITEMP        CP       IR0
MFLAG
   205E+03,       23,  1.0E-03,   1370.,      23,        450, 7.83E-03,
1
$   sy           siter,  stoler, arr_t1, elem1,   elem2, elem3, elem4
  360.0,         50,     1.e-2,   0.000, 33847,  33799,  26089, 26799
$ elem5, crvid,  cl
  26308,    3,  0.00
$
$----- MATERIAL MODEL upper jaw and load cell-------------------------
--------
$*MAT_ELASTIC
$      MID        RO         E        PR         K         N       SRC
SRP
```

```
$         4    2.7e-3    2.09e5      0.31
*MAT_USER_DEFINED_MATERIAL_MODELS
$      MID        RO        MT       LMC       NHV    IORTHO     IBULK
IG
         4, 8.100E-3,       50,      10,         2,        0,         2,
1
$    IVECT     IFAIL
         0,         1
$       G0        K0, inc_t1, trans_t1, e1, e2, e3, e4
     5.2e3, 68.853E3,  0.000, 0.000, 33847,33799, 0, 0
$    rho,  cl
  8.10e-3, 0.0
$
$
$
*SECTION_SOLID
$    SECID    ELFORM
         1         1
$
$
$---+----1----+----2----+----3----+----4----+----5----+----6----+----7-
---+----8
$
$ Contact Definitions
$
$---+----1----+----2----+----3----+----4----+----5----+----6----+----7-
---+----8
$
$ Cylinder(Slave) to Plate(Master)
$
$
$---+----1----+----2----+----3----+----4----+----5----+----6----+----7-
---+----8
$
$ Load Curve and Boundary Conditions
$
$---+----1----+----2----+----3----+----4----+----5----+----6----+----7-
---+----8
$
$
*BOUNDARY_PRESCRIBED_MOTION_SET
$   typeID       DOF       VAD      LCID        SF       VID     DEATH
BIRTH
         6         2         2         1       1.0
0
$
$
$
$Include File Containing FE Mesh Here
$
*INCLUDE
dtmesh.in
$
*INCLUDE
disp.insert
$
*END
```

LS-Dyna Deck for the TSHB simulation using the Johnson-Cook Constitutive Model

```
*KEYWORD 25000000
$
*TITLE
Single pulse failure
$
$ User supplied input:
$
$
$ User supplied input:
$
$---+----1----+----2----+----3----+----4----+----5----+----6----+----7-
---+----8
$
$ N-mm-ms-g-MPa
$
$ Optional Control Cards that have been modified.
$
$---+----1----+----2----+----3----+----4----+----5----+----6----+----7-
---+----8
$
*CONTROL_TERMINATION
$ Time (in millisec) that the simulation stops after.
$   ENDTIM    ENDCYC     DTMIN    ENDNEG    ENDMAS
         1         0
$
$
*CONTROL_HOURGLASS
$ Change the default hourglass control to a Flanagan-Belytschko with
exact volum
$ integration... recommended for large deformations
$      IHQ        QH
         3     0.100
$
$
*CONTROL_CONTACT
$ Allow the Shell thickness to be considered in surface to surface and
node to
$ surface type contacts.
$   SLSFAC    RWPNAL    ISLCHK    SHLTHK    PENOPT    THKCHG     ORIEN
     0.010     0.000         2         1         4         1         1
$   USRSTR    USRFAC     NSBCS    INTERM    XPENEN
         0         0        10         0     4.000
$
*CONTROL_ENERGY
$ Used to allow hourglass energy to be calculated and stored in the
$ GLSTAT and MATSUM ASCII files
$     HGEN      RWEN    SLNTEN     RYLEN
         2         2         2         1
$
$
$---+----1----+----2----+----3----+----4----+----5----+----6----+----7-
---+----8
$
```

```
$ ASCII and LS TAURUS output
$
$---+----1----+----2----+----3----+----4----+----5----+----6----+----7-
---+----8
$
*DATABASE_RCFORC
$       DT
 0.010E+00
$
$
*DATABASE_GLSTAT
$       DT
 0.050E+00
$
*DATABASE_BNDOUT
$       DT
 0.05E+00
$
$
*DATABASE_BINARY_D3PLOT
$  DT/CYCL      LCDT    NOBEAM
 0.010E+00
$
*DATABASE_EXTENT_BINARY
$    NEIPH     NEIPS    MAXINT    STRFLG    SIGFLG    EPSFLG    RLTFLG
ENGFLG
         0         0         7         1         1         1         1
1
$   CMPFLG    IEVERP    BEAMIP     DCOMP      SHGE     STSSZ
         0         0         0         2         0         0
$
$
$---+----1----+----2----+----3----+----4----+----5----+----6----+----7-
---+----8
$
$ Parts
$
$---+----1----+----2----+----3----+----4----+----5----+----6----+----7-
---+----8
$
*PART
Sample
$      PID     SECID       MID     EOSID      HGID      GRAV    ADPOPT
         2         1         2         0
$
*PART
Inc_bar
$      PID     SECID       MID     EOSID      HGID      GRAV    ADPOPT
         1         1         1         0
$
*PART
Trans_bar
$      PID     SECID       MID     EOSID      HGID      GRAV    ADPOPT
         3         1         1         0
$
$
```

```
$---+----1----+----2----+----3----+----4----+----5----+----6----+----7-
---+----8
$
$ material/section data
$
$---+----1----+----2----+----3----+----4----+----5----+----6----+----7-
---+----8
$
$----- MATERIAL MODEL upper jaw and load cell-------------------------
--------
*MAT_USER_DEFINED_MATERIAL_MODELS
$      MID        RO        MT       LMC       NHV    IORTHO     IBULK
IG
         1, 2.700E-3,       50,      10,         2,        0,         2,
1
$    IVECT     IFAIL
         0,         1
$       G0        K0, inc_t1, trans_t1, e1, e2, e3, e4
    26.4e3, 68.853E3,  0.000, 0.000,1890241,1886445,2078792,2074850
$    rho,  cl
  2.70e-3, 0.0
$
$----- MATERIAL MODEL FOR SAMPLE----------------------------------------
----
*MAT_USER_DEFINED_MATERIAL_MODELS
$      MID        R0        MT       LMC       NHV    IORTHO     IBULK
IG
         2,  7.83E-03,      49,       27,        5,        0,         9,
1
$    IVECT     IFAIL
         0,         1
$       G0         A         B         N         C         M
78.74E+03,   165.00,   968.57,    00.206,      0.0147,    0.837
$       BK      TREF      EREF     TMELT     ITEMP        CP       IR0
MFLAG
   205E+03,       23,  1.0E-03,   1640.,     294,        450, 7.83E-03,
1
$   sy           siter,  stoler, arr_t1, elem1,   elem2, elem3, elem4
  360.0,         50,     1.e-2,   0.000,  7199,   7307,   7421,  7472
$ elem5, crvid,  cl
   7594,    3,  0.00
$
*SECTION_SOLID
$    SECID    ELFORM
         1         1
$
$---+----1----+----2----+----3----+----4----+----5----+----6----+----7-
---+----8
$
$ Contact Definitions
$
$---+----1----+----2----+----3----+----4----+----5----+----6----+----7-
---+----8
$
$
$---+----1----+----2----+----3----+----4----+----5----+----6----+----7-
---+----8
```

```
$
$ Load Curve and Boundary Conditions
$
$---+----1----+----2----+----3----+----4----+----5----+----6----+----7-
---+----8
$
$
*BOUNDARY_PRESCRIBED_MOTION_SET
$   typeID       DOF       VAD      LCID        SF       VID     DEATH
BIRTH
         8         1         0         1       1.0
0
$
$
$
$Include File Containing FE Mesh Here
$
*INCLUDE
tshb.in
*INCLUDE
disp.insert
$
$
*END
```

Zerilli-Armstrong Material Model for IFWI Model

```
$----- MATERIAL MODEL FOR SAMPLE-------------------------------------
----
*MAT_MODIFIED_ZERILLI_ARMSTRONG
$      MID        R0         G        E0         N      TROOM       PC
IG
         2,  7.83E-03, 78.74E+03,    .001,    0.288,      294,
$       C1        C2        C3        C4        C5        C6     EFAIL
VP
    162.81,  7829.52,   0.0138,  0.00032,   889.21,        0      0.18
0
$       B1        B2        B3        B4        G1        G2        G3
BULK
      1.00,        0,        0,        0,        1,        0,        0,
```